National Library of Canada
Acquisitions and Bibliographic Services Branch
395 Wellington Street
Ottawa, Ontario
K1A 0N4

Bibliothèque nationale du Canada
Direction des acquisitions et des services bibliographiques
395, rue Wellington
Ottawa (Ontario)
K1A 0N4

Your file Votre référence

Our file Notre référence

NOTICE

The quality of this microform is heavily dependent upon the quality of the original thesis submitted for microfilming. Every effort has been made to ensure the highest quality of reproduction possible.

If pages are missing, contact the university which granted the degree.

Some pages may have indistinct print especially if the original pages were typed with a poor typewriter ribbon or if the university sent us an inferior photocopy.

Reproduction in full or in part of this microform is governed by the Canadian Copyright Act, R.S.C. 1970, c. C-30, and subsequent amendments.

AVIS

La qualité de cette microforme dépend grandement de la qualité de la thèse soumise au microfilmage. Nous avons tout fait pour assurer une qualité supérieure de reproduction.

S'il manque des pages, veuillez communiquer avec l'université qui a conféré le grade.

La qualité d'impression de certaines pages peut laisser à désirer, surtout si les pages originales ont été dactylographiées à l'aide d'un ruban usé ou si l'université nous a fait parvenir une photocopie de qualité inférieure.

La reproduction, même partielle, de cette microforme est soumise à la Loi canadienne sur le droit d'auteur, SRC 1970, c. C-30, et ses amendements subséquents.

Canada

University of Alberta

Diffraction Contrast of Twin Boundaries: Effects of Nearly Common Reflections and Rigid Body Translation Vectors

By

Dan Seale

A thesis submitted to the Faculty of Graduate Studies and Research in partial fulfillment of the requirements for the degree of **Master of Science**

In

Solid State Physics

Department of Physics

Edmonton, Alberta

Fall 1993

National Library
of Canada

Acquisitions and
Bibliographic Services Branch

395 Wellington Street
Ottawa, Ontario
K1A 0N4

Bibliothèque nationale
du Canada

Direction des acquisitions et
des services bibliographiques

395, rue Wellington
Ottawa (Ontario)
K1A 0N4

Your file Votre référence

Our file Notre référence

The author has granted an irrevocable non-exclusive licence allowing the National Library of Canada to reproduce, loan, distribute or sell copies of his/her thesis by any means and in any form or format, making this thesis available to interested persons.

L'auteur a accordé une licence irrévocable et non exclusive permettant à la Bibliothèque nationale du Canada de reproduire, prêter, distribuer ou vendre des copies de sa thèse de quelque manière et sous quelque forme que ce soit pour mettre des exemplaires de cette thèse à la disposition des personnes intéressées.

The author retains ownership of the copyright in his/her thesis. Neither the thesis nor substantial extracts from it may be printed or otherwise reproduced without his/her permission.

L'auteur conserve la propriété du droit d'auteur qui protège sa thèse. Ni la thèse ni des extraits substantiels de celle-ci ne doivent être imprimés ou autrement reproduits sans son autorisation.

ISBN 0-315-88406-1

Canada

University of Alberta

Release Form

NAME OF AUTHOR: **Daniel Joseph Seale**

TITLE OF THESIS: **Diffraction Contrast of Twin Boundaries: Effects of Nearly Common Reflections and Rigid Body Translation Vectors**

DEGREE: **M. Sc.**

YEAR THIS DEGREE GRANTED: **1993**

Permission is hereby granted to the University of Alberta Library to reproduce single copies of this thesis and to lend or sell such copies for private, scholarly or scientific research purposes only.

The author reserves all other publication and other rights in association with the copyright in the thesis, and, except as hereinbefore provided, neither the thesis nor any substantial portion thereof may be printed or otherwise reproduced in any material form whatever without the author's prior written permission.

Dan Seale

113 18th Avenue
Estevan, Saskatchewan, Canada
S4A 1G5

October 8, 1993.

University of Alberta

Faculty of Graduate Studies and Research

The undersigned certify that they have read, and recommend to the Faculty of Graduate Studies and Research for acceptance, a thesis entitled **Diffraction Contrast of Twin Boundaries: Effects of Nearly Common Reflections and Rigid Body Translation Vectors**, submitted by **Dan Seale**, in partial fulfillment of the requirements for the degree of **Master of Science** in **Physics**.

Supervisor
S. S. Sheinin (Physics)

F. W. Jones (Physics)

J. A. Jung (Physics)

External Examiner
D. G. Ivey (Metallurgical Engineering)

Date: September 23, 1993.

Abstract

A theory for the diffraction contrast of twin boundaries which is applicable to pseudo-merohedral and pseudo-reticular merohedral twins, which have nearly common reflections, has been developed. This theory has been applied to the determination of the rigid body translation vector of such twins. It has been found that the rigid body translation vector of a twin boundary can be completely determined by comparing three experimental images of the boundary with simulated images which make use of the above theory.

It has also been found that the orientation of the twinned crystals must be determined correctly in order for the procedure to give correct results. Therefore, a method has been found for correctly identifying the matrix and twin zone axes, partly through the use of computer simulations of twin boundary diffraction patterns. Work has also been done to aid in finding the exact orientation, as given by the tie point projection, as accurately as possible.

In order to create simulated images of a twin boundary, the elastic and inelastic scattering factors of the constituent atoms or ions in the crystal must be known. Up to the present, there has been no source of inelastic scattering factors for ions. Since many crystals which exhibit pseudo-merohedral and pseudo-reticular merohedral twins are ceramics which are bonded ionically, a method for calculating the inelastic scattering factors for ions was developed. In the process, a new method for calculating the inelastic scattering factors for neutral atoms, which is more accurate and easier to use than existing methods, was also developed.

Acknowledgement

I would like to express my sincere gratitude to my supervisor, Dr. S. S. Sheinin, for his guidance and encouragement during the course of this work. I would also like to thank the University of Alberta and the Department of Physics for the financial support which was provided.

Table of Contents

1. Introduction 1

2. Bloch Wave Form of the Dynamical Theory of Electron Diffraction 4

2.1. Solution of the Schrödinger Wave Equation 4

2.1.1. Boundary Conditions **7**

2.1.2. Calculation of Wave Vectors and Bloch Wave Amplitudes **9**

2.1.3. High Energy Approximation **11**

2.1.4. Symmetrical Laue Conditions **11**

2.1.5. Calculation of Bloch Wave Excitation Coefficients **15**

2.1.6. Diffracted Beam Intensities **17**

2.2. Inelastic Scattering 19

2.2.1. Inelastic Scattering Processes **19**

2.2.2. Inclusion of Inelastic Scattering in the Standard Theory **20**

2.2.3. Calculation of Intensity Including Inelastic Scattering **22**

2.3. Relativistic Corrections to Theory 23

3. Application of Theory to Twinned Crystals 24

3.1. Twinned Crystals 24

3.1.1. Definition and Classification **24**

3.1.2. Origin of Twinned Crystals **25**

3.1.3. Crystal Structures Likely to Exhibit Twinning **28**

3.1.4. Examples of Twinned Crystals **30**

3.2. Diffraction Contrast From Twinned Crystals 34

3.2.1. Early Dynamical Theories of Twin Boundary Contrast. **34**

3.3. Twinned Crystals Having Common Reflections 39

3.3.1. Column Approximation **41**

3.3.2. Solution of the Schrödinger Wave Equation **45**

3.4. Twinned Crystals Having Almost Common Reflections. 51

3.4.1. Two Beam Approximation **57**

4. Practical Aspects of Calculations 65

4.1. Calculation of Elements of the A Matrix 65

4.1.1. Diagonal Elements of A Matrix **65**

4.1.2. Non-Diagonal Elements of the A matrix **68**

4.1.3. Elastic Scattering Factors **71**

4.1.4. Debye Waller Factor and Relativistic Correction **72**

4.1.5. Imaginary Part of Fourier Coefficients **73**

4.2. Determination of Matrix and Twin Zone Axes 75

4.2.1. Initial Method **75**

4.2.2. Crystals With an Element of Pseudo-Symmetry **76**

4.2.3. Distinguishing Between the Matrix and Twin Crystals **83**

4.3. Determination of Tie Point Projection 90

4.3.1. Intersection of Ewald Sphere With Laue Zones **90**

4.3.2. Calculation of Diffraction Pattern Intensities **96**

5. Inelastic Scattering Factors 105

5.1. Introduction 105

5.2. Neutral Atom Scattering Factors 108

5.2.1. Bird and King's Interpolation Method **108**

5.2.2. New Parametrization of Inelastic Scattering Factors **109**

5.3. Ionic Inelastic Scattering Factors 121

5.3.1. Existing Form of Scattering Factors **121**

5.3.2. New Form of Ionic Inelastic Scattering Factors **123**

5.3.3. Ionic n Parameters **124**

5.3.4. Ionic b Parameters **126**

5.3.5. Ionic A Parameters **129**

5.3.6. Agreement With Existing Calculated Values **132**

5.4. Summary 137

6. Results and Conclusions 138

6.1. Determination of Rigid Body Translation Vector 138

6.1.1. Basic Method of Determination **138**

6.1.2. Effects of Inaccurate Tie Point Projections **161**

6.2. Conclusions and Recommendations 175

References: 178

Appendix A: Calculation of Excitation Coefficients 181

Appendix B: Principles of Twin Boundary Diffraction Patterns 187

List of Tables

Table 4.1. Geometrical diffraction pattern parameters for two zone axis families. **80**

Table 4.2. Diffraction pattern intensities in three different approximations. **104**

Table 5.1. Parameters for the calculation of A(B), needed for inelastic scattering factor calculation. **113**

Table 5.2. Parameters for the calculation of b(B) and n(B), needed for inelastic scattering factor calculation. **117**

Table 5.3. m_n parameters, needed for inelastic scattering factor calculation, for common ions. **126**

Table 5.4. m_b parameters, needed for inelastic scattering factor calculation, for common ions. **129**

Table 5.5. m_A parameters, needed for inelastic scattering factor calculation, for common ions. **132**

List of Figures

Fig. 2.1. Two-beam dispersion surface diagram for the non-symmetrical Laue case. **10**

Fig. 2.2. Two-beam dispersion surface diagram for the symmetrical Laue case. **13**

Fig. 3.1. Reflection twin. **25**

Fig. 3.2. Deformation twinning. **27**

Fig. 3.3. Twinned crystal with a coincidence site lattice. **28**

Fig. 3.4. Merohedral twin. **29**

Fig. 3.5. Stacking sequence for FCC crystals looking down the [111] direction. **31**

Fig. 3.6. Superimposed [001] planes of the reciprocal lattices of two $Y_1Ba_2Cu_3O_{7-\delta}$ crystals which are in a twin orientation to each other with a twin plane of (110). **32**

Fig. 3.7. Positions of matrix and twin crystals. **34**

Fig. 3.8. Diffraction pattern from a twin boundary in copper for a matrix zone axis of the [123] and a twin plane of (111). **35**

Fig. 3.9. Diffraction pattern from the (110) twin boundary of Aragonite for a matrix zone axis of [001]. **37**

Fig. 3.10. Diffraction pattern from a twin boundary in copper for a matrix zone axis of [123] and a twin plane of (111). **40**

Fig. 3.11. Two-beam dispersion surface diagram for the twin crystal for the non-symmetrical Laue case. **42**

Fig. 3.12. Column approximation. **43**

Fig. 3.13. Relation between the validity of the column approximation and the small Bragg angles, θ_B, for high energy electrons. **43**

Fig. 3.14. Assumed twin boundary orientation under the column approximation. **44**

Fig. 3.15. Rigid body translation vector. **45**

Fig. 3.16. Diffraction pattern from a (110) twin boundary in $Y_1Ba_2Cu_3O_{7-\delta}$ for a matrix zone axis of [001] including a typical dynamically coupled set. **52**

Fig. 3.17. Unit cell of the high temperature superconductor, $Y_1Ba_2Cu_3O_{7-\delta}$. **55**

Fig. 3.18. Twin boundary for the superconductor $Y_1Ba_2Cu_3O_{7-\delta}$ assuming a body translation vector of 0. **56**

Fig. 3.19. Reflections used in the two beam approximation. **58**

Fig. 4.1. Plot of the (111) reciprocal lattice plane of $Y_1Ba_2Cu_3O_{7-\delta}$ including the tie point projection of (0.8, 1.2, -2) and the intersection of the Ewald sphere with the zero order Laue zone. **66**

Fig. 4.2. Simulated diffraction pattern from a (110) twin boundary of $Y_1Ba_2Cu_3O_{7-\delta}$ for a matrix zone axis of [131]. **79**

Fig. 4.3. Simulated diffraction pattern from a (110) twin boundary of $Y_1Ba_2Cu_3O_{7-\delta}$ for a matrix zone axis of $[1\bar{3}1]$. **82**

Fig. 4.4. Simulated diffraction pattern from a (110) twin boundary of $Y_1Ba_2Cu_3O_{7-\delta}$, including combination reflections, for a matrix zone axis of [131]. **84**

Fig. 4.5. Simulated diffraction pattern from a (110) twin boundary of $Y_1Ba_2Cu_3O_{7-\delta}$ for a matrix zone axis of [131] including the tie point projection of (5.0, 1.33, 1.0) and the intersection of the Ewald sphere with the zero order Laue zone. **86**

Fig. 4.6. Simulated bright field images of a (110) twin boundary in $Y_1Ba_2Cu_3O_{7-\delta}$ for different inclinations of the twin boundary. **87**

Fig. 4.7. Simulated dark field images of a (110) twin boundary in $Y_1Ba_2Cu_3O_{7-\delta}$ for different inclinations of the twin boundary. **88**

Fig. 4.8. Illustration of the different points of intersection of the Ewald sphere with the matrix and twin zero order Laue zones. **91**

Fig. 4.9. Illustration of the calculation of the radius of the intersection of the Ewald sphere with the N-th order Laue zone. **93**

Fig. 4.10. Simulated diffraction pattern from a (110) twin boundary of $Y_1Ba_2Cu_3O_{7-\delta}$ for a matrix zone axis of [131] including the tie point projection of (1.0 0.333 -2.0) and the intersection of the Ewald sphere with the zero order Laue zones. **94**

Fig. 4.11. Simulated diffraction pattern from a (110) twin boundary of $Y_1Ba_2Cu_3O_{7-\delta}$ for a matrix zone axis of [131] including the tie point projection of (-6.0 1.13 2.62) and the intersection of the Ewald sphere with the zero and first order Laue zones. **95**

Fig. 4.12. Plot of beam intensity as a function of maximum thickness. **100**

Fig. 4.13. Plot of normalized beam intensity as a function of maximum thickness. **102**

Fig. 5.1. Variation of inelastic scattering factor as a function of s for atoms having atomic numbers ranging from 30 to 70 for a Debye parameter of 0.7 as given by Bird and King. **108**

Fig. 5.2. Variation of inelastic scattering factor as a function of s for atoms having atomic numbers ranging from 30 to 70 for a Debye parameter of 0.05 as given by Bird and King. **109**

Fig. 5.3. Variation of inelastic scattering factor as a function of s for atoms having atomic numbers ranging from 30 to 70 for a Debye parameter of 0.7 as given by present method. **111**

Fig. 5.4. Variation of inelastic scattering factor as a function of s for Zr, (Z = 40), for Debye parameters of 0.05, 0.3, and 1.3 as given by present method. **112**

Fig. 5.5. Plot of the difference between the corrected n value for a given ion, $n_{IC}(B)$, and the neutral atom value for the same atom as derived from Bird and King's data, $n_B(B)$, as a function of Debye parameter. **125**

Fig. 5.6. Plot of the difference between the neutral atom b values using Radi's data, $b_R(B)$, and using Bird and King's data, $b_B(B)$, as a function of Debye parameter. **127**

Fig. 5.7. Plot of the difference between the ionic b values using Radi's data, $b_I(B)$, and the neutral atom values, $b_B(B)$, as a function of Debye parameter. **128**

Fig. 5.8. Plot of $(A_{IC}(B) - A_B(B))/A_B(B)$ as a function of Debye parameter. **130**

Fig. 5.9. Plot of $\langle(A_{IC}(B) - A_B(B))/A_B(B)\rangle/(-\Delta Z)$ as a function of atomic number. **131**

Fig. 5.10. Plot of imaginary part of Fourier coefficient as a function of scattering vector, s, for the ionic crystal NaF. **133**

Fig. 5.11. Plot of imaginary part of Fourier as a function of scattering vector, s, for the ionic crystal RbF. **135**

Fig. 6.1. Simulated diffraction pattern from a (110) twin boundary of $Y_1Ba_2Cu_3O_{7-\delta}$ for a matrix zone axis of [131] and a matrix tie point projection of (-6.0 1.13 2.62). **139**

Fig. 6.2. Simulated bright field twin boundary images for a rigid body translation vector ranging from [0.5, 0, 0] to [0.5, 0.75, 0]. The matrix zone axis is [131] and the matrix tie point projection is (-6.0 1.13 2.62). **140**

Fig. 6.3. Simulated bright field twin boundary images for a rigid body translation vector ranging from [0, 0, 0] to [0, 0.75, 0]. The matrix zone axis is [131] and the matrix tie point projection is (-6 1.13 2.62). **141**

Fig. 6.4. Simulated bright field twin boundary images for a rigid body translation vector ranging from [0.5, 0.5, 0.167] to [0.5, 0.5, 0.667]. The matrix zone axis is [131] and the matrix tie point projection is (-6 1.13 2.62). **142**

Fig. 6.5. Simulated bright field twin boundary images based on two-beam and systematic row reflection calculations for a rigid body translation vector of [0.5, 0.5, 0]. The matrix zone axis is [131] and the matrix tie point projection is (-6 1.13 2.62). **147**

Fig. 6.6. Simulated dark field twin boundary images for a rigid body translation vector ranging from [0.5, 0, 0] to [0.5, 0.75, 0]. The matrix zone axis is [131] and the matrix tie point projection is (-6.0 1.13 2.62). **148**

Fig. 6.7. Simulated diffraction pattern from a (110) twin boundary of $Y_1Ba_2Cu_3O_{7-\delta}$ for a matrix zone axis of [101] and a matrix tie point projection of (-2.2 0.5 2.2). **149**

Fig. 6.8. Simulated bright field twin boundary images for a rigid body translation vector ranging from [0.5, 0, 0] to [0.5, 0.75, 0]. The matrix zone axis is [131] and the matrix tie point projection is (-2.2 0.5 2.2). **151**

Fig. 6.9. (a) One dimensional plot of bright field intensity as a function of distance along the exit surface for a constant total crystal thickness, t, of 600 Å. The rigid body translation vector ranges from [0.5, 0.25, 0] to [0.5, 0.75, 0]. The matrix zone axis is [131] and the matrix tie point projection is (-2.2 0.5 2.2).
(b) Two dimensional simulated bright field image for the same orientation as in (a) and a rigid body translation vector of [0.5, 0.5, 0]. **152**

Fig. 6.10. Simulated dark field twin boundary images for a rigid body translation vector ranging from [0.5, 0, 0] to [0.5, 0.75, 0]. The matrix zone axis is [101] and the matrix tie point projection is (-2.2 0.5 2.2). **153**

Fig. 6.11. Simulated diffraction pattern from a (110) twin boundary of $Y_1Ba_2Cu_3O_{7-\delta}$ for a matrix zone axis of [211] and a matrix tie point projection of (-0.9 2.67 -0.87). **155**

Fig. 6.12. Simulated bright field twin boundary images for a rigid body translation vector ranging from [0.5, 0, 0] to [0.5, 0.75,0]. The matrix zone axis is [211] and the matrix tie point projection is (-0.9 2.67 -0.87). **156**

Fig. 6.13. Simulated bright field twin boundary images for a rigid body translation vector ranging from [0.3, 0.7, 0] to [0.3, 0.7, 0.5]. The matrix zone axis is [211] and the matrix tie point projection is (-0.9 2.67 -0.87). **157**

Fig. 6.14. Simulated dark field twin boundary images for a rigid body translation vector ranging from [0.5, 0, 0] to [0.5, 0.75, 0]. The matrix zone axis is [211] and the matrix tie point projection is (-0.9 2.67 -0.87). **159**

Fig. 6.15. Simulated diffraction pattern from a (110) twin boundary of $Y_1Ba_2Cu_3O_{7-\delta}$ for a matrix zone axis of [131] and a matrix tie point projection of (-4.0 0.79 1.63). **162**

Fig. 6.16. Simulated bright field twin boundary images for a rigid body translation vector ranging from [0.5, 0, 0] to [0.5, 0.75, 0]. The matrix zone axis is [131] and the matrix tie point projection is (-4.0 0.79 1.63). **163**

Fig. 6.17. Simulated dark field twin boundary images for a rigid body translation vector ranging from [0.5, 0, 0] to [0.5, 0.75, 0]. The matrix zone axis is [131] and the matrix tie point projection is (-4.0 0.79 1.63). **164**

Fig. 6.18. Simulated diffraction pattern from a (110) twin boundary of $Y_1Ba_2Cu_3O_{7-\delta}$ for a matrix zone axis of [101] and a matrix tie point projection of (-2.2 0.75 2.2). **166**

Fig. 6.19. Simulated bright field twin boundary images for a rigid body translation vector ranging from [0.5, 0, 0] to [0.5, 0.75, 0]. The matrix zone axis is [101] and the matrix tie point projection is (-2.2 0.75 2.2). **167**

Fig. 6.20. Simulated bright field twin boundary images for a rigid body translation vector ranging from [0.5, 0.4, 0] to [0.5, 0.55, 0]. The matrix zone axis is [101] and the matrix tie point projection is (-2.2 0.75 2.2). **168**

Fig. 6.21. Simulated dark field twin boundary images for a rigid body translation vector ranging from [0.5, 0, 0] to [0.5, 0.75, 0]. The matrix zone axis is [101] and the matrix tie point projection is (-2.2 0.75 2.2). **170**

Fig. 6.22. Simulated diffraction pattern from a (110) twin boundary of $Y_1Ba_2Cu_3O_{7-\delta}$ for a matrix zone axis of [211] and a matrix tie point projection of (-1.9 3.56 0.24). **171**

Fig. 6.23. Simulated bright field twin boundary images for a rigid body translation vector ranging from [0.5, 0, 0] to [0.5, 0.75, 0]. The matrix zone axis is [211] and the matrix tie point projection is (-1.9 3.56 0.24). **172**

Fig. 6.24. Simulated dark field twin boundary images for a rigid body translation vector ranging from [0.5, 0, 0] to [0.5, 0.75, 0]. The matrix zone axis is [211] and the matrix tie point projection is (-1.9 3.56 0.24). **173**

Fig. B.1. The rotation of a matrix direction, [uvw], through 180 degrees about the twin axis. **188**

Fig. B.2. Diffraction pattern of $Y_1Ba_2Cu_3O_{7-\delta}$ for a matrix zone axis of [101] and a twin zone axis of $[01\bar{1}]$. **192**

Fig. B.3. The reflection of a matrix vector, [uvw], across a twin plane. **194**

1. Introduction

The use of the electron microscope is an important component in the study of the structure of materials. It is particularly useful in the characterization of crystal defects. One such defect which is commonly studied in the electron microscope is the twin boundary. A twin boundary is the boundary between two crystals which are orientated relative to each other according to some twin law. It is the purpose of this thesis to develop a general theory of electron diffraction contrast of twin boundaries, and to illustrate one practical application of the theory. This is the determination of the rigid body translation vector, which is a vector describing the position of one of the crystals with respect to the other. The knowledge of this translation vector is important in that it gives information regarding the structure of the twin boundary. This boundary structure, in turn, gives insight into the mechanism for the formation of the twins, and the effects of the twin boundaries on the mechanical and electrical properties of the material.

There have been several previous theories of twin boundary diffraction contrast. The earliest attempts to explain the contrast observed in the electron microscope were based on the assumption that only two beams were excited in each of the two crystals, the transmitted one, and one diffracted beam. Gevers, et. al.[1] derived a two beam theory which became the basis of a set of predictions, by Amelinckx and Van Landuyt[2], of the form of the twin boundary image obtained under certain specific diffraction conditions. This form of the theory allowed for the possibility that two beams, one from each crystal, which are travelling in slightly different directions, might pass through the objective aperture, and go on to form the image. However, it neglected many of the effects brought about by the difference in the directions of the two beams, and therefore can lead to inaccurate results.

The first theory in which many different beams could be taken into account in the calculation of image contrast was given by Sheinin and Corbett[3]. This version of the theory suffered from the fact that it did not account for common reflections. Common reflections are reflections which originate from different sides of the twin boundary, but from lattice planes which are common to both crystals. Therefore, the two diffracted beams are travelling in exactly the same direction. Because of the nature of the twin laws which determine

the orientations of the two crystals with respect to each other, these common reflections occur frequently and can have a significant effect on the image. Sutton and Pond[4] then developed a version of the theory which takes common reflections into account. The approach used by Sutton and Pond had a number of problems, however. As a result, their theory could give inaccurate results unless a large number of reflections were taken into account. Their version of the theory also required the diagonalization of a large number of matrices, making it somewhat inefficient. Sheinin and Perez[5], therefore developed a new version of the theory which addressed all of the problems of the version by Sutton and Pond, and gave correct, many beam, results for the diffraction contrast of twin boundaries for twins which have common reflections.

Even this theory could not be applied in many cases, however. This is because, in many crystals, especially those with a complex structure, the twins contain not only common reflections, but also nearly common reflections, which correspond to beams originating on different sides of the twin boundary which are travelling in almost, but not exactly, the same direction. The effect of these reflections is that, if the objective aperture of the microscope is centered around a particular reflection, there will usually be other beams, which are not travelling in the same direction, but which also pass through the aperture and contribute to the image. Therefore, a new version of the theory has been developed in this thesis to give the diffraction contrast of twin boundaries for twins which have these nearly common reflections.

In this thesis, a brief summary of the Bloch wave form of the dynamical theory of electron diffraction, and some of the approximations which are usually made in the theory, is given in Chapter 2. Chapter 3 deals with the application of this theory to the study of twin boundaries. Section 3.1 gives an introduction to twinned crystals and their geometry. An explanation of the approaches taken in the early, many beam, versions of the theory of twin boundary contrast is given in section 3.2. In order to develop the theory for twins which contain either common, or nearly common, reflections, the theory given by Sheinin and Perez for twins with common reflections had to be reformulated. This is done in section 3.3. Once this is done, the extension to twins which may also contain nearly common reflections can be obtained in a reasonably straightforward manner. This is done in section 3.4.

In order to do theoretical simulations of twin boundary contrast, there is a number of practical considerations which must be addressed. These are dealt with in Chapters 4 and 5. One of the most important is the determination of the orientations of the two crystals. In the case of twinned crystals which have nearly common reflections, this determination is made much more difficult than usual because of the nearly symmetric properties of the two crystals and their orientations. This problem is the subject of section 4.2. Another important consideration in these calculations is that it is crucial to know which crystal is the one that the electrons enter first, and which is the one from which the electrons emerge. A new method for making this determination is given in section 4.2.2.

Another important requirement for the theoretical calculations is that the elastic and inelastic scattering factors of the atoms which make up the crystal must be known. In many cases, particularly in the complex crystal structures which tend to produce twins having nearly common reflections, the crystal is actually made up of ions. It is therefore important to have the correct scattering factors for the ions involved. Up to the present, there has been no source of inelastic scattering factors for ions. Therefore, a new method for calculating these inelastic scattering factors for ions has been developed, and is given in Chapter 5. In the process, a new method for calculating the scattering factors for neutral atoms has also been developed, which is simpler, and more accurate, than existing methods.

In Chapter 6, a method for finding the rigid body translation vector of a twinned crystal is demonstrated. It is based on comparing experimental images of twin boundaries with theoretical simulations which employ the theory developed in section 3.2.3. The method allows the rigid body translation vector to be completely defined through the use of twin boundary images for three different crystal orientations.

2. Bloch Wave Form of the Dynamical Theory of Electron Diffraction

2.1. Solution of the Schrödinger Wave Equation

In this form of the theory of electron diffraction, which was originally developed by Bethe[6], the Schrödinger equation is solved for an electron in a crystal potential. For non-relativistic electrons, the steady-state wave function, $\Psi(\vec{r})$, is given by Schrödinger's equation:

$$\nabla^2\Psi(\vec{r}) + \frac{8\pi^2 me}{h^2}[E + V(\vec{r})]\Psi(\vec{r}) = 0 \tag{2.1}$$

For the vacuum outside of a crystal, $V(\vec{r}) = 0$, and the solution of this equation is given by:

$$\Psi(\vec{r}) = \exp(2\pi i\vec{\chi}\cdot\vec{r}) \tag{2.2}$$

where the magnitude of $\vec{\chi}$ is given by:

$$\frac{h^2\chi^2}{2m} = eE \tag{2.3}$$

and E is the voltage through which the incident electron has been accelerated.

In order to find the wavefunction inside the crystal, the Schrödinger equation must be solved for a potential made up of a superposition of all of the atomic potentials. Since this potential has the same periodicity as the lattice, it can be expanded as a Fourier series:

$$V(\vec{r}) = \sum_g V_g \exp(2\pi i\vec{g}\cdot\vec{r})$$

$$= \frac{h^2}{2me}\sum_g U_g \exp(2\pi i\vec{g}\cdot\vec{r}) \tag{2.4}$$

where each term in the summation corresponds to a reciprocal lattice vector, $\vec{g}$. For a periodic potential such as this, the solution must have the same periodicity. Such a solution is called a Bloch wave and has the following form:

$$\Psi(\vec{r}) = b(\vec{k}, \vec{r}) = \sum_g C_g(\vec{k}) \exp[2\pi i (\vec{k} + \vec{g}) \cdot \vec{r}] \tag{2.5}$$

If this solution is substituted into the Schrödinger equation, the following equation is obtained:

$$4\pi \Big[\sum_g \Big[\chi^2 + U_0 - (\vec{k} + \vec{g})^2 \Big] C_g(\vec{k}) \exp[2\pi i (\vec{k} + \vec{g}) \cdot \vec{r}]$$

$$+ \sum_{h \neq 0} \sum_{g'} U_h C_{g'}(\vec{k}) \exp[2\pi i (\vec{k} + \vec{g}' + \vec{h}) \cdot \vec{r}] \Big] = 0$$

In the second term on the left hand side of this equation, $\vec{g}'$ is summed over all reciprocal lattice vectors. Therefore, the summation can be done over a different reciprocal lattice vector, $\vec{g}$, which is related to $\vec{g}'$ by:

$$\vec{g} = \vec{g}' + \vec{h} \Rightarrow \vec{g}' = \vec{g} - \vec{h}$$

and the second term becomes:

$$\sum_{h \neq 0} \sum_g U_h C_{g-h}(\vec{k}) \exp[2\pi i (\vec{k} + \vec{g}) \cdot \vec{r}]$$

The summation over h is also over all reciprocal lattice vectors, so h can be replaced by a different reciprocal lattice vector, h′, which is given by:

$$h' = g - h \Rightarrow h = g - h'$$

When the prime on the h is dropped, the result is the following:

$$\sum_g \Big[\Big[\chi^2 + U_0 - (\vec{k} + \vec{g})^2 \Big] C_g(\vec{k}) + \sum_{h \neq g} U_{g-h} C_h(\vec{k}) \Big] \exp[2\pi i (\vec{k} + \vec{g}) \cdot \vec{r}] = 0 \tag{2.6}$$

Since this equation must hold for all vectors, $\vec{r}$, the coefficients of the term, $\exp[2\pi i (\vec{k} + \vec{g}) \cdot \vec{r}]$, must all be equal to zero. Therefore, the following set of equations

must be satisfied:

$$\left[K^2 - (\vec{k} + \vec{g})^2\right] C_g(\vec{k}) + \sum_{h \neq g} U_{g-h} C_h(\vec{k}) = 0 \qquad (2.7)$$

where

$$K^2 = \chi^2 + U_0 \qquad (2.8)$$

If N reciprocal lattice vectors, $\vec{g}$, are taken into account, there are N equations in the set. This set of equations can be put into matrix form:

$$\begin{bmatrix} K^2 - (\vec{k} + \vec{g}_1)^2 & U_{-g_2} & U_{-g_3} & \cdots & \cdots & \cdots \\ U_{g_2} & K^2 - (\vec{k} + \vec{g}_2)^2 & U_{g_2 - g_3} & & & \\ U_{g_3} & U_{g_3 - g_2} & K^2 - (\vec{k} + \vec{g}_1)^2 & & & \\ \cdots & & & \cdots & & \\ \cdots & & & & \cdots & \end{bmatrix} \begin{bmatrix} C_{g_1}(\vec{k}) \\ C_{g_2}(\vec{k}) \\ C_{g_3}(\vec{k}) \\ \cdots \\ \cdots \end{bmatrix} = 0 \qquad (2.9)$$

A solution to this set of equations will exist only if the determinant of the matrix is equal to zero.

$$\mathrm{DET}\begin{bmatrix} K^2 - (\vec{k} + \vec{g}_1)^2 & U_{-g_2} & U_{-g_3} & \cdots & \cdots & \cdots \\ U_{g_2} & K^2 - (\vec{k} + \vec{g}_2)^2 & U_{g_2 - g_3} & & & \\ U_{g_3} & U_{g_3 - g_2} & K^2 - (\vec{k} + \vec{g}_1)^2 & & & \\ \cdots & & & \cdots & & \\ \cdots & & & & \cdots & \end{bmatrix} = 0 \qquad (2.10)$$

Before this equation can be solved, the boundary conditions which must be met by the wavefunction, $\Psi(\vec{r})$, and, hence, the wave vector, $\vec{k}$, must be determined. This will be done in the next section, and the conditions which result will be used along with eq. 2.10 to find the wave vectors which can satisfy eq. 2.9.

2.1.1. Boundary Conditions

The boundary condition which is imposed is that the wavefunction, $\Psi(\vec{r})$, must be continuous at the crystal surface. The wavefunction of the incident beam is given by eq. 2.2:

$$\Psi_{out}(\vec{r}) = \exp(2\pi i \vec{\chi} \cdot \vec{r}) \tag{2.2}$$

where the subscript, out, refers to the fact that this is the wavefunction outside of the crystal on the entrance side. When eq. 2.10 is solved, the result will be N different solutions for $\vec{k}$, each of which corresponds to a different Bloch wave solution to Schrödinger's equation. The wavefunction inside the crystal is given by a linear combination of these N Bloch wave solutions:

$$\begin{aligned} \Psi_{in}(\vec{r}) &= \sum_i X^{(i)} b^{(i)}(k^{(i)}, \vec{r}) \\ &= \sum_{i,g} X^{(i)} C_g^{(i)}(\vec{k}^{(i)}) \exp\left[2\pi i (\vec{k}^{(i)} + \vec{g}) \cdot \vec{r}\right] \end{aligned} \tag{2.11}$$

where the $X^{(i)}$'s are referred to as the Bloch wave excitation coefficients since they determine the extent to which each Bloch wave is excited in the crystal. These two wavefunctions must be equal for any vector, $\vec{r}_{en}$, which defines a position on the entrance surface of the crystal. Therefore, the following relation must hold:

$$\exp(2\pi i \vec{\chi} \cdot \vec{r}_{en}) = \sum_{i,g} X^{(i)} C_g^{(i)} \exp\left[2\pi i (\vec{k}^{(i)} + \vec{g}) \cdot \vec{r}_{en}\right] \tag{2.12}$$

It is now useful to resolve the vectors in eq. 2.12 into components parallel to the crystal surface, labelled by the subscript, $\parallel$, and components normal to the surface, labelled by the subscript, $\perp$. i.e.

$$\vec{r}_{en} = \vec{r}_{en\parallel} + \vec{r}_{en\perp}$$

$$\vec{\chi} = \vec{\chi}_{\parallel} + \vec{\chi}_{\perp}$$

$$\vec{k}^{(i)} = \vec{k}_{\parallel}^{(i)} + \vec{k}_{\perp}^{(i)}$$

and therefore, eq. 2.12 can be rewritten as:

$$\exp(2\pi i \chi_\perp r_{en\perp})$$

$$= \sum_{i,g} X^{(i)} C_g^{(i)} \exp\left[2\pi i \left(k_\perp^{(i)} + g_\perp\right) r_{en\perp}\right] \exp\left[2\pi i \left(\hat{k}_\parallel^{(i)} + \hat{g}_\parallel - \vec{\chi}_\parallel\right) \cdot \hat{r}_{en_\parallel}\right]$$

where both sides of the equation have been divided by $\exp(2\pi i \vec{\chi}_\parallel \cdot \hat{r}_{en\parallel})$. This equation must hold at all points on the entrance surface. But $\hat{r}_{en_\parallel}$ is different at all of these points. Therefore, there are N^2 terms on the right hand side of this equation, each of which changes as the position on the entrance surface changes. The only way to solve this problem is to make most of these terms add up to zero. However, at least one term must be excluded from this sum and set to be equal to $\exp(2\pi i \chi_\perp r_{en\perp})$. Thus, at least one term must be constant, regardless of position on the entrance surface. This is accomplished by letting $\hat{k}_\parallel^{(i)} + \hat{g} + \vec{\chi}_\parallel = 0$ for some reciprocal lattice vector, $\hat{g}$, and some Bloch wave, i. Physically, it makes the most sense to choose the $\hat{g} = 0$ terms, and let it be true for all i. Therefore:

$$\hat{k}_\parallel^{(i)} - \vec{\chi}_\parallel = 0 \tag{2.13}$$

for all i. When this is assumed, the following equation results:

$$\exp(2\pi i \chi_\perp r_{en\perp}) = \sum_i X^{(i)} C_0^{(i)} \exp(2\pi i k_\perp^{(i)} r_{en\perp})$$

$$+ \sum_{g \neq 0} \sum_i X^{(i)} C_g^{(i)} \exp\left[2\pi i \left(k_\perp^{(i)} + g_\perp\right) r_{en\perp}\right] \exp\left(2\pi i \hat{g}_\parallel \cdot \hat{r}_{en\parallel}\right)$$

The second set of terms on the right hand side still involve $\exp(2\pi i \hat{g}_\parallel \cdot \hat{r}_{en\parallel})$. Therefore each of these terms is still different at all points of the entrance surface. The only way to make these terms add up to zero is to make each term in the summation over g equal to zero. Therefore:

$$\sum_i X^{(i)} C_g^{(i)} \exp\left[2\pi i \left(k_\perp^{(i)} + g_\perp\right) r_{en\perp}\right] \exp\left(2\pi i \hat{g}_\parallel \cdot \hat{r}_{en\parallel}\right) = 0 \qquad g \neq 0$$

Each equation can be divided by $\exp(2\pi i\vec{g}\cdot\vec{r}_{en})$ to get the following set of relations:

$$\exp(2\pi i\chi_{\perp}r_{en\perp}) = \sum_i X^{(i)}C_0^{(i)}\exp(2\pi ik_{\perp}^{(i)}r_{en\perp})$$
$$0 = \sum_i X^{(i)}C_g^{(i)}\exp(2\pi ik_{\perp}^{(i)}r_{en\perp}) \qquad g \neq 0 \tag{2.14}$$

These boundary conditions will be used later, in section 2.1.5, to calculate the Bloch wave excitation coefficients, $X^{(i)}$. In the mean time, a set of restrictions on the wave vectors, $\vec{k}^{(i)}$, has been found and is expressed in eq. 2.13. They state that the tangential components of all wave vectors on either side entrance surface must be equal. Thus, all that remains to be found in eq. 2.10 is the component of $\vec{k}$ which is normal to the crystal entrance surface.

2.1.2. Calculation of Wave Vectors and Bloch Wave Amplitudes

In section 2.1.1, the magnitude of K was defined by eq. 2.8. The vector, $\vec{K}$, can now be completely defined to be a vector with this amplitude and a direction defined by the restriction that its component parallel to the entrance surface of the crystal is equal to the tangential component of $\vec{\chi}$. Since the Bloch wave vectors, $\vec{k}^{(i)}$, have the same tangential component as $\vec{\chi}$, they can be expressed as follows:

$$\vec{k}^{(i)} = \vec{K} + \gamma^{(i)}\hat{n} \tag{2.15}$$

where $\hat{n}$ is a unit vector which is normal to the crystal entrance surface, and $\gamma^{(i)}$ is a number which must be determined.

The condition of tangential equality of wave vectors on either side of the entrance surface can now be represented graphically. This is shown in Figure 2.1. In order to ensure that all wave vectors have the same component parallel to the entrance surface, a line which is normal to the entrance surface of the crystal is drawn through the tail of the vacuum wave vector, $\vec{\chi}$. If all other wave vectors, $\vec{K}$, $\vec{k}^{(i)}$, also start somewhere on this line and extend to the origin, their tangential components must be equal to that of $\vec{\chi}$. The Ewald sphere is centered at the starting point of $\vec{K}$ and has a radius of K. The deviation parameter, s_g, is defined as the distance from the reciprocal lattice point, $\vec{g}$, to the Ewald sphere along a direction normal to the entrance surface. It is defined to be positive when the reciprocal

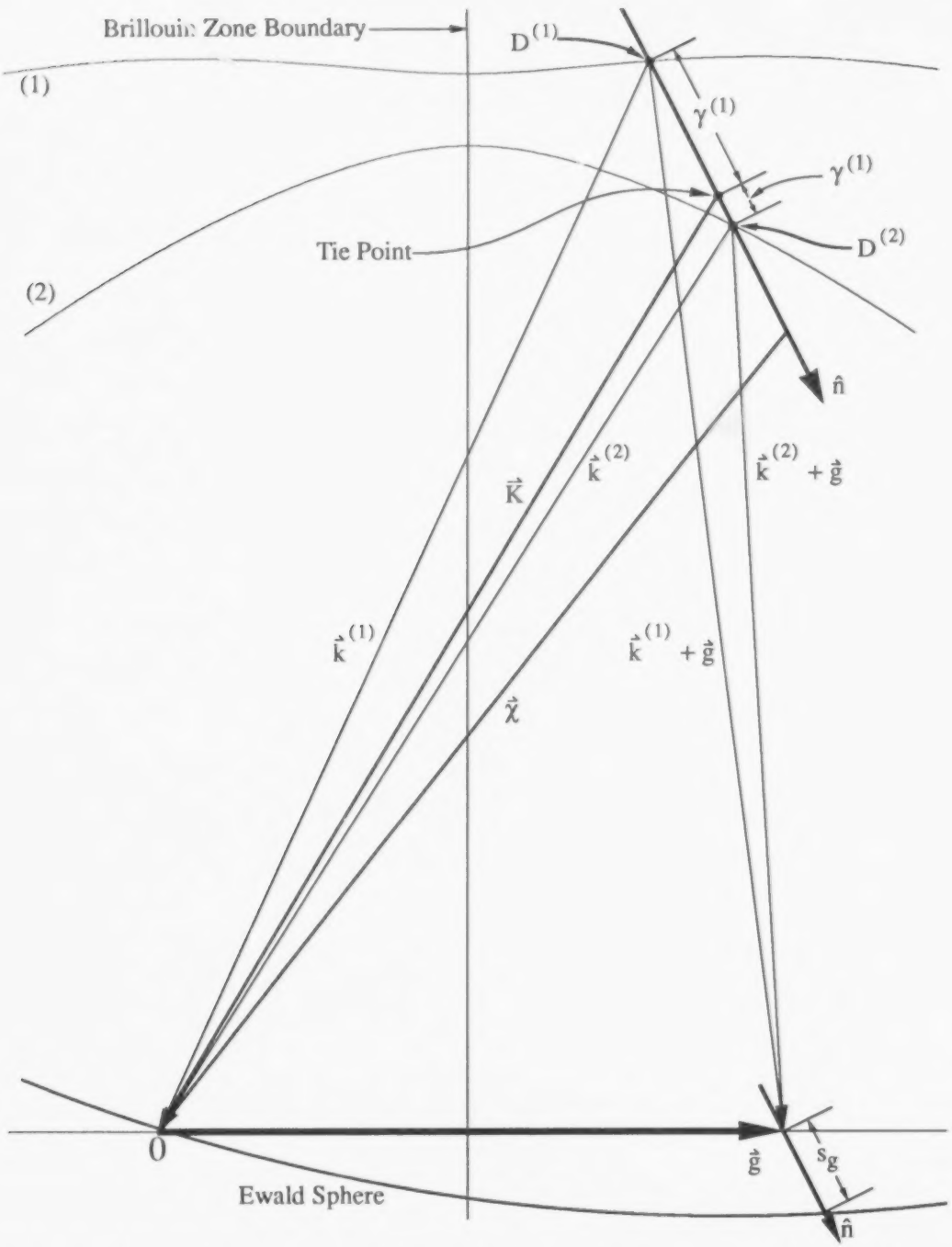

Fig. 2.1. Dispersion surface calculated using two beams -- 0 and g. $D^{(1)}$ and $D^{(2)}$ are called the excitation points and they are the starting points of $\vec{k}^{(1)}$ and $\vec{k}^{(2)}$ respectively. $\hat{n}$ is the normal to the entrance surface. S_g is the distance, in the direction, $\hat{n}$, from g to the Ewald sphere. $D^{(1)}$ and $D^{(2)}$ lie on the line normal to the entrance surface which goes through the starting point of $\vec{K}$.

lattice point is inside the Ewald sphere, as shown, and negative when outside the Ewald sphere. When the wave vectors, $\vec{k}^{(i)}$, have been determined for all possible crystal orientations, their starting points define the dispersion surface. This surface, which is similar to the Fermi surface for low energy electrons, defines all of the possible wave vectors for electrons of a given energy. A small portion of two branches of the dispersion surface are shown in Fig. 2.1.

2.1.3. High Energy Approximation

The diagonal terms in the matrix in eq. 2.9 can now be evaluated. Referring to Fig. 2.1, and using the law of cosines, it can be shown that:

$$(\vec{k}^{(i)} + \vec{g})^2 = K^2 + (\gamma^{(i)} - s_g)^2 + 2K(\gamma^{(i)} - s_g)\cos\theta_g \tag{2.16}$$

where θ_g is the angle between $\vec{K} + \vec{g}$ and the crystal surface normal, $\hat{n}$. Therefore, the diagonal term in eq. 2.9 becomes:

$$\begin{aligned} K^2 - (\vec{k}^{(i)} + \vec{g})^2 &= 2K(s_g - \gamma^{(i)})\cos\theta_g - (\gamma^{(i)} - s_g)^2 \\ &= 2K(s_g - \gamma^{(i)})\left[\cos\theta_g - \left(\frac{s_g - \gamma^{(i)}}{2K}\right)\right] \end{aligned} \tag{2.17}$$

The first approximation which must be used is the high energy approximation. The main idea of this approximation is that, because of the high energy of the electrons, it can be assumed that $K \gg s_g - \gamma^{(i)}$. Therefore:

$$\frac{s_g - \gamma^{(i)}}{2K} \cong 0$$

It can also be assumed that θ_g, the angle between $\vec{K} + \vec{g}$ and $\hat{n}$, is almost equal to θ_0, the angle between $\vec{K}$ and $\hat{n}$. This results in the following:

$$K^2 - (\vec{k}^{(i)} + \vec{g})^2 \cong 2K(s_g - \gamma^{(i)})\cos\theta_0 \tag{2.18}$$

2.1.4. Symmetrical Laue Conditions

Another approximation which is usually made is the assumption of symmetrical

Laue conditions. These conditions are satisfied when the entrance surface of the crystal is parallel to the zero order Laue zone, which is defined as the plane in reciprocal space which is most nearly perpendicular to the incident electron wave vector and which has low indices. In this case, the deviation parameters, s_g, are the distances from the reciprocal lattice points to the Ewald sphere in a direction parallel to the Brillouin Zone boundary, which will be assumed to be the $\hat{z}$ direction (see Fig. 2.2). The angle, θ_g, is now the angle between $\vec{K} + \hat{g}$ and $\hat{z}$. The high energy approximation, then, leads to:

$$\cos\theta_g \cong \cos\theta_0 = \frac{K_z}{K}$$

Therefore, eq. 2.19 becomes:

$$K^2 - (\hat{k}^{(i)} + \hat{g})^2 \cong 2K_z(s_g - \gamma^{(i)}) \tag{2.19}$$

In order to examine the validity of the assumption of symmetrical Laue conditions, the differences which result from the use of eq. 2.19, rather than eq. 2.18, in calculating the $\gamma^{(i)}$'s should be examined. In the symmetrical Laue case, eq. 2.9 can be rewritten in the form of an eigenvalue equation:

$$\mathbf{A}_s\mathbf{C}_s^{(i)} = \gamma_s^{(i)}\mathbf{C}_s^{(i)} \tag{2.20}$$

where the s subscripts signify that symmetrical Laue conditions are being assumed. $\mathbf{A}_s$ is a matrix with diagonal elements of $(A_{gg})_s = (s_g)_s$, and non-diagonal elements given by $(A_{gh})_s = U_{g-h}/2K_z$ where $g \neq h$. $\mathbf{C}^{(i)}$ is the column vector shown in eq. 2.9, and $\gamma^{(i)}$ is any of the eigenvalues of the $\mathbf{A}_s$ matrix. With the knowledge of these eigenvalues, the calculation of the wave vectors, $\hat{k}^{(i)}$, can now be completed using eq. 2.15. In the symmetrical Laue case, this equation becomes:

$$\begin{aligned} \hat{k}^{(i)} &= \vec{K} + \gamma^{(i)}\hat{z} \\ \text{or} \quad k_z^{(i)} &= K_z + \gamma^{(i)} \end{aligned} \tag{2.21}$$

In the non-symmetrical Laue case, eq. 2.9 is rewritten in the slightly different form:

$$\mathbf{A}\mathbf{C}^{(i)} = \lambda^{(i)}\mathbf{C}^{(i)} \tag{2.22}$$

where the diagonal elements of $\mathbf{A}$ are now given by $A_{gg} = s_g\cos\theta_0$ and the non-diagonal

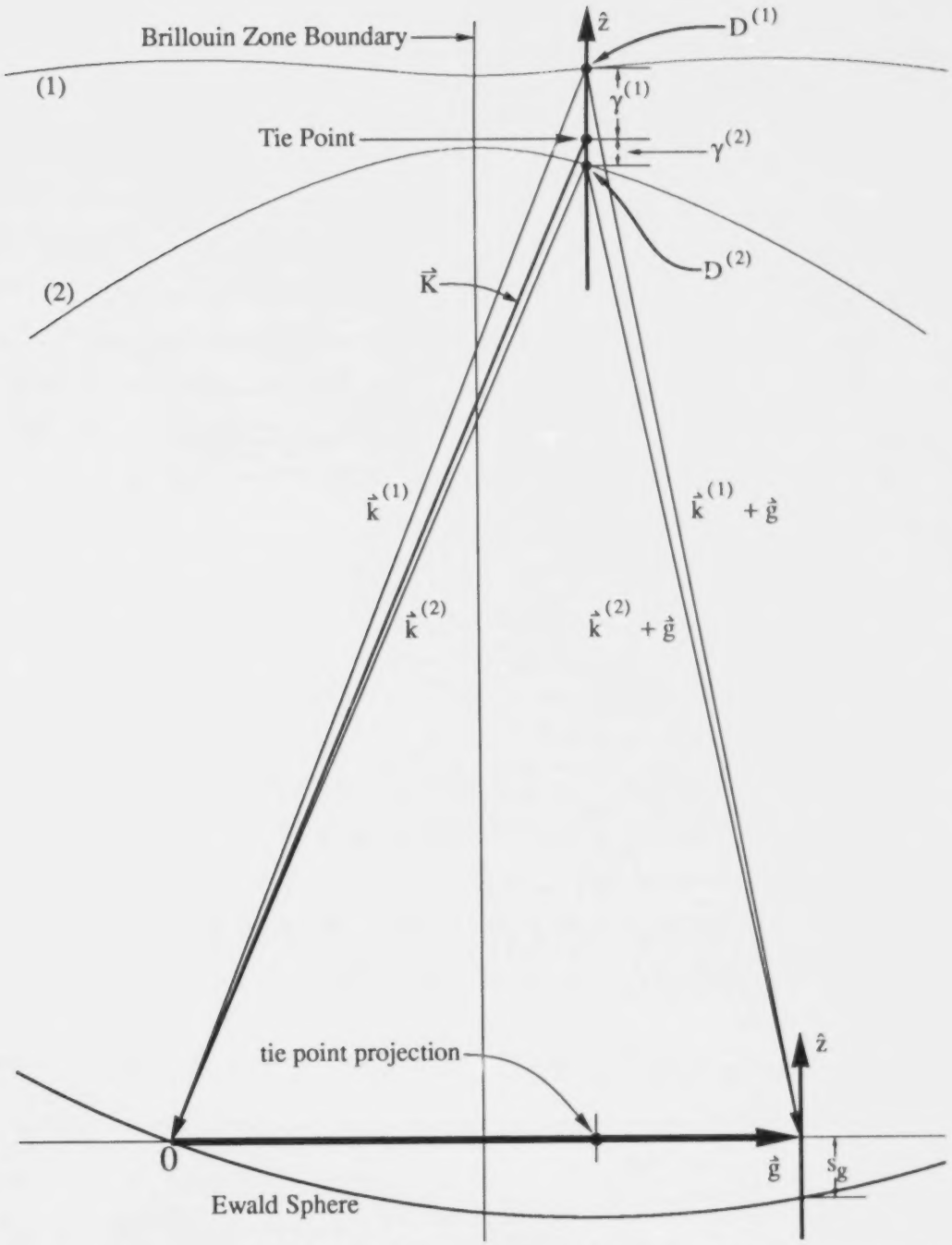

Fig. 2.2. Two beam dispersion surface illustrating the symmetrical Laue approximation. The normal to the entrance surface is now parallel with the $\hat{z}$ direction and perpendicular to the reciprocal lattice vectors of the zero order Laue zone. The starting points of all of the $\vec{k}_g^{(i)}$'s now lie on a line drawn parallel to the $\hat{z}$ direction which passes through the starting point of $\vec{K}$.

elements are almost the same as in the symmetrical Laue case, $(A_{gh})_s = U_{g-h}/2K$. The eigenvalues of the equation, $\lambda^{(i)}$, are related to the $\gamma^{(i)}$'s of eq. 2.16 by:

$$\lambda^{(i)} = \gamma^{(i)} \cos\theta_0 \tag{2.23}$$

The differences between the two cases in terms of their effects on the **A** matrix will now be examined. Since the energy of the electrons is very high, the Ewald sphere is actually very flat on this scale. The curvature of the Ewald sphere shown in Figs. 2.1 and 2.2 is greatly exaggerated. By comparing the two figures, and taking into account the difference in the definitions of the deviation parameter, s_g, in the two cases, it can be seen that the diagonal elements of the **A** matrix in eq. 2.22, $A_{gg} = s_g \cos\theta_0$, are actually quite close to the diagonal elements of $\mathbf{A}_s$ in eq. 2.20, $(A_{gg})_s = s_g$. This is especially true for small θ_0. Since the **A** matrices are very similar, it would be expected that the eigenvalues would be quite similar in either case.

$$\text{ie} \qquad \gamma_s^{(i)} \equiv \lambda^{(i)} = \gamma^{(i)} \cos\theta_0$$

Therefore the $\gamma^{(i)}$ in the non-symmetrical Laue case can be quite different from the $\gamma_s^{(i)}$ in the symmetrical Laue case, as would be expected from a comparison of Figs. 2.1 and 2.2. At this point, it would seem that the two cases would lead to very different results. However, it will be shown later that what is important in terms of image contrast is the factor $\vec{k}^{(i)} \cdot (\vec{r}_{ex} - \vec{r}_{en})$, where $\vec{r}_{en}$ defines the point on the entrance surface where the electrons enter the crystal, and $\vec{r}_{ex}$ is the point on the exit surface where the electrons emerge from the crystal. Therefore, $\vec{r}_{ex} - \vec{r}_{en}$ is a vector in the direction of $\vec{K}$, which is the direction of propagation of electrons in the crystal after refraction by the mean inner potential of the crystal, U_0.

$$\vec{k}^{(i)} \cdot (\vec{r}_{ex} - \vec{r}_{en}) = \frac{|\vec{r}_{ex} - \vec{r}_{en}|}{|\vec{K}|} (\vec{k}^{(i)} \cdot \vec{K})$$

$$= \frac{|\vec{r}_{ex} - \vec{r}_{en}|}{|\vec{K}|} (\vec{K} \cdot \vec{K} + \gamma^{(i)} \hat{n} \cdot \vec{K})$$

The important term involving $\gamma^{(i)}$ is, therefore:

$$\frac{|\vec{r}_{ex} - \vec{r}_{en}|}{|\vec{K}|} (\gamma^{(i)} \hat{n} \cdot \vec{K}) = |\vec{r}_{ex} - \vec{r}_{en}| \gamma^{(i)} \cos\theta_0$$

in the non-symmetrical Laue case, or:

$$\frac{|\vec{r}_{ex} - \vec{r}_{en}|}{|\vec{K}|} (\gamma^{(i)} \hat{z} \cdot \vec{K}) = \frac{K_z}{K} |\vec{r}_{ex} - \vec{r}_{en}| \gamma_s^{(i)} \cong |\vec{r}_{ex} - \vec{r}_{en}| \gamma_s^{(i)}$$

in the symmetrical Laue case.

Since these terms are usually quite similar, the symmetrical Laue approximation usually gives good results. Saldin, et. al.[7], using a different formulation of the dynamical theory, have shown that when only two beams are taken into account, the symmetrical Laue approximation leads to only small errors for angles of incidence of up to $\sim 70°$. There are cases, however, where this assumption can give poor results. One possible cause of such problems is the fact that the Ewald sphere is not completely flat. Thus, for large values of θ_0, there can be significant differences in the diagonal elements of the **A** matrices in the two cases. Another problem is that although the Ewald sphere is quite flat on this scale, it is not always perpendicular to the Brillouin zone boundary. Therefore, in regions of reciprocal space where the angle between the Ewald sphere and the zero order Laue zone is reasonably large, the assumption that $(s_g)_s \cong s_g \cos\theta_0$ breaks down. Sheinin and Jap[8] have shown that the assumption of symmetrical Laue conditions can lead to poor results in these cases, and Kim, Perez and Sheinin[9] have demonstrated this experimentally. However, as long as the component of $\vec{K}$ which is parallel to the zero order Laue zone is reasonably small, this will generally be a problem only for weak beams which have large deviation parameters. Since these reflections generally have a small effect of the calculations which will be done in this thesis, symmetrical Laue conditions will be assumed for the remainder of this thesis and the subscript, s, denoting the use of this approximation, will be dropped. The use of this assumption will result in greatly simplified equations in the following chapters.

2.1.5. Calculation of Bloch Wave Excitation Coefficients

If a total of N beams are taken into account in the eigenvalue equation, 2.20 or 2.22,

then N different eigenvalues will be found, and hence, N different solutions for the wave vector, $\vec{k}$, which are labelled, $\vec{k}^{(i)}$. There will also be N different eigenvectors, each of which corresponds to a different wave vector, $\vec{k}^{(i)}$. Therefore, there are N different Bloch wave solutions to the Schrödinger equation which have been completely defined. The total wavefunction of the high energy electrons in the crystal will, therefore, be a linear combination of these Bloch wave solutions as given by eq. 2.11.

In section 2.1.2, it was shown how, by applying the boundary conditions at the entrance surface, a set of equations involving the excitation coefficients could be derived. These equations, which are given in eq. 2.14, can be written in matrix form:

$$\mathbf{CEX} = \mathbf{E}_0 \tag{2.24}$$

where **C** is the matrix whose columns consist of the eigenvectors derived from eq. 2.19 or eq. 2.20.

$$\mathbf{C} = \begin{bmatrix} C_{g_1}^{(1)} & C_{g_1}^{(2)} & \cdots & \cdots & \cdots \\ C_{g_2}^{(1)} & C_{g_2}^{(2)} & & & \\ \cdots & & \cdots & & \\ \cdots & & & & \cdots \end{bmatrix}$$

$$\mathbf{E} = \begin{bmatrix} \exp(2\pi i k_\perp^{(1)} r_{en\perp}) & 0 & 0 & 0 \\ 0 & \exp(2\pi i k_\perp^{(2)} r_{en\perp}) & 0 & 0 \\ 0 & 0 & \exp(2\pi i k_\perp^{(3)} r_{en\perp}) & 0 \\ 0 & 0 & 0 & \cdots \end{bmatrix}$$

$$\mathbf{X} = \begin{bmatrix} X^{(1)} \\ X^{(2)} \\ X^{(3)} \\ \cdots \\ \cdots \end{bmatrix} \qquad \mathbf{E}_0 = \begin{bmatrix} \exp(2\pi i \chi_\perp r_{en\perp}) \\ 0 \\ 0 \\ \cdots \\ \cdots \end{bmatrix}$$

If eq. 2.24 is multiplied from the left by $\mathbf{E}^{-1}\mathbf{C}^{-1}$, the following expression for **X** is obtained:

$$\mathbf{X} = \mathbf{E}^{-1}\mathbf{C}^{-1}\mathbf{E}_0 \tag{2.25}$$

If the origin is chosen such that $V(\vec{r}) = V(-\vec{r})$, it can be said that the crystal is centrosymmetric and $U_g = U_{-g}$. In addition, if only elastic scattering is taken into account, the crystal potential is real, $V(\vec{r}) = V^*(\vec{r})$, and so:

$$U_g = U_{-g} = U^*_g$$

Therefore, the **A** matrix in eq. 2.20 or eq. 2.22 is real and symmetric. In this case the matrix **C** of normalized eigenvectors is orthogonal and so:

$$\mathbf{C}^{-1} = \mathbf{C}^{T} \tag{2.26}$$

where $\mathbf{C}^T$ is the transpose of **C**. The inverse of **E** is also given simply by:

$$\mathbf{E}^{-1} = \begin{bmatrix} \exp(-2\pi i k_\perp^{(1)} r_{en\perp}) & 0 & 0 & 0 \\ 0 & \exp(-2\pi i k_\perp^{(2)} r_{en\perp}) & 0 & 0 \\ 0 & 0 & \exp(-2\pi i k_\perp^{(3)} r_{en\perp}) & 0 \\ 0 & 0 & 0 & \ldots \end{bmatrix}$$

Therefore, when the matrix multiplication in eq. 2.25 is done, the following set of expressions for $X^{(i)}$ results:

$$X^{(i)} = C_0^{(i)} \exp\left[2\pi i (\chi_\perp - k_\perp^{(i)}) r_{en\perp}\right] \tag{2.27}$$

or, in the symmetrical Laue approximation:

$$X^{(i)} = C_0^{(i)} \exp\left[2\pi i (\vec{\chi} - \hat{k}^{(i)}) \cdot \vec{r}_{en}\right] \tag{2.28}$$

2.1.6. Diffracted Beam Intensities

Now that the excitation coefficients have been evaluated, they can be substituted back into eq. 2.11 to get the following:

$$\Psi(\vec{r}) = \sum_{i,g} C_0^{(i)} C_g^{(i)} \exp(2\pi i \vec{\chi} \cdot \vec{r}_{en}) \exp\left[2\pi i \hat{k}^{(i)} \cdot (\vec{r} - \vec{r}_{en})\right] \exp(2\pi i \vec{g} \cdot \vec{r}) \tag{2.29}$$

The different terms can now be separated according to the directions that the different waves are travelling:

$$\Psi(\vec{r}) = \sum_g \phi_g(\vec{r}) \tag{2.30}$$

where

$$\phi_g(\vec{r}) = \exp(2\pi i\vec{\chi}\cdot\vec{r}_{en})\exp(2\pi i\vec{g}\cdot\vec{r})\sum_i C_0^{(i)}C_g^{(i)}\exp\left[2\pi i\vec{k}^{(i)}\cdot(\vec{r}-\vec{r}_{en})\right] \quad (2.31)$$

The intensity of a particular beam at the exit surface of the crystal is then given by:

$$\begin{aligned} I_g(\vec{r}_{ex}) &= \left|\phi_g(\vec{r}_{ex})\right|^2 \\ &= \left|\sum_i C_0^{(i)}C_g^{(i)}\exp\left[2\pi i\vec{k}^{(i)}\cdot(\vec{r}_{ex}-\vec{r}_{en})\right]\right|^2 \end{aligned} \quad (2.32)$$

since the first two phase factors are eliminated when multiplied by their complex conjugates.

The last factor can be further simplified. Since the vector, $\vec{r}_{ex}-\vec{r}_{en}$, is in a direction very close to the $\hat{z}$ direction, it can be assumed that:

$$\vec{r}_{ex}-\vec{r}_{en} = t\hat{z} \quad (2.33)$$

where t is the thickness of the crystal. Therefore:

$$\vec{k}^{(i)}\cdot(\vec{r}_{ex}-\vec{r}_{en}) = \vec{K}\cdot(\vec{r}_{ex}-\vec{r}_{en})+\gamma^{(i)}\hat{z}$$

Thus, eq. 2.33 can be written as follows:

$$I_g(\vec{r}_{ex}) = \left|\exp[2\pi i\vec{K}\cdot(\vec{r}_{ex}-\vec{r}_{en})]\sum_i C_0^{(i)}C_g^{(i)}\exp(2\pi i\gamma^{(i)}t)\right|^2$$

Since the phase factor $\exp[2\pi i\vec{K}\cdot(\vec{r}_{ex}-\vec{r}_{en})]$ can be eliminated, the final result is the following:

$$I_g(\vec{r}_{ex}) = \left|\sum_i C_0^{(i)}C_g^{(i)}\exp(2\pi i\gamma^{(i)}t)\right|^2 \quad (2.34)$$

2.2. Inelastic Scattering

2.2.1. Inelastic Scattering Processes

So far, it has been assumed that the electrons travelling through the crystal undergo elastic scattering only. However, there are inelastic scattering processes which an electron can undergo before emerging from the crystal. These processes involve exciting the crystal into some higher energy state and, as a result, the incident electron is decreased in energy by some small amount. One result of the excitations is that the process can scatter the electron out of the Bragg reflection and into the background of the diffraction pattern. If an electron is scattered by a large enough angle that it no longer passes through the objective aperture, it can no longer contribute to the intensity of the image formed by that reflection. As a result, this process is commonly thought of as absorption.

The most important of these excitation processes are phonon excitation, plasmon excitation, and single electron excitation. Plasmons are long wavelength density oscillations in the electron gas of the crystal. In travelling through a crystal, an electron can excite a plasmon and, in the process, be scattered through a small angle. The mean free path for this type of process is in the range of 1000 - 5000 Å, and so it can be expected, in some cases, that almost all electrons travelling through a crystal will be scattered in this way. However, because of the long wavelengths of the plasmons, this process only scatters the electrons through a very small angle. Thus, most of the scattered electrons will still pass through the objective aperture of the microscope and contribute to the image, although they may not lead to the same contrast as electrons which have not been scattered by this process.

Single electron excitation is the process in which the high energy electron excites one of the core electrons of the crystal into a higher energy level. This process will generally scatter electrons through larger angles than plasmon excitation.

The third, and most important, excitation process is phonon excitation. This is the excitation of displacement waves of crystal atoms or ions from their equilibrium positions. This process causes a negligible decrease in the energy of the scattered electron, but the angle of scattering can be relatively large. Therefore, the scattered electrons will usually

not pass through the objective aperture of the microscope, and can be considered to be absorbed. Since this scattering depends on the thermal motion of the atoms of the crystal, it becomes more important as the temperature increases.

2.2.2. Inclusion of Inelastic Scattering in the Standard Theory

The phenomenon of inelastic scattering was first taken into account by Slater[10] and Molière[11], who proposed the concept of a complex lattice potential in a purely phenomenological way. The crystal potential is made complex by adding an imaginary part to the U_g's of eq. 2.4:

$$U_g \rightarrow U_g + iU_g'$$

Thus, the **A** matrix of eq. 2.20 or eq. 2.22 becomes complex, and the resulting eigenvalues, $\gamma^{(i)}$, also become complex. Therefore:

$$\gamma^{(i)} \rightarrow \gamma^{(i)} + iq^{(i)}$$

The effect of this change in the eigenvalues is that each Bloch wave is attenuated by the term, $\exp(-2\pi q^{(i)} t)$, and so the image intensity is decreased with increasing thickness. This will be shown in sec. 2.2.3.

This addition of an imaginary component to the potential was explained theoretically by Yoshioka[12]. Instead of solving the Schrödinger equation using a static potential, $V(\vec{r})$, as Bethe had done, Yoshioka used a potential which included the possibility that the crystal itself could be excited into higher energy states and, therefore, the potential which the high energy electron experienced would no longer be static. The result was a set of equations very similar to eq. 2.6 but in which U_h was replaced by $U_h + D_h$, where D_h was a complex number. He then went on to calculate the contribution to D_h from single electron excitations for MgO.

Since Yoshioka's work, it has been found that the real part of D_h is quite small compared to U_h, and it is usually ignored. Several authors have since calculated the contributions of the various excitation processes to the imaginary part of the potential, $\mathrm{Im}(D_g) = U_g'$. Humphreys and Hirsch[13] calculated the contributions to U_g' from single

electron excitations and phonon scattering for several crystals and found that phonon scattering was the most important process by far, except for very small values of g, and, in particular, for the g=0 term, U_0'. Radi[14] calculated the contributions of all three major excitation process on U_g' for many different crystals. He also found that phonon scattering is dominant for all $g \neq 0$. The U_0' term is not important for the diffraction contrast of an image since it uniformly attenuates all of the Bloch waves and does not affect the form of an image. For this reason, the contributions from single electron excitation and plasmon excitation are now commonly ignored.

In order to accurately calculate the phonon contribution to U_g', one must use calculations based on the phonon spectrum of the entire crystal. It is not possible, therefore, to calculate it as a sum of the contributions due to all of the atoms in the crystal. However, using the Einstein model, which assumes that all of the crystal ions vibrate independently of one another, Bird and King[15] and Weickenmeier and Kohl[16] have made available program subroutines which can calculate approximate values of the phonon contribution to the inelastic scattering factors. These factors permit the calculation of the phonon contribution to U_g' for any arbitrary crystal, rather than just the relatively few crystals for which U_g' had been calculated in the past.

There is another effect of thermal diffuse scattering which does not involve the excitation of phonons by the incident electrons. Rather, this effect is due to the thermal vibrations of the crystal ions which are present even without the influence of the high energy incident electrons. Thus, the atoms or ions at any particular time are not located at their equilibrium positions, and so the Fourier expansion of the crystal potential given in eq. 2.4 cannot be used without modification. The Fourier expansion used in eq. 2.4 can be expressed in the following way:

$$V_{eq}(\vec{r}) = \sum_{g} V_{eq_g} \exp(2\pi i \vec{g} \cdot \vec{r})$$

Since the positions of the atoms or ions are not constant, it is necessary to find an expression for the statistical average of the crystal potential, which does have the periodicity of

the ideal lattice:

$$\langle V(\vec{r})\rangle = \sum_g \langle V\rangle_g \exp(2\pi i \vec{g}\cdot\vec{r}) \tag{2.35}$$

$$\text{where} \qquad \langle V\rangle_g = V_{eq_g}\exp(-\frac{1}{4}B|g|^2) \tag{2.36}$$

and $\exp(-B|g|^2/4)$ is the Debye-Waller factor, $B = 8\pi^2\langle u_x^2\rangle$ and $\langle u_x^2\rangle$ is the average squared displacement in a given direction of the crystal ions from their equilibrium positions. Therefore, the Fourier components are generally multiplied by the Debye-Waller factor or, in the case of polyatomic crystals, are calculated using the Debye-Waller factors of each atom in the crystal. This leads to a general decrease in the intensity of each Bragg reflection and an increase in the background of the diffraction pattern.

2.2.3. Calculation of Intensity Including Inelastic Scattering

When inelastic scattering processes are included, the Fourier components of the crystal potential become complex. As was indicated in the previous section, one effect of this is that the **A** matrix in eq. 2.20 or eq. 2.22 now becomes complex. Thus, the assumption made in section 2.1.6 of a real **A** matrix is no longer valid. The result is that **C** is a complex matrix and it can no longer be said that $\mathbf{C}^{-1} = \mathbf{C}^{T}$ as was done in eq. 2.26. Therefore, the matrix, $\mathbf{C}^{-1}$, in eq. 2.25 must now be calculated numerically by computer. When this is done, the following expression for the excitation coefficient, $X^{(i)}$, is obtained:

$$X^{(i)} = C_{i1}^{-1}\exp\left[2\pi i\,(\vec{\chi} - \vec{k}^{(i)})\cdot\vec{r}_{en}\right] \tag{2.37}$$

where C_{i1}^{-1} is the element in the i^{th} row and 1^{st} column of $\mathbf{C}^{-1}$.

Therefore, the intensity at the exit surface of the g^{th} Bragg reflection is given by:

$$I_g(\vec{r}_{ex}) = \left|\sum_i C_{i1}^{-1}C_g^{(i)}\exp(-2\pi q^{(i)}t)\exp(2\pi i\gamma^{(i)}t)\right|^2 \tag{2.38}$$

where C_{i1}^{-1} and $C_g^{(i)}$ are now complex numbers.

2.3. Relativistic Corrections to Theory

The preceding theory is based on the non-relativistic Schrödinger wave equation. However, even electrons which have been accelerated through a potential of only 100 kV have a velocity greater than half the velocity of light. As a result, the relativistic effects on diffraction contrast can be expected to be quite significant. The dynamical theory of relativistic electron diffraction was first developed by Fujiwara[17], who applied Dirac's relativistic wave equation to the case of electron diffraction. His results were later confirmed by Howie[18]. Their results showed that the relativistic effect on diffraction contrast can be taken into account by making two changes to the non-relativistic theory. First, the non-relativistic electron wavelength must be replaced by a relativistically correct one.

$$\lambda = \lambda_0 \left(1 + \frac{eE}{2m_0c^2}\right)^{-1/2} = \frac{h\sqrt{1-\beta^2}}{m_0 v} \tag{2.39}$$

where $\lambda_0 = h/(\sqrt{2m_0eE})$ is the non-relativistic wavelength, m_0 is the rest mass of the electron, v is the velocity of the electron, c is the velocity of light, and $\beta = v/c$.

The second correction which must be made is that the relativistic mass of the electron must be used instead of the rest mass. However, since the electron mass appears in the equations of the dynamical theory only as part of the Fourier coefficients of the crystal potential, this correction can be incorporated into the calculation of U_g as follows:

$$U_g = \frac{2me}{h^2} V_g = \frac{2m_0e}{h^2} \frac{V_g}{\sqrt{1-\beta^2}} \tag{2.40}$$

Thus, the non-relativistic Fourier coefficient must be multiplied by the term $(1-\beta^2)^{-1/2}$.

The variation of U_g with electron speed given by eq. 2.42 has been verified experimentally by Hashimoto, et. al.[19], Hashimoto[20] and many others.

3. Application of Theory to Twinned Crystals

3.1. Twinned Crystals

3.1.1. Definition and Classification

A twinned crystal can be defined as any crystal which is made up of two or more parts, each of which has the same structure and is oriented relative to the other parts according to some symmetry rule. It is common to refer to one part of the crystal as the parent crystal or matrix, and an adjacent part as the twin. The plane of contact between the two parts is called the *composition plane*.

There are two basic symmetry rules or twin laws which can relate the orientation of a twin to that of its parent crystal. The first and most common twin law states that the orientation of the twin can be obtained by a reflection of the parent crystal about some plane, called the *twin plane*, which has low, rational indices. A twin which is oriented according to this law is called a *reflection twin*. Figure 3.1 shows a typical reflection twin.

The second twin law requires that the twin orientation be obtainable by rotating the parent crystal by 180°, 120°, 90°, or 60° about some axis, with low, rational indices, which is called the *twin axis*. A twin of this kind is called a *rotation twin*.

In centrosymmetric crystals, it can be shown that the operation of reflection across a plane produces identical results to the operation of rotation through 180° about a twin axis which is normal to the plane of reflection. Thus, crystals with this symmetry can loosely be considered either reflection or rotation twins, although the twin axis may not have rational indices. There is a slightly different classification which has come into use for the description of deformation twinning. Reflection twins, in which the plane of reflection has low indices, are called type 1 twins. Since this operation can also be described as a rotation of 180° about an axis normal to the twin plane, these are also sometimes called normal twins. In deformation twinning, one can define a direction of shear which is the direction the atoms must move in the twinning process. Twins with a low index axis of rotation parallel

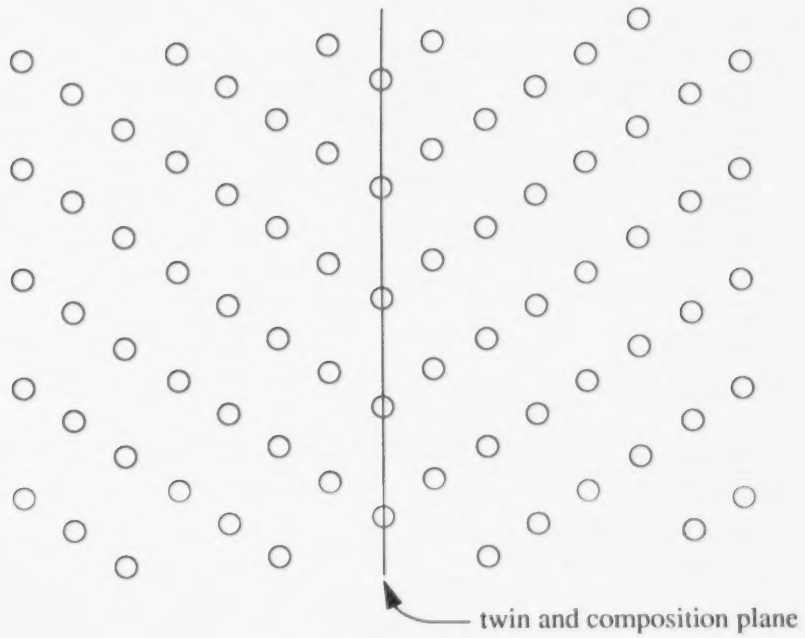

Fig. 3.1. Reflection twin

to the shear direction are called type 2 or parallel twins. Many twins, including all those found in cubic crystals, can be described by both a reflection across a twin plane and a rotation about a twin axis which is parallel to the twin plane. These are called *compound twins*.

When the twin plane (in the case of reflection twins) is also the composition plane, the twin is called a contact twin and is said to be *coherent*. This same term is also loosely applied to rotation twins which have a twin axis parallel to the composition plane.

3.1.2. Origin of Twinned Crystals

Twinned crystals can also be classified according to their origin. There are three major causes of twin formation -- growth twins, transformation twins, and deformation twins.

Growth twins are formed as a crystal grows either from the liquid phase or from vapour deposition. Annealing twins, in which twins form during the growth of one grain at the expense of another, can also be considered growth twins. A theory for the formation of

growth twins has been put forward by Buerger[21]. When an atom lands on a crystal surface, its energy is the sum of the energies of the atom due to the potential fields of the other atoms in the crystal. The lowest energy locations are those which lead to the continuation of the regular crystal structure. A location corresponding to a twinned orientation has a higher energy, but only moderately higher since its energy due to its nearest neighbours is the same as it would be in the ideal location. Therefore, if an atom were to land in a twin position, it would be in a small energy well, but it would likely soon lose its place due to thermal agitation and atomic bombardment, unless it was immediately followed by other atoms which also landed in the neighbouring twin positions. Thus, a high rate of addition of atoms to the surface would increase the probability of twin formation by this method. The chances of survival would also be increased if a cluster of atoms were to land in the twin position, especially if it were quickly followed by other atoms or clusters arriving in the twin positions. It would be expected that the energy barrier to the removal of a cluster of atoms in the twin position would be greater if some of the atoms in the cluster were also in, or very near to, their locations of lowest energy with respect to the rest of the crystal. Thus, the more atoms in the twin which are in the same location as they would be if the lattice had continued to grow ideally, the more likely it should be that twin continues to grow. This condition is borne out in reality as sill be seen in the next section. Growth twinning is common in FCC metals.

Transformation twins are formed when a crystal undergoes a transition from a high symmetry phase to a low symmetry phase. In general, crystals which have high and low temperature phases have a higher symmetry in the high temperature phase. i.e. the low temperature phase is lacking some of the symmetry operations of the high temperature phase. Therefore, when such a crystal is cooled through the transition temperature, there is more than one orientation which a nucleus of the low temperature phase can have. The nuclei will usually be located at the grain boundaries, and the transformation will spread from these centers until the nuclei make contact with each other. If the nuclei which meet each other are in different orientations, they are twins.

Deformation twinning is the process in which an external shear force causes the atoms on one side of the composition plane to move to new positions. These positions

correspond to an identical structure as the one on the other side of the interface, but in a twinned orientation. Thus, each atom on the twin side of the interface moves parallel to the shear direction through a distance proportional to the distance of the atom from the interface. Figure 3.2 shows the atom movements necessary for deformation twinning. The open

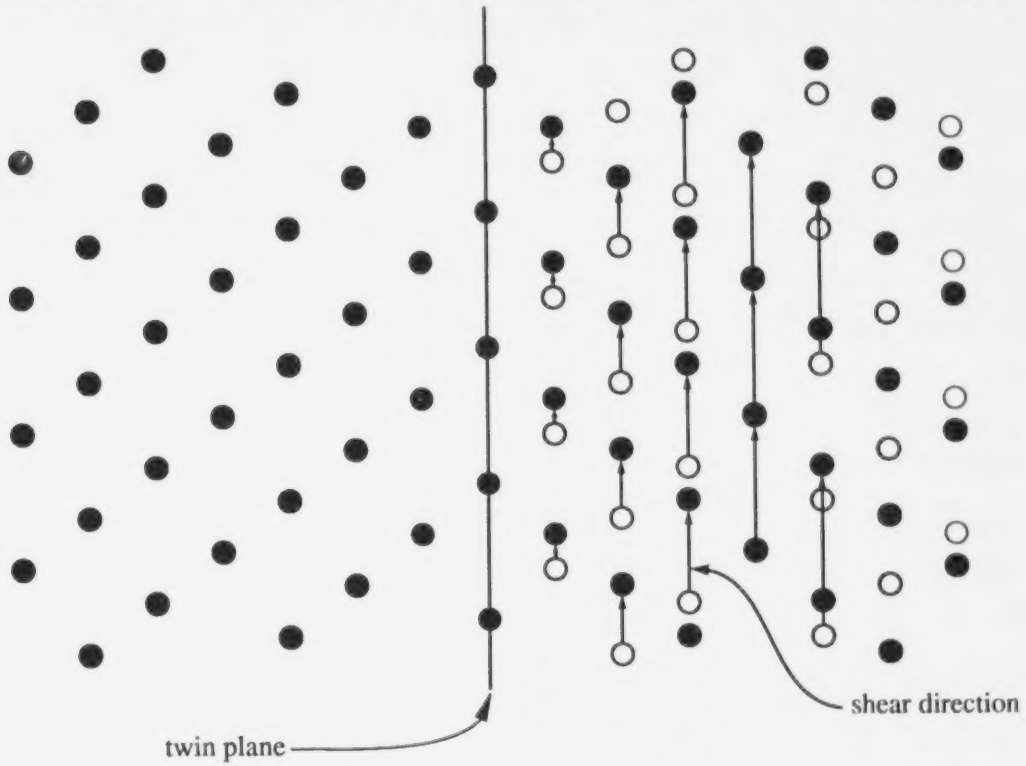

Fig. 3.2. Deformation twinning. The open circles indicate the positions of the atoms in the untwinned crystal, and the closed circles indicate the atom positions after twinning.

circles indicate the positions of the atoms in the untwinned crystal, and the closed circles indicate the atom positions after twinning. The arrows show the directions and distances each atom moves in the process. As a mode of plastic deformation, twinning must compete with slip, in which the orientation is the same on either side of the interface. Whether a crystal deforms by twinning or by slip depends on the energy barriers which the atoms must overcome to travel in the slip direction as opposed to the shear direction for twins. Since slip requires only a small amount of energy in FCC metals, deformation twins are not generally seen in these metals.

3.1.3. Crystal Structures Likely to Exhibit Twinning

For any given twin law, it is possible to determine whether or not this will be a frequent form of twinning by considering two properties of the twin structure -- the index and the obliquity. In the previous section, it was suggested that twinning might be more common if some atoms in the twin have the same positions as they would have in an untwinned crystal. The *index* of the twin is the ratio of the total number of lattice points in the twin to the number of lattice points which occupy lattice positions for the parent crystal. Figure 3.3 shows a crystal in which some of the atoms in the twin have the same positions as they would have in an untwinned crystal. The lattice points which are common to both

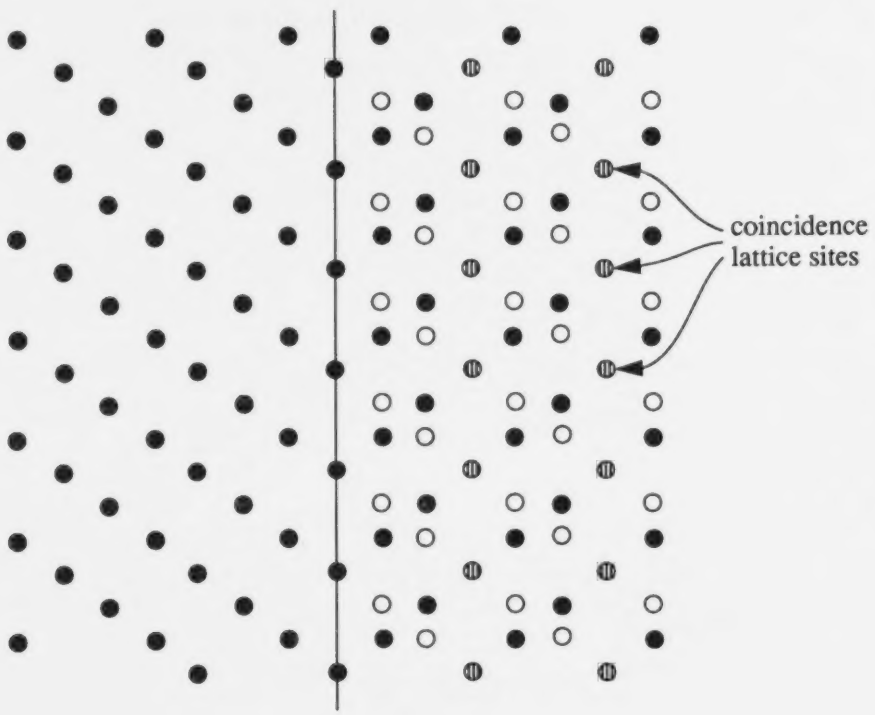

Fig. 3.3. Twinned crystal with a coincidence site lattice. The index of the twin is 3.

the twin and the parent crystal make up what is called the coincidence lattice. The *obliquity* of a twin is the angle between the true normal to the twin plane and the lattice row (in which

the lattice points are closely spaced) which is nearest to being normal to the twin plane. If the obliquity is not zero, then the coincidence lattice is slightly deviated at the twin boundary. A survey of the known twinning modes suggests that the smaller the index and the obliquity of a twinning mode, the more frequently the twin occurs[22]. Thus, the more atoms which are in or near their lowest energy positions, particularly near the twin boundary, the more likely the twin is to form.

This concept has led to yet another system of classification of twins due to Friedel[23]. The first category is twinning by merohedry. A merohedral crystal has a symmetry which is a subgroup of the symmetry of the lattice. For example, Figure 3.4 shows a lattice which is cubic even though the structure itself does not have 4-fold symmetry. Thus, after under-

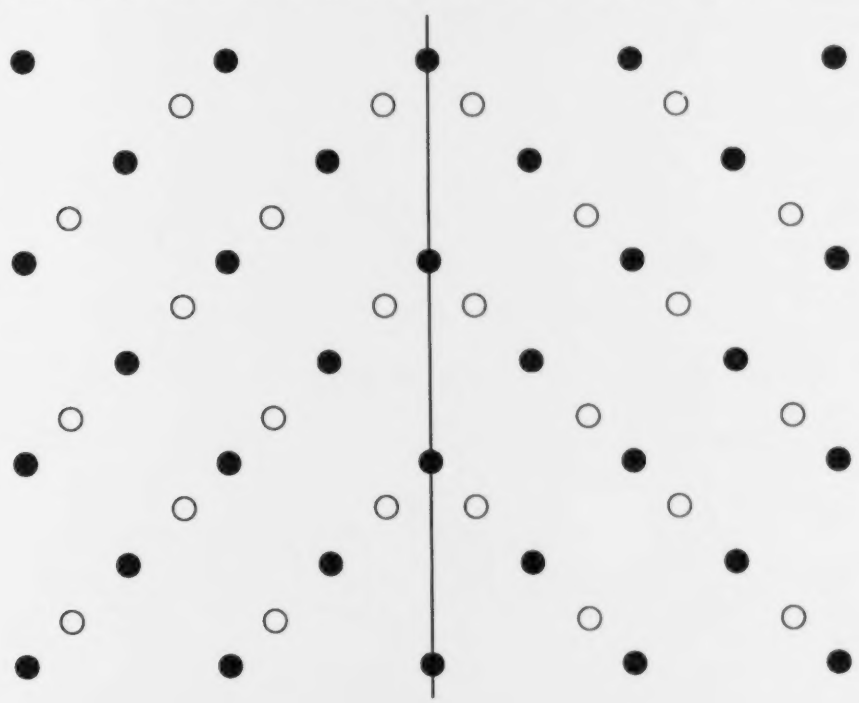

Fig. 3.4. A merohedral twin. The lattice has cubic symmetry, but the structure does not. The open and filled dots represent different kinds of atoms.

going a twinning operation, the crystal has a new orientation but the lattice is completely unchanged. Therefore, the index of the twin is 1 and the obliquity is 0. In such a crystal, the reciprocal lattice of the twin would be identical to the reciprocal lattice of the parent crystal

or matrix, and the coincidence lattice.

The second type is twinning by reticular or lattice merohedry. This is the case in which the coincidence lattice exists, but is not identical with the crystal lattice of the untwinned structure. In other words, the index is greater than 1 and the obliquity is 0. Thus, the reciprocal lattices of the matrix and the twin will have some common points but most points will be uniquely due to one crystal or the other. This is a common form of twinning in cubic crystals.

The third type is twinning by pseudo-merohedry. This is very similar to twinning by merohedry except that the lack of a certain symmetry element in the crystal structure has resulted in a lattice which also lacks the symmetry element. However, the lattice is still nearly symmetric with respect to this symmetry element. This lack of perfect symmetry leads to a non-zero obliquity. As a result, the reciprocal lattice of the matrix will only have one plane in common with the reciprocal lattice of the twin, but the rest of its points, at least those with low indices, will be almost common with one point in the twin reciprocal lattice. The common plane is perpendicular to the twin plane. This type of twinning is common among minerals and artificial compounds[23].

The last type is twinning by reticular pseudo-merohedry. This form is similar to reticular merohedry in the same way that pseudo-merohedry is similar to merohedry. The index of this kind of twin is greater than 1 and the obliquity is greater than 0. The reciprocal lattice of the matrix will again have one plane in common with the twin reciprocal lattice, but in this case, the reciprocal lattices will have many points which are neither common nor almost common. There are good review articles on twinned crystals by Cahn[24] and by Clark and Craig[25].

3.1.4. Examples of Twinned Crystals

It is now useful to give two examples of twinned crystals, the second of which will be referred to often throughout the remainder of this thesis. The first example is the face centered cubic system (e.g. copper), which has compound twins with a twin plane of the type {111}. These are growth twins and twinning is by reticular merohedry. Twinning on the {111} plane in FCC structures means that the normal stacking sequence, ABCABC

(see Fig. 3.5) is reversed at some point, for example ABCBACBA where the C layer is the

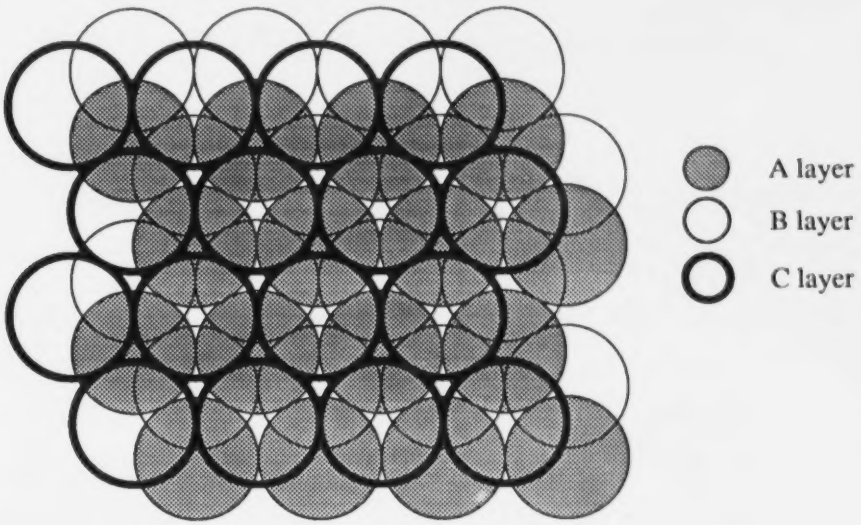

Fig. 3.5. Stacking sequence for FCC crystals looking down the [111] direction.

composition plane. Since the twinning is by reticular merohedry, the reciprocal lattices of the matrix and twin will have some points in common, but most matrix points will not coincide with twin points and vice versa.

The second example will be the high temperature superconductor, $Y_1Ba_2Cu_3O_{7-\delta}$, where δ will generally be between 0 and 0.5. This compound undergoes a transformation from a high symmetry phase to a low symmetry phase at ~700° C. The high symmetry, high temperature phase has a tetragonal structure with lattice parameters of a=3.85Å and c=11.70Å. At ~700° C, it transforms into an orthogonal structure with a=3.82Å, b=3.89Å, and c=11.68Å[26]. This slight change in the symmetry results in the formation of transformation twins. The twins are of the compound type with twinning planes of the type {110}. Twinning is by pseudo-merohedry. As a result, the reciprocal lattices of the matrix and twin have one plane in common, and most reciprocal lattice planes in the matrix have one row of points in common with the twin reciprocal lattice. In addition, every matrix point with reasonably low indices is almost coincident with a twin point. Figure 3.6 shows the [001]

planes of the matrix and twin reciprocal lattices superimposed in the correct orientation for a twin plane of (110). This is very similar to the diffraction pattern one would observe when

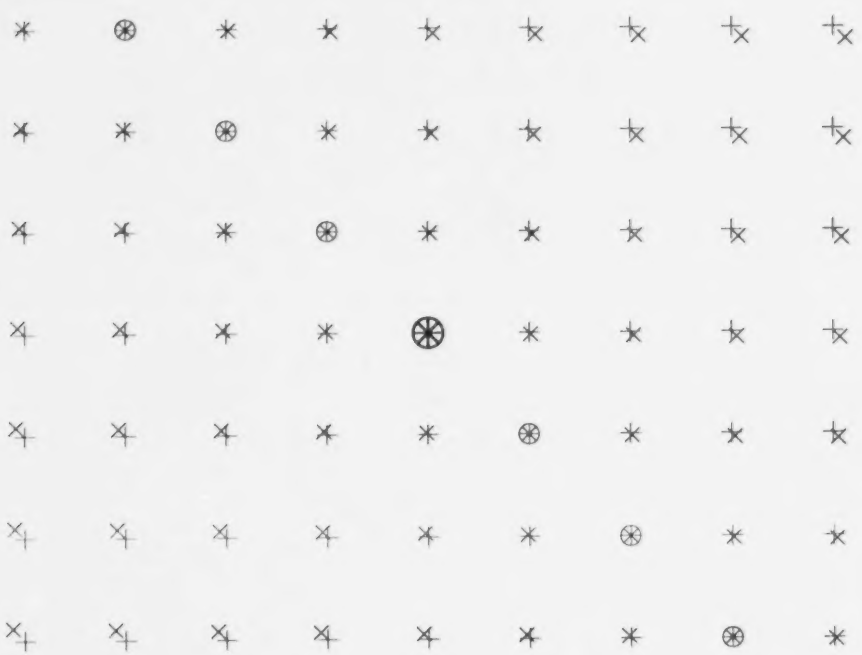

Fig. 3.6. Superimposed [001] planes of the reciprocal lattices of two $Y_1Ba_2Cu_3O_{7-\delta}$ crystals which are in a twin orientation to each other with a twin plane of (110).

looking at such a twin from the [001] direction in the matrix crystal. As a result of the near coincidence of the points, any diffraction contrast image formed by selecting one of the beam directions will actually have contributions from more than one beam having different

directions. Therefore, there will be interference effects between these different waves which will be very important in image contrast. They will be discussed in more detail in sections 3.4, 4.2.2, and in Chapter 6.

3.2. Diffraction Contrast From Twinned Crystals

3.2.1. Early Dynamical Theories of Twin Boundary Contrast.

When an electron beam passes through a twin boundary, each reflection which is excited in the upper portion of the crystal can in turn be reflected into a different direction in the lower crystal. For simplicity, the upper crystal will be referred to as the matrix and the lower crystal as the twin, as shown in Figure 3.7. As a result, the diffraction pattern

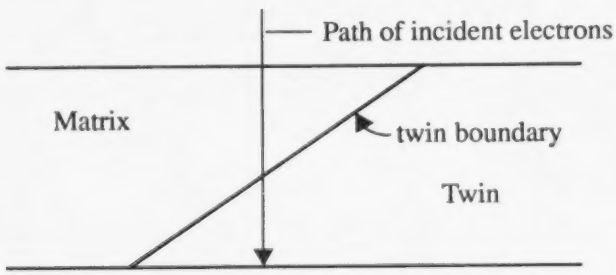

Fig. 3.7. Positions of matrix and twin crystals.

obtained from a twin boundary will be more than a superposition of the diffraction patterns which one would obtain from either crystal alone. Any combination of matrix and twin reflections can appear as one of the reflections in such a diffraction pattern. Fig. 3.8 shows the diffraction pattern of a (111) twin boundary in copper. The zone axis of the matrix is (123) compared to (321) for the twin. The reflections originating from the matrix alone are labelled g_i, while those from the twin alone are labelled h_i. Reflections common to the matrix and twin are labelled q_i. The reflections which can arise only as a combination of matrix and twin reflections are labelled f_i.

The problem of calculating the diffraction contrast obtained from a twin boundary has been studied by several authors. The earliest attempts were based on the assumption that only two beams were excited in the two crystals and that the excited reflections were

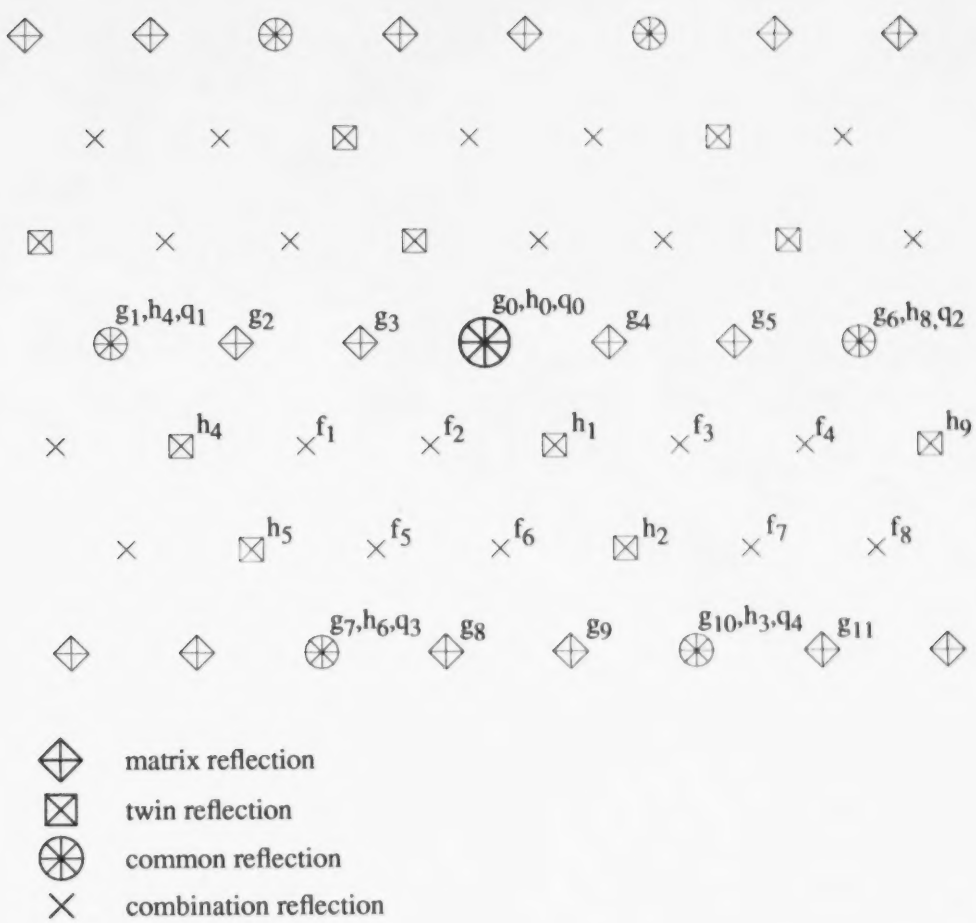

Fig. 3.8. Diffraction pattern from a twin boundary in copper. The zone axis of the matrix is [123] and the twin plane is (111).

the same in the twin as in the matrix[1,27,28]. In general, however, this condition will not be satisfied and so a theory is needed which can take into account many beams in both the matrix and the twin. The first such many-beam theory was developed by Sheinin and Corbett[3] and confirmed experimentally by Corbett and Sheinin[29]. In this version of the theory, the wavefunction of the electrons in the matrix was calculated at the twin boundary. This wavefunction would be a superposition of Bloch waves travelling in directions $\vec{k}^{(i)} + \vec{g}$, where $\vec{g}$ is a reciprocal lattice vector in the matrix. Each of these waves was then

considered to be the incident wave on the twin crystal. After equating the two wavefunctions at the twin boundary, the intensity of a particular reflection at the bottom surface of the twin was found in the usual way. Thus, in order to calculate the intensity due to the reflection f_1 in Fig 3.8, the matrix reflection, g_2, was allowed to be diffracted by the twin reflection, h_1, into the direction, $f_1 = g_2 + h_1$. However, a problem can arise in this kind of treatment when there are common reflections present, as in merohedral and reticular merohedral twins. The problem is that $g_2 + h_1$ may not be the only combination of matrix and twin reflections which will result in f_1. Since the common reflections are both matrix and twin reflections, $g_2 + q_2$ is still a matrix reflection, and $h_1 - q_2$ is still a twin reflection. If the matrix reflection, $g_2 + q_2$ is further diffracted in the twin by the reflection, $h_1 - q_2$, the resulting direction is $g_2 + q_2 + h_1 - q_2 = g_2 + h_1 = f_1$. Thus, the image intensity due to the reflection, f_1, will have contributions from more than one matrix reflection. Even if there are no common reflections, but only pseudo-common reflections as in pseudo-merohedral or pseudo-reticular merohedral twins, the same problem will arise. By referring to Figure 3.9, it can be seen that the reflections g_1 and h_6 are almost common. This means that for any given reflection, for example $f_1 = g_3 + h_1$, there will be another reflection which is almost common with it, in this case $f_2 = g_3 + g_1 + h_1 - h_6 = g_3 + h_1 + (g_1 - h_6) \approx g_3 + h_1 = f_1$. Thus, if the objective aperture is centered around the reflection, f_1, the image intensity will also have contributions from f_2. This does not mean that this form of the theory cannot be used. If the aperture is centered around a reflection which originates from the matrix reflection, g_3, the theory of Sheinin and Corbett can be used without modification as long as no reflections of the form $g_3 + q_i$, where q_i is a common or pseudo-common reflection not equal to 0, are excited in the matrix crystal.

There are times, however, when such matrix reflections will be excited, and so a theory was required to account for this possibility. Sutton and Pond solved the problem by simply taking a linear superposition of all of the different possible contributions to the diffracted beam amplitude (which result from common, but not pseudo-common, reflections). In other words, if $\phi_{g_3 + h_1}$ is the diffracted beam amplitude as calculated by Sheinin and Corbett, which results from the matrix reflection g_3 being further diffracted in the twin by the reflection h_1, then the total diffracted beam amplitude for the reflection f_1 in Fig. 3.8

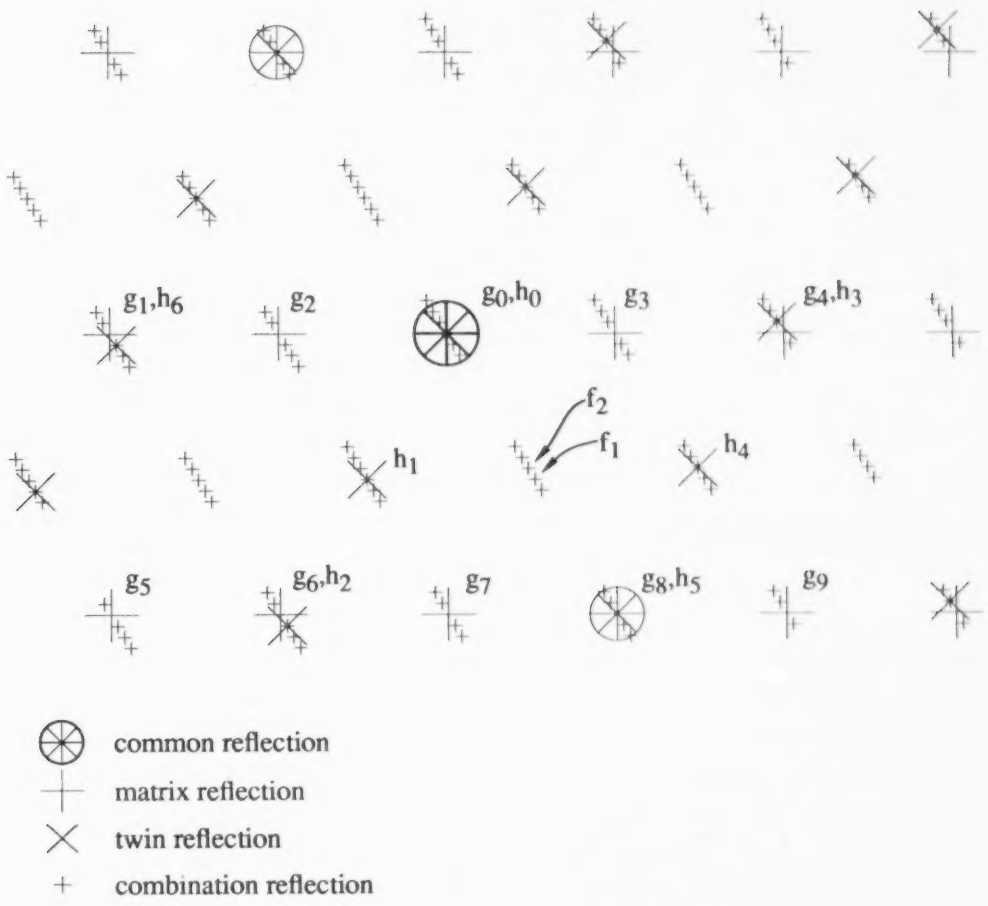

Fig. 3.9. Diffraction pattern from the (110) twin boundary of Aragonite, which is the orthorhombic form of calcium carbonate, $CaCO_3$. The twins in this crystal are pseudo-reticular merohedral twins. The matrix zone axis is [001].

is given by:

$$\phi_{f_1} = \sum_i \phi_{(g_3 + q_i) + (h_1 - q_i)} \tag{3.1}$$

where the summation is over all common reflections, q_i, such that the matrix reflection, $g_3 + q_i$, is sufficiently excited to be taken into account.

This approach also has a number of shortcomings. The first one, which was pointed out by Gomez, et. al.[30], is that in this method, one **A** matrix must be diagonalized for each

term in eq. 3.1. They also criticized that the matrix equation used by Sutton and Pond, which is similar to eq. 2.20, was not strictly correct for the following reason. The equation which leads up to Sutton and Pond's matrix equation is the following:

$$\sum_{\mathbf{h}}\left[\left[K^2-(\vec{\mathbf{k}}+\vec{\mathbf{g}}+\vec{\mathbf{h}})^2\right]C_{\mathbf{g}+\mathbf{h}}+\sum_{\mathbf{h}'\neq 0}U_{\mathbf{h}'}C_{\mathbf{h}-\mathbf{h}'}\right]\exp\left[2\pi i\,(\vec{\mathbf{k}}+\vec{\mathbf{g}}+\vec{\mathbf{h}})\cdot\vec{\mathbf{r}}\right]=0 \quad (3.2)$$

However, the exponential terms are no longer all different, since $\mathbf{g}_i + \mathbf{h}_j$ can be the same as $\mathbf{g}_k + \mathbf{h}_l$ for certain reciprocal lattice vectors, $\mathbf{g}_i$, $\mathbf{g}_k$, $\mathbf{h}_j$, and $\mathbf{h}_l$. Thus, it no longer follows that

$$\left[K^2-(\vec{\mathbf{k}}+\vec{\mathbf{g}}+\vec{\mathbf{h}})^2\right]C_{\mathbf{g}+\mathbf{h}}+\sum_{\mathbf{h}'\neq 0}U_{\mathbf{h}'}C_{\mathbf{h}-\mathbf{h}'}=0 \quad (3.3)$$

However, it will be shown later that the **A** matrices used by Sutton and Pond can give correct results, provided that the correct twin reflections (or enough twin reflections) are included in the formation of the **A** matrices. Gomez et. al. therefore suggested changes to the theory which are similar to those which will be demonstrated in the next section.

Another criticism to the approach of Sutton and Pond was put forward by Gratias and Portier[31]. They argued that some of the dynamical couplings of beams can be ignored in this method. In fact, this problem would only arise if the number of twin reflections included is quite small and the same twin reflections are used in combination with each matrix reflection. For example, if the matrix reflections $\mathbf{g}_2$, $\mathbf{g}_3$, and $\mathbf{g}_2 + \mathbf{q}_2 = \mathbf{g}_4$ in Fig. 3.8 were included along with the twin reflections $\mathbf{h}_1$ and $\mathbf{h}_2$, the reflections $\mathbf{f}_1$ and $\mathbf{f}_5$ should be dynamically coupled with $\mathbf{f}_3$ and $\mathbf{f}_7$, but the method of Sutton and Pond would not take this into account. They have, therefore, derived their own theory which is based on a different formulation of the dynamical theory of diffraction contrast. It can be shown, however, that this version of the theory gives the same results as the theory which will be presented in the next section[5].

3.3. Twinned Crystals Having Common Reflections

The present version of the theory of diffraction contrast from twin boundaries was derived by Sheinin and Perez[5]. They incorporated the idea of the dynamically coupled set into the Bloch wave approach to the dynamical theory of electron diffraction. Figure 3.10 illustrates the concept of the dynamically coupled set. Unlike Fig. 3.8, any arbitrary reflection in the twin is now referred to by the symbol, f_i. All of the reflections which are connected by lines in the figure are dynamically coupled to each other. This is because they are all related to each other by a twin reciprocal lattice vector. Thus, all of these reflections can be considered to be in the same dynamically coupled set. Clearly, in this diffraction pattern, there are only three dynamically coupled sets, one containing g_0, one with g_4, and one with g_5. The set of reflections labelled by g_p will be defined to consist of only these three matrix reciprocal lattice vectors. In the general case, the g_p's will span the set of dynamically coupled sets. The set of q_m's will be the entire set of common reflections. Thus, the set of reflections defined by $g_p + q_m$ consists of all possible matrix reflections. The set of h_n's will be defined to consist of all twin reflections. Therefore, any reflection can be expressed as a sum of reflections in the following way:

$$f_k = g_p + q_m + h_n$$

for example:

$$f_9 = g_3 + q_0 + h_1$$

and

$$f_8 = g_2 + q_2 + h_4$$

However, these expressions are not unique. For example, f_9 can also be expressed as follows:

$$\begin{aligned} f_9 &= g_3 + (q_0 + q_2) + (h_1 - q_2) \\ &= g_3 + q_2 + h_4 \end{aligned}$$

Thus, there are as many different ways to describe each reflection as there are common reflections. This corresponds with the fact that each reflection can originate from this same

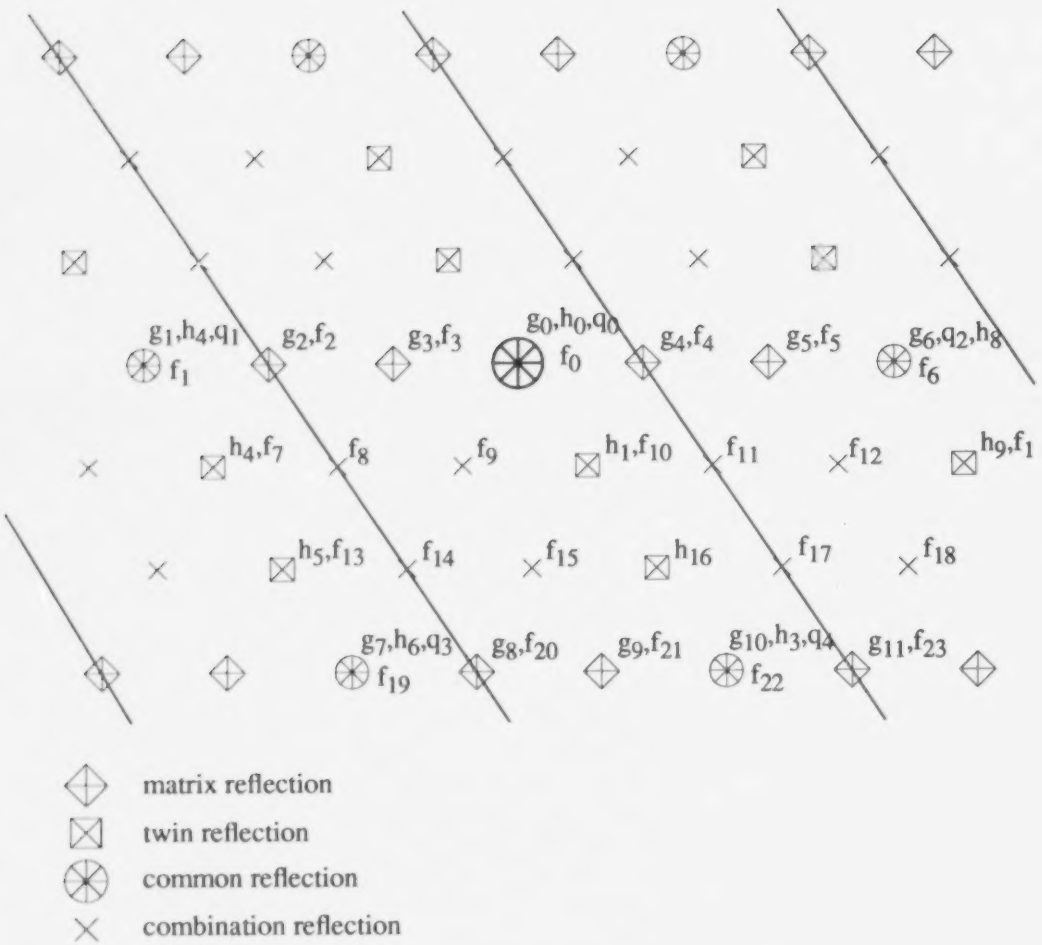

Fig. 3.10. Diffraction pattern from a twin boundary in copper. The zone axis of the matrix is [123] and the twin plane is (111). The lines indicate those reflections which are in one dynamically coupled set.

number of different matrix reflections.

A Bloch wave which describes electrons in a particular dynamically coupled set can be defined as follows:

$$b_p^{(i)} = \exp\left[2\pi i\,(\vec{k}^{(i)} + \vec{g}_p)\cdot\vec{r}\right]\sum_m\sum_n C^{(i)}_{g_p,\,q_m,\,h_n}\exp\left[2\pi i\,(\vec{q}_m + \vec{h}_n)\cdot\vec{r}\right] \qquad (3.4)$$

where the sum over m is over all reciprocal lattice vectors in the coincidence lattice and the sum over n is over all reciprocal lattice vectors in the twin. Since each q_m is also a reciprocal lattice vector in the twin, this function has the periodicity of the twin crystal and is, therefore, an acceptable Bloch wave. For simplicity, it will be assumed at first that only elastic scattering processes are important. The correction for the inclusion of inelastic scattering processes will be made at the end of the calculations.

The dispersion surface diagram for the twin is shown in Figure 3.11 for the case where the two matrix wave vectors, $\vec{k}_{ma}^{(1)} + \vec{g}$ and $\vec{k}_{ma}^{(2)} + \vec{g}$, are being further diffracted by the twin crystal. The origins of these two vectors no longer lie on the dispersion surface since the dispersion surface has now been rotated (just as the twin is rotated compared to the matrix) and it is a different portion of the surface which is shown in the diagram. The boundary condition at the twin boundary requires that the wave vectors in the twin must have the same component tangential to the twin boundary as the matrix wave vectors from which they originate. Thus, a line normal to the twin boundary, is drawn through the starting point of each wave vector in the matrix, $\vec{k}_{ma}^{(i)} + \vec{g}$, and the points where it crosses the different branches of this new region of the dispersion surface are the starting points of the twin wave vectors, $\vec{k}_{tw}^{(i,j)}$, where j runs from 1 to the number of branches of the dispersion surface. In general, the number of branches which are taken into account is the same as the number of reflections that are used in the calculations. Thus, if N_d is the number of matrix reflections in a particular dynamically coupled set to be taken into account, and N_t is the number of twin reflections, there will be N_d x N_t Bloch waves for each dynamically coupled set in the twin, each of which involves N_t different wave vectors, $\vec{k}_{tw}^{(i,j)} + \vec{g}_p + \vec{h}_n$, where n=1,2,...,$N_t$. This obviously leads to a very complicated set of equations. This situation can be simplified considerably by the use of the column approximation.

3.3.1. Column Approximation

The column approximation is based on the idea that all of the contributions to the wavefunction of the high energy electrons at a point on the exit surface come from a very thin column of the crystal as shown in Figure 3.12. The justification for this comes from the very small Bragg angle, θ_B, for electrons, which is of the order of 10^{-2} radians. Figure 3.13, which is due to Takagi[32], illustrates the relation between the Bragg angle and the

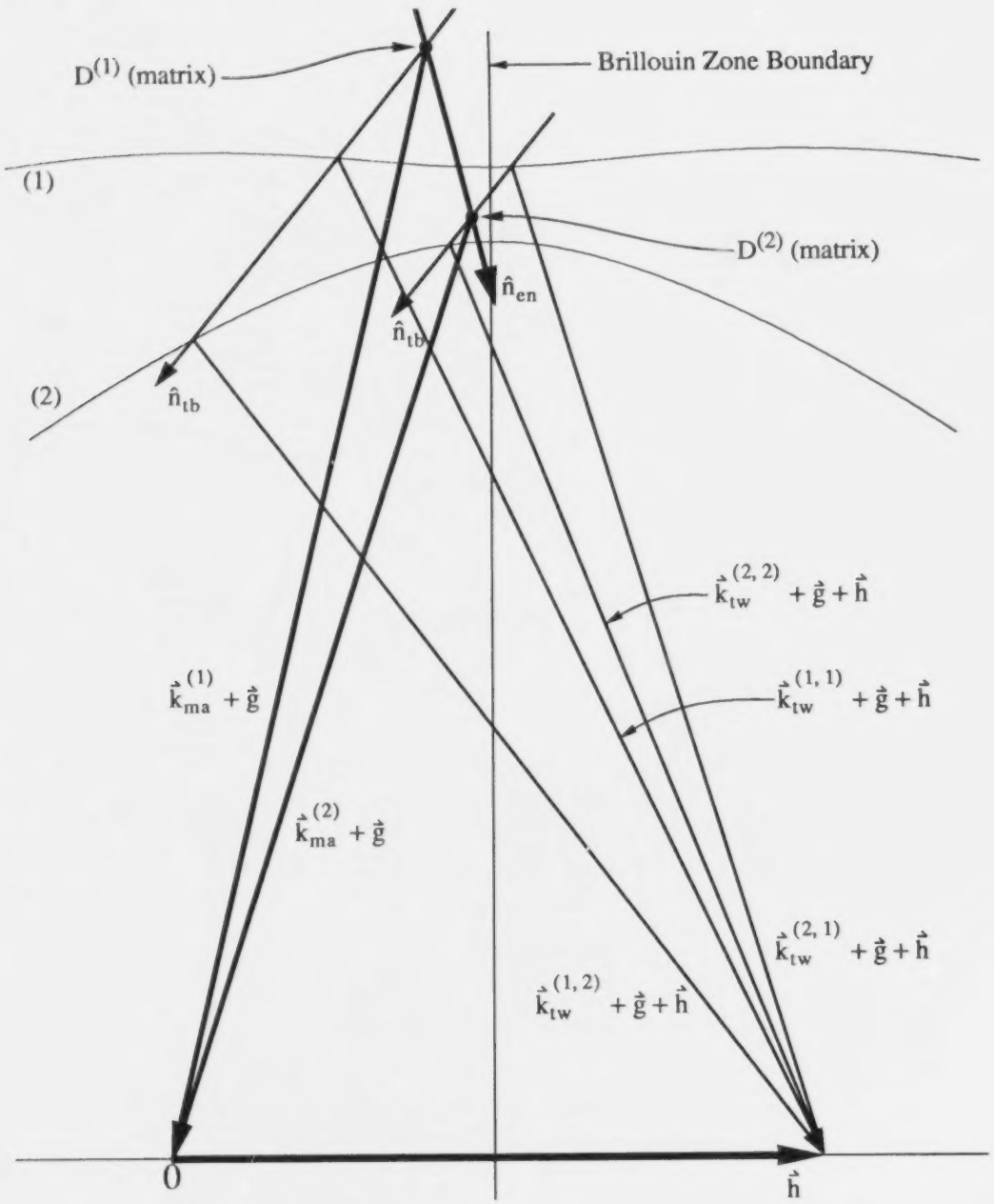

Fig. 3.11. Dispersion surface diagram for the twin crystal in the two beam approximation. $\hat{n}_{en}$ is the normal to the crystal entrance surface and $\hat{n}_{tb}$ is the normal to the twin boundary. A line parallel to $\hat{n}_{tb}$ is drawn through the starting point of each matrix wave vector. The wave vectors in the twin which originate from this matrix wave vector have their starting points on this line. There should also be vectors of the type, $\vec{k}_{tw}^{(i,j)} + \vec{g}$, which end at the origin, but these have been omitted for simplicity.

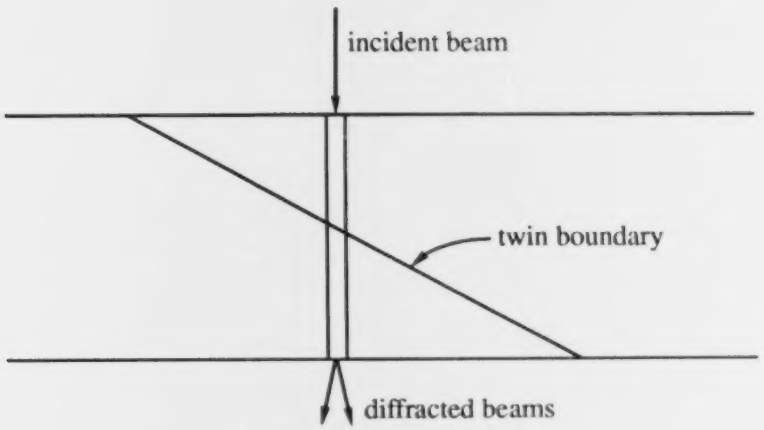

Fig. 3.12. Diagram illustrating the column approximation.

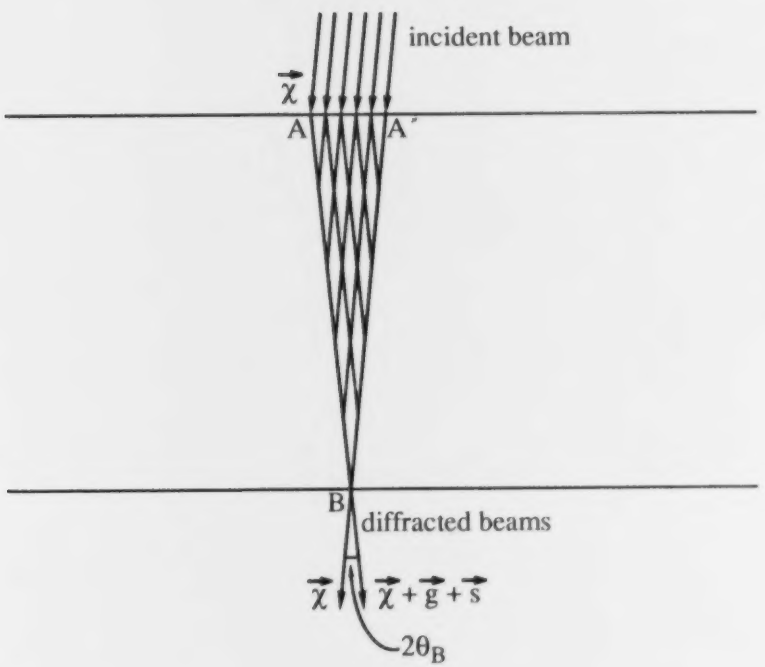

Fig. 3.13. Illustration of the relation between the validity of the column approximation and the small Bragg angles, θ_B, for high energy electrons.

column approximation. The figure is based on the two-beam approximation, but the idea still applies in the case of many beams. It can be seen from the diagram that all of the contributions to the wavefunction at B actually come from a very slender triangle, rather than a column.

The effect of this approximation is that the position of a crystal defect, in the present case the twin boundary, can be assumed to be at a constant depth throughout the column. Thus, the twin boundary can be assumed to be parallel to the entrance surface of the crystal, as shown in Figure 3.14. The wavefunction at the bottom of a different column can be

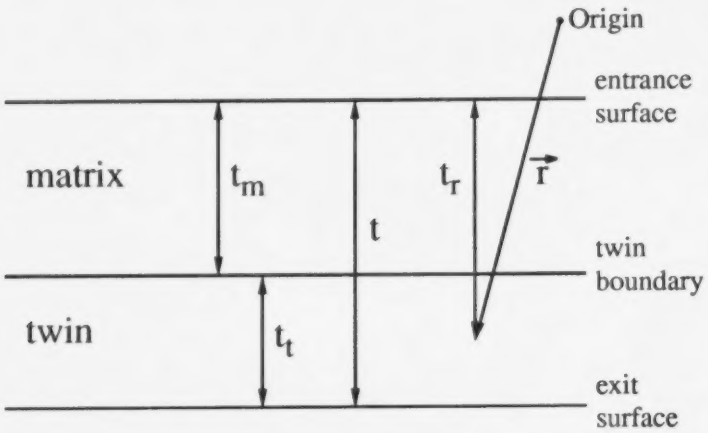

Fig. 3.14. Assumed twin boundary orientation under the column approximation.

calculated by simply using the new values for t_m and t_t. This simplifies the calculations considerably since now all of the wave vectors still have their origins on a line drawn in the z-direction through the origin of $\vec{\chi}$, as shown in Figure 2.2.

Therefore, there will be only one Bloch wave, $b_p^{(i)}$, for each branch of the dispersion surface, to describe high energy electrons in a particular dynamically coupled set. As a result, the total wavefunction of high energy electrons in the twin crystal is given by:

$$\Psi = \sum_i \sum_p X^{(i)} b_p^{(i)} \tag{3.5}$$

3.3.2. Solution of the Schrödinger Wave Equation

Once again, the Schrödinger equation, given in eq. 2.1, must be solved. However, this time the wavefunction given in eq. 3.5 and the twin potential are used. The potential in the twin is given by:

$$V(r) = \frac{h^2}{2me}\sum_j U_{h_j} \exp(2\pi i \vec{h}_j \cdot \vec{r}) \tag{3.6}$$

It is possible that the twin crystal is shifted, relative to the matrix, by a rigid body translation vector, $\vec{T}$, as shown in Figure 3.15. The Fourier coefficients, U_{h_j}, in eq. 3.6, are

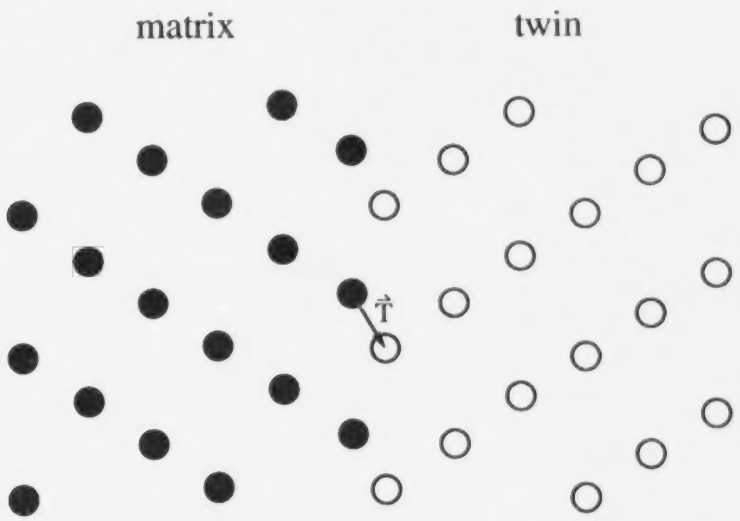

Fig. 3.15. Illustration of the rigid body translation vector, $\vec{T}$.

calculated assuming that the twin crystal is positioned in a certain way, relative to the matrix. If it is assumed to be positioned as shown in Fig. 3.1, but it is actually positioned as shown in Fig. 3.15, the resulting solution will not be valid. This is taken into account by writing the actual potential, $V'(\vec{r})$, in terms of the potential for no translation vector,

$V(\vec{r})$, which is given in eq. 3.6. This is done in the following way:

$$V'(\vec{r}+\vec{T}) = V(\vec{r})$$

Therefore,

$$V'(\vec{r}) = V(\vec{r}-\vec{T}) = \frac{h^2}{2me}\sum_j U_{h_j} \exp[2\pi i \vec{h}_j \cdot (\vec{r}-\vec{T})] \tag{3.7}$$

Similarly, the new Bloch function must be written as:

$$b'^{(i)}_p = \exp\left[2\pi i (\vec{k}^{(i)} + \vec{g}_p) \cdot (\vec{r}-\vec{T})\right] \sum_{m,n} C^{(i)}_{g_p, q_m, h_n} \exp[2\pi i (\vec{q}_m + \vec{h}_n) \cdot (\vec{r}-\vec{T})] \tag{3.8}$$

When the potential and the total wavefunction are substituted into the Schrödinger equation, the following equation results:

$$\sum_{i,p,m,n}\left[K^2 - (\vec{k}^{(i)} + \vec{g}_p + \vec{q}_m + \vec{h}_n)^2\right] C^{(i)}_{g_p, q_m, h_n} X^{(i)} \exp\left[2\pi i (\vec{k}^i + \vec{g}_p + \vec{q}_m + \vec{h}_n) \cdot (\vec{r}-\vec{T})\right]$$

$$+ \sum_j U_{h_j} C^{(i)}_{g_p, q_m, h_n} X^{(i)} \exp\left[2\pi i (\vec{k}^i + \vec{g}_p + \vec{q}_m + \vec{h}_n + \vec{h}_j) \cdot (\vec{r}-\vec{T})\right] = 0$$

In both summations, there are many terms which have the same exponential term. Any reflection, f_k, can be expressed as g_p+h_n. Such a reflection will now be labelled as $f_{p,n}$. Any other combination of matrix and twin reflections which results in a reflection travelling in the same direction can be described as $f_{p,n}=(g_p+q_m)+(h_n-q_m)$ for any common reflection, q_m. Although g_p+h_n and $(g_p+q_m)+(h_n-q_m)$ represent beams travelling in the same direction, the Bloch wave amplitudes, $C^{(i)}_{g_p, q_m, h_n}$ and $C^{(i)}_{g_p, (q_m+q_{m'}), (h_n-q_{m'})}$, are not the same. However, all of the terms which have the same exponential term can be collected together in the following way:

$$\sum_{i,p,n}\left(\left[K^2 - (\vec{k}^{(i)} + \vec{g}_p + \vec{h}_n)^2\right]\left[\sum_m C^{(i)}_{g_p, q_m, (h_n-q_m)}\right] + \sum_{j\neq 0} U_{h_j}\left[\sum_m C^{(i)}_{g_p, q_m, (h_n-q_m-h_j)}\right]\right)$$

$$\times X^{(i)} \exp\left[2\pi i (\vec{k}^{(i)} + \vec{g}_p + \vec{h}_n) \cdot (\vec{r}-\vec{T})\right] = 0$$

Once again, this equation must hold for all vectors, $\vec{r}$, and so the coefficients of the

exponential terms must all be zero.

$$\left[K^2 - (\vec{k}^{(i)} + \vec{g}_p + \vec{h}_n)^2\right]\left[\sum_m C^{(i)}_{g_p, q_m, (h_n - q_m)}\right] + \sum_{j \neq 0} U_{h_j}\left[\sum_m C^{(i)}_{g_p, q_m, (h_n - q_m - h_j)}\right] = 0 \quad (3.9)$$

It is now helpful to make the following definition:

$$C^{(i)}_{p, n} = \sum_m C^{(i)}_{g_p, q_m, (h_n - q_m)}$$

and

$$C^{(i)}_{p, n-j} = \sum_m C^{(i)}_{g_p, q_m, (h_n - h_j - q_m)}$$

Using this new definition, eq. 3.9 can be rewritten as follows:

$$\left[K^2 - (\vec{k}^{(i)} + \vec{g}_p + \vec{h}_n)^2\right] C^{(i)}_{p, n} + \sum_{j \neq 0} U_{h_j} C^{(i)}_{p, n-j} = 0 \quad (3.10)$$

Since the second term is summed over all twin reciprocal lattice vectors, the summation can be done over a different reciprocal lattice vector, h_n', which is related to h_j by:

$$h_n' = h_n - h_j \Rightarrow h_j = h_n - h_n'$$

Equation 3.10 then becomes:

$$\left[K^2 - (\vec{k}^{(i)} + \vec{g}_p + \vec{h}_n)^2\right] C^{(i)}_{p, n} + \sum_{n' \neq n} U_{h_n - h_{n'}} C_{n'}{}^{(i)} = 0 \quad (3.11)$$

The second term in this equation is what couples one equation to all of the others. However, it can be seen that the summation in this term actually only covers other reflections in the same dynamically coupled set. This reflects the fact that there is no dynamical coupling between reflections which are in different dynamically coupled sets. The effect of this is that there is one set of equations for each dynamically coupled set and each set is independent of all of the rest. Each set of equations can be expressed as a matrix equation, just as was done in sec. 2.1. For example, the matrix equation for the 2nd dynamically

coupled set would be the following:

$$\begin{bmatrix} K^2 - (\vec{k}^{(i)} + \vec{g}_2 + \vec{h}_1)^2 & U_{h_1-h_2} & U_{h_1-h_3} & \cdots\ \cdots\ \cdots \\ U_{h_2-h_1} & K^2 - (\vec{k} + \vec{g}_2 + \vec{h}_2)^2 & U_{h_2-h_3} & \\ U_{h_3-h_1} & U_{h_3-h_2} & K^2 - (\vec{k} + \vec{g}_2 + \vec{h}_3)^2 & \\ \cdots & & \cdots & \\ \cdots & & \cdots & \end{bmatrix} \begin{bmatrix} C_{2,1}^{(i)} \\ C_{2,2}^{(i)} \\ C_{2,3}^{(i)} \\ \cdots \\ \cdots \end{bmatrix} = 0$$

These matrix equations can be put into the more familiar form involving the **A** matrix:

$$\mathbf{A}_p \mathbf{C}_p^{(i)} = \gamma_p^{(i)} \mathbf{C}_p^{(i)} \tag{3.12}$$

where:

$$\mathbf{A}_p = \begin{bmatrix} s_{g_p+h_1} & U_{h_1-h_2} & U_{h_1-h_3} & \cdots\ \cdots\ \cdots \\ U_{h_1-h_3} & s_{g_p+h_2} & U_{h_1-h_3} & \\ U_{h_1-h_3} & U_{h_1-h_3} & s_{g_p+h_3} & \\ \cdots & & \cdots & \\ \cdots & & & \cdots \end{bmatrix} \tag{3.13}$$

and

$$\mathbf{C}_p^{(i)} = \begin{bmatrix} C_{p,1}^{(i)} \\ C_{p,2}^{(i)} \\ C_{p,3}^{(i)} \\ \cdots \\ \cdots \end{bmatrix}$$

Each **A** matrix has different values on its diagonal and, therefore, each matrix equation represented by eq. 3.12 will have a different set of eigenvalues and eigenvectors. It is important to realize that the eigenvectors of one **A** matrix are in no way related to those of a different **A** matrix. In other words, $\mathbf{C}_p^{(i)}$ will not be the same as $\mathbf{C}_q^{(i)}$ for any given value of i, nor will it in general have the same number of components. Therefore, any summation over i, i.e. over Bloch waves for a particular dynamically coupled set, should properly be over i_p, since each dynamically coupled set has a different set of eigenvalues and

eigenvectors.

Total electron wavefunction, using this new convention, can be rewritten as follows:

$$\Psi = \sum_{p} \sum_{i_p} X^{(i_p)} b_p{}'^{(i_p)}$$

$$= \sum_{p,\,m,\,n} \sum_{i_p} X^{(i_p)} C^{(i_p)}_{g_p,\,q_m,\,h_n} \exp\left[2\pi i\,(\vec{k}^{(i_p)} + \vec{g}_p + \vec{q}_m + \vec{h}_n) \cdot (\vec{r} - \vec{T})\right]$$

$$= \sum_{p,\,n,\,i_p} X^{(i_p)} \left[\sum_{m} C^{(i_p)}_{g_p,\,q_m,\,(h_n - q_m)}\right] \exp\left[2\pi i\,(\vec{k}^{(i_p)} + \vec{g}_p + \vec{h}_n) \cdot (\vec{r} - \vec{T})\right]$$

If this wavefunction is separated in terms of its component waves which are travelling in different directions, the following is obtained:

$$\Psi = \sum_{p,\,n} \phi_{f_{p,\,n}} \tag{3.14}$$

where

$$\phi_{f_{p,\,n}} = \phi_{p,\,n} = \sum_{i_p} X^{(i_p)} C^{(i_p)}_{p,\,n} \exp\left[2\pi i\,(\vec{k}^{(i_p)} + \vec{g}_p + \vec{h}_n) \cdot (\vec{r} - \vec{T})\right] \tag{3.15}$$

and where from this point forward, the symbol, $\phi_{f_{p,\,n}}$, will be replaced by the symbol, $\phi_{p,\,n}$, for simplicity.

This wavefunction must now be equated to the wavefunction in the matrix at the twin boundary. When this is done, the excitation coefficients, $X^{(i_p)}$, can be determined. The method involved in this calculation can be found in Appendix A. In the end, the following expression for the twin wavefunction amplitudes is achieved:

$$\phi_{p,\,n} = \exp(2\pi i \vec{\chi} \cdot \vec{r}_{en}) \exp[2\pi i \vec{K} \cdot (\vec{r} - \vec{r}_{en})] \exp[2\pi i\,(\vec{g}_p + \vec{h}_n) \cdot \vec{r}]$$

$$\times \sum_{i_p,\,m} \Phi_{g_p + q_m} C^{(i_p)}_{p,\,n_m} C^{(i_p)}_{p,\,n} \exp[2\pi i\,(\vec{q}_m - \vec{h}_n) \cdot \vec{T}] \exp[2\pi i \gamma^{(i_p)} \hat{z} \cdot (\vec{r} - \vec{r}_{tb})] \tag{3.16}$$

where $C^{(i_p)}_{p,\,n_m}$ is the Bloch wave amplitude (in the p^{th} dynamically coupled set) for the twin reflection, $g_p + h_{n_m}$, and $h_{n_m} \equiv q_m$. Also,

$$\Phi_{g_p + q_m} = \sum_{j} D^{(j)}_0 D^{(j)}_{g_p + q_m} \exp(2\pi i \gamma^{(j)}_{ma} t_m) \tag{3.17}$$

where $\gamma^{(j)}_{ma}$ is the eigenvalue of the j^{th} Bloch wave in the matrix and the $D^{(j)}_g$'s are the wave

vector components in the matrix. This expression for $\Phi_{g_p + q_m}$ is the same as the one given in eq. 2.34 for the amplitude which was used to calculate $I_{g_p + q_m}$.

Thus, the intensity which results from allowing this set of reflections, which are all travelling in the same direction, to pass through the aperture is given by:

$$I_{p,n} = \left|\phi_{p,n}(\vec{r}_{ex})\right|^2$$

where $\vec{r}_{ex}$ is a vector which ends at the point of exit of the electrons on the exit surface. Therefore:

$$I_{p,n} = \left|\sum_{i_p, m} \Phi_{g_p + q_m} C^{(i_p)}_{p, n_m} C^{(i_p)}_{p, n} \exp\left[2\pi i\,(\vec{q}_m - \vec{h}_n)\cdot\vec{T}\right] \exp\left(2\pi i \gamma^{(i_p)} t_t\right)\right|^2 \qquad (3.18)$$

where $t_t = (\vec{r}_{ex} - \vec{r}_{tb})\cdot\hat{z}$ is the thickness of the twin crystal in the z-direction.

When inelastic scattering is taken into account, this equation must be altered to give the correct intensity. The intensity, including inelastic scattering, is given by:

$$I_{p,n} = \left|\sum_{i_p, m} \Phi_{g_p + q_m} C^{-1}_{i,p,m} C^{(i_p)}_{p,n} \exp\left[2\pi i\,(\vec{q}_m - \vec{h}_n)\cdot\vec{T}\right] \exp\left(-2\pi q^{(i_p)} t_t\right) \exp\left(2\pi i \gamma^{(i_p)} t_t\right)\right|^2 \qquad (3.19)$$

where $C^{-1}_{i,p,m}$ is the element in the $i_p{}^{th}$ row and the $(N_t \times (p-1) + n_m)^{th}$ column of $\mathbf{C}^{-1}$ and $\Phi_{g_p + q_m}$ is given by:

$$\Phi_{g_p + q_m} = \sum_j D^{-1}_{j1} D^{(j)}_{g_p + q_m} \exp\left(-2\pi q^{(j)}_{ma} t_m\right) \exp\left(2\pi i \gamma^{(j)}_{ma} t_m\right) \qquad (3.20)$$

where t_m is the thickness of the matrix crystal in the z-direction, and $\gamma^{(j)}_{ma} + i q^{(j)}_{ma}$ is the eigenvalue of the j^{th} Bloch wave in the matrix crystal.

3.4. Twinned Crystals Having Almost Common Reflections.

In section 3.1.3, it was stated that pseudo-merohedral twins and pseudo-reticular merohedral twins will contain almost common, or pseudo-common reflections. In the former case, all of the matrix reflections will be common or pseudo-common with a twin reflection. As a result, any image formed by allowing a particular reflection to pass through the objective aperture of the microscope will generally also have contributions from other reflections which also pass through the aperture but which are not exactly common with the first. In the case of pseudo-reticular merohedral twins, there will be some reflections which are neither common nor pseudo-common. This is the situation shown in Fig. 3.9. However, in general, if the aperture is centered around the reflection, g+h, and there exists a pseudo-common matrix reflection, g', such that the matrix reflection, $g + g'$, is excited strongly enough to be included in the calculations, there will be at least one other, non-common reflection which contributes to the image. If the twin reflection which is almost common with g' is written, $h' = g' + \delta$, then the reflection, $f = g + h + g' - h' = g + h - \delta$, will be close enough to g+h to pass through the objective aperture.

The wavefunction of all electrons which pass through the aperture will, therefore, be a linear superposition of the wavefunctions of the diffracted beams which pass through. These wavefunctions are given by eq. 3.16.

$$\phi'_{p,n} = \sum_{p'} \phi_{p',n'} \tag{3.21}$$

where the summation is over all reflections which pass through the aperture.

The summation is over p' only, since only reflections which are in different dynamically coupled sets can be almost common with each other. As an example of this, Figure 3.16 shows the diffraction pattern of $Y_1Ba_2Cu_3O_{7-\delta}$. The zone axis of the matrix crystal is [001]. It can be seen that there is one row of common reflections in the diffraction pattern, and this row is perpendicular to the twin plane. Therefore, there are as many dynamically coupled sets as there are rows of matrix reflections parallel to the common row. The matrix reflections in one dynamically coupled set are indicated by the dashed line. If the objective

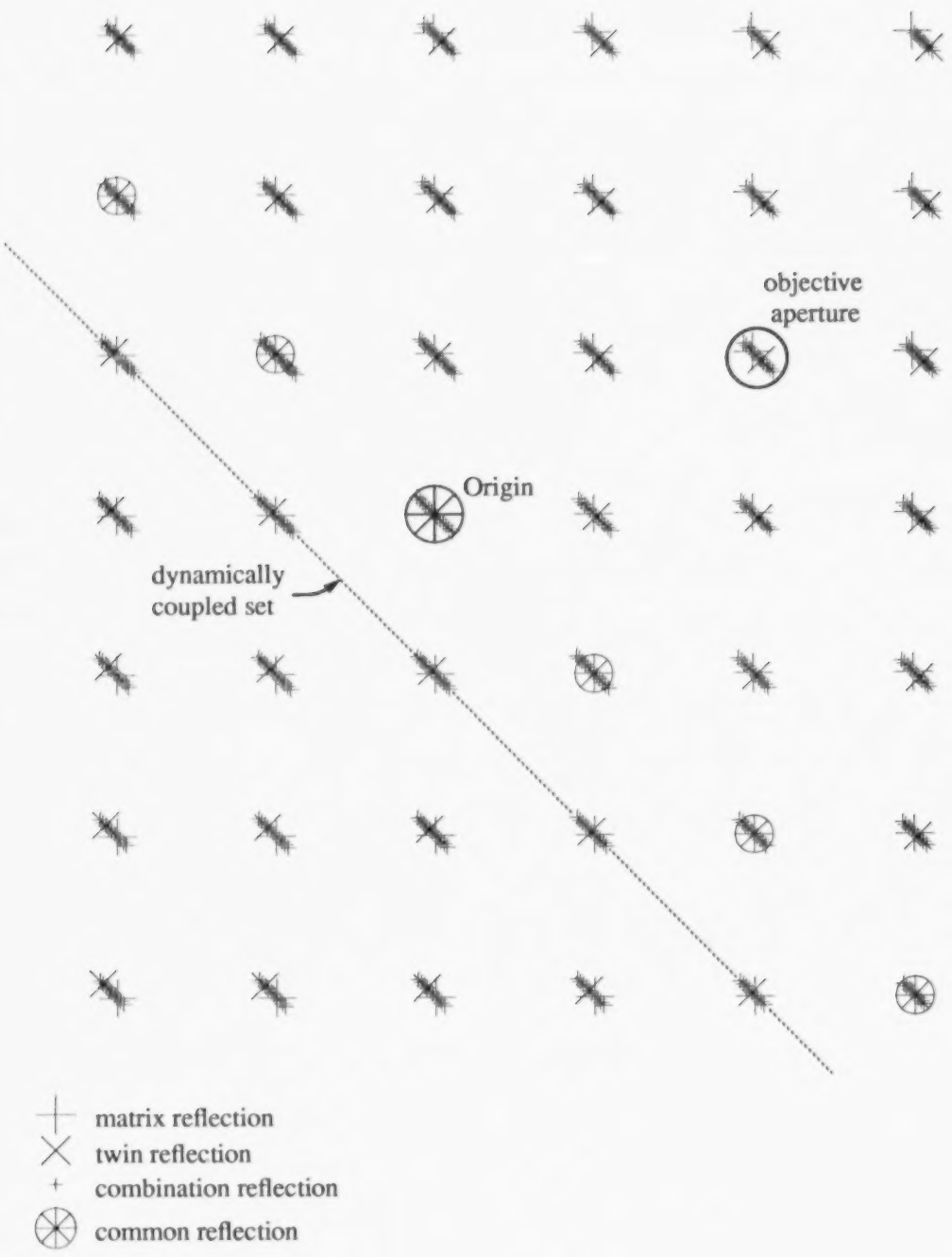

Fig. 3.16. Diffraction pattern from a (110) twin boundary in $Y_1Ba_2Cu_3O_{7-\delta}$. The matrix zone axis is [001] while the twin zone axis is [00$\bar{1}$]. A typical dynamically coupled set is indicated by the dashed line.

aperture is positioned around a set of reflections as shown by the circle in the figure, each plus sign in the circle represents a reflection which gives a contribution to the summation in eq. 3.21. In general, if the aperture is placed around the reflection, $f_{p,n}$, the summation will have contributions from any dynamically coupled set which has at least one reflection which is pseudo-common with a reflection in the set defined by $g_{p'}$.

Equation 3.21 can be expanded to give:

$$\phi'_{p,n} = \exp(2\pi i\vec{\chi}\cdot\vec{r}_{en})\exp(2\pi i\vec{K}\cdot\vec{r})\sum_{p'}\exp[2\pi i(\vec{g}_{p'}+\vec{h}_{n'})\cdot\vec{r}]$$

$$\times\sum_{i_{p'}}\sum_{m}\Phi_{g_{p'}+q_m}C^{(i_{p'})}_{p',n_m}C^{(i_{p'})}_{p',n'}\exp[2\pi i(\vec{q}_m-\vec{h}_{n'})\cdot\vec{T}]\exp[2\pi i\gamma^{(i_{p'})}(t_r-t_m)]$$

where t_r is the depth of $\vec{r}$ in the crystal as shown in Figure 3.14, and $h_{n'}$ is the twin reflection given by $\vec{h}_{n'}\equiv\vec{g}_p+\vec{h}_n-\vec{g}_{p'}$. The term $\exp[2\pi i(\vec{g}_{p'}+\vec{h}_{n'})\cdot\vec{r}]$ cannot be dropped now, since it is different for each term in the summation over p'. Therefore, the intensity which results from this set of reflections passing through the aperture is given by:

$$I'_{p,n} = \left|\phi'_{p,n}(\vec{r}_{ex})\right|^2$$

$$= \left|\sum_{p'}\exp[2\pi i(\vec{g}_{p'}+\vec{h}_{n'})\cdot\vec{r}_{ex}]\left(\sum_{i_{p'}}\sum_{m}\Phi_{g_{p'}+q_m}C^{(i_{p'})}_{p',n_m}C^{(i_{p'})}_{p',n'}\right.\right.$$

$$\left.\left.\times\ \exp[2\pi i(\vec{q}_m-\vec{h}_{n'})\cdot\vec{T}]\exp(2\pi i\gamma^{(i_{p'})}t_t)\right)\right|^2 \qquad (3.22)$$

where $\Phi_{g_{p'}+q_m}$ is given by eq. 3.17. When inelastic scattering is taken into account, this equation becomes:

$$I'_{p,n} = \left|\sum_{p'}\exp[2\pi i(\vec{g}_{p'}+\vec{h}_{n'})\cdot\vec{r}_{ex}]\left(\sum_{i_{p'}}\sum_{m}\Phi_{g_{p'}+q_m}C^{-1}_{i_{p'},p',n_m}C^{(i_{p'})}_{p',n'}\right.\right.$$

$$\left.\left.\times\ \exp[2\pi i(\vec{q}_m-\vec{h}_{n'})\cdot\vec{T}]\exp(-2\pi q^{(i_{p'})}t_t)\exp(2\pi i\gamma^{(i_{p'})}t_t)\right)\right|^2 \qquad (3.23)$$

where $\Phi_{g_{p'}+q_m}$ is given by eq. 3.20.

Equations 3.22 and 3.23 both have one term, $\exp[2\pi i(\vec{g}_{p'}+\vec{h}_{n'})\cdot\vec{r}_{ex}]$, which seems to depend on the choice of the origin. However, this is not the case as long as the

choice of origin is used consistently throughout the calculations. The Fourier coefficients, U_g, which are used to calculate $\Phi_{g_{p'}+q_{m'}}$, are calculated assuming a certain origin. This origin usually coincides with the location of a certain atom in the unit cell. For example, in the superconductor $Y_1Ba_2Cu_3O_{7-\delta}$, the origin is chosen to be one of the copper atoms, as shown in Figure 3.17. Therefore, the origin must be chosen to be at one of the lattice sites which correspond with this atom.

The origin dependent term can be split up into a product of two terms:

$$\exp(2\pi i \vec{g}_{p'} \cdot \vec{r}_{ex}) \exp(2\pi i \vec{h}_{n'} \cdot \vec{r}_{ex})$$

The first term has the periodicity of the matrix crystal. i.e.

$$\exp[2\pi i \vec{g}_{p'} \cdot (\vec{r}_{ex} + u\vec{a} + v\vec{b} + w\vec{c})] = \exp(2\pi i \vec{g}_{p'} \cdot \vec{r}_{ex})$$

where $\vec{a}$, $\vec{b}$, and $\vec{c}$ are the primitive lattice vectors of the matrix. Therefore, any point in space, which differs from the position of one of the corner copper atoms by a matrix lattice vector, can be chosen as the origin and will give the same result for the term, $\exp(2\pi i \vec{g}_{p'} \cdot \vec{r}_{ex})$.

Likewise, the twin Fourier coefficients, U_h, are calculated assuming that the origin coincides with the same corner copper atom. Any point which is on the lattice defined by these copper atoms can be chosen as the origin, and will give the same result for the term, $\exp(2\pi i \vec{h}_{n'} \cdot \vec{r}_{ex})$. The problem is that the lattice of corner copper atoms in the matrix does not coincide with this lattice in the twin. The only place where they do coincide is on the twin boundary, as shown in Figure 3.18. Thus, one of these copper sites on the twin boundary must be chosen as the origin.

It is important to note that this does not mean that the rigid body translation vector is being assumed to be zero, as implied by Fig. 3.18. It simply means that Fourier coefficients are calculated assuming this configuration, and the possibility that the twin crystal is translated by some amount is accounted for by the use of the vector, $\vec{T}$, in eq. 3.22 and eq. 3.23. Therefore, this vector, $\vec{T}$, refers to the translation of the twin crystal from the position it has in Fig. 3.18.

Thus, it has been shown that one of the copper sites on the twin boundary must be

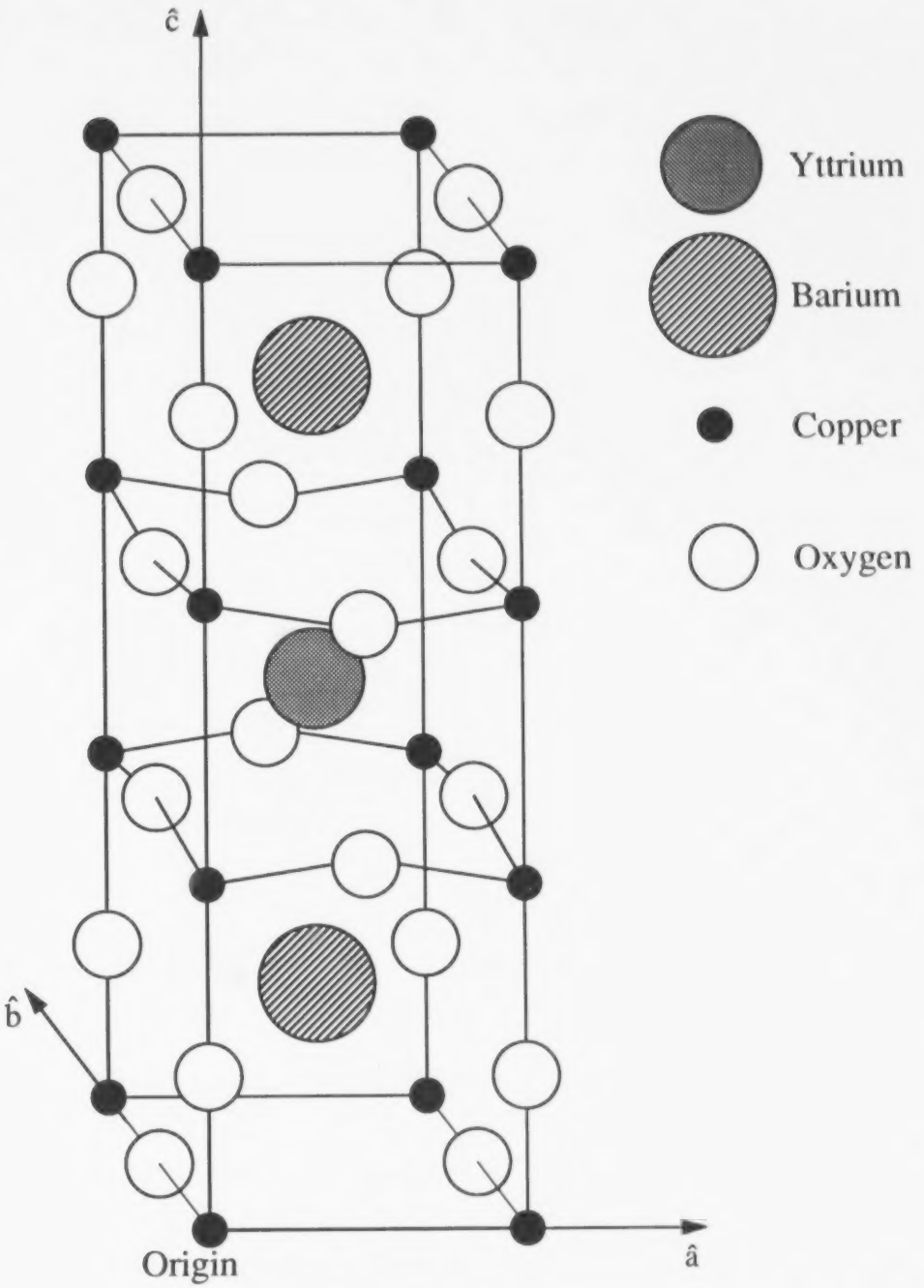

Fig. 3.17. Unit cell of the high temperature superconductor, $Y_1Ba_2Cu_3O_{7-\delta}$.

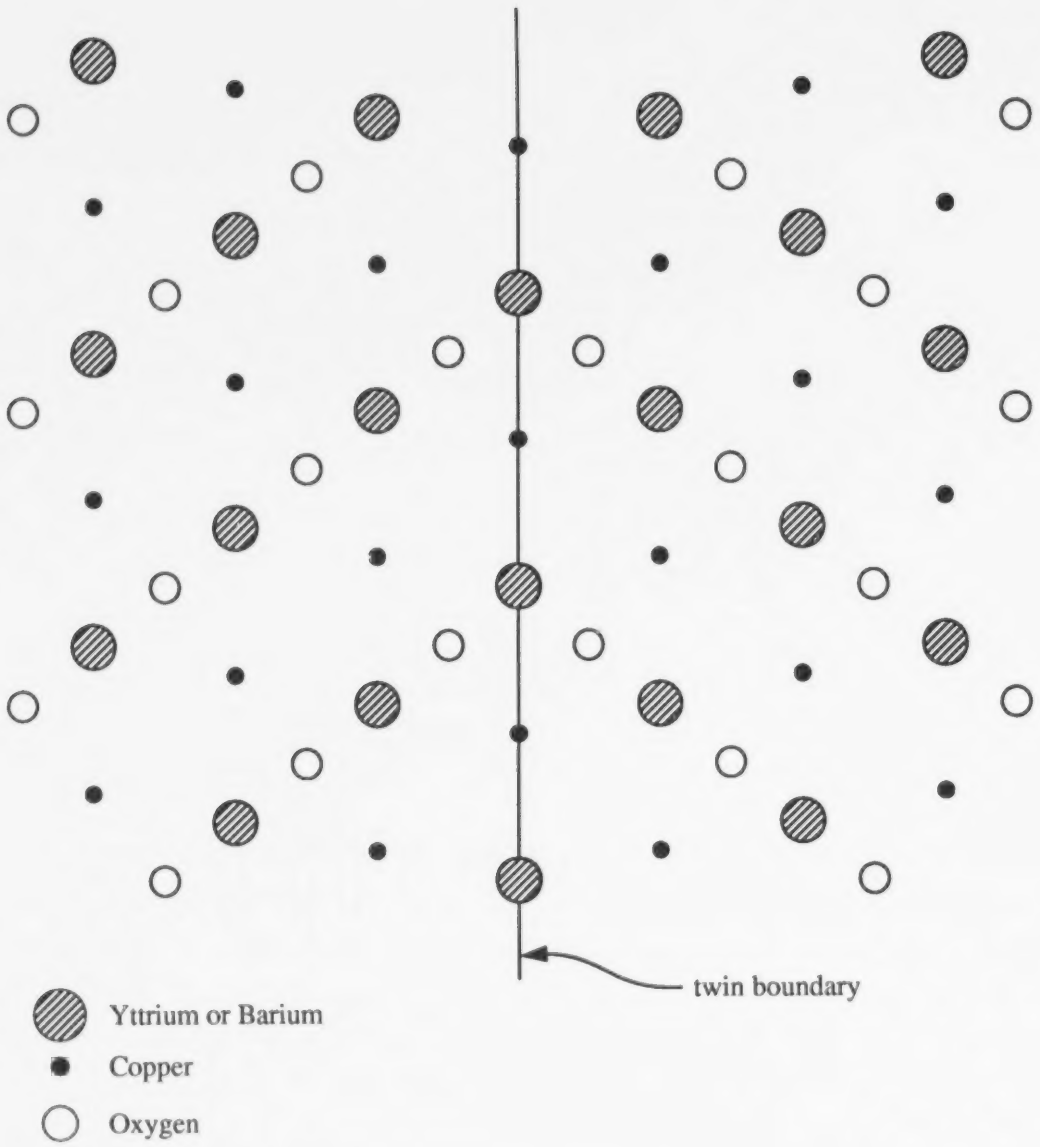

Fig. 3.18. Twin boundary for the superconductor $Y_1Ba_2Cu_3O_{7-\delta}$ assuming a body translation vector of 0. Only the basal plane is shown along with the positions of the Yttrium and Barium ions. The difference between the a and b lattice parameters has been exaggerated.

chosen as the origin. But it is impossible to know exactly where the copper atoms are located. It might seem that this would lead to inaccuracies in the predicted intensity on a very small scale. This does not happen, however. This is because, for pseudo-merohedral

twins and pseudo-reticular merohedral twins, the difference between two almost coincident reciprocal lattice vectors, $\vec{g} - \vec{h} = \Delta\vec{g}$, is normal to the twin plane[33]. In the case of parallel rotation twins, $\Delta\vec{g}$ is perpendicular to the twin axis. One effect of this is that all of the almost common reflections differ from each other by a vector which is normal to the twin boundary, in the case of reflection and compound twins. Therefore, the term, $\vec{g}_{p'} + \vec{h}_{n'}$, can be rewritten as follows:

$$\begin{aligned}\vec{g}_{p'} + \vec{h}_{n'} &= \vec{g}_p + \vec{h}_n + \Delta\vec{g}_{p',n'} \\ &= \vec{g}_p + \vec{h}_n + \varepsilon_{p',n'}\vec{n}_{tb}\end{aligned}$$

The exponential term then becomes:

$$\exp[2\pi i(\vec{g}_{p'} + \vec{h}_{n'}) \cdot \vec{r}_{ex}] = \exp[2\pi i(\vec{g}_p + \vec{h}_n) \cdot \vec{r}_{ex}] \exp[2\pi i\varepsilon_{p',n'}\vec{n}_{tb} \cdot \vec{r}_{ex}]$$

The first of these terms. however, can be taken out of the summation in eq. 3.22 and eq. 3.23. And the second term will give the same result regardless of where on the twin boundary the origin is chosen to be. The second term, therefore, becomes:

$$\exp(2\pi i\varepsilon_{p',n'}d_{tb})$$

where d_{tb} is the perpendicular distance from the twin boundary of the point of exit of the electrons.

3.4.1. Two Beam Approximation

It is sometimes desirable, in order to gain insight into the form of the diffraction contrast images, to have an analytical expression for the intensity which does not involve unknown terms such as $\gamma^{(i_{p'})}$ and $C^{(i_{p'})}_{f_{p',n'}}$, which can only be found through the diagonalization of a matrix. The only case in which such a solution is possible is when only two beams are strongly excited. In the case of twin boundary contrast, this means there are have two matrix reflections, 0 and g, each of which leads to two twin reflections, 0 and h, and g and g-h respectively. Therefore, if the objective aperture is centered around the transmitted beam, there are actually two beams contributing, 0 and g-h. This is shown in Figure 3.19. Similarly, two beams, g and h, contribute if the aperture is centered around the one major diffracted beam.

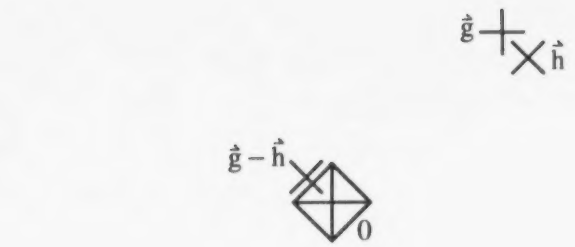

matrix reflection

twin reflection

Fig. 3.19. Illustration of the reflections which must be taken into account in the two beam approximation.

The first thing which must be done is the eigenvalue equations for the matrix and twin crystals must be solved. The following results are for the case where inelastic scattering is taken into account. In the matrix, eq. 2.20 can be written as:

$$\begin{bmatrix} iU_0' - \gamma_{ma} & \frac{U_g + iU_g'}{2K} \\ \frac{U_g + iU_g'}{2K} & s_g + iU_0' - \gamma_{ma} \end{bmatrix} \begin{bmatrix} D_0 \\ D_g \end{bmatrix} = 0 \qquad (3.24)$$

Therefore, the determinant of the matrix must be equal to zero.

$$(iU_0' - \gamma_{ma})(s_g + iU_0' - \gamma_{ma}) - \frac{(U_g + iU_g')^2}{4K^2} = 0$$

$$\gamma_{ma} = \frac{1}{2}\left(s_g \pm \sqrt{s_g^2 + \frac{(U_g + iU_g')^2}{K^2}}\right) + iU_0'$$

The rest of the calculations can now be simplified by introducing the dimensionless parameter, w, defined by:

$$w_g = \frac{s_g K}{(U_g + iU_g')} \qquad (3.25)$$

The eigenvalues can be rewritten in terms of this parameter:

$$\gamma_{ma}^{(j)} = \frac{U_g + iU_g'}{2K}\left[w_g - (-1)^j\sqrt{1+w_g^2}\right] + iU_o' \tag{3.26}$$

If these eigenvalues are substituted back into eq. 3.24, the normalized the eignenvectors, D_0 and D_g, can be found to be given by the following expressions:

$$D_0^{(1)} = \sqrt{\frac{1}{2}\left(1 - \frac{w_g}{\sqrt{1+w_g^2}}\right)} \qquad D_0^{(2)} = \sqrt{\frac{1}{2}\left(1 + \frac{w_g}{\sqrt{1+w_g^2}}\right)}$$

$$D_g^{(1)} = \sqrt{\frac{1}{2}\left(1 + \frac{w_g}{\sqrt{1+w_g^2}}\right)} \qquad D_g^{(2)} = -\sqrt{\frac{1}{2}\left(1 - \frac{w_g}{\sqrt{1+w_g^2}}\right)} \tag{3.27}$$

These expressions can be substituted back into eq. 3.17 to find the following expressions for the matrix beam amplitudes:

$$\Phi_0 = \exp(-2\pi U_o' t_m)\left[\cos\left(\frac{\pi U_g t_m}{K}\sqrt{1+w_g^2}\right) - \frac{iw_g}{\sqrt{1+w_g^2}}\sin\left(\frac{\pi U_g t_m}{K}\sqrt{1+w_g^2}\right)\right]$$

$$\Phi_g = \exp(-2\pi U_o' t_m)\left[\frac{i}{\sqrt{1+w_g^2}}\sin\left(\frac{\pi U_g t_m}{K}\sqrt{1+w_g^2}\right)\right] \tag{3.28}$$

where the phase factor, $\exp(\pi i s_g t_m)$, has been dropped from both amplitudes, since it will not affect the image intensity. It is easy to see from these equations that the imaginary part of the Fourier coefficient for g=0, U_0', does not affect the image contrast, but rather it reduces the intensity of the entire image uniformly.

In the twin, there are two dynamically coupled sets involved, each of which has a different matrix equation. The first dynamically coupled set, which is defined by g_1=0, has the following matrix equation:

$$\begin{bmatrix} iU_0' - \gamma & \frac{U_h + iU_h'}{2K} \\ \frac{U_h + iU_h'}{2K} & s_h + iU_0' - \gamma \end{bmatrix}\begin{bmatrix} C_{0,0} \\ C_{0,h} \end{bmatrix} = 0 \tag{3.29}$$

The resulting eigenvalues and eigenvectors are completely analogous to the matrix crystal

case:

$$\gamma^{(i_0)} = \frac{U_h + iU_h'}{2K}\left[w_h - (-1)^{i_0}\sqrt{1+w_h^2}\right] + iU_0' \tag{3.30}$$

$$C_{0,0}^{(1_0)} = \sqrt{\frac{1}{2}\left(1 - \frac{w_h}{\sqrt{1+w_h^2}}\right)} \qquad C_{0,0}^{(2_0)} = \sqrt{\frac{1}{2}\left(1 + \frac{w_h}{\sqrt{1+w_h^2}}\right)}$$

$$C_{0,h}^{(1_0)} = \sqrt{\frac{1}{2}\left(1 + \frac{w_h}{\sqrt{1+w_h^2}}\right)} \qquad C_{0,h}^{(2_0)} = -\sqrt{\frac{1}{2}\left(1 - \frac{w_h}{\sqrt{1+w_h^2}}\right)} \tag{3.31}$$

The second dynamically coupled set is defined by $g_2 = g$. The matrix equation is, therefore, given by:

$$\begin{bmatrix} s_g + iU_0' - \gamma & \frac{U_h + iU_h'}{2K} \\ \frac{U_h + iU_h'}{2K} & s_{g-h} + iU_0' - \gamma \end{bmatrix} \begin{bmatrix} C_{g,0} \\ C_{g,-h} \end{bmatrix} = 0 \tag{3.32}$$

The eigenvalues are as follows:

$$\gamma^{(i_g)} = \frac{1}{2}\left(s_g + s_{g-h} - (-1)^{i_g}\sqrt{(s_g - s_{g-h})^2 + \frac{(U_h + iU_h')^2}{K^2}}\right) + iU_0'$$

Here, the normal definition for w_g cannot be used. However, the equations can be simplified by the definition of new dimensionless parameters:

$$w_{g,h} = \frac{s_g K}{(U_h + iU_h')} \qquad \text{and} \qquad w_{g-h,h} = \frac{s_{g-h} K}{(U_h + iU_h')} \tag{3.33}$$

The eigenvalues and eigenvectors can, thus, be written as follows:

$$\gamma^{(i_g)} = \frac{U_h + iU_h'}{2K}\left[w_{g,h} + w_{g-h,h} - (-1)^{i_g}\sqrt{(w_{g,h} - w_{g-h,h})^2 + 1}\right] + iU_0' \tag{3.34}$$

$$C_{g,0}^{(1_g)}=\sqrt{\frac{1}{2}\left(1-\frac{w_{g-h,h}-w_{g,h}}{\sqrt{1+(w_{g-h,h}-w_{g,h})^2}}\right)} \quad C_{g,0}^{(2_g)}=\sqrt{\frac{1}{2}\left(1+\frac{w_{g-h,h}-w_{g,h}}{\sqrt{1+(w_{g-h,h}-w_{g,h})^2}}\right)}$$

$$C_{g,-h}^{(1_g)}=\sqrt{\frac{1}{2}\left(1+\frac{w_{g-h,h}-w_{g,h}}{\sqrt{1+(w_{g-h,h}-w_{g,h})^2}}\right)} \quad C_{g,-h}^{(2_g)}=-\sqrt{\frac{1}{2}\left(1-\frac{w_{g-h,h}-w_{g,h}}{\sqrt{1+(w_{g-h,h}-w_{g,h})^2}}\right)} \tag{3.35}$$

First, the case where g and h are common reflections will be examined. Referring to eq. 3.22, it can be seen that the summation over p′ now contains only one term, $g_p = 0$, since only one dynamically coupled set is involved. This summation can, therefore, be ignored and references to $g_{p'}$ can be replaced by $g_p = 0$. For the case of the transmitted beam, references to $h_{n'}$ are replaced by $h_n = 0$. The summation over m contains two terms, $q_1 = 0$, and $q_2 = g = h$. Eq. 3.28, thus, becomes:

$$I_{0,0} = \left|\sum_{m,\,i_0} \Phi_{q_m} C_{0,n_m}^{(i_0)} C_{0,0}^{(i_0)} \exp(2\pi i \vec{q}_m \cdot \vec{T}) \exp(2\pi i \gamma^{(i_0)} t_t)\right|^2$$

$$= \left|\Phi_0 \sum_{i_0} (C_{0,0}^{(i_0)})^2 \exp(2\pi i \gamma^{(i_0)} t_t)\right.$$

$$\left. + \Phi_g \exp(2\pi i \vec{h} \cdot \vec{T}) \sum_{i_0} C_{0,0}^{(i_0)} C_{0,h}^{(i_0)} \exp(2\pi i \gamma^{(i_0)} t_t)\right|^2 \tag{3.36}$$

When the expressions for Φ, C, and γ, are substituted into this expression, the following equation is obtained:

$$I_{0,0} = \exp(-2\pi U_0' t)\left|\left(\cos(2\pi\sigma_g t_m) - \frac{i w_g}{\sqrt{1+w_g^2}} \sin(2\pi\sigma_g t_m)\right)\right.$$

$$\times \left(\cos(2\pi\sigma_h t_t) - \frac{i w_h}{\sqrt{1+w_h^2}} \sin(2\pi\sigma_h t_t)\right)$$

$$\left. - \exp(2\pi i \vec{h} \cdot \vec{T}) \frac{\sin(2\pi\sigma_g t_m) \sin(2\pi\sigma_h t_t)}{\sqrt{(1+w_g^2)(1+w_h^2)}}\right|^2 \tag{3.37}$$

where

$$\sigma_g = \frac{U_g + iU_g'}{2K}\sqrt{1 + w_g^2} = \sqrt{\left(\frac{U_g + U_g'}{2K}\right)^2 + s_g^2} \tag{3.38}$$

and

$$\sigma_h = \frac{U_h + iU_h'}{2K}\sqrt{1 + w_h^2} = \sqrt{\left(\frac{U_h + U_h'}{2K}\right)^2 + s_h^2} \tag{3.39}$$

Note that θ_g and θ_h are different, not only in the subscripts of U and s, but also in the thickness involved.

The intensity of the common diffracted beam can now be evaluated. It is possible to either let $g_p = 0$ and $h_n = h$, or let $g_p = g$ and $h_n = 0$, and the result will be the same. In keeping with the practice in previous sections, the dynamically coupled set will be defined by $g_p = 0$ and, therefore, $h_n = h$. Therefore:

$$I_{0,h} = \left| \exp\left[2\pi i \vec{h} \cdot \vec{r}_{ex}\right] \sum_{m,\, i_0} \Phi_{q_m} C_{0,n_m}^{(i_0)} C_{0,h}^{(i_0)} \exp\left(2\pi i \left(\vec{q}_m - \vec{h}\right) \cdot \vec{T}\right) \exp\left(2\pi i \gamma^{(i_0)} t_t\right) \right|^2$$

$$= \left| \Phi_0 \left[\exp\left(-2\pi i \vec{h} \cdot \vec{T}\right)\right] \sum_{i_0} C_{0,0}^{(i_0)} C_{0,h}^{(i_0)} \exp\left(2\pi i \gamma^{(i_0)} t_t\right) \right.$$

$$\left. + \Phi_g \sum_{i_0} \left(C_{0,h}^{(i_0)}\right)^2 \exp\left(2\pi i \gamma^{(i_0)} t_t\right) \right|^2 \tag{3.40}$$

When the expressions for the matrix amplitudes and the eigenvalues and eigenvectors are inserted into this equation, the following is obtained:

$$I_{0,h} = \exp\left(-2\pi U_0' t\right) \left| \left(\cos\left(2\pi\sigma_g t_m\right) - \frac{iw_g}{\sqrt{1 + w_g^2}} \sin\left(2\pi\sigma_g t_m\right)\right) \right.$$

$$\times \left(\frac{i}{\sqrt{1 + w_h^2}} \sin\left(2\pi\sigma_h t_t\right)\right) + \exp\left(2\pi i \vec{h} \cdot \vec{T}\right) \left(\frac{i}{\sqrt{1 + w_g^2}} \sin\left(2\pi\sigma_g t_m\right)\right)$$

$$\left. \times \left(\cos\left(2\pi\sigma_h t_t\right) + \frac{iw_g}{\sqrt{1 + w_h^2}} \sin\left(2\pi\sigma_h t_t\right)\right) \right|^2 \tag{3.41}$$

The case where g and h are not common, but are almost common, will now be solved. In the first case it will be assumed that the aperture is centered around the transmitted beam and the reflection, g-h. The summation over p′ now has two terms, one for the $g_1 = 0$ dynamically coupled set, and one for the $g_2 = g$ set. The corresponding h_n's are $h_1 = 0$, and $h_2 = -h$. Each dynamically coupled set contains only one reflection, so the summation over m contains only one term, $q_1 = 0$.

$$I_{0,0} =$$

$$\left| \sum_{p'} \left(\exp\left[2\pi i \left(\vec{g}_{p'} + \vec{h}_{n'}\right) \cdot \vec{r}_{ex}\right] \sum_{i_{p'}} \Phi_{g_{p'}} C_{p',0}^{(i_{p'})} C_{p',n'}^{(i_{p'})} \exp\left(-2\pi i \vec{h}_{n'} \cdot \vec{T}\right) \exp\left(2\pi i \gamma^{(i_{p'})} t_t\right) \right) \right|^2$$

$$= \left| \Phi_0 \sum_{i_0} \left(C_{0,0}^{(i_0)}\right)^2 \exp\left(2\pi i \gamma^{(i_0)} t_t\right) \right.$$

$$\left. + \Phi_g \exp\left[2\pi i \left(\vec{g} - \vec{h}\right) \cdot \vec{r}_{ex}\right] \exp\left(2\pi i \vec{h} \cdot \vec{T}\right) \sum_{i_g} C_{g,0}^{(i_g)} C_{g,-h}^{(i_g)} \exp\left(2\pi i \gamma^{(i_g)} t_t\right) \right|^2 \tag{3.42}$$

If it is assumed that $\vec{g} - \vec{h}$ is normal to the twin boundary, the term, $\exp\left[2\pi i \left(\vec{g} - \vec{h}\right) \cdot \vec{r}_{ex}\right]$, can be written as:

$$\exp\left[2\pi i \left(\vec{g} - \vec{h}\right) \cdot \hat{n}_{tb} d_{tb}\right] = \exp\left[2\pi i \varepsilon_{g,-h} d_{tb}\right]$$

Finally, the following expression is achieved:

$$I_{0,0} = \exp\left(-2\pi U_0' t\right) \left| \exp\left(\pi i s_h t_t\right) \left(\cos\left(2\pi \sigma_g t_m\right) - \frac{i w_g}{\sqrt{1 + w_g^2}} \sin\left(2\pi \sigma_g t_m\right) \right) \right.$$

$$\times \left(\cos\left(2\pi \sigma_h t_t\right) - \frac{i w_h}{\sqrt{1 + w_h^2}} \sin\left(2\pi \sigma_h t_t\right) \right)$$

$$- \exp\left[\pi i \left(s_g + s_{g-h}\right) t_t\right] \left(\exp\left(2\pi i \varepsilon_{g,-h} d_{tb}\right) \exp\left(2\pi i \vec{h} \cdot \vec{T}\right) \right)$$

$$\left. \times \left(\frac{\sin\left(2\pi \sigma_g t_m\right) \sin\left(2\pi \sigma_{g,h} t_t\right)}{\sqrt{\left(1 + w_g^2\right)\left(1 + \left(w_{g-h,h} - w_{g,h}\right)^2\right)}} \right) \right|^2 \tag{3.43}$$

where

$$\sigma_{g,h} = \frac{U_h + iU_h'}{2K}\sqrt{1 + (w_{g-h,h} - w_{g,h})^2} = \sqrt{\left(\frac{U_h + iU_h'}{2K}\right)^2 + (s_{g-h} - s_g)^2} \quad (3.44)$$

If the aperture is centered around the strong diffracted beams, the only change is that the $h_{n'}$'s are now $h_1 = h$, and $h_2 = 0$. Therefore:

$$I_{g,0} = \Big|\Phi_0 \exp(2\pi i\vec{h}\cdot\vec{r}_{ex}) \exp(-2\pi i\vec{h}\cdot\vec{T}) \sum_{i_0} C_{0,0}^{(i_0)} C_{0,h}^{(i_0)} \exp(2\pi i\gamma^{(i_0)} t_t)$$

$$+ \Phi_g \exp(2\pi i\vec{g}\cdot\vec{r}_{ex}) \sum_{i_g} (C_{g,0}^{(i_g)})^2 \exp(2\pi i\gamma^{(i_g)} t_t)\Big|^2 \quad (3.45)$$

If the phase factor, $\exp(2\pi i\vec{h}\cdot\vec{r}_{ex}) \exp(-2\pi i\vec{h}\cdot\vec{T})$, is removed from the expression and the matrix amplitudes, eigenvalues and eigenvectors, are inserted into eq. 3.45, the following solution is obtained:

$$I_{g,0} = \exp(-2\pi U_0' t)\Big|\exp(\pi i s_h t_t)\left(\cos(2\pi\sigma_g t_m) - \frac{iw_g}{\sqrt{1+w_g^2}}\sin(2\pi\sigma_g t_m)\right)$$

$$\times\left(\frac{i}{\sqrt{1+w_h^2}}\sin(2\pi\sigma_h t_t)\right)$$

$$+ \exp[\pi i(s_g + s_{g-h})t_t]\exp(2\pi i\varepsilon_{g,-h}d_{tb})\exp(2\pi i\vec{h}\cdot\vec{T})\left(\frac{i}{\sqrt{1+w_g^2}}\sin(2\pi\sigma_g t_m)\right)$$

$$\times\left(\cos(2\pi\sigma_{g,h}t_t) - \frac{i(w_{g-h,h} - w_{g,h})}{\sqrt{1+(w_{g-h,h} - w_{g,h})^2}}\sin(2\pi\sigma_{g,h}t_t)\right)\Big|^2 \quad (3.46)$$

4. Practical Aspects of Calculations

4.1. Calculation of Elements of the A Matrix

4.1.1. Diagonal Elements of A Matrix

The methods of calculating the elements of the **A** matrix will now be examined. In order to do these calculations, it is necessary to know the orientation of the matrix and twin crystals. In this section, it will be assumed that the crystal orientations are known. The problem of determining these orientations will be dealt with in section 4.2.

The usual method of expressing the precise orientation is to first define the zero order Laue zone. This is the low order reciprocal lattice plane which contains the origin of the reciprocal lattice and which is closest to being perpendicular to the beam direction. The orientation is then defined by specifying the component, $\vec{K}_{||}$, of the wavevector $\vec{K}$ (defined in sec. 2.1.2), which is parallel to this reciprocal lattice plane. This is expressed in terms of the tie point, which is the starting point of the wavevector, $\vec{K}$ (refer to Fig. 2.1). The point of intersection of a line drawn through the tie point, in the direction of the zone axis, and the zero order Laue zone, is called the tie point projection. Therefore, $\vec{K}_{||}$ is the vector which starts at the tie point projection, and ends at the origin of the reciprocal lattice. Once the tie point projection is known, the intersection of the Ewald sphere with the zero order Laue zone can easily be plotted. Figure 4.1 shows the (111) reciprocal lattice plane of $Y_1Ba_2Cu_3O_{7-\delta}$. The tie point projection is indicated by the diamond symbol and the intersection of the Ewald sphere with the zero order Laue zone is shown by the circle which is centered at the tie point projection and which passes through the origin of the reciprocal lattice. The coordinates of the tie point projection in this case are (0.8, 1.2, -2).

In sec. 2.1.4, it was shown that in the symmetrical Laue approximation, the diagonal elements of the **A** matrix are given by:

$$A_{gg} = s_g$$

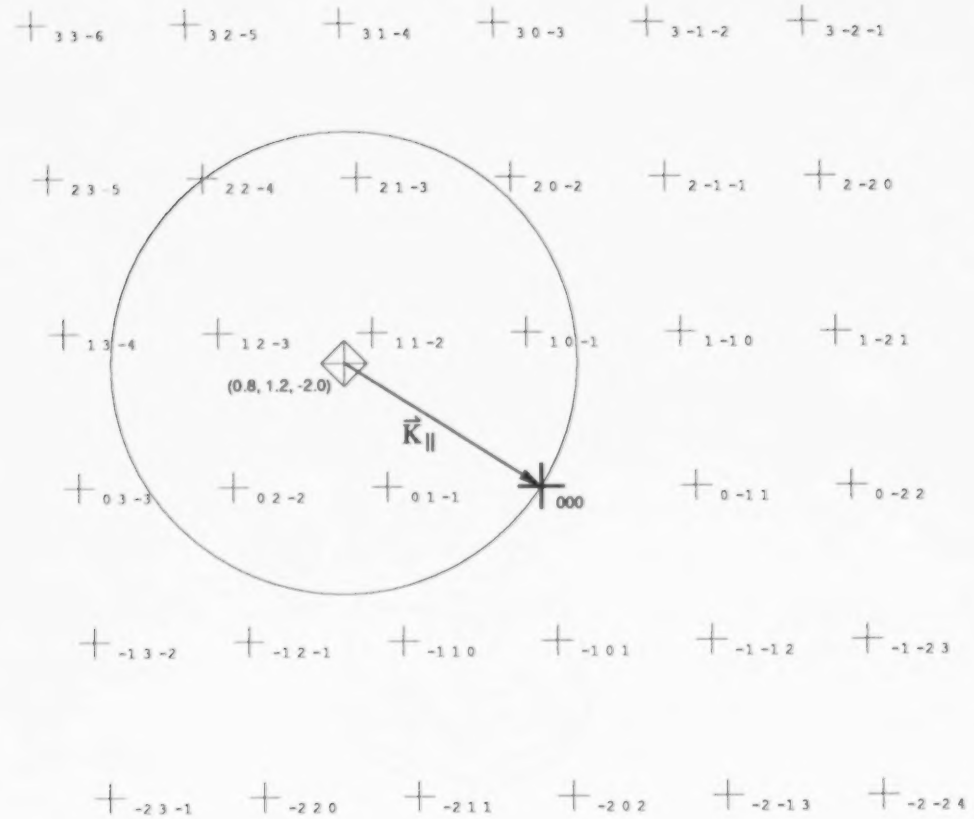

reciprocal lattice point

tie point projection

Fig. 4.1. Plot of the (111) reciprocal lattice plane of $Y_1Ba_2Cu_3O_{7-\delta}$. The tie point projection is (0.8, 1.2, -2) and is indicated by the diamond symbol. The intersection of the Ewald sphere with the zero order Laue zone is indicated by the circle.

or, in the non-symmetrical Laue case:

$$A_{gg} = s_g \cos\theta_0$$

The value, s_g, is defined as the distance from the reciprocal lattice point, g, to the Ewald sphere in a direction parallel to the normal to the entrance surface of the crystal (refer to Fig. 2.1). It is obvious from this definition that any zero order Laue zone reciprocal lattice point in Figure 4.1, which lies near the circle will have a low value of s_g, and will

therefore be close to its Bragg condition.

A method for the calculation of s_g for both the symmetrical and non-symmetrical Laue cases will now be shown. The equation of the Ewald sphere is given by:

$$(x+K_x)^2+(y+K_y)^2+(z+K_z)^2 = K^2 \tag{4.1}$$

The coordinates of the point of intersection of the Ewald sphere and a line which goes through g and runs in a direction parallel to the entrance surface normal, $\hat{n}$, are given by:

$$\begin{aligned} x &= g_x + s_g(\hat{n})_x \\ y &= g_y + s_g(\hat{n})_y \\ z &= g_z + s_g(\hat{n})_z \end{aligned} \tag{4.2}$$

When these coordinates are substituted into eq. 4.1, the resulting equation can be solved for s_g, giving:

$$(g_x + s_g(\hat{n})_x + K_x)^2 + (g_y + s_g(\hat{n})_y + K_y)^2 + (g_z + s_g(\hat{n})_z + K_z)^2 = K^2$$

This can be simplified to give:

$$g^2 + s_g^2 + 2\vec{K}\cdot\vec{g} + 2s_g(\vec{K}+\vec{g})\cdot\hat{n} = 0 \tag{4.3}$$

When this equation is solved for s_g, the result is the following:

$$s_g = -(\vec{K}+\vec{g})\cdot\hat{n} \pm \sqrt{[(\vec{K}+\vec{g})\cdot\hat{n}]^2 - (2\vec{K}+\vec{g})\cdot\vec{g}}$$

This equation gives two values of s_g, one for the intersection of the line with the bottom portion of the Ewald sphere, and one for the intersection at the top of the sphere. s_g should take on both positive and negative values, depending on whether or not the point, g, lies inside of the sphere. Therefore, since the first term of this equation will always be negative, the positive root must be chosen or else s_g must always be negative. Therefore, the equation for s_g is:

$$s_g = -(\vec{K}+\vec{g})\cdot\hat{n} + \sqrt{[(\vec{K}+\vec{g})\cdot\hat{n}]^2 - (2\vec{K}+\vec{g})\cdot\vec{g}} \tag{4.4}$$

In the symmetrical Laue case, $\hat{n}$ is simply replaced by $-\hat{z}$, (refer to Fig. 2.2) to get

the following expression:

$$s_g = (\vec{K} + \hat{g}) \cdot \hat{z} + \sqrt{[(\vec{K} + \hat{g}) \cdot \hat{z}]^2 - (2\vec{K} + \hat{g}) \cdot \hat{g}}$$

This can be simplified to give the following:

$$s_g = K_z + \hat{g} \cdot \hat{z} + \sqrt{K_z^2 + (\hat{g} \cdot \hat{z})^2 - 2(\vec{K}_{||} + \hat{g}) \cdot \hat{g}} \qquad (4.5)$$

where K_z is a negative quantity because of the definition of $\hat{z}$.

In order to evaluate eqs. 4.4 or 4.5, expressions for $\vec{K}$ and K_z are needed. K_z is given by the following equation:

$$K_z = -\sqrt{K^2 - K_{||}^2} \qquad (4.6)$$

where the formula for K is given in eq. 2.7, and $K_{||}^2$ is given by:

$$K_{||}^2 = \frac{h_{K_{||}}^2}{a^2} + \frac{k_{K_{||}}^2}{b^2} + \frac{l_{K_{||}}^2}{c^2}$$

where $h_{K_{||}}$, $k_{K_{||}}$, and $l_{K_{||}}$ are the components of the vector, $\vec{K}_{||}$, in the reciprocal lattice coordinate system, and a, b, and c are the crystal lattice parameters. The vector, $\vec{K}$, is the sum of the vectors, $\vec{K}_z$ and $\vec{K}_{||}$. $\vec{K}_z$ is the vector with length, $|K_z|$, and which is anti-parallel to the direction of the zone axis, [uvw]. Therefore, the expression for $\vec{K}$ is:

$$\vec{K} = \frac{K_z}{\sqrt{(ua)^2 + (vb)^2 + (wc)^2}}(ua^2\hat{x} + vb^2\hat{y} + wc^2\hat{z}) + h_{K_{||}}\hat{x} + k_{K_{||}}\hat{y} + l_{K_{||}}\hat{z} \qquad (4.7)$$

where $\hat{x}$, $\hat{y}$, and $\hat{z}$ are the unit vectors of the reciprocal lattice coordinate system. Note that the first term describes a vector which is anti-parallel to [uvw] because K_z is negative.

4.1.2. Non-Diagonal Elements of the A matrix

The expressions for the non-diagonal elements of the **A** matrix, in terms of the U_g's were given in sec. 2.1.4. In this section, it will be shown how to the calculate the U_g's and the Fourier coefficients, V_g. In sec. 2.1, the crystal potential was expanded as a

Fourier series:

$$V(\vec{r}) = \sum_{g} V_g \exp(2\pi i \vec{g} \cdot \vec{r})$$

$$= \frac{h^2}{2me} \sum_{g} U_g \exp(2\pi i \vec{g} \cdot \vec{r})$$

The Fourier coefficients are given by the following relation:

$$V_g = \frac{1}{V_c} \int_{V_c} V(\vec{r}) \exp(-2\pi i \vec{g} \cdot \vec{r}) \, d^3r \tag{4.8}$$

where the integral is over the unit cell of the crystal, V_c is the volume of the unit cell and $\vec{g}$ is a reciprocal lattice vector of the crystal. In evaluating the integral, it is usually assumed that the potential is made up of a superposition of all of the atomic or ionic potentials. Therefore, the potential of the unit cell is usually expressed as follows:

$$V_{uc}(\vec{r}) = \sum_{k} \phi_k (\vec{r} - \vec{r}_k) \tag{4.9}$$

where the summation over k is over all of the atoms or ions in the unit cell, and $\vec{r}_k$ and $\phi_k(\vec{r})$ are the position in the unit cell and the potential of the k^{th} atom or ion respectively. Since the potential being used is that of the unit cell, rather than the entire crystal, the limits of integration can be extended to infinity. Therefore, the Fourier coefficient can be written as follows:

$$V_g = \frac{1}{V_c} \int_{-\infty}^{\infty} \sum_{k} \phi_k (\vec{r} - \vec{r}_k) \exp(-2\pi i \vec{g} \cdot \vec{r}) \, d^3r$$

$$= \frac{1}{V_c} \sum_{k} \int_{-\infty}^{\infty} \phi_k (\vec{r} - \vec{r}_k) \exp(-2\pi i \vec{g} \cdot \vec{r}) \, d^3r$$

If the variable of integration is changed from $\vec{r}$ to $\vec{r}' = \vec{r} - \vec{r}_k$, then $d^3r = d^3r'$ and the

result is the following:

$$V_g = \frac{1}{V_c}\sum_k \int_{-\infty}^{\infty} \phi_k(\vec{r}') \exp\left[-2\pi i \vec{g} \cdot (\vec{r}' + \vec{r}_k)\right] d^3r'$$

$$= \frac{1}{V_c}\sum_k \exp(-2\pi i \vec{g} \cdot \vec{r}_k) \int_{-\infty}^{\infty} \phi_k(\vec{r}) \exp(-2\pi i \vec{g} \cdot \vec{r})\, d^3r$$

At this point another assumption is usually made to facilitate this calculation. It is assumed that each of the atomic potentials is spherically symmetric. When this is done, and the integral, which is just the Fourier transform of the atomic potential, is put into spherical coordinates, the expression for the Fourier coefficients becomes the following:

$$V_g = \frac{1}{V_c}\sum_k \exp(-2\pi i \vec{g} \cdot \vec{r}_k) \left[4\pi \int_0^{\infty} \phi_k(r) \frac{\sin(2\pi gr)}{2\pi gr} r^2 dr \right] \tag{4.10}$$

In the Born approximation, the electron scattering factors have been expressed by Doyle and Turner[35] as:

$$f_{el}(s) = \frac{8\pi^2 me}{h^2} \int_0^{\infty} r^2 \phi(r) \frac{\sin(4\pi sr)}{(4\pi sr)} dr \tag{4.11}$$

where $s = \sin\theta/\lambda = g/2$. Therefore, the Fourier coefficients can be expressed in terms of the electron scattering factor as follows:

$$V_g = \frac{h^2}{2\pi me V_c}\sum_k \exp(-2\pi i \vec{g} \cdot \vec{r}_k) f_{el_k}\left(\frac{g}{2}\right) \tag{4.12}$$

The U_g's are then given by:

$$U_g = \frac{2me V_g}{h^2} = \frac{1}{\pi V_c}\sum_k \exp(-2\pi i \vec{g} \cdot \vec{r}_k) f_{el_k}\left(\frac{g}{2}\right) \tag{4.13}$$

From this expression, it is easy to see why the **A** matrix is real and symmetric for centrosymmetric crystals. In such crystals, if the origin is the center of symmetry, for every atom located at $\vec{r}_k$, there is an identical atom at $-\vec{r}_k$. Thus, there is also an identical atom, in the same unit cell, located at $\vec{r}_{k'} = \vec{a} + \vec{b} + \vec{c} - \vec{r}_k$. Therefore, the summation in eq. 4.13

can be written as:

$$\frac{1}{2}\sum_{k}\left[\exp(-2\pi i\vec{g}\cdot\vec{r}_k)\,f_{el_k}(\frac{g}{2})+\exp(-2\pi i\vec{g}\cdot\vec{r}_{k'})\,f_{el_k}(\frac{g}{2})\right]$$

$$=\frac{1}{2}\sum_{k}\left[\exp(-2\pi i\vec{g}\cdot\vec{r}_k)\,f_{el_k}(\frac{g}{2})+\exp[-2\pi i\vec{g}\cdot(\vec{a}+\vec{b}+\vec{c})]\exp(2\pi i\vec{g}\cdot\vec{r}_k)\,f_{el_k}(\frac{g}{2})\right]$$

$$=\sum_{k}\left[\frac{\exp(2\pi i\vec{g}\cdot\vec{r}_k)+\exp(-2\pi i\vec{g}\cdot\vec{r}_k)}{2}f_{el_k}(\frac{g}{2})\right]$$

where the factor, $1/2$, is due to the fact that every atom is now being included twice in the summation. Therefore:

$$U_g=\frac{1}{\pi V_c}\sum_{k}\cos(2\pi\vec{g}\cdot\vec{r}_k)\,f_{el_k}(\frac{g}{2}) \tag{4.14}$$

Thus, the U_g's are all real for centrosymmetric crystals. In addition, the **A** matrix is symmetric because:

$$U_{-g}=\frac{1}{\pi V_c}\sum_{k}\cos(-2\pi\vec{g}\cdot\vec{r}_k)\,f_{el_k}(\frac{g}{2})$$

$$=\frac{1}{\pi V_c}\sum_{k}\cos(2\pi\vec{g}\cdot\vec{r}_k)\,f_{el_k}(\frac{g}{2})=U_g$$

4.1.3. Elastic Scattering Factors

The atomic scattering factors for electrons, $f_{el}(s)$, have been calculated using many different approximations. The most accurate available scattering factors have been tabulated by Doyle and Cowley[36] in the *International Tables for X-Ray Crystallography*, volume IV, for intervals of s of between 0.01 and 0.1 $Å^{-1}$. However, it is often desirable, especially for computing purposes, to have an analytical approximation for $f_{el}(s)$. Doyle and Turner[35] have fitted their data to an expression of the form:

$$f(s)=\sum_{i=1}^{4}a_i\exp(-b_i s^2) \tag{4.15}$$

They have listed their parameters for the fit, a_i, b_i, for a large number of atoms and ions. These parameters are based on the most accurate available data for those atoms and ions since they are included in the data which are given by Doyle and Cowley. However, for

those atoms and ions not listed by Doyle and Turner, it is possible to calculate the electron scattering factors from the x-ray scattering factors, $f_x(s)$, using the Mott formula[37]:

$$f_{el}(s) = \frac{me^2}{2h^2}\left[\frac{Z-f_x(s)}{s^2}\right] \tag{4.16}$$

where Z is the atomic number of the atom or ion. The x-ray scattering factors have also been fitted to an expression similar to eq. 4.15. The most accurate parameters for the fit to the x-ray scattering factors have been given by Cromer and Waber[38] in the *International Tables for X-Ray Crystallography*, volume IV. The parameters are not given for the ion O^{-2}. This ion is quite common in ionic crystals and is one of the constituent ions in the superconductor, $Y_1Ba_2Cu_3O_{7-\delta}$, which will be used as example in the rest of the thesis. For that ion, Sanger[39] has given parameters for the analytical approximation of $f_x(el)$. The Mott formula becomes less accurate as s approaches zero, especially in the case of ions, where the electron scattering factor tends to plus or minus infinity. Therefore, it is best to use the value of $f_{el}(0)$ given by Doyle and Cowley, rather than using the analytical approximation to the x-ray scattering factor and the Mott formula.

4.1.4. Debye Waller Factor and Relativistic Correction

In sec. 2.2.2, it was shown how the thermal vibrations of the crystal ions cause the Fourier coefficients, as calculated above, to be slightly inaccurate. These vibrations can be accounted for in an approximate way by multiplying the Fourier coefficients, and hence the U_g's, by the Debye Waller factor as follows:

$$U_g = \frac{1}{\pi V_c}\sum_k \exp(-2\pi i\vec{g}\cdot\vec{r}_k)\, f_{el_k}(\tfrac{g}{2}) \exp[-2\pi^2(\langle u_{k1}^2\rangle g_1^2 + \langle u_{k2}^2\rangle g_2^2 + \langle u_{k3}^2\rangle g_3^2)] \tag{4.17}$$

where $\langle u_{ki}^2\rangle$ is the average squared displacement, in the i-direction, of the k^{th} atom or ion from its equilibrium position. In most cases, the average displacement is not given in anisotropic form, and so eq. 4.17 reduces to:

$$U_g = \frac{1}{\pi V_c}\sum_k \exp(-2\pi i\vec{g}\cdot\vec{r}_k)\, f_{el_k}(s) \exp(-B_k s^2) \tag{4.18}$$

where $s = g/2$ and $B_k = 8\pi^2\langle u_{kg}^2\rangle$ is called the Debye parameter for the k^{th} atom or ion in the unit cell. $\langle u_{kg}^2\rangle$ is the average squared displacement of the k^{th} atom or ion in the

g-direction. In the isotropic case, $\langle u_{kg}^2 \rangle = (1/3)\langle u_k^2 \rangle$, where $\langle u_k^2 \rangle$ is the average total squared displacement of the k^{th} atom or ion, and therefore $B_k = 8\pi^2 \langle u_k^2 \rangle / 3$. The Debye parameter generally depends not only on the type of atom involved, but also the crystal structure surrounding the atom. Therefore, it is not possible to use a given Debye parameter for a certain type of atom without regard to the other atoms in the crystal. The Debye parameters used should be those which are measured experimentally for the structure being studied. In the *International Tables for X-Ray Crystallography*, vol. III, Ibers, et. al.[40] have listed the Debye parameters for many different monatomic crystals and for some other crystals with relatively simple structures. For crystals which are not listed, it is best to find a reference which gives the parameters for that particular structure. For example, the Debye parameters for the superconductor, $Y_1Ba_2Cu_3O_{7-\delta}$, are given in many different references[41-48]. These references also give precise data on the structure of the crystal which is necessary for the structure factor calculation. If no such references are available, an approximate value of the Debye parameter can be found by using the values given by Ibers, et. al. for a monatomic crystal with a similar atomic number. Since the Debye Waller factor is a measure of thermal vibration, the Debye parameter will increase with increasing temperature, so care must be taken to use the parameters for the correct temperature.

Another correction which must be made is the relativistic correction given in sec. 2.3. The resulting formula for U_g is:

$$U_g = \frac{1}{\pi V_c \sqrt{1-\beta^2}} \sum_k \exp(-2\pi i \vec{g} \cdot \vec{r}_k) f_{el_k}(s) \exp(-B_k s^2) \qquad (4.19)$$

4.1.5. Imaginary Part of Fourier Coefficients

The imaginary part of the matrix elements, U_g', which is due to inelastic scattering, will now be evaluated. As was mentioned in sec. 2.2.2, the most important part of this term is due to phonon excitation. Plasmon and single electron excitation also contribute to U_g', but their contribution is small except for very small values of g. Since the U_0' term is not important for diffraction contrast, the contributions from these two processes will be neglected except to say that Radi[14] has calculated them for many different crystals. However, Ritchie and Howie[49] have reported that Radi's values for the plasmon contribution are too high.

The phonon contribution to U_g' is very difficult to calculate accurately. It is not possible to calculate it as a sum of contributions from the different atoms in the crystal unless the Einstein model, in which all atoms vibrate independently of one another, is used. Even in this case, the calculation is difficult, since the contribution of each atom depends not only on the scattering parameter, s, as it did in the elastic scattering case, but also on the Debye Waller factor, and hence the crystal structure around the atom. The imaginary potential due to thermal diffuse scattering was given originally by Hall and Hirsch[50] for the case of a monatomic crystal. Bird and King[15] have given this potential in the form necessary for a crystal with more than one kind of atom:

$$V_g' = \frac{h^2}{2\pi m e V_c}\frac{2h}{\beta mc}\sum_k \exp(-2\pi i\vec{g}\cdot\vec{r}_k)\int f_{el_k}(s')\,f_{el_k}(|\vec{s}-\vec{s}'|)$$

$$\times\,(\exp(-B_k s^2) - \exp(-B_k s'^2)\exp[-B_k(\vec{s}-\vec{s}')^2])\,d^2\vec{s}' \qquad (4.20)$$

This equation can be converted to a form more like eq. 4.19, making it possible to calculate V_g' for any given crystal:

$$U_g' = \frac{1}{\pi V_c}\sum_k \exp(-2\pi i\vec{g}\cdot\vec{r}_k)\,f_k'(s, B_k)\exp(-B_k s^2) \qquad (4.21)$$

In Chapter 5, the different sources which are available for the inelastic scattering factors, $f_k'(s, B_k)$ will be reviewed. Also, a new method for calculating $f_k'(s, B_k)$ will be proposed. This method will be applicable to both neutral atoms and ions. This is necessary, since there is a lack of useful sources of inelastic scattering factors for ions.

4.2. Determination of Matrix and Twin Zone Axes

4.2.1. Initial Method

All of the preceding calculations depend on a knowledge of the matrix and twin crystal orientations. Therefore, it is critical to correctly interpret the experimental diffraction pattern in order to determine these orientations. One method of doing this would be to first obtain diffraction patterns from either side of the boundary in order to obtain the zone axes of both crystals. This is a relatively straightforward procedure for cubic crystals which is described in detail in other places[51,52]. This step is not so straightforward, however, in the case of non-cubic crystals. The procedure is particularly difficult in crystals which lack a certain symmetry element, but which almost have this symmetry element. In other words, these crystals have an element of pseudo-symmetry. Unfortunately, these are the very crystals which are most likely to exhibit twinning by pseudo-merohedry or pseudo-reticular merohedry.

In order to aid in the process of interpreting diffraction patterns obtained from non-cubic crystals, a computer program has been written by the author which calculates certain parameters which are characteristic of the geometry of any given reciprocal lattice plane. The parameters calculated are the lengths of the two shortest, non-colinear reciprocal lattice vectors in the plane, the ratio of these lengths, the angle between these vectors, and the area of the parallelogram which has these two vectors as its sides. The different reciprocal lattice planes can be listed in ascending order of area or of any other parameter. If the camera length of the electron microscope is known, the area of the smallest parallelogram which has reflections at its corners can be calculated and the list of possible zone axes can be easily shortened to a very small number. If the camera length is not accurately known, one must rely solely on the ratios of reciprocal lattice vector lengths and the angles between the vectors, since these do not depend on the camera length.

In either case, this method will soon lead to a short list of possible zone axes for both crystals. For cubic crystals, this procedure would generally lead to a determination which is unique for the purposes of this thesis, but for crystals with an element of pseudo-

symmetry, there will usually be more than one reciprocal lattice plane which has parameters very nearly matching those of the diffraction pattern. In order to determine the zone axis, therefore, a more in depth analysis of the diffraction patterns must be done.

4.2.2. Crystals With an Element of Pseudo-Symmetry

The previous procedure for narrowing down the possible matrix and twin zone axis possibilities is most easily done with separate diffraction patterns for the matrix and the twin, although it is possible with a single diffraction pattern of the twin boundary region. However, in order to reduce the number of possible zone axes to one, reference must be made to a diffraction pattern of the twin boundary. This is because only such a diffraction pattern can show how the diffraction spots which originate in the two different crystals are positioned with respect to each other. In crystals with an element of pseudo-symmetry, there will generally be spots which are so close to each other that they resemble a single spot which is either elongated in one direction, or which has been split into more than one spot. A knowledge of which spots appear to be split or streaked, along with the direction of this splitting or streaking, can give information about the orientations of the two crystals.

Diffraction Patterns

As was discussed before, a diffraction pattern of the twin boundary region is actually made up of matrix, twin, and combination reflections, which are matrix reflections which have been diffracted again by the twin. An example of this is shown in Fig. 3.10. However, for crystals with an element of pseudo-symmetry, the combination reflections tend to be clumped together in small groups, as shown in Fig. 3.16. These small groups will generally lie along a straight line and, hence, can give the impression of streaked diffraction spots. In the case of pseudo-merohedral twins, each small group of reflections will contain a matrix reflection and a twin reflection (i.e. a twin reflection which is derived from the transmitted beam, not one of the matrix reflections). Since the matrix and twin reflections will usually be more intense than the combination reflections around them, and since the direction of splitting of the matrix and twin reflections is the same as the direction of streaking which would be caused by the combination reflections, the combination reflections will be ignored in simulations of twin boundary diffraction patterns in the future. It is important to

note, however, that this cannot be done in the case of pseudo-reticular merohedral twins (or reticular merohedral twins), since in this case, there are many small groups of combination reflections which do not include either a matrix or a twin reflection (refer to Fig. 3.9).

A computer program which can generate theoretical twin boundary diffraction patterns, either including or ignoring combination reflections, has been written by the author. The detailed principles used in the program in order to generate these diffraction patterns are given in Appendix B. Using this program, all that has to be determined is the matrix zone axis. Once this is done, and a certain twin boundary is assumed, the twin direction which is parallel to the matrix zone axis is calculated by the program. In many cases, this twin direction will not be rational, and a rational, low index, twin direction must be found which is close to being parallel to the irrational one, and, therefore, to the matrix zone axis. If such a low index twin direction can be found, it represents the twin zone axis, which is close to, but not exactly, parallel to the matrix zone axis. In pseudo-reticular merohedral twins (and reticular merohedral twins), however, there will be many cases where a low index twin zone axis cannot be found by this method. In these cases, the twin zone axis has to be found separately, using a diffraction pattern from the twin crystal alone. It must then be checked to make sure that it is close to being parallel to the irrational twin direction which is parallel to the matrix zone axis.

In pseudo-merohedral and pseudo-reticular merohedral twins, the only cases where the matrix and twin zone axes are parallel are when they are both parallel to the twin plane. In such cases, the beam direction is nearly parallel to the twin plane and, hence, the twin plane appears in the microscope only as a thin line. The theory presented in Chapter 3 is not applicable in such cases. In all other cases, the two zone axes, and, hence, the two reciprocal lattice planes which are normal to these zone axes, are not parallel. One effect of this is that the Ewald sphere does not intersect the two reciprocal lattice planes in the same place. Therefore, the fact that a certain matrix reflection is close to its Bragg condition does not mean that a twin reflection which appears to be close to the matrix reflection in the diffraction pattern will be close to its Bragg condition. These effects will be investigated further in sec. 4.3. The degree to which the two zero order Laue zones are not parallel depends directly on the obliquity of the twin.

Once a set of matrix and twin zone axes have been obtained, the simulated diffraction pattern for these orientations must be compared with the experimental twin boundary diffraction pattern. Very often, the two diffraction patterns will not match. For example, the split or streaked reflections in the experimental pattern may not be split in the simulated pattern, or the direction of the splitting or streaking may be different. In this case, the matrix zone axis which was initially assumed must be incorrect. It may be, however, that a different matrix zone axis which is a member of the same family of directions (i.e. which has the sign of one or more of its indices reversed) will lead to a simulated diffraction pattern which matches the experimental pattern. In general, most of the possible matrix zone axes which were not eliminated by the method described in sec. 4.2.1 will be eliminated in this way.

Example of Determination of Zone Axes

The simplest way to describe the procedure for determining the matrix and twin zone axes, and to illustrate some of the problems which may arise, is to use an example. The example which will be used is that of the (110) twins in the high temperature superconductor, $Y_1Ba_2Cu_3O_{7-\delta}$. As was mentioned previously, these twins are pseudo-merohedral twins. Therefore, for any matrix zone axis which is not parallel to the twin plane, the matrix and twin reciprocal lattice planes will be almost, but not quite, parallel. For this example, it will be assumed that the actual matrix zone axis is [131]. The twin direction which is parallel to the [131] matrix direction is [3.068 0.932 -1] (in twin coordinates). Obviously, then, the $(31\bar{1})$ twin reciprocal lattice plane will be very close to the (131) matrix reciprocal lattice plane, and the reflections of both planes will be visible in the diffraction pattern. Therefore, the twin zone axis is $[31\bar{1}]$. Figure 4.2 shows the (131) matrix reciprocal lattice plane along with the projection of the $(31\bar{1})$ twin reciprocal lattice plane on the matrix plane in the correct orientation. This is very similar to the diffraction pattern that one would see in the electron microscope for this crystal orientation.

Suppose that the zone axes for a pair of twinned crystals which are oriented as described above must now be determined. The first step is to measure the lengths of the two shortest reciprocal lattice vectors and the angle between them in a diffraction pattern from one side of the twin boundary (or even a diffraction pattern from the twin boundary itself,

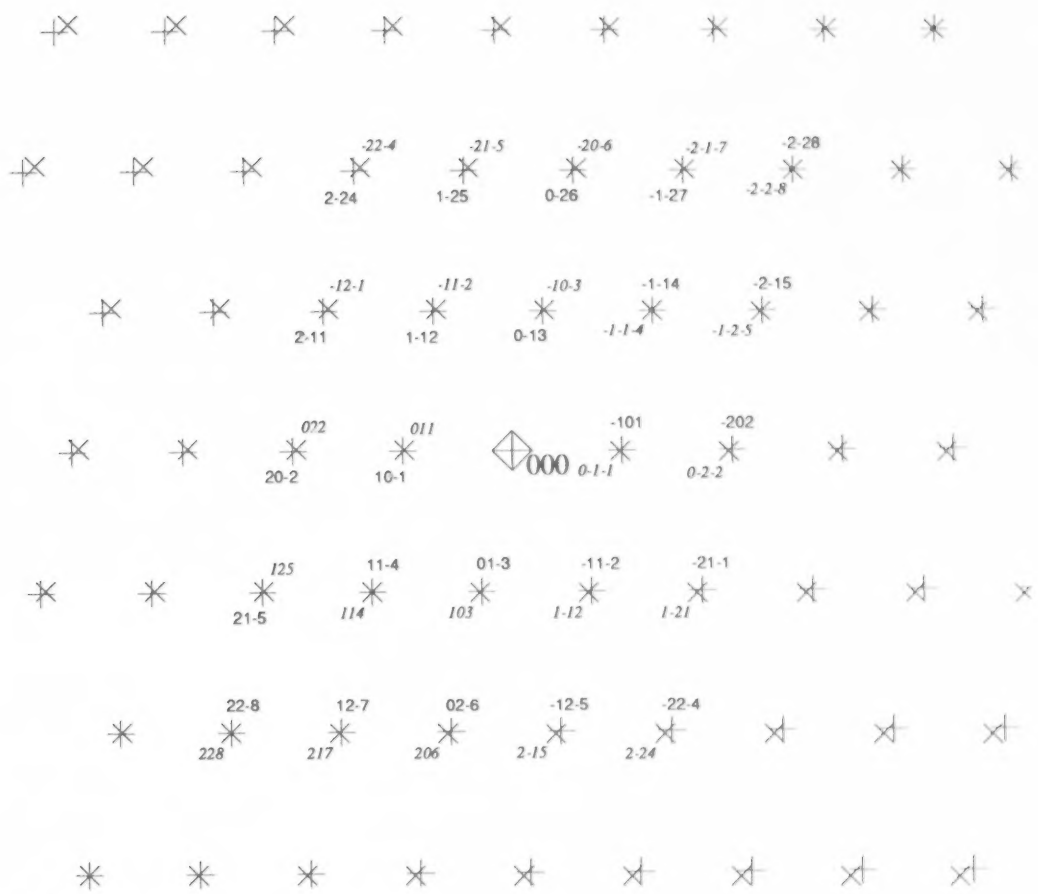

hkl matrix reflection

hkl twin reflection

Fig. 4.2. Simulated diffraction pattern from a (110) twin boundary of $Y_1Ba_2Cu_3O_{7-\delta}$. The matrix zone axis is [131] and the twin zone axis is $[31\bar{1}]$. The Miller indices of some of the reflections are indicated in their own coordinate systems.

since it can be seen from Fig. 4.2 that the measurements would not change significantly). By comparing these parameters with those calculated by the computer program described in sec. 4.2.1, the number of possible families of zone axes could quickly be reduced to two. Table 4.1 shows the calculated parameters for the two possible candidates for matrix zone axis family, for a camera length of 160 cm. The similarity of these two zone axes is a conse-

Zone Axis Family	Length of Shortest Reciprocal Lattice Vector	Length of 2nd Shortest Reciprocal Lattice Vector	Ratio of Lengths	Angle Between Two Shortest Reciprocal Lattice Vectors	Area of Smallest Possible Parallelogram
⟨131⟩	1.6304 cm	2.0548 cm	0.7567	77.309 deg	3.4276 cm^2
⟨311⟩	1.6078 cm	2.1717 cm	0.7403	77.229 deg	3.4052 cm^2

Table 4.1. Geometrical diffraction pattern parameters for two zone axis families.

quence of the fact that the *a* and *b* lattice parameters for $Y_1Ba_2Cu_3O_{7-\delta}$ are nearly equal. Because of this similarity, it is impossible to choose between the two possibilities. This is also apparent from the diffraction pattern shown in Fig. 4.2 which displays two patterns (matrix and twin) which have the two sets of parameters listed in Table 4.1.

In fact, for pseudo-merohedral twins, the situation will generally be like this. There will be two families of zone axes which have parameters nearly matching those of the experimental diffraction pattern taken from either side of the twin boundary. One of these families will correspond to the matrix crystal and one will correspond to the twin crystal. Therefore, there are three more steps which must be carried out in order to accurately determine the orientations of the two crystals. In one of these steps, it must be determined which crystal corresponds with which zone axis family. Another step involves selecting the correct member of each zone axis family for the orientation of each crystal. The final step is the determination of which crystal is the matrix crystal in the sense referred to in Fig. 3.7 (i.e. which crystal is the one which the electrons enter first). This is the most difficult step in the process, and a method for correctly identifying the matrix crystal will be presented in the next section.

It will usually be easiest to do the second step, involving the determination of the

correct member of each zone axis family, before the first step. Thus, for this step, it is not important to know which crystal belongs to the ⟨131⟩ family, and which belongs to the ⟨311⟩ family of zone axes. Any zone axis from either of these families can be chosen as the matrix zone axis. The computer program described above will then determine the twin zone axis and will generate a simulated diffraction pattern corresponding to these two orientations. The simulated diffraction pattern is then compared with an experimental pattern of the twin boundary region in order to verify that the two patterns match. For example, if it is assumed that the matrix zone axis is $[31\bar{1}]$, the twin zone axis would have to be [131] and the diffraction pattern would look exactly the same as Fig. 4.2. Similarly, a matrix zone axis of $[\bar{1}\bar{3}1]$ would have a twin zone axis of $[\bar{3}\bar{1}\bar{1}]$ and the diffraction pattern would look identical and would result in identical twin boundary images using the theory of Chapter 3.

There are, however, some members of the two zone axis families which would not lead to correct results. For example, Figure 4.3 shows a simulated diffraction pattern for a matrix zone axis of $[1\bar{3}1]$ and a twin zone axis of $[\bar{3}1\bar{1}]$ It can be seen that in Fig. 4.2, the $(11\bar{4})$ matrix reflection is coincident with the (114) twin reflection. Also, all of the other matrix and twin pairs in the same row are common, but those on other rows are not common and appear to be split. However, in Fig. 4.3, the row of common points consists of reflections of the type {112}, rather than {114}, as in Fig. 4.2. Since these reflections have different Fourier coefficients, this is an important difference. In an experimental diffraction pattern, it would be apparent that one row of reflections consisted of unsplit points, and by comparison of the experimental pattern with Figs. 4.2 and 4.3, one could see that the unsplit row of reflections were of the type {114}, as in Fig. 4.2. Thus, it would be clear that the matrix zone axis could be [131], but could not be $[1\bar{3}1]$.

There is one more detail to be considered in conjunction with this step. A decision must also be made as to whether the twin boundary is actually the (110) plane, or the $(1\bar{1}0)$ plane, since both planes can be twinning planes in these crystals. However, this is not, in fact, a problem. If the $(1\bar{1}0)$ plane were chosen as the twin plane, it would still be possible to find an orientation for which the simulated diffraction pattern would match the observed diffraction pattern. But in this case, the matrix zone axis could be $[1\bar{3}1]$ or

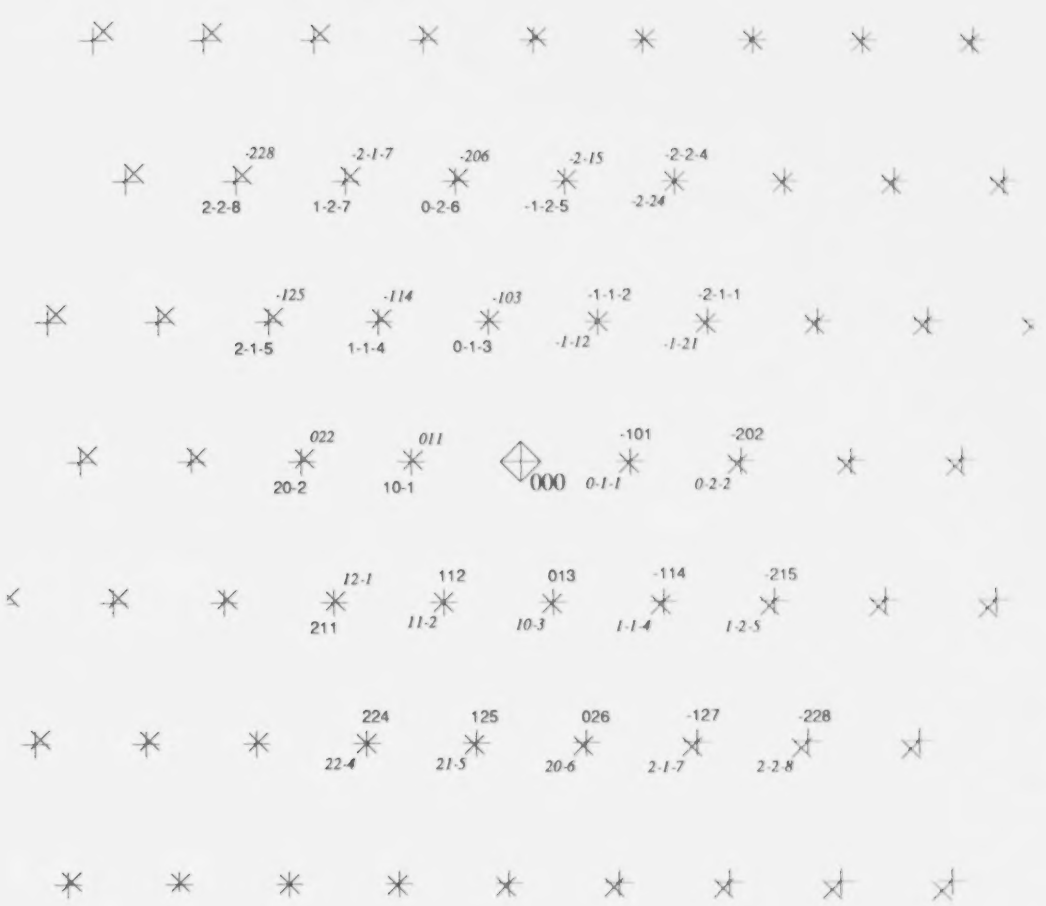

hkl matrix reflection

hkl twin reflection

Fig. 4.3. Simulated diffraction pattern from a (110) twin boundary of $Y_1Ba_2Cu_3O_{7-\delta}$. The matrix zone axis is $[1\bar{3}1]$ and the twin zone axis is $[\bar{3}1\bar{1}]$. The Miller indices are indicated for some of the reflections in their own coordinate systems.

$[1\bar{3}\bar{1}]$, or alternately $[3\bar{1}1]$ or $[\bar{3}11]$, but not [131] as before. Thus, the twin plane can be chosen arbitrarily, but then a matrix zone axis must be selected which results in a diffraction pattern which agrees with the experimental pattern.

Thus, so far, it has been found that one crystal has the [131] zone axis and the other has the $[31\bar{1}]$ zone axis. The next step is to determine which crystal (on which side of the boundary) has the [131] zone axis, and which has the $[31\bar{1}]$ zone axis. This is done by taking diffraction patterns from both crystals, on either side of the boundary, and comparing them with each other, and with the simulated pattern shown in Fig. 4.2. For sets of points in the diffraction pattern of the twin boundary region where the splitting is noticeable, it could be determined from which side of the boundary each member of the pair originates. This would be done by comparing the positions and intensities of each member of the pair with those of the corresponding points on the diffraction patterns which have been taken from either side of the boundary. In this way, it could be determined which crystal (on which side of the twin boundary in the experimental image of the boundary) has the [131] zone axis, and which crystal has a zone axis of $[31\bar{1}]$.

4.2.3. Distinguishing Between the Matrix and Twin Crystals

In order to compare an experimental image with a theoretical image obtained by the methods presented in this thesis, it must be determined which crystal is the upper one, which the electrons enter first, and which is the lower one. These two crystals are referred to as the matrix and the twin in Fig. 3.7. Corbett and Sheinin[29] have given a method for this determination, but it depends on the ability to differentiate between the different combination reflections, which result from a matrix reflection being further diffracted by the twin, and also distinguish these reflections from the matrix and twin reflections. In the case of pseudo-merohedral twins, that is not possible since the matrix, twin and combination reflections are so close together. This is illustrated in Figure 4.4, which is the same as Fig. 4.2, except that combination reflections are included. Since it is very difficult to distinguish a twin boundary diffraction pattern in which the top crystal zone axis is [131] from one in which the top crystal has a $[31\bar{1}]$ zone axis, this information can only be obtained by looking at an actual image of the twin boundary.

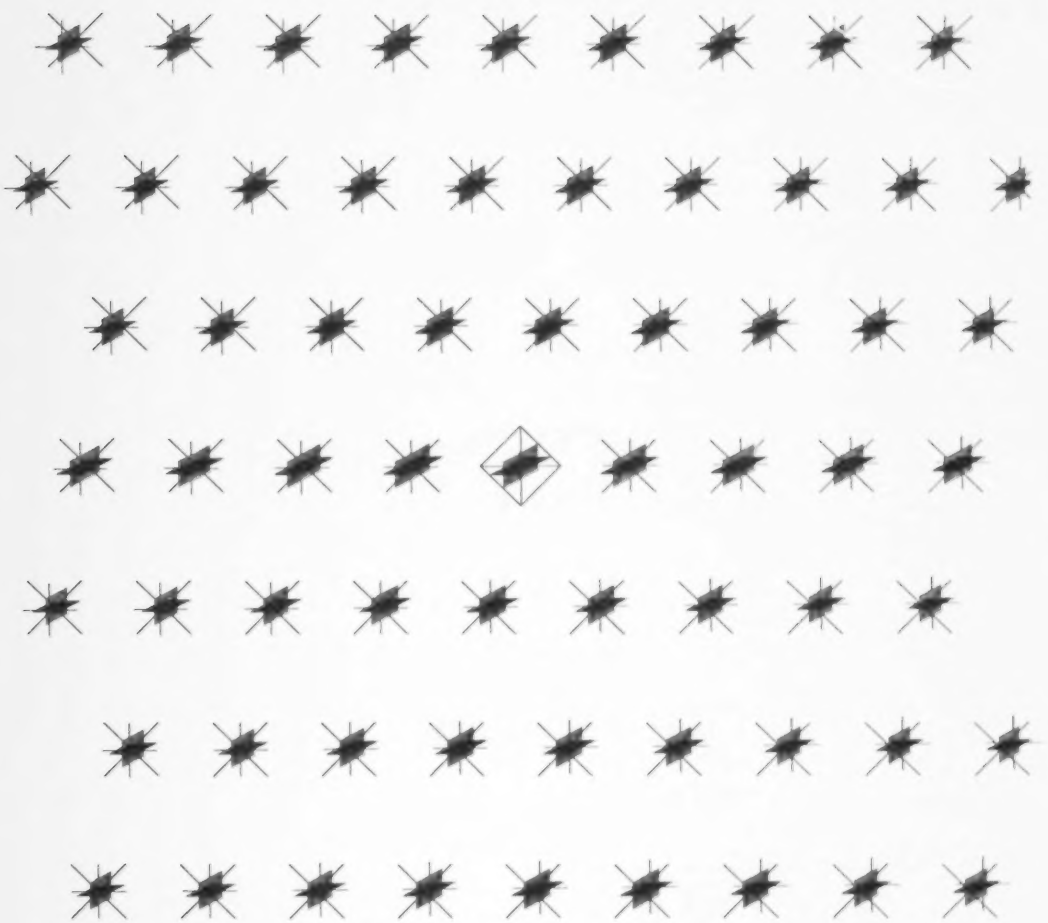

matrix reflection
twin reflection
combination reflection

Fig. 4.4. Simulated diffraction pattern from a (110) twin boundary of $Y_1Ba_2Cu_3O_{7-\delta}$, including combination reflections. The matrix zone axis is [131] and the twin zone axis is $[31\bar{1}]$.

The method which will be demonstrated for obtaining this information depends on the fact that a reflection in the matrix crystal can be further diffracted in the twin, whereas if the same reflection occurred in the twin, it would be essentially unaffected by the presence of the matrix. In order to isolate the effects of one such reflection, an orientation must be found for which only one member of a matrix/twin pair of reflections is strongly excited, and all other reflections in the diffraction pattern are relatively weakly excited. An example of such an orientation is shown in Figure 4.5. The matrix zone axis is [131], and the twin zone axis is $[31\bar{1}]$. The intersection of the Ewald sphere with the matrix reciprocal lattice plane is indicated by the solid line, while the dashed line shows the intersection with the twin reciprocal lattice plane. It can be seen that the $(01\bar{3})$ matrix reciprocal lattice vector is in the Bragg condition. The twin reflection which is closest to its Bragg condition is (103), but it is not nearly as strongly excited as the $(01\bar{3})$ matrix reflection. It is, however, just as possible that the matrix zone axis is $[31\bar{1}]$, and the twin zone axis is [131]. In this case, the most strongly excited reflection, $(01\bar{3})$, would be a twin reflection.

Figure 4.6 shows a pair of simulated bright field twin boundary images for these two possibilities. In both images, the crystal with the [131] zone axis is assumed to be to the right of the twin boundary, and the crystal with the $[31\bar{1}]$ zone axis is to the left. In the image on the left, the right hand crystal with the [131] zone axis is assumed to be the matrix. Therefore, the strongly excited reflection, $(01\bar{3})$, is a matrix reflection. In the image on the right, the left hand crystal is assumed to be the matrix, and $(01\bar{3})$ is a twin reflection. The first thing to notice is that the thickness fringes on one side of the boundary are faint and narrow, while on the other side, the thickness fringes are wide and intense. This confirms, and is a consequence of, the fact that only one member of the $(01\bar{3})/(103)$ pair of reflections is strongly excited, and all other reflections in the diffraction pattern are relatively weakly excited. This is the desired set of diffraction conditions. The next thing which will be noticed is that the two situations for the two images lead to very similar bright field images. This is not, however, the case in dark field images.

Figure 4.7 shows the simulated dark field images for the same sets of diffraction conditions. The objective aperture is assumed to be centered around the $(01\bar{3})$ and (103) pair of reflections. The difference between the two images is very noticeable. In particular,

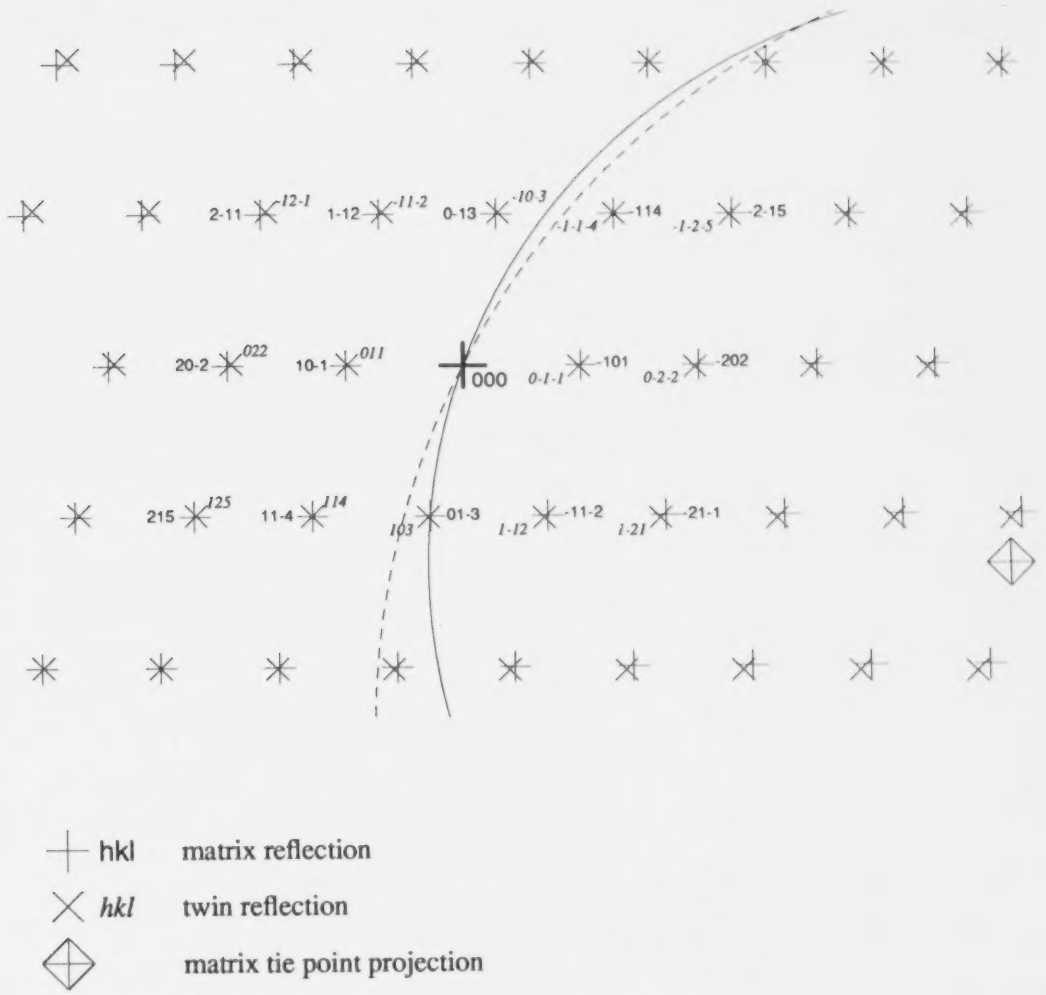

Fig. 4.5. Simulated diffraction pattern from a (110) twin boundary of $Y_1Ba_2Cu_3O_{7-\delta}$. The matrix zone axis is [131] and the twin zone axis is $[31\bar{1}]$. The Miller indices are indicated for some of the reflections in their own coordinate systems. The intersection of the Ewald sphere with the matrix zero order Laue zone is indicated by the solid line while the intersection with the twin zero order Laue zone is shown as a dashed line. The matrix tie point projection is (-5.0, 1.33, 1.0).

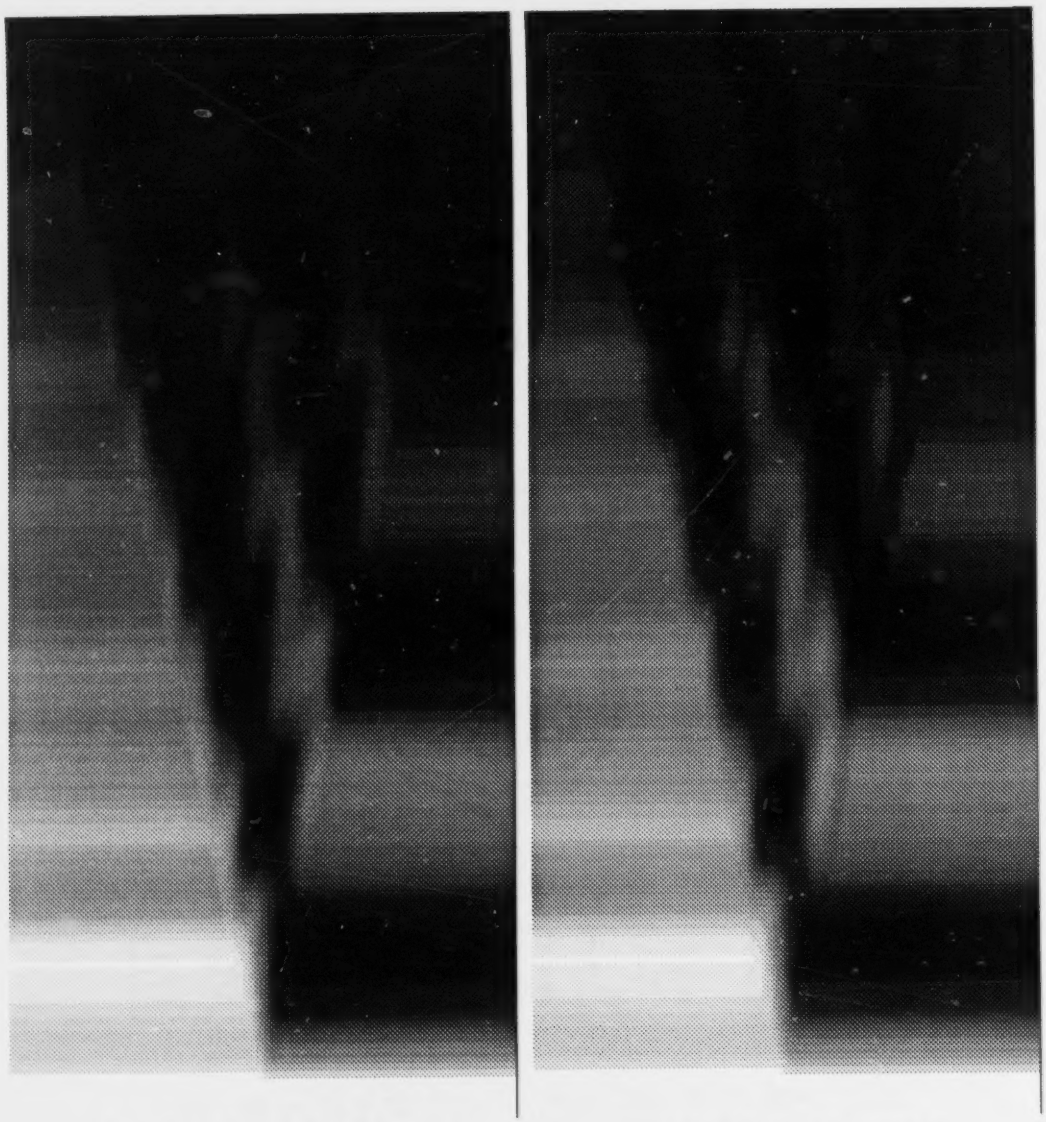

Simulated Image for Matrix
Crystal to the right of the boundary

Simulated Image for Matrix
Crystal to the left of the boundary

Fig. 4.6. Simulated bright field images of a (110) twin boundary in $Y_1Ba_2Cu_3O_{7-\delta}$. The crystal to the right of the boundary has a zone axis of [131], and a tie point projection of (-5.0, 1.33, 1.0). The crystal to the left has a zone axis of $[3\bar{1}1]$ and a tie point projection of (2.38, -6.87, 0.29).

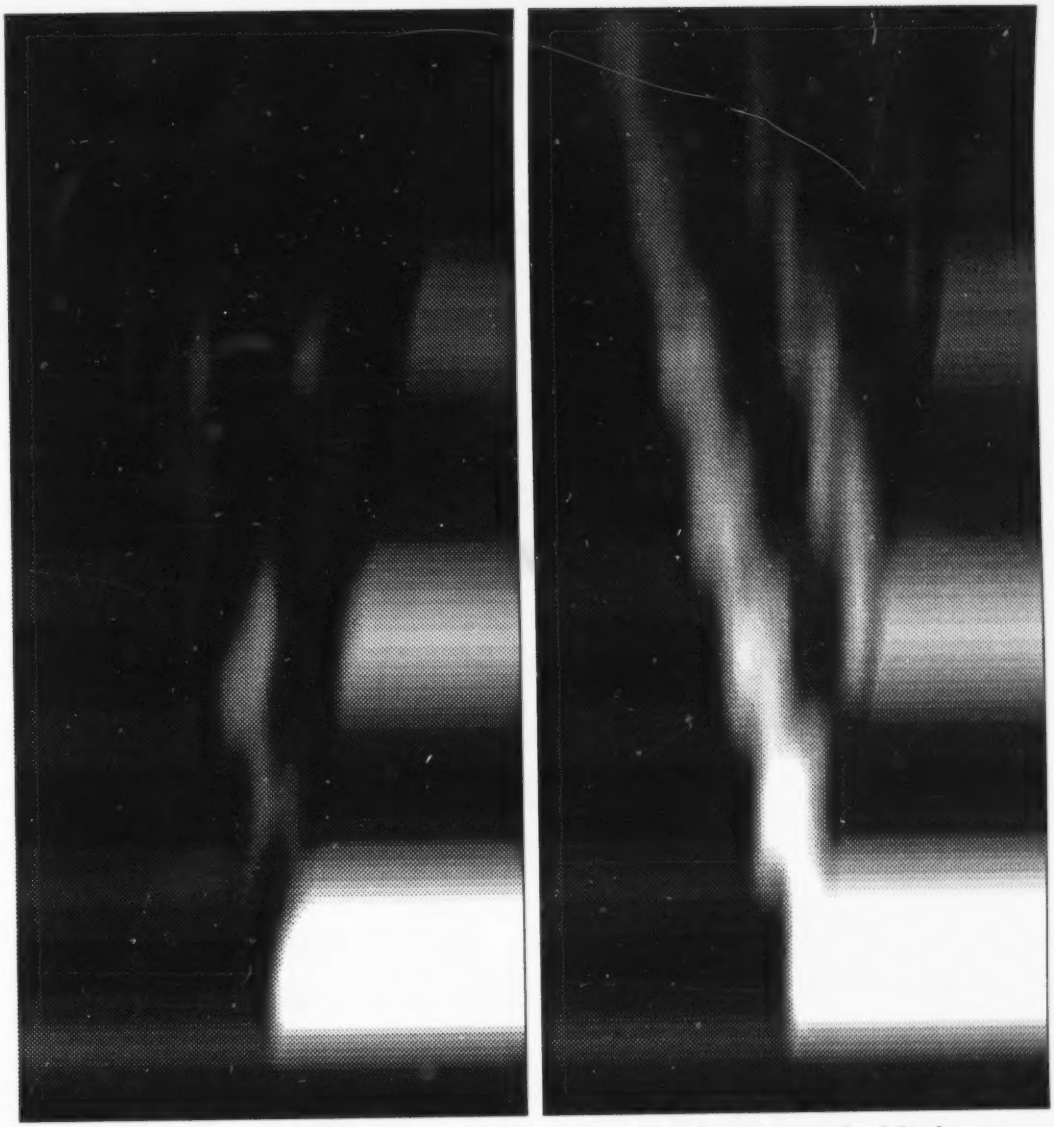

Simulated Image for Matrix
Crystal to the right of the boundary

Simulated Image for Matrix
Crystal to the left of the boundary

Fig. 4.7. Simulated dark field images of a (110) twin boundary in $Y_1Ba_2Cu_3O_{7-\delta}$. The crystal to the right of the boundary has a zone axis of [131], and a tie point projection of (-5.0, 1.33, 1.0). The crystal to the left has a zone axis of $[31\bar{1}]$ and a tie point projection of (2.38, -6.87, 0.29).

the image on the left, in which the strongly excited reflection, $(01\bar{3})$, is a matrix reflection, shows a complicated set of fringes in the twin boundary and is generally less intense in the twin boundary than the image on the right. In the image on the right, the twin boundary contrast is dominated by a set of contours of equal twin thickness, t_t, since the twin crystal is to the right of the boundary. Thus, in this image, the matrix crystal which is to the left of the boundary appears to have had little effect on the contrast of the twin boundary. This is to be expected since there are no strongly excited reflections in the matrix crystal. The difference in the image on the left is that there are two strong beams in the matrix crystal, the transmitted beam and the $(01\bar{3})$ diffracted beam. The diffracted beam can be further diffracted in the twin by the reflection, $(\bar{1}0\bar{3})$, since the resulting reflection will be very close to the origin of the diffraction pattern, and, hence, close to its Bragg condition.

Simulated images have been examined for different rigid body translation vectors, $\vec{T}$, and for several different orientations for which only one member of the matrix/twin pair of reflections is strongly excited. In all cases, the twin boundary contrast had the same general characteristics as in the example shown above. Thus, if the crystal which has the strongly excited reflection is the matrix crystal, the twin boundary will generally show a complicated set of fringes. If, however, the twin crystal has the strongly excited reflection, the twin boundary's most noticeable feature is a set of fringes of equal twin thickness which are parallel to the intersection of the twin boundary and the exit surface.

4.3. Determination of Tie Point Projection

4.3.1. Intersection of Ewald Sphere With Laue Zones

Once the zone axis has been determined, all that remains to be done in order to completely specify the crystal orientation is to find the tie point projection. This is usually accomplished in one of several ways. One method involves the use of Kikuchi lines which are often visible on the diffraction pattern and which move as the crystal is rotated. The details of the use of these lines in the determination of the crystal orientation has been given elsewhere[51,53,54], and will not be repeated here. Another method depends on the intersection of the Ewald sphere with the reciprocal lattice. Reflections which fall close to this intersection have small deviation parameters, s, and are, therefore, close to the Bragg condition. These reflections can often be identified since they will appear more intense than other reflections in the same area of the diffraction pattern. If there are two or more non-colinear reflections in the pattern which are very close to their Bragg conditions, they will define a circle, the center of which is close to the tie point projection.

This approach is complicated in the case of twin boundary diffraction patterns, because the twin zone axis will often not be parallel to the matrix zone axis. Thus, the two zero order Laue zones will not be parallel and hence, the Ewald sphere will not intersect them in the same place. Although the difference in the orientation of the two reciprocal lattices will generally be very small, this difference has a large effect on where the Ewald sphere intersects them, as is illustrated in Figure 4.8, which shows a view of the two reciprocal lattice planes and the Ewald sphere. Therefore, if there are two reflections in a diffraction pattern of a twin boundary which are close to or in their Bragg conditions, they may be on or near the intersections of the Ewald sphere with two different reciprocal lattice planes. If it was assumed that they define the tie point projection, a serious error in the determination of the orientation might result. Therefore, the best method is to determine the tie point projection for the two crystals separately. When this is done, it must be verified that these two orientations, as defined by their tie point projections, are compatible. Therefore, it is necessary to have an expression for the tie point projection on the twin zero order Laue zone for a given matrix tie point projection.

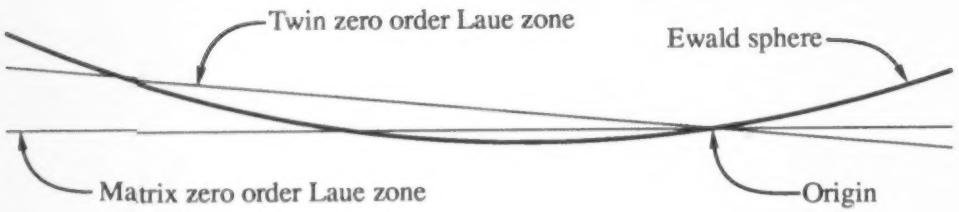

Fig. 4.8. Illustration of the different points of intersection of the Ewald sphere with the matrix and twin zero order Laue zones. The difference in orientation of the two reciprocal lattice planes has been exaggerated, as has the curvature of the Ewald sphere.

It has been mentioned before, in the case of the matrix, that the coordinates of tie point projection are the negatives of the coordinates of the tip of $\vec{K}_{||}$. This is also the case for the twin tie point projection. Its coordinates are the negatives of the component of $\vec{K}$ which is parallel to the twin zero order Laue zone, $\vec{K}_{T||}$. $\vec{K}_{T||}$ is given by the following expression:

$$\vec{K}_{T||} = \vec{K} - \vec{K}_{T\perp} \tag{4.22}$$

where $\vec{K}_{T\perp}$ is the component of $\vec{K}$ which is perpendicular to the twin zero order Laue zone. If $[u_T v_T w_T]$ is the direction, in matrix coordinates, of the normal to the twin zero order Laue zone, then $\vec{K}_{T\perp}$ can be expressed as follows:

$$\vec{K}_{T\perp} = \frac{(\vec{K} \cdot [u_T, v_T, w_T])\ (u_T a^2 \hat{x} + v_T b^2 \hat{y} + w_T c^2 \hat{z})}{\sqrt{(u_T^2 + v_T^2 + w_T^2)\ (u_T a^2 + v_T b^2 + w_T c^2)}} \tag{4.23}$$

where $\hat{x}$, $\hat{y}$, and $\hat{z}$ are the unit vectors of the matrix reciprocal lattice coordinate system, and the expression for $\vec{K}$ is given in eq. 4.7. The twin zone axis can be found using the methods described in Appendix B. Once this is done, the components of this direction in matrix coordinates, u_T, v_T, and w_T, can also be found using the methods found in Appendix B. Therefore, eq. 4.22, along with eqs. 4.7 and 4.23, gives the component of $\vec{K}$

which is parallel to the twin zero order Laue zone.

Thus, the intersection of the Ewald sphere and the twin zero order Laue zone is a circle centered at the coordinates of the tip of the vector, $-\vec{K}_{\|}$, which has a radius, r_0, corresponding to the length of $\vec{K}_{\|}$, and which can be given as:

$$r_0 = \sqrt{K^2 - K_{T\perp}^2}$$

The intersection of the Ewald sphere with other Laue zones can also easily be found. It is also a circle centered at the appropriate tie point projection, but with a different radius. By referring to Figure 4.9, it can be seen that the appropriate equation for the radius of the circle for the N-th order Laue zone, r_N, is the following:

$$r_N = \sqrt{K^2 - (K_{T\perp} - h_N)^2} \tag{4.24}$$

where h_N is the distance between the N-th order Laue zone and the zero order Laue zone and is given by:

$$h_N = \frac{N}{\sqrt{u^2a^2 + v^2b^2 + w^2c^2}} \tag{4.25}$$

where [uvw] is the matrix or twin zone axis in its own coordinate system.

An example will now be considered in order to illustrate the differences which can be present in the intersections of the Ewald sphere and the matrix and twin Laue zones. Figure 4.10 shows the intersections of the Ewald sphere with the matrix and twin zero order Laue zones for a crystal which has a matrix tie point projection of (1.0 0.333 -2.0). The twin tie point projection, as calculated by eq. 4.22, is (-0.75 1.47 -3.52). It can be seen that there is a substantial difference in the intersections of the Ewald sphere and the two zero order Laue zones. The next example illustrates the way in which the Ewald sphere can intersect a higher order Laue zone. Figure 4.11 shows the situation for a crystal which has a matrix tie point projection of (-6.0 1.13 2.62). The twin tie point projection is (-7.72 2.35 1.36). In this example, the intersections of the Ewald sphere and the 1st order Laue zones are shown as well as those of the zero order Laue zones. The reflections of the 1st order Laue zones of the two crystals are also shown. It can be seen from this figure that some higher order Laue zone reflections are close to their Bragg conditions and may be

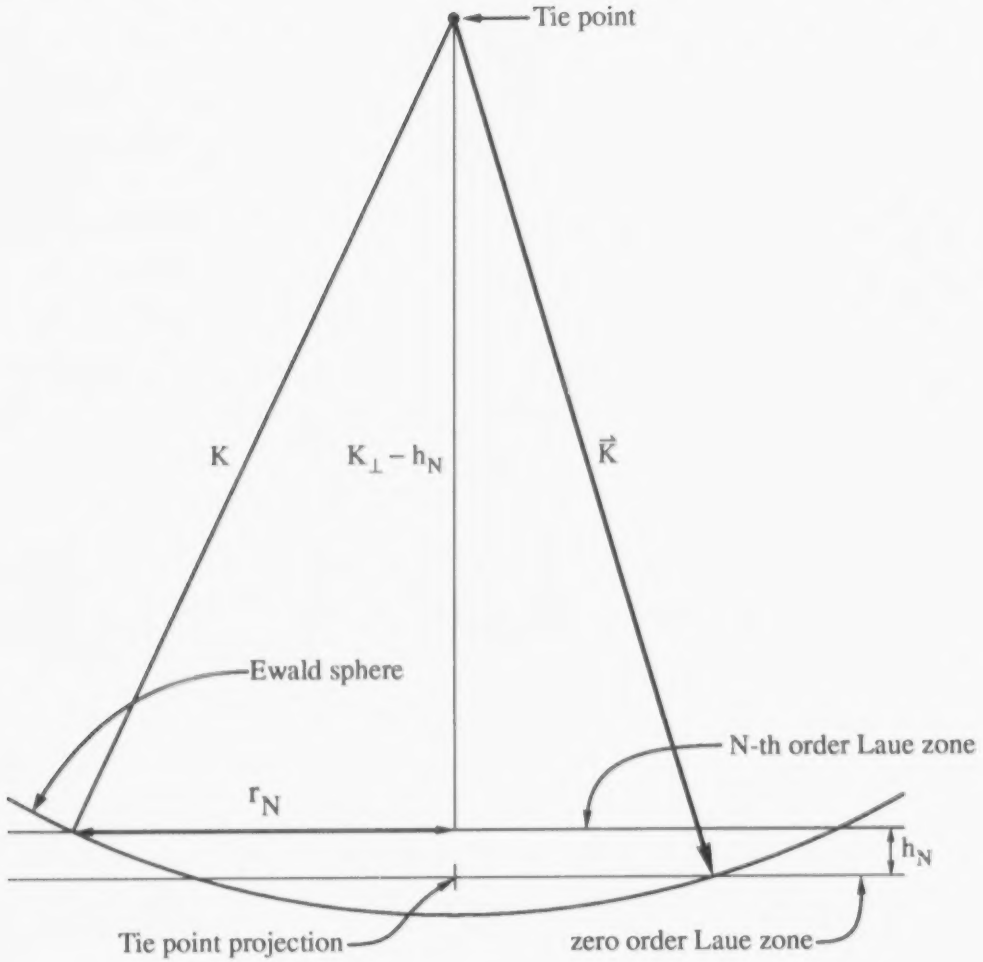

Fig. 4.9. Illustration of the calculation of the radius of the intersection of the Ewald sphere with the N-th order Laue zone.

important to the image contrast for orientations which have large tie point projections. This is particularly true for more complex structures, since a larger unit cell in the crystal with correspondingly smaller reciprocal lattice vectors can result in reciprocal lattice planes which are relatively close together. The closer together that the different Laue zones are, the more likely that higher order (or lower order) Laue zone reflections will become impor-

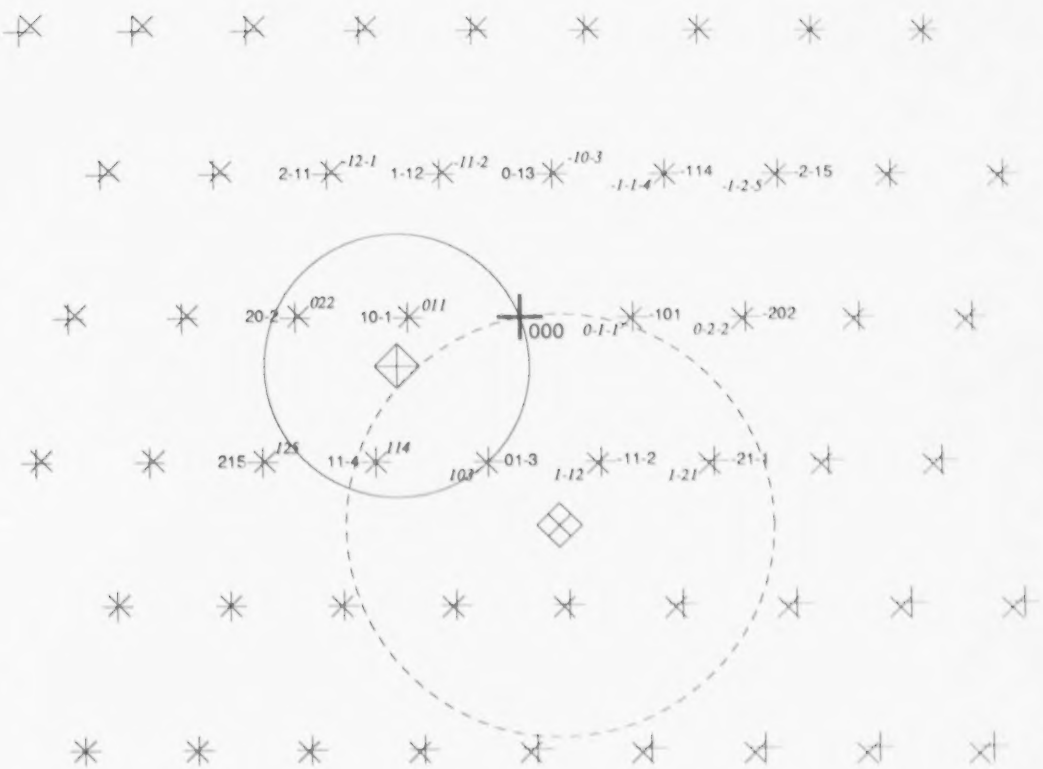

hkl matrix reflection

hkl twin reflection

matrix tie point projection

twin tie point projection

Fig. 4.10. Simulated diffraction pattern from a (110) twin boundary of $Y_1Ba_2Cu_3O_{7-\delta}$. The matrix zone axis is [131] and the twin zone axis is $[31\bar{1}]$. The Miller indices are indicated for some of the reflections in their own coordinate systems. The intersection of the Ewald sphere with the matrix zero order Laue zone is indicated by the solid line while the intersection with the twin zero order Laue zone is shown as a dashed line. The matrix tie point projection is (1.0 0.333 -2.0) and the twin tie point projection is (-0.75 1.47 -3.52).

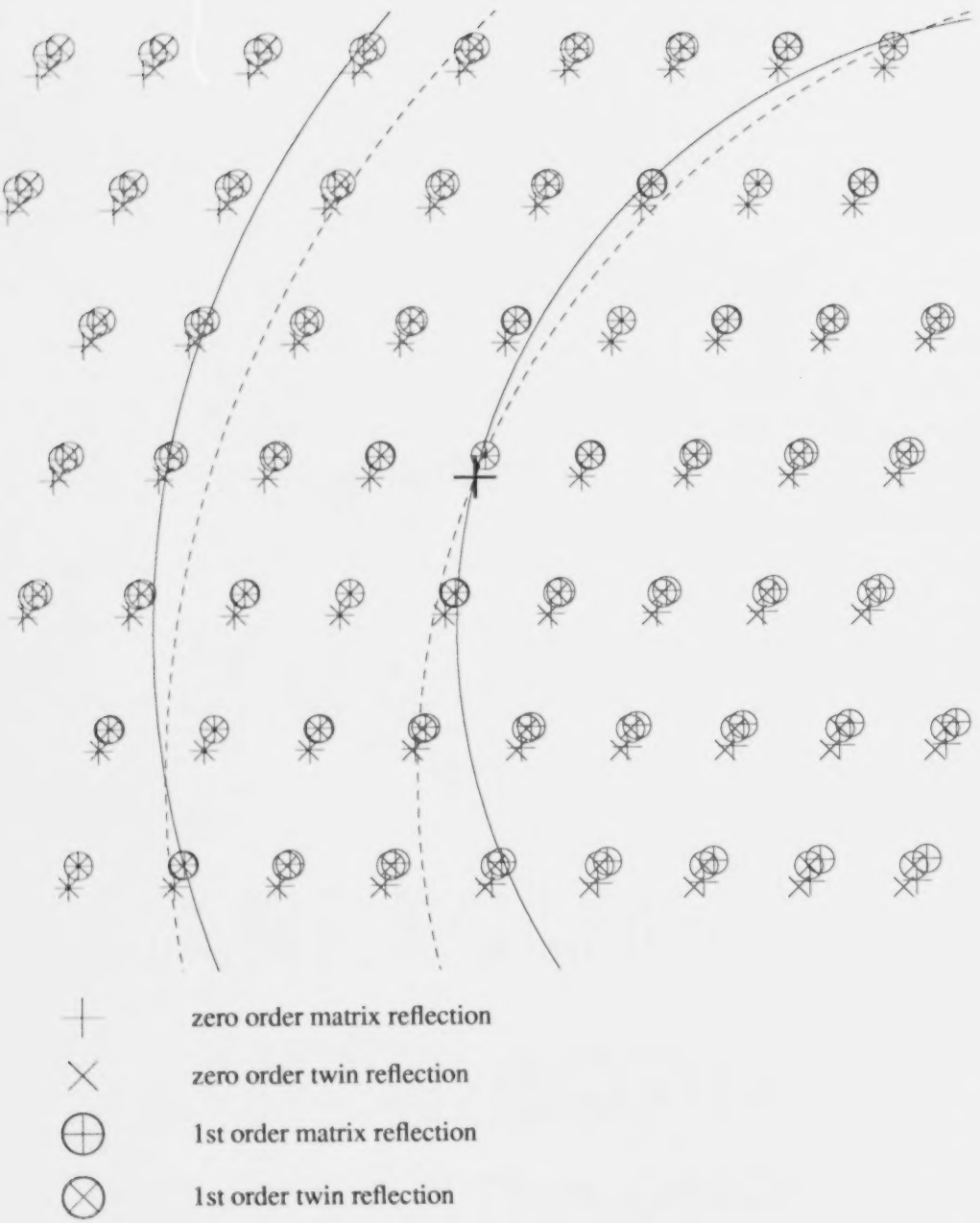

Fig. 4.11. Simulated diffraction pattern from a (110) twin boundary of $Y_1Ba_2Cu_3O_{7-\delta}$. The matrix zone axis is [131] and the twin zone axis is $[31\bar{1}]$. The intersections of the Ewald sphere with the matrix Laue zones are indicated by the solid lines while the intersections with the twin Laue zones are shown as dashed lines. The matrix tie point projection is (-6.0 1.13 2.62) and the twin tie point projection is (-0.75 1.47 -3.52).

tant. Another reason is that complex crystal structures do not have as many reflections which have a structure factor of zero as more symmetric crystal structures. Thus, while a face centered cubic structure will have entire planes of zero structure factor reflections in its reciprocal lattice (because of the symmetry of the structure), a more complex structure will never have this situation, and hence, all of its reciprocal lattice planes will contain reflections which can contribute to the image.

The fact that the Ewald sphere intersects with the two zero order Laue zones in different ways makes it difficult to be sure that a suspected tie point projection is, in fact, the correct tie point projection. This situation is complicated even more by the fact that higher order Laue zone reflections are more likely to be important in complex structures than they are in simpler cubic structures. Therefore, it would be desirable to have a way of calculating the intensities of the reflections on the diffraction pattern for a given selection of tie point projection. These intensities could then be compared with the experimental diffraction pattern to determine if the tie point projection used is correct. In the following section, a method will be derived for calculating the intensities of the different reflections contained in a diffraction pattern for a given tie point projection.

4.3.2. Calculation of Diffraction Pattern Intensities

The problem of calculating diffracted beam intensities in a diffraction pattern is quite different from the intensity in a diffraction contrast image. In an image, the calculation of diffracted beam intensity is done separately for every different crystal thickness. However, the intensity of a reflection in a diffraction pattern is generally from an area of the crystal over which the thickness is not constant. Thus, in a sense, the intensity of a diffraction pattern reflection represents an average of the intensities of the image formed from this reflection over the range of thicknesses allowed by the selected area aperture.

In this calculation, the intensity of a reflection which has been diffracted by a perfect crystal only will be considered. The expressions derived in this section will, therefore, only be applicable to diffraction patterns which do not include the twin boundary.

The first thing which will be evaluated will be the intensity of a reflection considering elastic scattering only. Later, the extension to include inelastic scattering will be given. The

intensity of the image formed by the reflection, g, at a crystal thickness of t was given in eq. 2.35 as:

$$I_g(\vec{r}_{ex}) = \left| \sum_i C_0^{(i)} C_g^{(i)} \exp(2\pi i \gamma^{(i)} t) \right|^2$$

This equation can be rewritten in the following way:

$$I_g = \sum_{i,j} C_0^{(i)} C_g^{(i)} C_0^{(j)} C_g^{(j)} \exp[2\pi i (\gamma^{(i)} - \gamma^{(j)}) t] \qquad (4.26)$$

In order to obtain the intensity of this reflection, g, in the diffraction pattern, I_g must be integrated over t, from t = 0 to t = T, where T is the maximum thickness of the crystal through which electrons passing through the selected area aperture have passed. Thus, it is being assumed that the minimum thickness of crystal which is exposed by the selected area aperture is zero. This will not always be the case, but it will be shown that if the range of thicknesses is large enough, neither the lower limit of t, nor the upper limit has much effect on the final result. Another assumption is that the selected area aperture is rectangular. Although this is not the correct shape, the effect of this will be relatively small, and will not be serious as long as the results obtained are only used as a guide to show the relative intensities of the different reflections. The integration must also be done in a direction perpendicular to the direction of increasing t, which will be called the x-direction. Therefore, the intensity of the reflection, g, in the diffraction pattern, ι_g, is given by the following:

$$\iota_g = \int_{x_1}^{x_2} \int_0^T I_g \, dt \, dx$$

$$= (x_1 - x_2) \sum_{i,j} C_0^{(i)} C_g^{(j)} C_0^{(j)} C_g^{(j)} \int_0^T \exp[2\pi i (\gamma^{(i)} - \gamma^{(j)}) t] \, dt \qquad (4.27)$$

The factors, x_1 and x_2, are arbitrary as long as they are kept consistent for all of the different reflections whose intensities are being calculated. In these calculations, x_1 and x_2 will be chosen in such a way as to ensure that the total area of the selected area aperture remains constant as the maximum thickness, T, is being varied. Thus, x_1-x_2 will be taken

to be:

$$x_1 - x_2 = \frac{1}{T}$$

Since the length of the selected area aperture in the direction of increasing t is directly related to T, this condition ensures that the total area of the crystal exposed by the aperture is constant, regardless of T. Therefore, eq. 4.27 can be evaluated to give the following:

$$\iota_g = \sum_{i,j} C_0^{(i)} C_g^{(j)} C_0^{(j)} C_g^{(j)} \frac{\sin\left[2\pi(\gamma^{(i)} - \gamma^{(j)})T\right]}{2\pi(\gamma^{(i)} - \gamma^{(j)})T}$$

$$+ i\sum_{i,j} C_0^{(i)} C_g^{(j)} C_0^{(j)} C_g^{(j)} \frac{(1 - \cos\left[2\pi(\gamma^{(i)} - \gamma^{(j)})T\right])}{2\pi(\gamma^{(i)} - \gamma^{(j)})T} \qquad (4.28)$$

The summations over i and j are over the same set of Bloch waves. Therefore, for each term, for which $i=i_1$ and $j=j_1$, and $\gamma^{(i)} - \gamma^{(j)} = \gamma^{(i_1)} - \gamma^{(j_1)}$, there is another term for which $i=i_2$ and $j=j_2$ and $\gamma^{(i)} - \gamma^{(j)} = \gamma^{(i_2)} - \gamma^{(j_2)} = -(\gamma^{(i_1)} - \gamma^{(j_1)})$. Thus, eq. 4.28 can be rewritten in the following way:

$$\iota_g = \sum_i (C_0^{(i)} C_g^{(j)})^2 \left(\frac{\sin\left[2\pi(\gamma^{(i)} - \gamma^{(i)})T\right]}{2\pi(\gamma^{(i)} - \gamma^{(i)})T} + i\frac{(1 - \cos\left[2\pi(\gamma^{(i)} - \gamma^{(i)})T\right])}{2\pi(\gamma^{(i)} - \gamma^{(i)})T} \right)$$

$$+ \sum_{i<j} C_0^{(i)} C_g^{(j)} C_0^{(j)} C_g^{(j)} \left[\left(\frac{\sin\left[2\pi(\gamma^{(i)} - \gamma^{(j)})T\right]}{2\pi(\gamma^{(i)} - \gamma^{(j)})T} + \frac{\sin\left[2\pi(\gamma^{(i)} - \gamma^{(i)})T\right]}{2\pi(\gamma^{(i)} - \gamma^{(i)})T} \right) \right.$$

$$\left. + i\left(\frac{(1 - \cos\left[2\pi(\gamma^{(i)} - \gamma^{(j)})T\right])}{2\pi(\gamma^{(i)} - \gamma^{(j)})T} - \frac{(1 - \cos\left[2\pi(\gamma^{(i)} - \gamma^{(j)})T\right])}{2\pi(\gamma^{(i)} - \gamma^{(j)})T} \right) \right]$$

In the second summation term, account has been taken of the fact that $\sin(-\theta) = -\sin(\theta)$ and $\cos(-\theta) = \cos(\theta)$. Thus, clearly the imaginary part of the second summation is equal to zero. In the first summation term both the real and imaginary parts are of the form of zero divided by zero. However, in the limit as $\gamma^{(i)} - \gamma^{(i)}$ tends to zero, the real term becomes one while the imaginary term becomes zero. Therefore, the intensity can be written as follows:

$$\iota_g = \sum_i (C_0^{(i)} C_g^{(j)})^2 + 2\sum_{i<j} C_0^{(i)} C_g^{(j)} C_0^{(j)} C_g^{(j)} \frac{\sin\left[2\pi T(\gamma^{(i)} - \gamma^{(j)})\right]}{2\pi T(\gamma^{(i)} - \gamma^{(j)})} \qquad (4.29)$$

The second term on the right hand side of this equation will vary from positive to negative values, but will tend to zero as T is increased. Since the actual value of T is not known, the exact value of this term cannot be known exactly, but to a good approximation, it can be assumed to be zero. This leaves the following approximate expression for ι_g:

$$\iota_g \cong \sum_i \left(C_0^{(i)} C_g^{(j)}\right)^2 \tag{4.30}$$

When inelastic scattering is taken into account, the equations become much more complex, but the same general procedure can be used to find the following expression for ι_g:

$$\begin{aligned}\iota_g = & \sum_i \frac{\left(C_{i1}^{-1} C_g^{(i)}\right)^2}{4\pi q^{(i)} T} \left[1 - \exp\left(-4\pi T q^{(i)}\right)\right] \\ & + \sum_{i<j} \frac{C_{i1}^{-1} C_g^{(i)} C_{j1}^{-1} C_g^{(j)}}{\pi T\left[\left(q^{(i)} + q^{(j)}\right)^2 + \left(\gamma^{(i)} - \gamma^{(j)}\right)^2\right]} \\ & \times \Bigg[\left(q^{(i)} + q^{(j)}\right) + \exp\left[-2\pi T\left(q^{(i)} + q^{(j)}\right)\right] \\ & \times \left\{\left(\gamma^{(i)} - \gamma^{(j)}\right) \sin\left[2\pi T\left(\gamma^{(i)} - \gamma^{(j)}\right)\right] - \left(q^{(i)} + q^{(j)}\right) \cos\left[2\pi T\left(\gamma^{(i)} - \gamma^{(j)}\right)\right]\right\}\Bigg]\end{aligned} \tag{4.31}$$

The value of this expression tends to decrease as T is increased. This is because the inelastic scattering causes the contributions from the thicker part of the crystal to be attenuated to the point where they are negligible. This is reflected by the fact that the exponential terms become negligible as T becomes large. The rate at which these exponential terms decrease depends on the $q^{(i)}$'s which represent the fact that some electrons have been scattered out of the diffracted beams and into the background of the diffraction pattern.

Figure 4.12 shows the intensities of the transmitted beam and the most intense diffracted beam for the diffraction conditions shown in Fig. 4.11. The dashed lines represent the intensities calculated by eq. 4.29, which does not include inelastic scattering. The dotted lines represent the approximation to the intensities not including inelastic scattering, calculated using eq. 4.30. The solid lines represent intensities including inelastic scattering

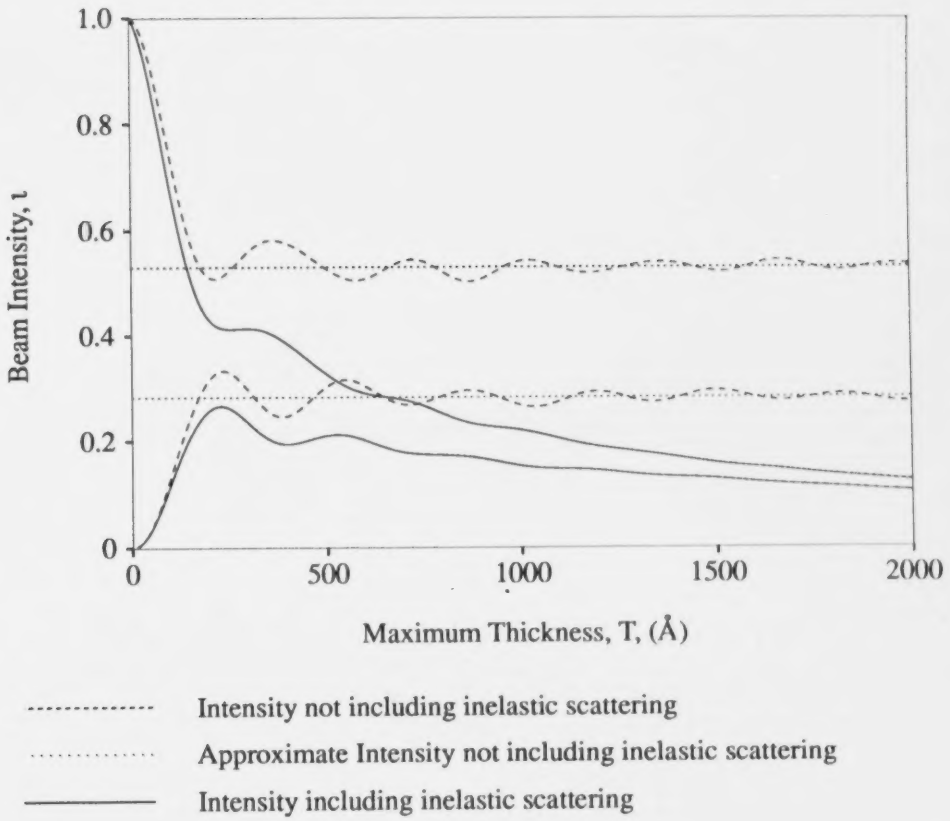

Fig. 4.12. Plot of beam intensity divided by maximum crystal thickness through which contributing electrons have passed as a function of maximum thickness. The crystal is $Y_1Ba_2Cu_3O_{7-\delta}$, the zone axis is [131] and the tie point projection is (-6 1.13 2.62). The upper lines represent the transmitted beam intensities and the lower lines represent the $(01\bar{3})$ diffracted beam intensities.

calculated using eq. 4.31. It can be seen from this figure that the values of intensity given by eq. 4.30 are a good approximation to the elastic scattering only values, given by eq. 4.29, for maximum thicknesses greater than around 700 Å or a couple of extinction distances. The most obvious difference between these values and the intensities which include inelastic scattering, is that the latter values decline rapidly as maximum thickness is increased, as expected. One other thing that can be noticed is that the wobbles in intensity tend to be damped out much earlier when inelastic scattering is included.

The problem with the intensity including inelastic scattering is that it drops continuously, and never reaches a constant value. Therefore, it is impossible to find an approximation to eq. 4.31 which is independent of T (for sufficiently large values of T) as was done in the elastic case. Also, a graph of intensity as a function of T (calculated using eq. 4.31) does not clearly show how the intensity of a given reflection relative to the other reflections varies as T is increased. This problem can be solved by normalizing the values given by eq. 4.31 so that the intensities of all of the beams add up to one for any given value of T. The fact that this procedure results in higher diffracted beam intensities than given by eq. 4.31 is of no importance, since only the relative intensities of the different reflections are of interest. Incidentally, the condition that all of the intensities add up to one is automatically satisfied by the values given in eqs. 4.29 and 4.30. This fact will make it easy to see what happens to the relative intensity of a particular reflection as a result of inelastic scattering. Figure 4.13 shows the normalized intensities including inelastic scattering compared with those which do not include inelastic scattering. It can be seen that there are significant differences between the values calculated including inelastic scattering and those calculated assuming elastic scattering only. In this case, the relative intensity of the transmitted beam tends to decrease as maximum thickness is increased, while the relative intensity of the diffracted beam tends to increase. This is not always the case, and just as often the transmitted beam will tend to become more intense relative to the other beams or stay constant.

The diffraction conditions assumed in the calculation of intensities are the same as those for Fig. 4.12. In this figure, however, the dotted line represents an approximate value of intensity including inelastic scattering. These values were calculated by using the expression given in eq. 4.31, but dropping the second summation term completely:

$$\iota_g \cong \sum_i \frac{\left(C_{i1}^{-1} C_g^{(i)}\right)^2}{4\pi T q^{(i)}} \left[1 - \exp\left(-4\pi T q^{(i)}\right)\right] \tag{4.32}$$

It can be seen from the figure that this gives a good approximation to the more accurate values calculated using eq. 4.31, as shown by the solid lines. It can also be seen that the intensities calculated including inelastic scattering do not become constant, as T increases, until T is very large, around 3000 Å or nine extinction distances. The actual maximum

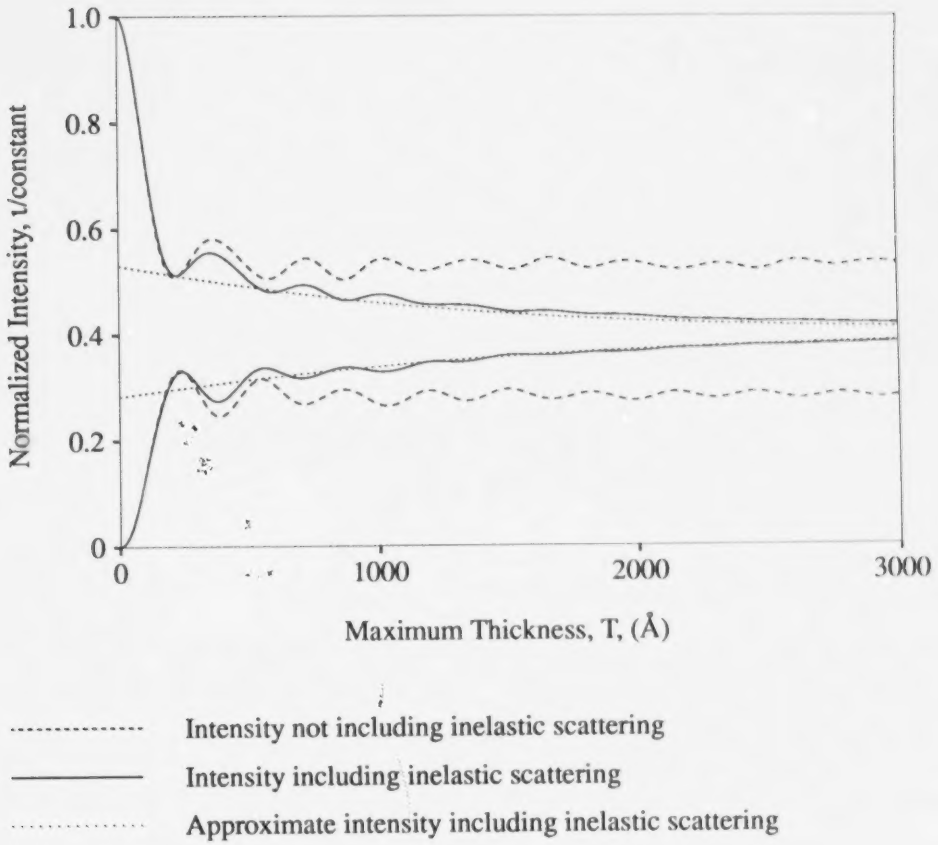

Fig. 4.13. Plot of normalized beam intensity as a function of maximum thickness. The crystal is $Y_1Ba_2Cu_3O_{7-\delta}$, the zone axis is [131] and the tie point projection is (-6 1.13 2.62). The upper lines represent the transmitted beam intensities and the lower lines represent the $(01\bar{3})$ diffracted beam intensities.

thickness would very often be smaller than this, so the values that the intensities tend towards as T becomes very large are not necessarily good approximations to the intensities of the reflections in an experimental diffraction pattern. However, it can be seen that the experimental intensity would generally be between these values and the values for zero T shown by the dotted lines.

This approximate zero T intensity can be evaluated as follows. Each term in eq. 3.32 involves the term, $(1-\exp(-4\pi Tq^{(i)}))/(4\pi Tq^{(i)})$, which tends to one as T tends

towards zero. Therefore, for T equals zero, the following expression remains:

$$\iota_g \equiv \sum_i \left(C_{i1}^{-1} C_g^{(i)}\right)^2 \tag{4.33}$$

This is very similar the eq. 4.29, since C_{i1}^{-1}, calculated including inelastic scattering, is very close to $C_0^{(i)}$, calculated without inelastic scattering. As T becomes very large, the exponential term in eq. 4.32 becomes very small, and the expression in eq. 4.32 becomes the following:

$$\iota_g \equiv \sum_i \frac{\left(C_{i1}^{-1} C_g^{(i)}\right)^2}{4\pi q^{(i)}} \tag{4.34}$$

Therefore, the values given in eqs. 4.33 and 4.34 can be thought of as limiting values for the intensity including inelastic scattering. Of course, if a more accurate value is desired, and the maximum thickness can be estimated, eq. 4.32 can be used. However, it is impossible to ever achieve truly accurate values, since the exact maximum thickness can never be known, nor is it even precisely defined, since all of the preceding calculations were done assuming a rectangular field limiting aperture.

Table 4.2 gives a comparison of the intensities of the eight brightest beams using three different approximations. The first row uses eq. 4.29, which assumes elastic scattering only. However, only two beams are used in the calculation, the transmitted beam and the beam whose intensity is being calculated. These values were then normalized to unity to facilitate comparison with the next two approximations. The two beam approximation is reasonably accurate for the brightest beams which are close to the Bragg condition. However, the two beam approximation seriously underestimates the intensities of those beams which derive a lot of their intensity from other, nearby, beams.

Reflection	000	$01\bar{3}$	$0\bar{1}3$	$\bar{1}\bar{2}7$	$02\bar{6}$	$\bar{1}3\bar{8}$	$0\bar{2}6$	$\bar{1}\bar{1}4$
Two-beam. Elastic scattering only	0.5127	0.2948	0.1648	0.0095	0.0085	0.0012	0.0051	0.0002
Many-beam Elastic scattering only	0.5301	0.2825	0.1140	0.0484	0.0116	0.0052	0.0051	0.0006
Many-beam Inelastic scattering included	0.4067	0.3955	0.1297	0.0423	0.0124	0.0056	0.0051	0.0008

Table 4.2. Diffraction pattern intensities in three different approximations.

The second row was calculated using the same equation as the first row, but with many beams included in the calculations. Inelastic scattering was not, therefore, included in these calculations. These values are also very close to the values which would be calculated by eq. 4.33. Thus, they can be considered to be limiting values (for low T) for the intensities when inelastic scattering is included.

The third row was calculated using eq. 4.34, which is the large T approximation for the intensities including inelastic scattering. Therefore, the experimental beam intensities which one would actually observe in the microscope probably lies somewhere in between the values given in the second and third rows. Therefore, it can be seen that the error introduced by using the many beam, elastic scattering only, formula, eq. 4.29, can be as high as ~ 40% in the case of the $(01\bar{3})$ reflection, although that estimate of the error is the maximum possible error for that reflection. For lack of a better approximation, this relation, eq. 4.29, is probably the best equation to use, being simpler than eq. 4.32 or eq. 4.34, and probably just as accurate. In any case, it can be seen that the intensities calculated in this way will give an accurate ranking of the reflections in terms of their intensities, but will not be accurate enough to be used as absolute intensities.

5. *Inelastic Scattering Factors*

5.1. Introduction

The imaginary part of the Fourier coefficients, U_g' result from different processes which excite the crystal into some higher energy state. The most important of these processes are phonon excitation, plasmon excitation and single electron excitation. Plasmon excitation and single electron excitation result in contributions to U_g' which are relatively insignificant, except for very small values of g. In general, only the g=0 term will be significantly affected. However, the U_0' term does not affect diffraction contrast, but rather attenuates all of the Bloch waves uniformly. Therefore, it does not affect the form of the image, and as a result, plasmon and single electron excitations are commonly ignored in diffraction contrast calculations.

As was mentioned in sec. 4.1.5, the phonon contribution to U_g' can be expressed as follows:

$$U_g' = \frac{1}{\pi V_c}\sum_k \exp(-2\pi i \vec{g}\cdot\vec{r}_k)\, f_k'(s, B_k)\exp(-B_k s^2) \qquad (5.1)$$

where the subscript, k, is over all of the atoms in the unit cell. $f_k'(s, B_k)$ is the inelastic scattering factor of the k^{th} atom due to phonon excitation, and has been given by Bird and King[15] as follows:

$$f_k'(s, B_k) = \frac{2h}{\beta mc}\int f_{el_k}(s')\, f_{el_k}(|\vec{s}-\vec{s}'|)\,(1-\exp[-2B_k(s'^2-\hat{s}\cdot\hat{s}')]) \qquad (5.2)$$

Using eqs. 5.1 and 5.2, the phonon contribution to U_g' can be calculated for any arbitrary crystal as long as the Debye parameter, B_k, is known for each atom in the crystal. This is made possible by the use of the Einstein model, in which each atom in the crystal is assumed to vibrate independently of the others. If this model is not used, the calculation of U_g' requires knowledge of the phonon spectrum of the entire crystal. Since this is not generally known, the Einstein model provides the best results which can normally be obtained.

The inelastic scattering factor due to phonon excitation, $f_k'(s, B_k)$, depends not

only on the scattering vector, s, but also on the Debye parameter of the atom, which in turn depends on the chemical environment around the atom in the crystal, and is therefore not the same for a given atom from one crystal to another. For this reason, it has not, up to the present, been parametrized as a function of scattering vector, s, in the same way that the elastic scattering factors have.

Instead of parametrizing the inelastic scattering factors, Bird and King have calculated values of $f_k'(s, B_k)$, using eq. 5.2, and tabulated them as a function of s and B_k for all neutral atoms with atomic numbers between 1 and 98. These tables contain values of $f_k'(s, B_k)$ for six different Debye parameters, and ten different scattering vectors for each Debye parameter, for a total of 60 values for each atom. They have given these values in the form of a computer subroutine which calculates $f_k'(s, B_k)\exp(-B_k s^2)$ by interpolation from the tabulated values. This approach suffers from several disadvantages. One small problem is that the subroutine requires a relatively large amount of computer memory and time to do the calculations. This problem is becoming relatively insignificant, however, with modern high speed computers which have a lot of memory and are very fast. Another more significant problem is that Bird and King's tables of values only include Debye parameters between 0.05 and 2.0. Debye parameters greater than 2.0 are fairly common and for atoms which have such a Debye parameter, Bird and King's subroutine cannot be used at all. The last disadvantage is that, although the interpolation routine included in Bird and King's subroutine generally gives accurate values of $f_k'(s, B_k)\exp(-B_k s^2)$ for large scattering vectors and Debye parameters, it can give quite inaccurate results for atoms which have very small Debye parameters. This problem is most serious for small scattering vectors and for large atoms.

Weickenmeier and Kohl[16] have taken a different approach to the calculation of inelastic scattering factors. They derived a formula for the calculation of $f_k'(s, B_k)$ which depends on their own parametrization of the elastic scattering factors found in the *International Tables for X-Ray Crystallography*, volume IV[36]. This formula is very long and complicated, so they have also made available a computer subroutine which does the calculation. Their subroutine, although it is only about one third of the size of Bird and King's subroutine, takes much longer to calculate the inelastic scattering factors. The results

generated by the subroutine are also subject to inaccuracies, although they may not be significant in light of the fact that the Einstein model is not particularly accurate in the first place. Weickenmeier and Kohl's method does have one potentially serious problem, however, in that it does not cover the full range of atoms covered by Bird and King.

The purpose of this chapter is to propose yet another method for the calculation of the inelastic scattering factors. This method involves a parametrization of the values tabulated by Bird and King. This parametrization method does not suffer from any of the disadvantages of the previous two methods, since it requires only a small number of parameters and a simple formula which can be evaluated quickly. Also, this method is very accurate and is valid for all atoms with atomic numbers between 1 and 98 and all Debye parameters.

Although the parametrization method has several advantages over previous methods for calculating the inelastic scattering factors for neutral atoms, these advantages were not the primary motivation for this work. The primary motivation is to find a way of calculating inelastic scattering factors for ions. At present, there is no source of inelastic scattering factors for ions which can be used for any given Debye parameter. Radi[14] has calculated the imaginary part of the Fourier coefficients for a small number of ionic crystals which have the rock salt structure. These coefficients can only be used for these crystals, however, and they do not provide a method for calculating the imaginary part of the Fourier coefficients for a crystal with a different structure or different Debye parameters. However, it is possible to extract the inelastic scattering factors for the constituent atoms from the coefficients given by Radi. By a comparison of these inelastic scattering factors and those of the corresponding neutral atoms, as calculated by the parametrization method discussed above, a method will be presented to calculate the inelastic scattering factors for the ions. This will involve modifying the parameters of the corresponding neutral atom, and using the same parametrization formula used for neutral atoms. This will allow the inelastic scattering factors to be calculated for any arbitrary ion, even those not dealt with by Radi, and for any Debye parameter. This could not be done without a parametrization of the inelastic scattering factors for neutral atoms. This situation made the above described parametrization work for neutral atoms necessary.

5.2. Neutral Atom Scattering Factors

5.2.1. Bird and King's Interpolation Method

The first thing to do is examine the form of the function, $f_k'(s, B_k)\exp(-B_k s^2)$, as given by Bird and King's subroutine, as it varies with scattering vector, s. In the following discussion, the subscript, k, on B_k, will be dropped with the understanding that B is the Debye parameter of the atom in question and may be different for different atoms in the same crystal. Figure 5.1 shows $f_k'(s, B)\exp(-Bs^2)$ as a function of s for a Debye parameter of 0.7 for a set of atoms with atomic numbers ranging from 30 to 70. The dots show

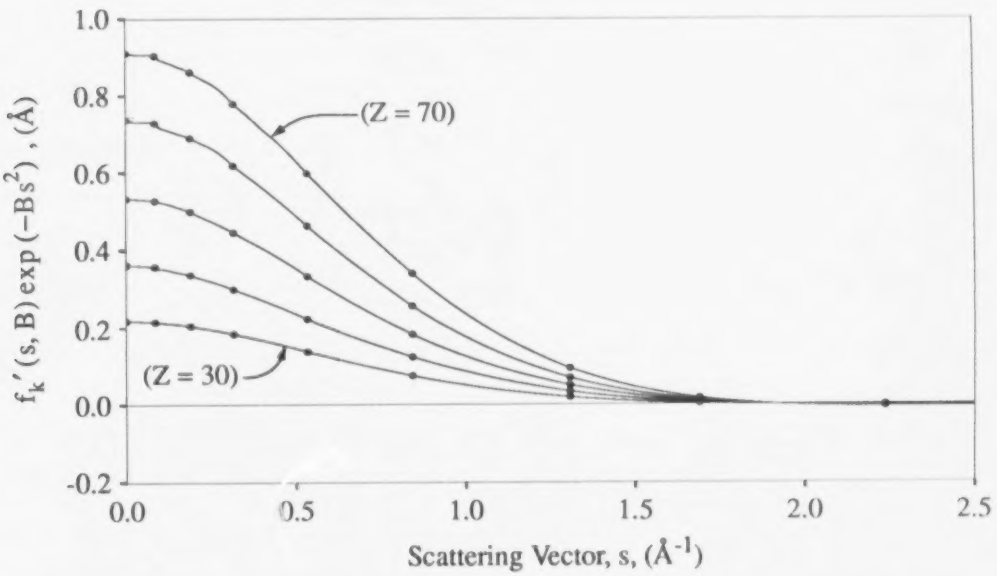

Fig. 5.1. Variation of $f_k'(s, B)\exp(-Bs^2)$ as a function of s for atoms having atomic numbers ranging from 30 to 70 for a Debye parameter of 0.7 as given by Bird and King. The dots represent values actually calculated by Bird and King. The lines show values given by Bird and King's interpolation subroutine.

the values which were actually calculated by Bird and King. The values given by the lines have been interpolated from the calculated values by the subroutine given by Bird and King. There are some small irregularities in the interpolated values which can be seen for small values of s, especially for the atoms with larger atomic numbers. These irregularities

are insignificant for reasonably large values of the Debye parameter, B, but they do become more of a problem for small B values. Figure 5.2 shows the variation in $f_k'(s, B)\exp(-Bs^2)$ with s for the same atoms but for a Debye parameter of 0.05. It can

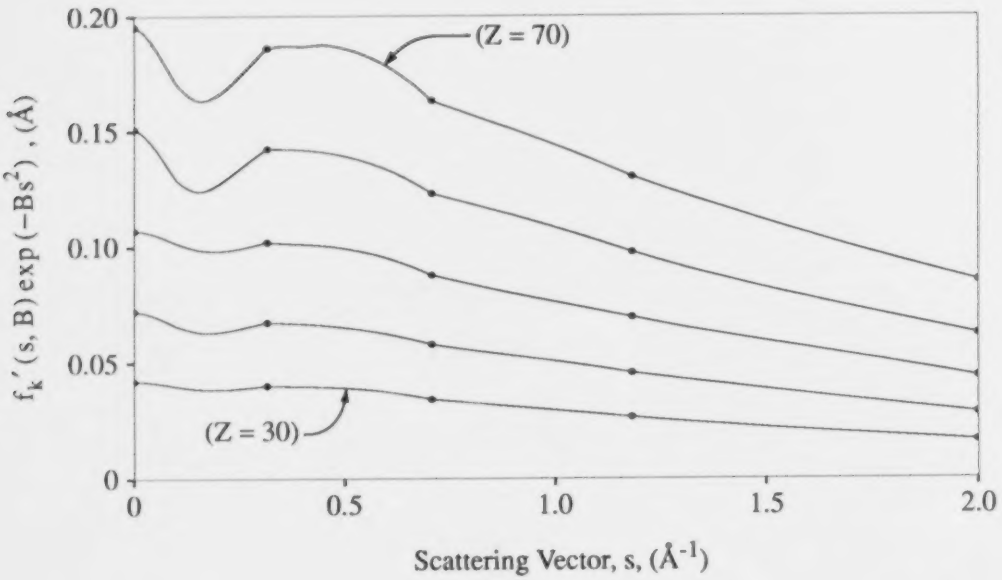

Fig. 5.2. Variation of $f_k'(s, B)\exp(-Bs^2)$ as a function of s for atoms having atomic numbers ranging from 30 to 70 for a Debye parameter of 0.05 as given by Bird and King. The dots represent values actually calculated by Bird and King. The lines show values given by Bird and King's interpolation subroutine.

be seen that the irregularities in the interpolated values are much more significant in this case and can lead to inaccurate values of $f_k'(s, B)\exp(-Bs^2)$ for small values of s.

5.2.2. New Parametrization of Inelastic Scattering Factors

In this section, a method will be presented by which Bird and King's calculated values for any particular atom and any Debye parameter can be approximated by a relatively simple formula. It was found that the formula which provides the best approximation to Bird and King's values has the following form:

$$f_k'(s, B)\exp(-Bs^2) = A(B)\exp[b(B)s^{n(B)}] \qquad (5.3)$$

where A(B), b(B), and n(B) are the parameters which must be determined for every atom and for every value of B. Although it is common to parametrize elastic scattering factors with a series of exponential terms, as was done by Doyle and Turner[35], it was decided that the parametrization of inelastic scattering factors should be kept as simple as possible by using a single exponential. This is because, as has been mentioned before, $f_k'(s, B)\exp(-Bs^2)$ depends on the Debye parameter, B, as well as s. Therefore, each parameter used in eq. 5.3 also depends on B, and so must itself be parametrized as a function of B. It was found that the variation of these three parameters, A, b, and n, as a function of B could be given as follows:

$$A(B) = A_A[(B+b_A)^{n_A} - 1] + C_A$$

$$b(B) = A_b B^{n_b} + C_b$$

$$n(B) = A_n \exp(b_n\sqrt{B}) + C_n \qquad (5.4)$$

There is, therefore, a total of 10 parameters (A_A, b_A, n_A, C_A, A_b, n_b, C_b, A_n, b_n, C_n) required to give each atom's variation in $f_k'(s, B)\exp(-Bs^2)$ with s and B. These parameters are list in Tables 5.1 and 5.2.

In order to assess the accuracy of the parametrization, it is necessary to compare the values of $f_k'(s, B)\exp(-Bs^2)$ obtained by the parametrization method with the values calculated by Bird and King for a number of different atoms and different Debye parameters. Figure 5.3 shows the agreement achieved between the values given by eq. 5.3 and eq. 5.4, with the parameters given in Tables 5.1 and 5.2, and the values calculated by Bird and King for the same set of atoms as in Fig. 5.1, and for a Debye parameter of 0.7. Bird and King's values are shown by the dots while the lines indicate the values calculated by eqs. 5.3 and 5.4. Figure 5.4 shows the agreement between the two sets of values for the atom, Zr, (Z = 40), with Debye parameters of 0.05, 0.3, and 1.3. It can be seen from the two figures that the calculated values show excellent agreement with the values calculated by Bird and King. There are two areas, however, where the agreement is not as good. One is for the point, s=0. It was found that Bird and King's value for this point was consistently lower than that given by eqs. 5.3 and 5.4. This is not an important difference, however,

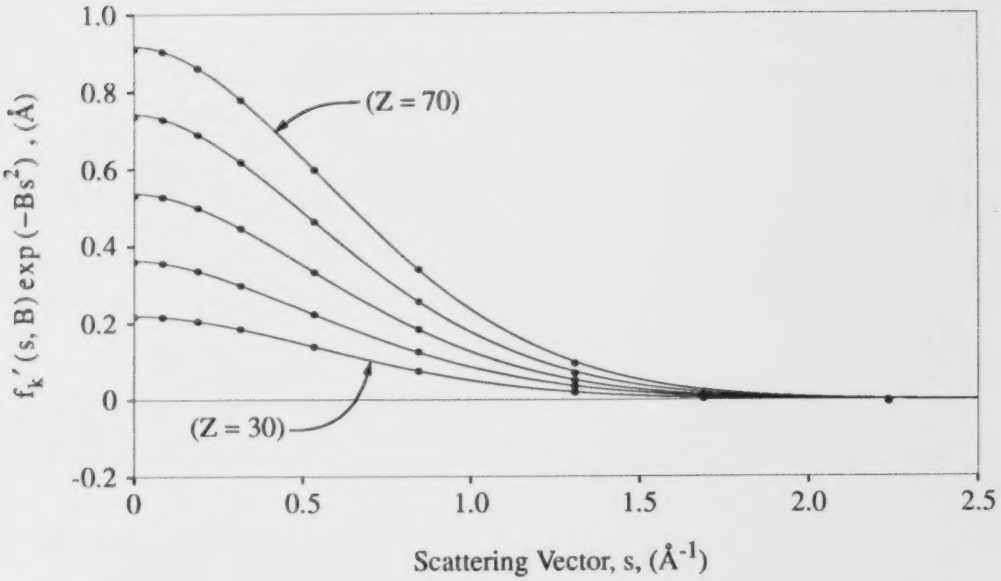

Fig. 5.3. Variation of $f_k'(s, B)\exp(-Bs^2)$ as a function of s for atoms having atomic numbers ranging from 30 to 70 for a Debye parameter of 0.7. The dots represent values actually calculated by Bird and King. The lines show values given by eqs. 5.3 and 5.4 using the appropriate parameters.

since the s=0 point contributes only to the V_0' term of the lattice potential, and this term does not affect image contrast. The other area where the agreement is not as good as it might be is for high values of s. These high values are not as important as lower values of s, however, since reflections with large scattering vectors are usually too weak to contribute much to the final image. Bird and King's values of $f_k'(s, B)\exp(-Bs^2)$ actually become negative at high values of s. This is in contrast to the values given by eqs. 5.3 and 5.4, which are always positive. However, in both cases, $f_k'(s, B)\exp(-Bs^2)$ is very close to zero, and could easily be neglected without bringing about noticeable differences in the final image.

The parameters needed for the use of eq. 5.4 are given for each atom covered by Bird and King, (Z=1 to Z=98), in Tables 5.1 and 5.2. Table 5.1 contains the parameters necessary for the calculation of A(B) and Table 5.2 contains the parameters needed to calculate b(B) and n(B).

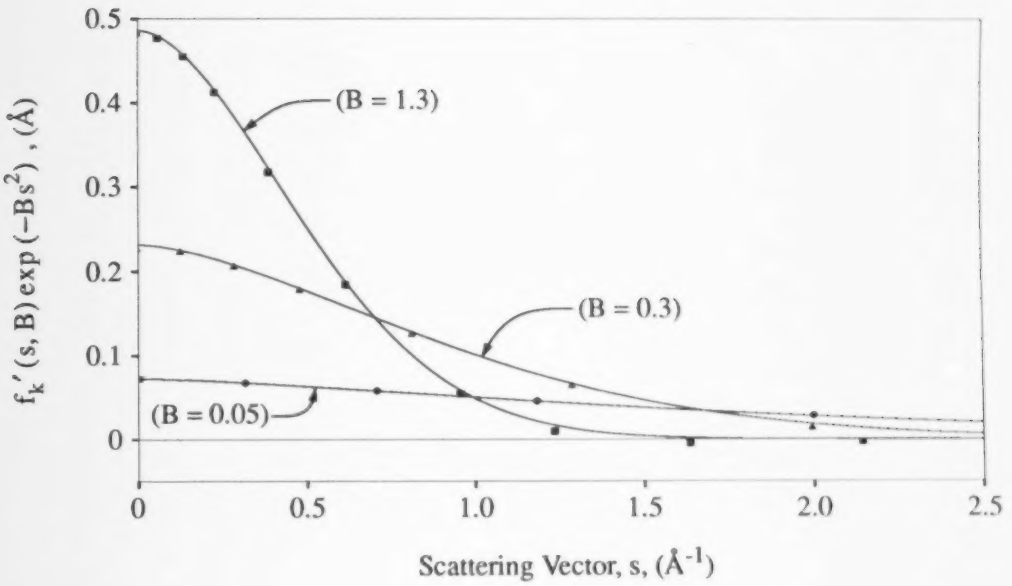

Fig. 5.4. Variation of $f_k'(s, B_k) \exp(-B_k s^2)$ as a function of s for Zr, (Z = 40), for Debye parameters of 0.05, 0.3, and 1.3. The dots represent values actually calculated by Bird and King. The lines show values given by eqs. 5.3 and 5.4 using the appropriate parameters.

Z	A_A	b_A	n_A	C_A
1	0.001759	0.243512	0.319410	6.71010e-04
2	0.008683	0.214749	0.141464	1.78832e-03
3	0.006172	0.057556	0.454130	4.50675e-03
4	0.011434	0.070895	0.468686	8.25517e-03
5	0.020568	0.118518	0.409288	1.23608e-02
6	0.030758	0.131513	0.372853	1.69252e-02
7	0.050057	0.178447	0.295446	2.09500e-02
8	0.071180	0.183704	0.246661	2.55869e-02
9	0.114317	0.202808	0.177857	2.98699e-02
10	0.187312	0.206696	0.120684	3.44013e-02
11	0.159246	0.175575	0.162867	4.14113e-02
12	0.123839	0.127493	0.237462	4.98839e-02
13	0.120279	0.099438	0.281421	5.91559e-02
14	0.117879	0.076867	0.330948	6.91122e-02
15	0.133254	0.075038	0.335002	7.88934e-02
16	0.166212	0.093772	0.306956	8.83690e-02
17	0.180825	0.090519	0.313283	9.85143e-02
18	0.229388	0.112740	0.276317	1.07902e-01
19	0.261973	0.117574	0.272746	1.20303e-01
20	0.262244	0.108960	0.303605	1.33610e-01
21	0.310066	0.120277	0.280789	1.45130e-01
22	0.336384	0.116860	0.276967	1.57079e-01
23	0.378453	0.123935	0.263563	1.67892e-01
24	0.525379	0.151493	0.201649	1.75270e-01
25	0.495723	0.132344	0.224186	1.89990e-01
26	0.581505	0.143063	0.201958	1.99307e-01
27	0.726939	0.151140	0.168897	2.09779e-01

Table 5.1. Parameters for the calculation of A(B).

Z	A_A	b_A	n_A	C_A
28	0.869765	0.156354	0.146658	2.19702e-01
29	1.11621	0.157634	0.116198	2.28575e-01
30	1.30930	0.158927	0.103569	2.40540e-01
31	1.11581	0.142370	0.125493	2.55666e-01
32	1.15067	0.137190	0.127289	2.70817e-01
33	1.00547	0.125131	0.151915	2.86376e-01
34	0.942374	0.112574	0.168430	3.03224e-01
35	0.985109	0.111585	0.169101	3.18723e-01
36	0.984789	0.105355	0.176337	3.35805e-01
37	0.978933	0.103019	0.188147	3.54478e-01
38	0.948222	0.099542	0.205917	3.73739e-01
39	0.905302	0.088125	0.224655	3.94832e-01
40	0.896629	0.082337	0.237454	4.14609e-01
41	0.989284	0.086814	0.223393	4.30986e-01
42	1.15610	0.101518	0.202072	4.46843e-01
43	1.14001	0.094782	0.213845	4.69037e-01
44	1.24558	0.099141	0.202384	4.85124e-01
45	1.26311	0.099447	0.207587	5.03415e-01
46	1.48930	0.110483	0.182215	5.17413e-01
47	1.53514	0.108435	0.183107	5.38126e-01
48	1.67881	0.113363	0.174515	5.57702e-01
49	1.72028	0.112474	0.176863	5.79713e-01
50	1.81859	0.114192	0.174017	6.01562e-01
51	1.75887	0.110786	0.186564	6.23322e-01
52	1.90980	0.114532	0.179091	6.47091e-01
53	1.90562	0.112334	0.186094	6.70552e-01
54	1.91656	0.107196	0.190601	6.96948e-01

Table 5.1. (Continued) Parameters for the calculation of A(B).

Z	A_A	b_A	n_A	C_A
55	1.98522	0.111667	0.193142	7.21245e-01
56	1.68101	0.088314	0.233314	7.57723e-01
57	1.81995	0.094904	0.225330	7.83547e-01
58	1.89750	0.092751	0.219608	8.05482e-01
59	2.27030	0.104120	0.185809	8.16017e-01
60	2.30161	0.104628	0.187725	8.35216e-01
61	2.64130	0.111869	0.166868	8.51857e-01
62	2.91707	0.115060	0.154253	8.71376e-01
63	3.15960	0.118500	0.145149	8.87423e-01
64	3.08729	0.109689	0.150204	9.15670e-01
65	3.70308	0.117559	0.126649	9.27050e-01
66	4.11014	0.121264	0.115837	9.42956e-01
67	4.46374	0.121333	0.108955	9.66760e-01
68	4.75050	0.118829	0.102140	9.80856e-01
69	5.50722	0.123746	0.089542	9.95198e-01
70	7.76783	0.130858	0.064427	1.00997
71	5.15365	0.113126	0.097424	1.03959
72	5.97465	0.118445	0.086007	1.05888
73	5.63481	0.113124	0.092491	1.08476
74	5.50470	0.111443	0.096527	1.10832
75	5.55355	0.111316	0.097596	1.13226
76	5.38000	0.106605	0.102162	1.15912
77	5.20558	0.103544	0.107335	1.18366
78	5.45920	0.104745	0.104186	1.20591
79	6.02054	0.107634	0.096545	1.23052
80	5.96948	0.105908	0.099255	1.25784
81	6.03820	0.103902	0.099989	1.28682

Table 5.1. (Continued) Parameters for the calculation of A(B).

Z	A_A	b_A	n_A	C_A
82	5.53847	0.102379	0.111836	1.31807
83	5.51319	0.100962	0.114881	1.34446
84	5.10572	0.098001	0.126943	1.37485
85	5.92212	0.104577	0.112584	1.40206
86	5.17671	0.095883	0.130508	1.43699
87	4.99958	0.092399	0.138597	1.47535
88	4.96510	0.090660	0.142821	1.50988
89	4.37197	0.084342	0.166702	1.54689
90	4.81951	0.087953	0.154649	1.58008
91	4.92415	0.089331	0.153743	1.60421
92	5.32423	0.092503	0.145341	1.63352
93	5.20504	0.091415	0.151162	1.66153
94	5.75319	0.092351	0.137615	1.68782
95	5.99594	0.097166	0.135344	1.71259
96	6.21861	0.095058	0.132079	1.74590
97	7.03940	0.102488	0.119172	1.76829
98	6.56648	0.096858	0.129077	1.80077

Table 5.1. (Continued) Parameters for the calculation of A(B).

Z	A_b	n_b	C_b	A_n	b_n	C_n
1	-1.986665	0.929590	-0.642503	-1.413940	-1.103895	2.158958
2	-1.724686	0.881042	-0.439397	-1.461397	-2.408083	2.023975
3	-1.871647	0.708538	-0.283205	-0.476169	-2.033448	1.563754
4	-1.933530	0.839714	-0.411109	-3.763690	-0.109301	4.832222
5	-1.983416	0.909836	-0.478359	-2.432531	-0.278312	3.389488
6	-1.992366	0.914272	-0.468743	-1.511784	-0.738773	2.374922
7	-1.950901	0.895840	-0.453316	-1.363268	-1.308167	2.119058
8	-1.872678	0.885387	-0.432101	-1.406819	-1.800575	2.054518
9	-1.799814	0.867691	-0.400281	-1.453983	-2.253954	2.023345
10	-1.726648	0.862393	-0.369201	-1.504521	-2.622043	2.018062
11	-1.691385	0.823747	-0.336461	-1.390789	-3.111982	1.904290
12	-1.681261	0.811611	-0.316692	-1.153041	-3.058700	1.833728
13	-1.707785	0.804566	-0.298029	-0.879853	-2.292827	1.807980
14	-1.716355	0.822608	-0.302784	-0.803086	-2.019052	1.800270
15	-1.753406	0.840628	-0.296633	-0.779632	-1.296612	1.897678
16	-1.773774	0.867532	-0.307328	-0.939730	-0.889186	2.076222
17	-1.780523	0.892905	-0.325808	-1.031383	-0.931547	2.126174
18	-1.794440	0.899186	-0.324719	-1.124091	-0.878763	2.205923
19	-1.801243	0.875460	-0.322345	-1.105916	-0.873751	2.173448
20	-1.802090	0.863886	-0.322174	-1.001004	-1.181383	2.017111
21	-1.799773	0.860544	-0.321573	-1.025474	-1.276102	2.011338
22	-1.797811	0.855655	-0.312343	-1.024081	-1.449865	1.988050
23	-1.772666	0.858334	-0.319515	-1.086281	-1.770228	1.961475
24	-1.760371	0.859360	-0.308236	-1.126907	-1.860222	1.993262
25	-1.729919	0.860008	-0.315921	-1.137347	-1.980853	1.969387
26	-1.718279	0.855285	-0.302021	-1.186952	-2.347792	1.954224
27	-1.699315	0.845683	-0.290731	-1.176977	-2.385505	1.955004

Table 5.2. Parameters for the calculation of b(B) and n(B).

Z	A_b	n_b	C_b	A_n	b_n	C_n
28	-1.665664	0.857467	-0.298174	-1.236677	-2.525040	1.966418
29	-1.639050	0.859221	-0.288425	-1.259771	-2.615712	1.985478
30	-1.632103	0.850586	-0.275043	-1.219546	-2.687121	1.971445
31	-1.610075	0.855285	-0.279548	-1.208218	-2.750101	1.955348
32	-1.608431	0.852362	-0.270102	-1.100160	-2.524680	1.947478
33	-1.598020	0.854957	-0.270679	-1.119686	-2.766798	1.923801
34	-1.605819	0.856656	-0.264067	-1.013298	-2.425520	1.931028
35	-1.615431	0.856670	-0.254598	-0.965929	-2.308991	1.933821
36	-1.625603	0.862676	-0.247498	-0.893642	-1.922210	1.962374
37	-1.625963	0.849400	-0.244808	-0.855144	-2.037827	1.916469
38	-1.626665	0.846200	-0.243765	-0.838738	-2.113711	1.891640
39	-1.630199	0.857039	-0.249680	-0.821962	-1.850837	1.912655
40	-1.640270	0.856330	-0.246625	-0.817521	-1.836173	1.913389
41	-1.651186	0.873413	-0.247770	-0.854381	-1.540920	1.984742
42	-1.649695	0.876300	-0.253144	-0.877371	-1.503855	1.995304
43	-1.662578	0.874023	-0.245699	-0.857033	-1.393382	2.010240
44	-1.661315	0.881260	-0.248966	-0.903249	-1.469941	2.024716
45	-1.652438	0.885376	-0.257134	-0.944298	-1.714029	1.999234
46	-1.652384	0.887102	-0.255833	-0.978188	-1.742854	2.018930
47	-1.657086	0.876578	-0.246610	-0.951874	-1.692441	2.015820
48	-1.655954	0.879735	-0.248015	-0.957061	-1.659757	2.023546
49	-1.652898	0.868700	-0.245794	-0.951619	-1.796670	1.992847
50	-1.654099	0.869394	-0.244940	-0.945472	-1.752125	1.997237
51	-1.653246	0.868626	-0.246694	-0.992560	-1.976016	1.976098
52	-1.650690	0.863461	-0.245375	-0.946068	-1.876495	1.971046
53	-1.654832	0.864195	-0.243592	-0.941810	-1.914700	1.964732
54	-1.661738	0.865199	-0.238697	-0.909872	-1.667091	1.991103

Table 5.2. (Continued) Parameters for the calculation of b(B) and n(B).

Z	A_b	n_b	C_b	A_n	b_n	C_n
55	-1.657391	0.858270	-0.242309	-0.910703	-1.854390	1.950284
56	-1.655672	0.849444	-0.240356	-0.886463	-1.952557	1.916487
57	-1.659332	0.847254	-0.237539	-0.859314	-1.876102	1.914003
58	-1.653071	0.852009	-0.239667	-0.876255	-1.822777	1.933517
59	-1.643020	0.860787	-0.240646	-0.907159	-1.746547	1.972517
60	-1.631147	0.854950	-0.236954	-0.933783	-2.111735	1.937363
61	-1.623098	0.862526	-0.240964	-0.952531	-2.033513	1.959220
62	-1.621774	0.850902	-0.228969	-0.926692	-2.118826	1.944848
63	-1.616163	0.851845	-0.225430	-0.951036	-2.283776	1.943621
64	-1.612344	0.861249	-0.230670	-0.924578	-1.991886	1.970209
65	-1.597413	0.856374	-0.225794	-0.957210	-2.243035	1.960481
66	-1.579944	0.859895	-0.229998	-0.988109	-2.360619	1.958290
67	-1.587462	0.856377	-0.220566	-0.919997	-2.125830	1.967931
68	-1.564611	0.861032	-0.224175	-0.957012	-2.266854	1.969484
69	-1.555885	0.859016	-0.221139	-1.007868	-2.610657	1.955081
70	-1.566862	0.849777	-0.202618	-0.948141	-2.455979	1.964546
71	-1.544702	0.860236	-0.215859	-0.970936	-2.570164	1.955588
72	-1.543978	0.862058	-0.213676	-0.961784	-2.562161	1.957285
73	-1.544020	0.864496	-0.212798	-0.939239	-2.456653	1.961720
74	-1.547950	0.866707	-0.207156	-0.903382	-2.368461	1.967208
75	-1.535765	0.870064	-0.216321	-0.944200	-2.444025	1.962179
76	-1.534443	0.870070	-0.214299	-0.909917	-2.327395	1.964720
77	-1.542489	0.873679	-0.209039	-0.903272	-2.305750	1.974319
78	-1.536233	0.877843	-0.214107	-0.936735	-2.365699	1.976997
79	-1.536529	0.874948	-0.210939	-0.918784	-2.323019	1.975788
80	-1.537397	0.877450	-0.210191	-0.909345	-2.272919	1.979094
81	-1.547653	0.876079	-0.204106	-0.852836	-2.009983	1.992805

Table 5.2. (Continued) Parameters for the calculation of b(B) and n(B).

Z	A_b	n_b	C_b	A_n	b_n	C_n
82	-1.533539	0.878307	-0.211083	-0.911676	-2.318238	1.964894
83	-1.545397	0.867540	-0.201825	-0.870254	-2.353759	1.953557
84	-1.540020	0.872088	-0.206445	-0.889392	-2.464191	1.943878
85	-1.554040	0.867150	-0.197564	-0.807687	-2.070266	1.959567
86	-1.548214	0.880996	-0.208349	-0.842724	-1.993683	1.977315
87	-1.550769	0.868860	-0.202828	-0.788686	-1.952663	1.952171
88	-1.560198	0.868403	-0.199066	-0.756494	-1.709677	1.968540
89	-1.557996	0.859053	-0.197050	-0.768892	-2.188917	1.912209
90	-1.569007	0.864094	-0.195343	-0.728476	-1.600641	1.964328
91	-1.559897	0.869525	-0.204145	-0.791256	-1.883349	1.952736
92	-1.571793	0.861946	-0.192703	-0.744449	-1.744257	1.957278
93	-1.564316	0.870557	-0.201181	-0.804320	-2.012999	1.949633
94	-1.567844	0.878892	-0.202487	-0.810608	-1.646172	2.004970
95	-1.560300	0.871174	-0.201647	-0.830104	-2.031987	1.960396
96	-1.569565	0.874194	-0.198139	-0.802902	-1.683549	1.998831
97	-1.566217	0.872064	-0.199439	-0.833288	-1.865513	1.987068
98	-1.563563	0.870842	-0.198410	-0.841724	-1.997957	1.975332

Table 5.2. (Continued) Parameters for the calculation of b(B) and n(B).

5.3. Ionic Inelastic Scattering Factors

5.3.1. Existing Form of Scattering Factors

The problem of inelastic scattering factors for atoms which are ionically bound in the crystal will now be considered. Radi[9] has calculated the total imaginary part of the Fourier coefficient, V_g', for a series of ionic crystals which have the rock salt structure. In order to analyse the inelastic scattering factors used by Radi in his calculations, the first thing which must be done is that the inelastic scattering factors must be extracted from the imaginary Fourier coefficients which were given by Radi. Each V_g' value involves the inelastic scattering factors of two different ions. However, the formula for V_g' is different when g has all even indices from when g has all odd indices. These two different sets of V_g' values can be fitted to two different formulae and the relation between the two will give the different scattering factors for the two ions.

For crystals which have the rock salt structure, the formula for V_g' given in eq. 5.1 reduces to:

$$V_g' = \frac{2h^2}{\pi m e V_c} [f_1'(s, B_1) \exp(-B_1 s^2) + f_2'(s, B_2) \exp(-B_2 s^2)] \qquad (5.5a)$$

for h,k,l all even, and

$$V_g' = \frac{2h^2}{\pi m e V_c} [f_1'(s, B_1) \exp(-B_1 s^2) - f_2'(s, B_2) \exp(-B_2 s^2)] \qquad (5.5b)$$

for h,k,l all odd, where $f_1'(s, B)$ and $f_2'(s, B)$ are the inelastic scattering factors used for the two ions. In Radi's calculations, the two constituent ions were assumed to have the same Debye parameter. Thus, in this case, $B_1=B_2=B$. Therefore, if a function, $g_1(s, B)$, can be found which gives all of the V_g's for which h,k,l are all even, and another function, $g_2(s, B)$, which describes those V_g's for which h,k,l are all odd, the

$f_k'(s, B)\exp(-Bs^2)$ values can be found in the following manner:

$$f_1'(s, B)\exp(-Bs^2) = \frac{\pi m e V_c}{4h^2}[g_1(s, B) + g_2(s, B)]$$

$$f_2'(s, B)\exp(-Bs^2) = \frac{\pi m e V_c}{4h^2}[g_1(s, B) - g_2(s, B)] \qquad (5.6)$$

It was found that a formula of the form given by eq. 5.3 was a reasonable first guess at g(s,B). Therefore, all of the V_g' for Radi's ionic crystals which have even Miller indices were fitted to this formula and the same was done for those with odd indices. Equation 5.6 was then used to calculate a set of points for the two functions, $f_k'(s, B)\exp(-Bs^2)$. These points were then fitted to a formula with the form given by eq. 5.3 to derive a first guess at $f_k'(s, B)\exp(-Bs^2)$ for each of the constituent ions. Different procedures were then tried to improve on these initial guesses, each of which involved assuming that the guess for one of the ions was correct and going back to the Radi's original V_g' values to improve on the other guess. The set of $f_k'(s, B)\exp(-Bs^2)$'s which gave the best agreement with the V_g' values given by Radi when inserted back into eq. 5.6 were then assumed to be correct. Obviously, this procedure cannot give as accurate values as were obtained for the neutral atom scattering factors using Bird and King's data. For one thing, each ion's scattering factor is somewhat obscured by the contribution of the other ion's factor in each value of V_g'. In some cases, this problem makes it impossible to determine accurate parameters for one of the ions involved because the other ion's contribution to V_g' is so much larger. Therefore, for example, it was impossible to accurately parametrize $f_k'(s, B)\exp(-Bs^2)$ for Li^{+1}, for any of the compounds in which it was involved, since its contribution to V_g' was always swamped by the other ion's contribution. Another problem which affected the accuracy was the fact that Radi did not calculate the V_g' values to sufficient precision, with some values having as few as one or even zero significant digits (e.g. the V_g' value was listed as 0.000 for anything below a certain threshold value, presumably 0.0005). However, despite these problems, accurate parametrizations were obtained for most of the ions considered by Radi.

5.3.2. New Form of Ionic Inelastic Scattering Factors

The above procedure resulted in a set of parameters, $A(B_0)$, $b(B_0)$, $n(B_0)$ for eq. 5.3, for each constituent ion, where B_0 is the Debye parameter for the crystal involved. Because of the inaccuracies in these parameters, and the lack of enough parameters for different values of B, for a given ion, it was impossible to find accurate values of the parameters such as A_A, b_A, etc., which are needed for eq. 5.4, for each ion. An alternative approach was, therefore, required. It was decided to try to develop some simple rules for finding the $f_k'(s, B)\exp(-Bs^2)$ values for a given ion using the parameters given in Table 5.1 and Table 5.2 for the corresponding neutral atom. This would then allow one to calculate $f_k'(s, B)\exp(-Bs^2)$ for all ions, even those not considered by Radi. The initial attempts to find such a set of rules was largely unsuccessful. It is believed that this is due to an error in integration which Radi made in his calculations and which was reported by Bird and King[15]. The result of this error is that even values of V_g' which were calculated by Radi for crystals made up of neutral atoms were different than those which resulted from the use of Bird and King's data. Because Radi's data is the only available data for ionic crystals, it was decided that an attempt should be made to find the effect that this error has on values of $A(B_0)$, $b(B_0)$, and $n(B_0)$,which are derived by fitting eq. 5.3 to Radi's data. It might then be possible to correct for this error in the ionic parameters before comparing them with the corresponding neutral atom parameters from Bird and King's data.

Radi also calculated V_g' for a number of monatomic crystals which consist of neutral atoms. From these V_g' values, the inelastic scattering factors could be derived and a set of parameters, $A_R(B_0)$, $b_R(B_0)$, and $n_R(B_0)$ were obtained (in the following discussion, those A, b, and n parameters which were derived from Radi's neutral atom crystal data will have the subscript, R. The parameters derived from Bird and King's neutral atom data will have the subscript, B, and parameters derived from Radi's ionic crystal data will have the subscript, I). These parameters were then compared to the corresponding parameters (i.e. for the same atom and the same Debye parameter, B_0), $A_B(B_0)$, $b_B(B_0)$, and $n_B(B_0)$, for neutral atoms which were derived from Bird and King's data. In each case, it was found that the difference between the two corresponding parameters, (e.g. between $n_R(B_0)$ and $n_B(B_0)$), followed a consistent pattern, and could be expressed in analytical

form. The average difference between $n_R(B)$ and $n_B(B)$ will be referred to as $d_n(B)$. Thus, since $n_R(B)$-$n_B(B)$ is approximately equal to $d_n(B)$, a rough correction for Radi's error in calculations could be made by simply adding $d_n(B)$ to Radi's n parameters, $n_R(B)$.

Next, it was assumed that this same correction could be used to correct Radi's error for ionic crystals. Therefore, a correct n parameter for a particular ion, (which will be labelled, $n_{IC}(B)$ -- the C stands for corrected), could be obtained by adding $d_n(B)$ to the n parameter derived for that ion from Radi's ionic crystal data, $n_I(B)$. This corrected value, $n_{IC}(B)$, could then be compared with the n parameter for the corresponding neutral atom, $n_B(B)$, as derived from Bird and King's data. In this way, the difference in parameters for neutral atoms and ions could be found, leading to the possibility that a method for deriving the ionic parameters from the corresponding neutral atom parameters could be obtained..

5.3.3. Ionic n Parameters

It was found that the n values from Radi's neutral atom data, $n_R(B)$, were consistently larger than those resulting from Bird and King's data, $n_B(B)$. It was calculated that on average, $n_R(B)$ was 8.7% larger than $n_B(B)$ for the same Debye parameter, B. Although there were random variations from the average, there was no discernable trend in this difference as a function of B. Therefore:

$$n_R(B) \cong n_B(B) + d_n(B)$$

where

$$d_n(B) = 0.087 n_B(B)$$

It will now be assumed that the same difference, $d_n(B)$, would characterize the relationship between Radi's ionic n parameters, $n_I(B)$, and Bird and King's neutral atom n parameters, $n_B(B)$. Therefore, $0.087n_B(B)$ is subtracted from the value, $n_I(B)$, which was derived from Radi's data for ionic crystals, and then this new value, $n_{IC}(B)=n_I(B)-d_n(B)$ is compared with $n_B(B)$, making sure that the same Debye parameter is used throughout for a given data point. Figure 5.5 shows a plot of $n_{IC}(B)$-$n_B(B)$ as a function of B for all of the ions for which good parameters were available. The squares represent data for positive ions while the circles represent negative ions.

First of all, it can be seen that all of the points are clustered around zero. This

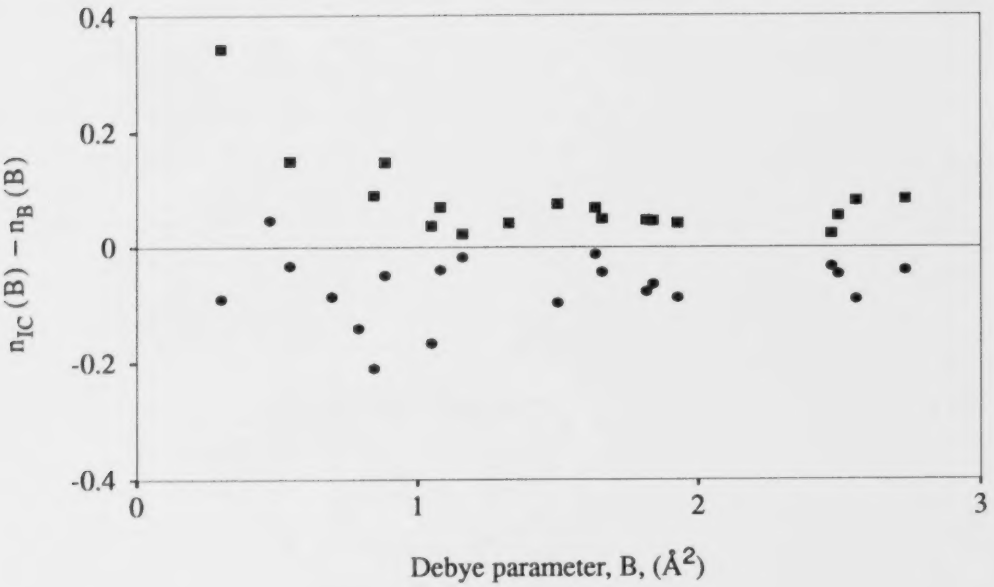

Fig. 5.5. Plot of the difference between the corrected n value for a given ion, $n_{IC}(B)$, and the neutral atom value for the same atom as derived from Bird and King's data, $n_B(B)$, as a function of Debye parameter. The circles represent negative ions while the squares represent positive ions.

indicates that the ionic n parameters, $n_I(B)$, are also generally 8.7% larger than the n parameters for the same atoms derived from Bird and King's data, $n_B(B)$. Thus since all of the n parameters derived from Radi's data, whether for neutral atoms or ions, tend to differ from Bird and King's n parameters by the same amount, it is reasonable to assume that the same correction, (namely, the subtraction of $d_n(B)$) can be made for ions as for neutral atoms. Secondly, it is clear that the negative ions tend to have a lower n parameter than their neutral atom counterparts (which would generally fall around zero on this plot) and the positive ion n parameters are higher than the neutral atom values. This behaviour is reasonable for any parameter which characterizes atoms and ions. Based on this fact, a simple relation between the corrected ionic n parameter, $n_{IC}(B)$, and the neutral atom n parameter, $n_B(B)$, can be found which can be calculated using eq. 5.4 and Tables 5.1 and 5.2.

If ΔZ is taken to be the extra charge on the ion in question (e.g. Na^{+1} has $\Delta Z=1$) then

the new values, $n_{IC}(B)$ can be expressed as follows:

$$n_{IC}(B) \cong n_B(B) + m_n \Delta Z \tag{5.7}$$

where m_n is a factor which depends on the ion, but for atoms which were not treated by Radi, an average value, m_{nav}, can be used.

$$m_{nav} = 0.06 \tag{5.8}$$

The set of m_n values for those atoms covered by Radi for which accurate values of $n_I(B)$ could be obtained is given in Table 5.3

Atom	Z	ΔZ	m_n
O	8	-2	0.045
F	9	-1	0.058
Na	11	+1	0.091
Mg	12	+2	0.172
Cl	17	-1	0.098
K	19	+1	0.051
Se	34	-2	0.105
Br	35	-1	0.044
Rb	37	+1	0.052
Ag	47	+1	0.063
Te	52	-2	0.083
I	53	-1	0.006
Cs	55	+1	0.042
Pb	82	+2	0.046

Table 5.3. m_n parameters for common ions.

5.3.4. Ionic b Parameters

Now, an attempt will be made to find a relationship between the corrected ionic b values, $b_{IC}(B)$, and the neutral atom b values obtained from eq. 5.4 and Tables 5.1 and 5.2, $b_B(B)$. Once again, the first thing to do is to compare the b values obtained from Radi's neutral atom data, $b_R(B)$, with the corresponding values from Bird and King's data, $b_B(B)$.

Figure 5.6 shows the difference between these two values as a function of B for all of the bcc and fcc neutral atom crystals considered by Radi. The difference between the two

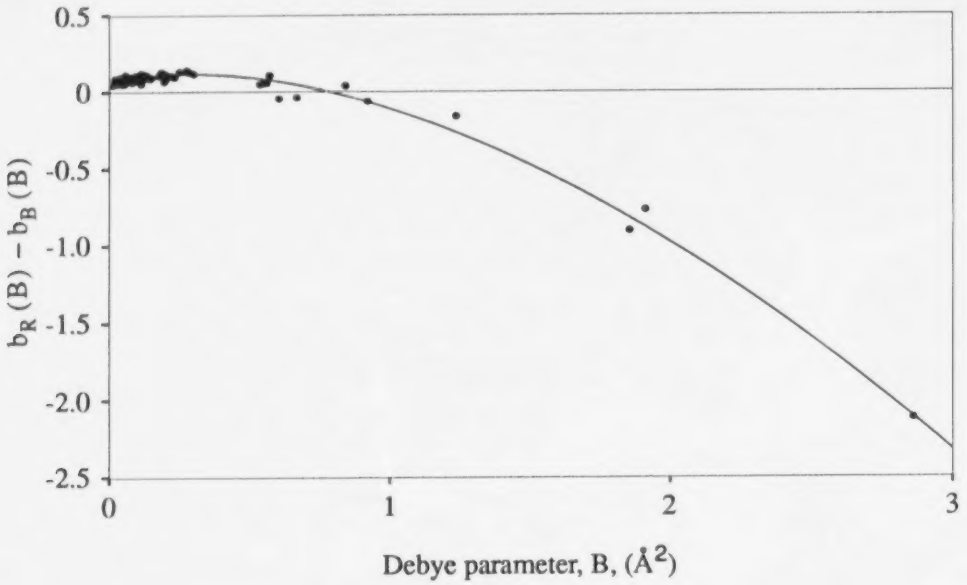

Fig. 5.6. Plot of the difference between the neutral atom b values using Radi's data, $b_R(B)$, and using Bird and King's data, $b_B(B)$, as a function of Debye parameter. The line indicates the average difference, $d_b(B)$.

values, $d_b(B)$, was found to be given approximately by:

$$b_R(B) - b_B(B) \cong d_b(B) = 0.059366 + 0.186865B - 0.130802B^{1.564162}$$

Figure 5.7 shows the difference between the ionic data b values, $b_I(B)$, and the $b_B(B)$ values for the same neutral atom with the same Debye parameter as a function of B. As in Fig. 5.6, the function, $d_b(B)$ is indicated by the line. The positive ions are represented by the squares and the circles represent the negative ions. Again, it can be seen that the ionic b parameters, $b_I(B)$, tend to differ from the corresponding Bird and King neutral atom b parameters, $b_B(B)$ by the same amount as Radi's neutral atom b parameters do. It can also be seen that the positive ion b values tend to be larger than the average neutral atom values obtained from Radi's data, whereas the negative ion values tend to be lower, as was the case

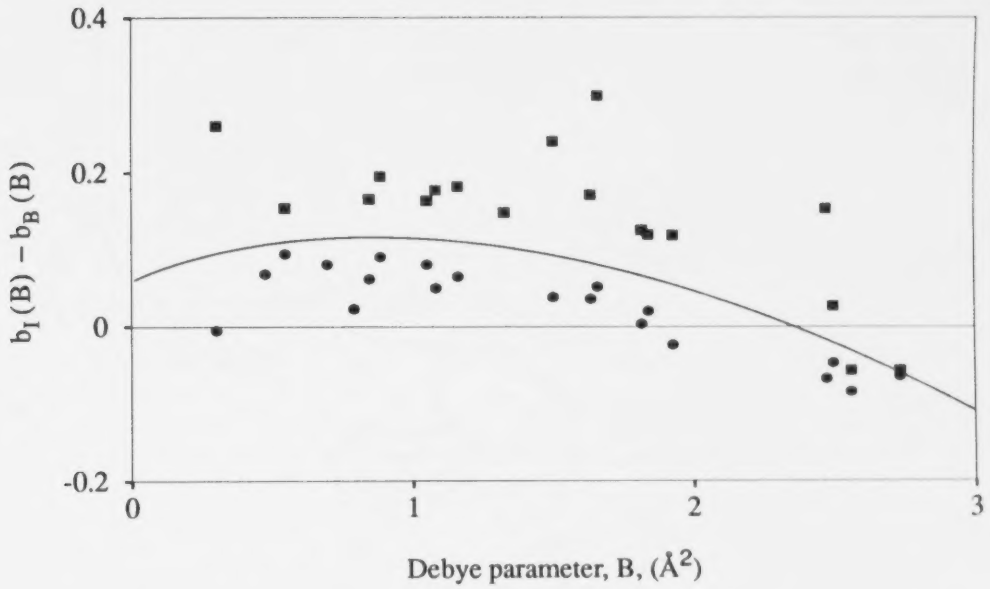

Fig. 5.7. Plot of the difference between the ionic b values using Radi's data, $b_I(B)$, and the neutral atom values, $b_B(B)$, as a function of Debye parameter. The line represents $d_b(B)$, the average difference between Radi's neutral atom values, $b_R(B)$, and $b_B(B)$. The circles represent the negative ions while the squares represent the positive ions.

for the n parameters.

Again, a simple relationship between the corrected parameters derived from Radi's ionic crystal data, $b_{IC}(B)=b_I(B)-d_b(B)$, and the neutral atom parameters which are based on Bird and King's data, $b_B(B)$, could be found. This relationship is given by the following formula:

$$b_{IC}(B) = b_B(B) + m_b \Delta Z \tag{5.9}$$

where m_b depends on Z and ΔZ, but an average value, m_{bav}, can be used for atoms which were not treated by Radi.

$$m_{bav} = 0.075 \tag{5.10a}$$

for positive ions, and:

$$m_{bav} = 0.045 \tag{5.10b}$$

for negative ions. For those atoms for which Radi's data gave useable results, Table 5.4

gives the best value of m_b:

Atom	Z	ΔZ	m_b
O	8	-2	0.050
F	9	-1	0.041
Na	11	+1	0.148
Mg	12	+2	0.082
Cl	17	-1	0.069
K	19	+1	0.097
Se	34	-2	0.027
Br	35	-1	0.033
Rb	37	+1	0.045
Ag	47	+1	0.015
Te	52	-2	0.017
I	53	-1	0.034
Cs	55	+1	0.044
Pb	82	+2	0.024

Table 5.4. m_b parameters for common ions.

5.3.5. Ionic A Parameters

Finally, it is necessary to look for a formula for $A_{IC}(B)$, the corrected ionic A value, in terms of the neutral atom A values, $A_B(B)$, obtained from eq. 5.4 and the parameters in Tables 5.1 and 5.2. First, $A_B(B)$ is compared with Radi's neutral atom A values, $A_R(B)$. This comparison is made more difficult by the fact that the difference between these two values depends on Z as well as B. In spite of this difficulty, the following relationship was found:

$$A_R(B) = A_B(B) + d_A(Z, B)$$

where

$$d_A(Z, B) = A_B(B)\,(1.3B\exp(-11B) - 0.01086B + 0.00124Z - 0.01)$$

The corrected ionic A values, $A_{IC}(B) = A_I(B)$-$d_A(Z,B)$, are now compared with Bird and

King's neutral atom A values, $A_B(B)$. Figure 5.8 shows a plot of $(A_{IC}(B) - A_B(B))/A_B(B)$ as a function of B. Again, the circles represent the nega-

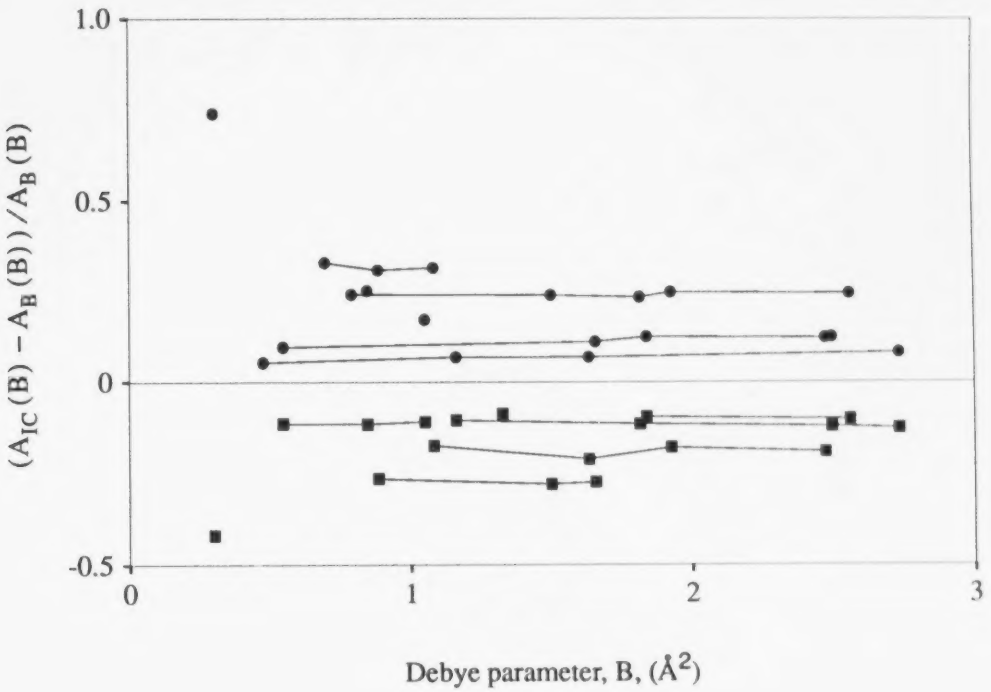

Fig. 5.8. Plot of $(A_{IC}(B) - A_B(B))/A_B(B)$ as a function of Debye parameter. Those points which represent the same atom are connected by lines. The circles represent the negative ions while the squares represent the positive ions.

tive ions, while the positive ions are represented by squares. The lines connect those points which represent the same atom, but at different Debye parameters. It can be seen that $(A_{IC}(B) - A_B(B))/A_B(B)$ is relatively constant for a given atom as B is varied. It is also clear that positive ions tend to have $A_{IC}(B)$ lower than the $A_B(B)$ value for the corresponding neutral atom, while for negative ions, $A_{IC}(B)$ is larger. Figure 5.9 shows a plot of the average value of $(A_{IC}(B) - A_B(B))/A_B(B)$ for each atom, $\langle (A_{IC}(B) - A_B(B))/A_B(B) \rangle$, divided by $-\Delta Z$. It has been found that the relationship between these values and Z is given approximately by the following function:

$$(A_{IC}(B) - A_B(B))/A_B(B)/(-\Delta Z) \cong \frac{1.73}{Z^{0.76}}$$

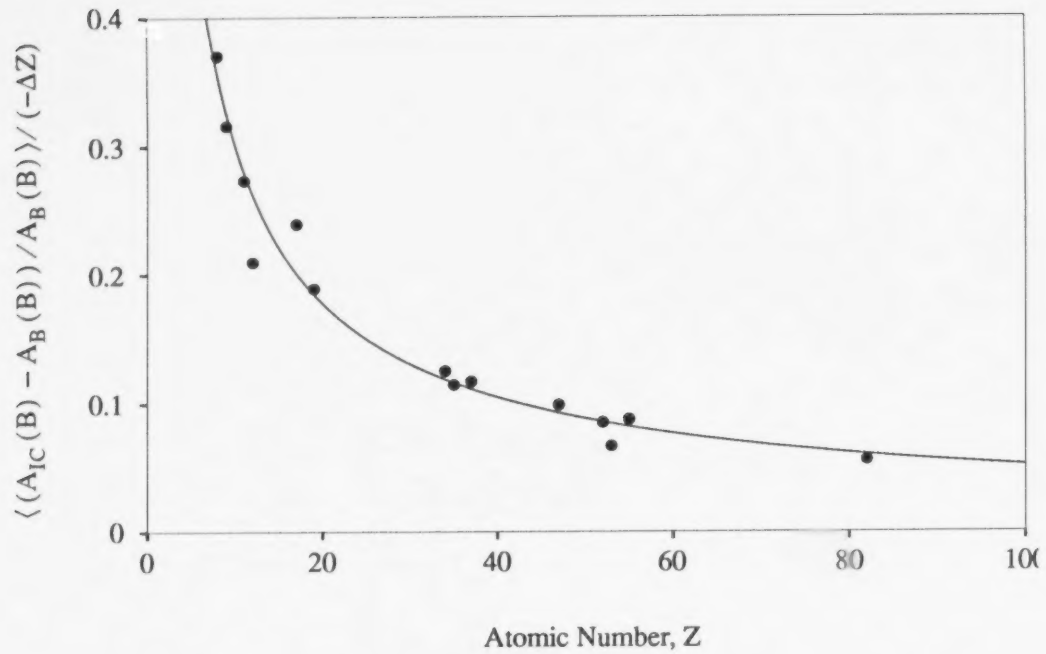

Fig. 5.9. Plot of $\langle (A_{IC}(B) - A_B(B)) / A_B(B) \rangle / (-\Delta Z)$ as a function of atomic number. The line indicates a best fit to these values, given by $1.73/Z^{0.76}$.

Therefore, the following expression for $A_{IC}(B)$ can be obtained:

$$A_{IC}(B) \cong A_B(B) \left(1 - \frac{m_A \Delta Z}{Z^{0.76}}\right) \tag{5.11}$$

where m_A is a factor which depends on Z and ΔZ, but for ions which have not been dealt with by Radi, the following average value, m_{Aav}, can be used:

$$m_{Aav} = 1.73 \tag{5.12}$$

For those ions which were covered by Radi and for which accurate $A_I(B)$ values could be obtained, the best values of m_A can be found in Table 5.5.

Atom	Z	ΔZ	m_A
O	8	-2	1.80
F	9	-1	1.68
Na	11	+1	1.69
Mg	12	+2	1.39
Cl	17	-1	2.06
K	19	+1	1.77
Se	34	-2	1.82
Br	35	-1	1.71
Rb	37	+1	1.82
Ag	47	+1	1.84
Te	52	-2	1.72
I	53	-1	1.37
Cs	55	+1	1.84
Pb	82	+2	1.60

Table 5.5. m_A parameters for common ions.

5.3.6. Agreement With Existing Calculated Values

It is now important to check to see if the preceding procedure for calculating $f_k'(s, B)\exp(-Bs^2)$ for atoms which are ionically bonded in the crystal yields accurate results. Therefore, a comparison of the Radi's values of V_g' with those obtained using the inelastic scattering factors calculated by the method developed in the previous sections should be made for a number of ionic crystals. This will be done in this section.

Because the corrections which were made for Radi's error in integration involve changes to the parameters used in eq. 5.3, $n(B_0)$, $b(B_0)$, and $A(B_0)$, it is not possible to directly correct the V_g' values calculated by Radi, in order to compare them with those generated using the new inelastic scattering factors and eq. 5.5. Instead, those corrections in the calculations of $n(B_0)$, $b(B_0)$, and $A(B_0)$ must be undone in order to make the

resulting inelastic scattering factors comparable to those used by Radi.

Figure 5.10 shows a plot of V_g' as a function of scattering vector, s, for the ionic crystal, NaF. The dots indicate Radi's data for the ionic crystal. The dashed line shows the

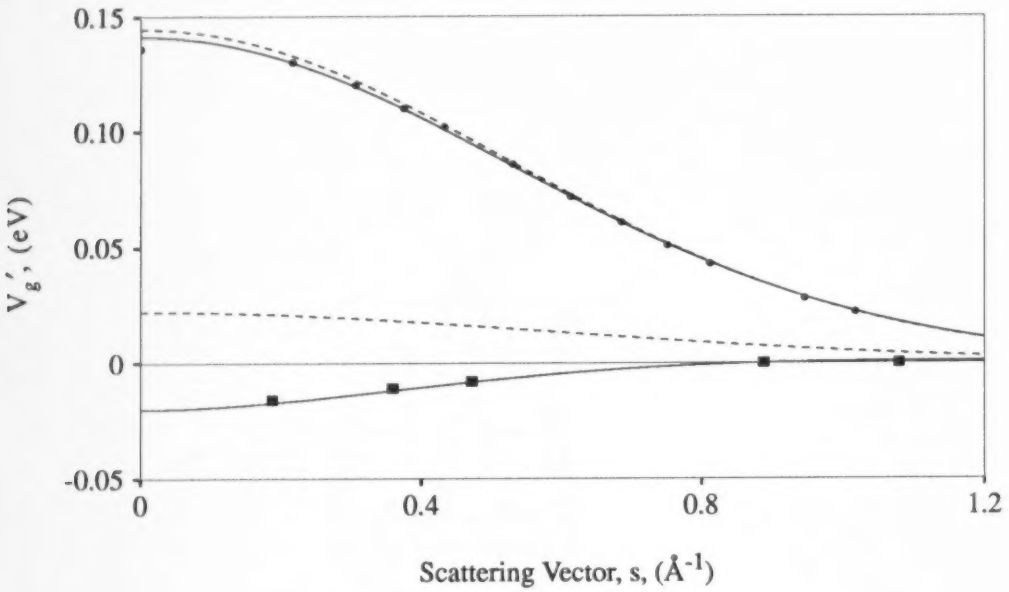

Fig. 5.10. Plot of V_g' as a function of scattering vector, s, for the ionic crystal NaF. The dots indicate Radi's data which assumes ionic bonding. The circles represent scattering vectors for which h,k,l are all even, while the squares are for those which are all odd. The dashed line represents the values obtained using eqs. 5.3 and 5.4 and Tables 5.1 and 5.2 and adjusting for the difference between Radi's and Bird and King's neutral atom results. The solid line indicates the result of accounting for the ionic bonding as outlined above.

result of using eqs. 5.4 and Tables 5.1 and 5.2 to obtain $A_B(B)$, $b_B(B)$, and $n_B(B)$. These parameters were then altered to account for the difference between Radi's and Bird and King's neutral atom data. i.e. the appropriate d(B) value was added to each parameter (whereas, earlier, the appropriate d(B) value was subtracted from the parameters obtained from Radi's ionic crystal data, $A_I(B)$, $b_I(B)$, and $n_I(B)$). These new parameters were then inserted into eq. 5.3 to find the result of using neutral atom data to calculate V_g' (including a reverse correction). The solid line shows the values of $f_k'(s, B)\exp(-Bs^2)$ obtained using the same approach as for the dashed line, but in addition, eqs. 5.7, 5.9, and 5.11, and

the m values in Tables 5.3, 5.4, and 5.5 were used to further alter n(B), b(B), and A(B) respectively before using eq. 5.3 to calculate $f_k'(s, B)\exp(-Bs^2)$. For both the solid lines and the dashed lines, the upper line corresponds to cases where h, k, and l are all even, while the lower line is for h,k,l all odd.

It is important to note that the above procedure does not imply that the d(B) values should be added to the A(B), b(B), and n(B) in practice. This is done here only to compensate for the error made in Radi's calculations of V_g'. In practice, the only alterations which need to be done to the parameters generated by eq. 5.4 is that eqs. 5.7, 5.9, and 5.11 need to be applied with the appropriate m values. The effect of these alterations is represented be the difference between the solid lines and the dashed lines.

It can be seen from Figure 5.10, that the calculated values which have been altered by using eqs. 5.7, 5.0, and 5.11 on the neutral atom parameters (solid lines) are much more accurate than those derived from the neutral atom parameters alone (dashed lines). Figure 5.10 also illustrates an interesting property of the transformation of the A parameter which is brought about by eq. 5.11. For two atoms of similar atomic number, the increase brought about by eq. 5.11 on the A parameter of a negative ion is approximately the same as the resulting decrease in the A parameter of the positive ion. This is especially true for two ions which fall on either side of a noble gas in the periodic table, such as Na and F. The effect of this for crystals which have the rock salt structure is that for reflections which have all even indices, the two effects essentially cancel each other. This can be seen by the similarity of the two upper lines in Fig. 5.10. However, for reflections which have all odd indices, the two effects are additive and the result is that the ionic V_g' is approximately the opposite of that for neutral atoms. In effect, it is as if the two atoms have switched identities. However, this simple situation is not the case for more complex crystal structures. Also, when the two atoms are less similar in size, the effect of ionic bonding is significant for both kinds of reflections.

Figure 5.11 shows a plot of V_g' as a function of s for the ionic crystal, RbF. Once again, the values which result from the procedure developed in the previous sections (solid lines) are much more accurate than those which are derived from the neutral atom parameters alone (dashed lines). In this case, it can be seen that the decrease in the A parameter

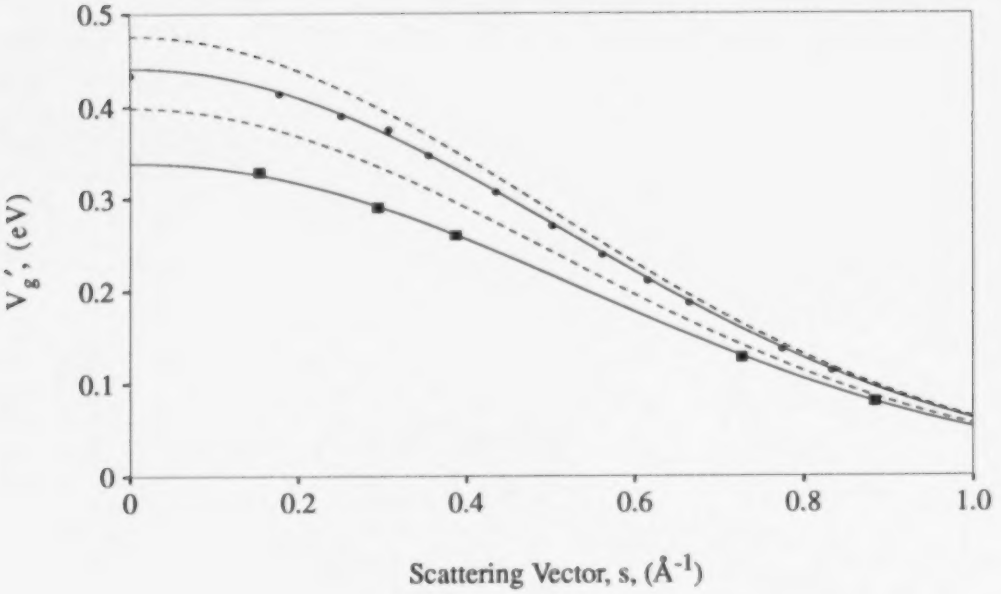

Fig. 5.11. Plot of V_g' as a function of scattering vector, s, for the ionic crystal RbF. The dots indicate Radi's data which assumes ionic bonding. The circles represent scattering vectors for which h,k,l are all even, while the squares are for those which are all odd. The dashed line represents the values obtained using eqs. 5.3 and 5.4 and Tables 5.1 and 5.2 and adjusting for the difference between Radi's and Bird and King's neutral atom results. The solid line indicates the result of accounting for the ionic bonding as outlined above.

of Rb as a result of eq. 5.11 is much larger than the increase in the A parameter of F. Therefore, the V_g' values, for both even and odd indiced reflections, of the ionic crystal are smaller than those which result from the assumption of neutral atoms. Another difference between this plot and Fig. 5.10 is that the m values used in the calculation of the solid line values are the average values given by eqs. 5.8, 5.10, and 5.12, rather than those given in the tables. The agreement is still very good, and it has been found that, in general, the use of the average m values results in very accurate values of V_g', although not quite as good as those resulting from the m values given in Tables 5.3, 5.4, and 5.5.

One final point is worth noting. For positive ions, the A parameter is always decreased from that of the same neutral atom. However, the b parameter of the positive ion is larger than that of the corresponding neutral atom. For negative ions, the situation is

reversed in both cases. The effect of an increase in the b parameter is that the $f_k'(s, B)\exp(-Bs^2)$ values decrease more slowly as s increases. In other words, the larger b value raises the value of $f_k'(s, B)\exp(-Bs^2)$, especially for large values of s. This reduces the effect of the smaller A parameter for positive ions as s increases. The change in n parameters reduces the effect even further for values of s which are less than 1.0. Therefore, for both positive and negative ions, the difference between ionic and neutral atom values tends to decrease as the scattering vector, s, is increased. However, the most important $f_k'(s, B)\exp(-Bs^2)$ values are those with small s values, and those are the values for which the difference between the ionic and neutral atom values is the greatest.

Therefore, it can be seen that the method described in the preceding sections produces much more accurate values of V_g' than those which can be achieved using neutral atom inelastic scattering factors. Also, the necessary transformation from the neutral atom parameters to the ionic parameters is accomplished through the use of a simple formula for each parameter. In the next section, a summary of the procedure will be given for both neutral atoms and ions.

5.4. Summary

It has been found that the inelastic scattering factors for both neutral atoms and ions can be calculated through the use of a simple parametrization. In the case of neutral atoms, the inelastic scattering factor is calculated by first inserting the correct parameters from Tables 5.1 and 5.2 and the correct Debye parameter into eq. 5.4. The A(B), b(B), and n(B) parameters which result from this step are then inserted into eq. 5.3, along with the desired scattering vector, s, to find $f_k'(s, B)\exp(-Bs^2)$.

For ions the procedure is the same, except for one additional step. As in the case of neutral atoms, the first step is to insert the correct parameters from Tables 5.1 and 5.2 and the correct Debye parameter into eq. 5.4 to calculate $A_B(B)$, $b_B(B)$, and $n_B(B)$. These parameters are then modified through the use of eqs. 5.7, 5.9, and 5.11 in the following way. It is necessary to find the correct m parameter for a given ion for use in these equations. If the ion in question is listed in Tables 5.3, 5.4, and 5.5, the appropriate m parameters should be taken from these tables. Otherwise, a good approximation to the correct m parameters can be found in eqs. 5.8, 5.10, and 5.12. Once the best m parameters have been found, they are used, along with $n_B(B)$, $b_B(B)$, and $A_B(B)$, in eqs. 5.7, 5.9, and 5.11, to find $n_{IC}(B)$, $b_{IC}(B)$, and $A_{IC}(B)$, respectively. These new parameters, $n_{IC}(B)$, $b_{IC}(B)$, and $A_{IC}(B)$, are then inserted, along with the desired scattering vector, s, into eq. 5.3. The result of this step is the correct $f_k'(s, B)\exp(-Bs^2)$ value for the ion in question.

6. *Results and Conclusions*

6.1. Determination of Rigid Body Translation Vector

6.1.1. Basic Method of Determination

In this section, the basic method for the determination of the rigid body translation vector of a twin boundary will be demonstrated. In the next section, the effect of slight inaccuracies in the tie point projection which is assumed to describe the crystal orientation will be examined. This section will give an idea of the typical error involved in the determination of the rigid body translation vector by this method.

In order to demonstrate the method for determining the rigid body translation vector, which will be referred to as $\vec{T}$, it is necessary to assume a particular translation vector for the hypothetical twin boundary. Since the twin boundary is hypothetical, the choice of which translation vector will be assumed is completely arbitrary. In this case, it will be assumed that the rigid body translation vector of the twin boundary is equal to [0.5, 0.5, 0]. Also, the calculations will be based on the assumption that the twin boundary lies on the (110) plane of the superconductor, $Y_1Ba_2Cu_3O_{7-\delta}$. Therefore, if the theory presented in Chapter 3 gives accurate results, an experimental image of such a twin boundary in this material would resemble the simulated images which are calculated using these assumptions.

[131] Matrix Zone Axis

The basic method in determining the translation vector is to obtain simulated images for various translation vectors (using eq. 3.23) in an attempt to find images which match the experimental image. For the purposes of demonstrating the method it will be assumed that the experimental image closely resembles a standard image, which is calculated using $\vec{T}$ = [0.5, 0.5, 0]. Figures 6.2, 6.3, and 6.4 show a number of simulated bright field images of the twin boundary, each assuming different values of $\vec{T}$. The diffraction conditions are shown in Fig. 6.1. The matrix zone axis is [131] and the matrix tie point projection is

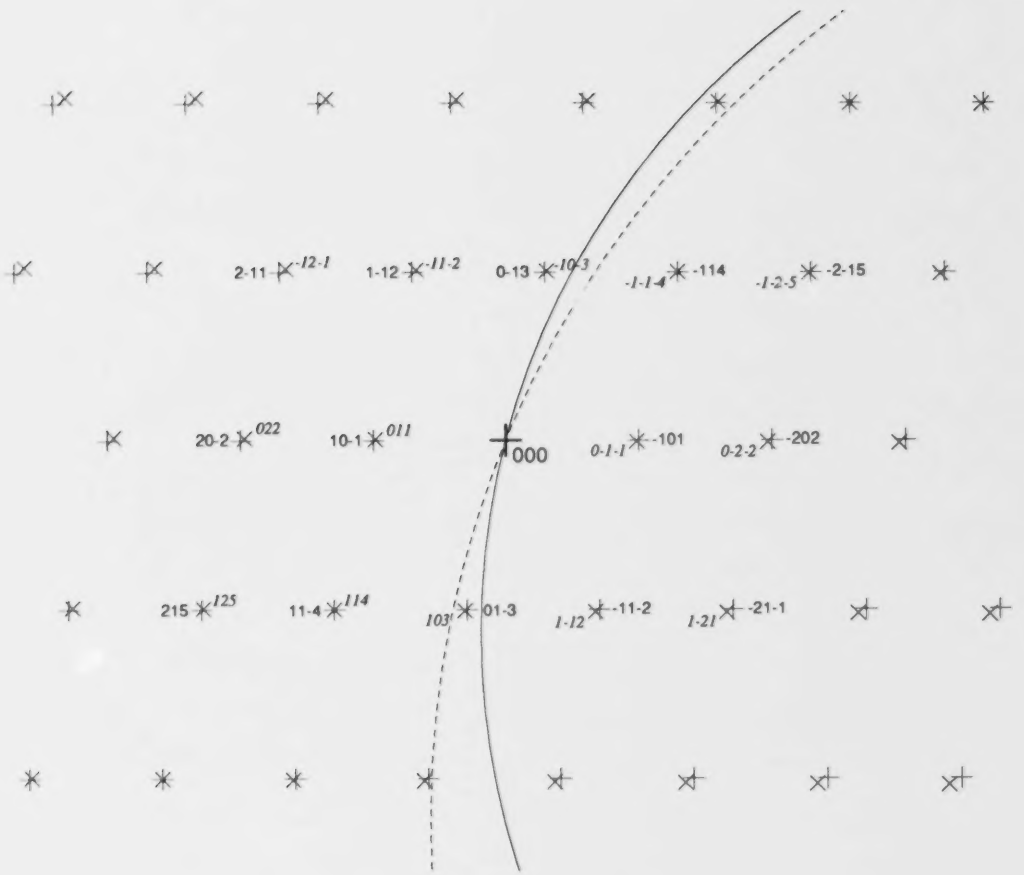

Fig. 6.1. Simulated diffraction pattern from a (110) twin boundary of $Y_1Ba_2Cu_3O_{7-\delta}$. The matrix zone axis is [131] and the twin zone axis is $[31\bar{1}]$. The Miller indices are indicated for some of the reflections in their own coordinate systems. The intersections of the Ewald sphere with the matrix and twin zero order Laue zones are indicated by the solid and dashed lines respectively. The matrix tie point projection is (-6.0 1.13 2.62).

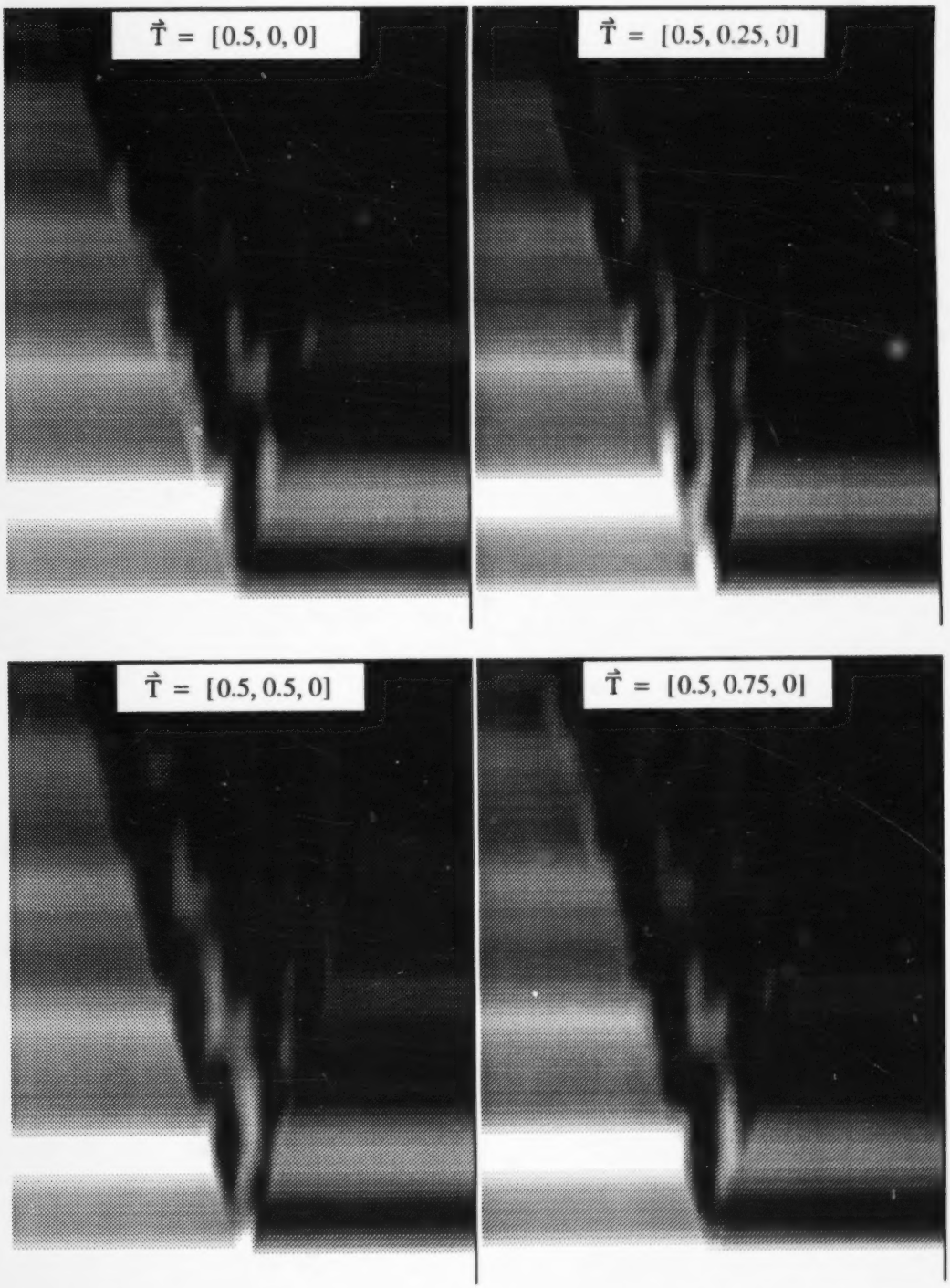

Fig. 6.2. Simulated bright field twin boundary images for a rigid body translation vector ranging from $\vec{T}$ = [0.5, 0, 0] to $\vec{T}$ = [0.5, 0.75, 0]. The matrix zone axis is [131] and the matrix tie point projection is (-6.0 1.13 2.62).

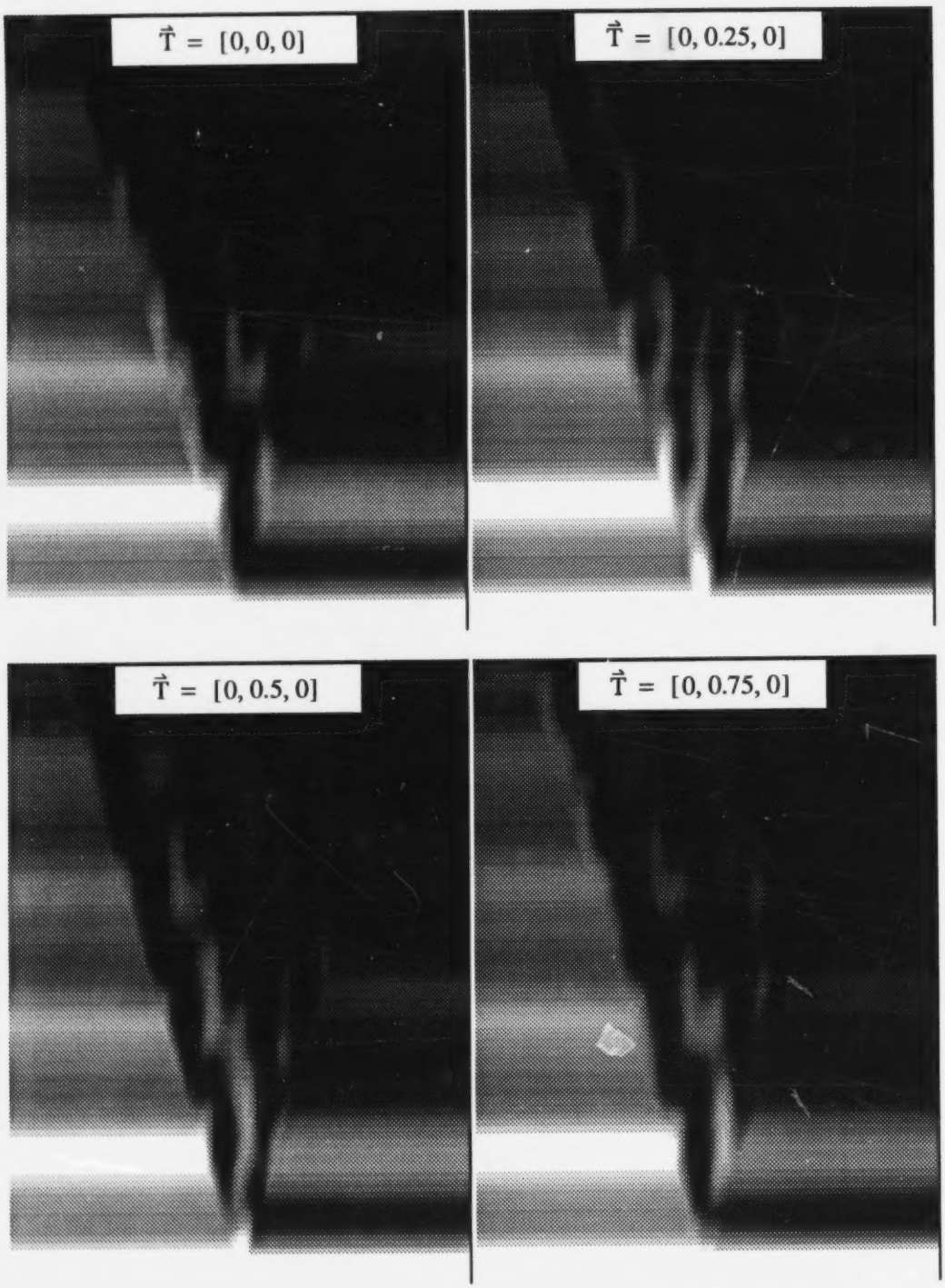

Fig. 6.3. Simulated bright field twin boundary images for a rigid body translation vector ranging from $\vec{T}$ = [0, 0, 0] to $\vec{T}$ = [0, 0.75, 0]. The matrix zone axis is [131] and the matrix tie point projection is (-6 1.13 2.62).

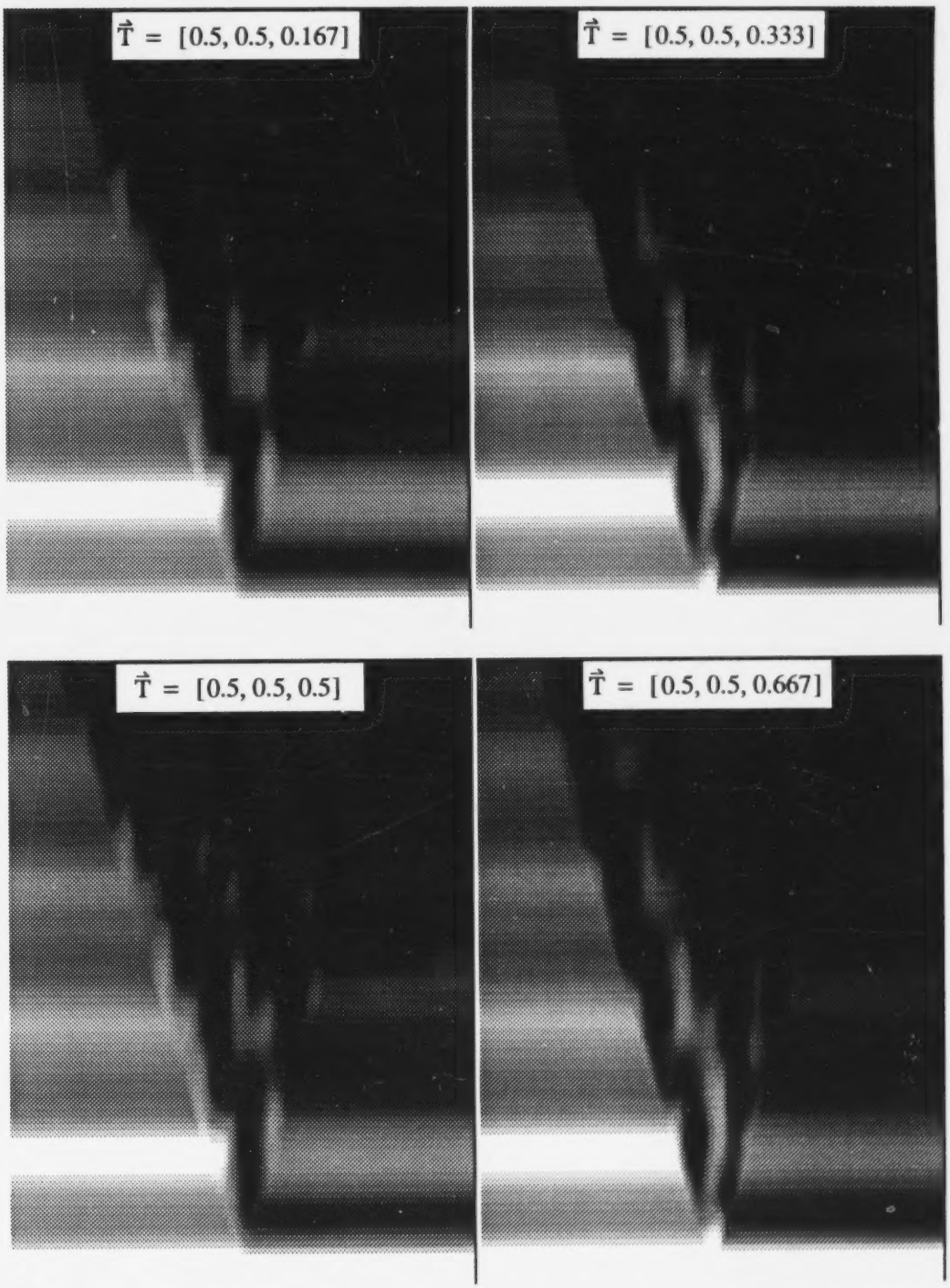

Fig. 6.4. Simulated bright field twin boundary images for a rigid body translation vector ranging from $\vec{T}$ = [0.5, 0.5, 0.167] to $\vec{T}$ = [0.5, 0.5, 0.667]. The matrix zone axis is [131] and the matrix tie point projection is (-6 1.13 2.62).

(-6 1.13 2.62). The major diffracted beams are the matrix reflection, $(01\bar{3})$, and the twin reflection, (103). Fig. 6.2 shows the variation in the simulated image as $\vec{T}$ is varied from [0.5, 0, 0] to [0.5, 0.75, 0]. The lower left image is the standard image with $\vec{T}$ = [0.5, 0.5, 0]. It can be seen that the images change noticeably with each change in $\vec{T}$. Assuming that the experimental image looked like the lower left image in Fig. 6.2, it would be possible, with a good quality experimental image, to reject the other three rigid body translations vectors by comparison with the experimental image. Fig. 6.3 shows the variation in the simulated image contrast for $\vec{T}$ ranging from [0, 0, 0] to [0, 0.75, 0]. Thus, the only difference between the images in this figure and those in Fig. 6.2 is that the first component of $\vec{T}$ has been changed from 0.5 to 0. It can be seen by comparison of Fig. 6.2 and Fig. 6.3 that this change has made almost no difference in the images. In this case, the lower left image, with $\vec{T}$ = [0, 0.5, 0], resembles the standard image. Therefore, [0, 0.5, 0] could be considered as a candidate for the rigid body translation vector of the hypothetical twin boundary. Figures. 6.2 and 6.3 have shown that changing the first component of the rigid body translation vector from 0.5 to 0 has almost no effect on the simulated images. In fact, it has been found that this is true for any value of the first component of $\vec{T}$.

Figure 6.4 shows a series of simulated images of the twin boundary in which the third component of $\vec{T}$ is being varied. In this case, $\vec{T}$ ranges from [0.5, 0.5, 0.167] to [0.5, 0.5, 0.667]. By comparing Fig. 6.4 with the standard image in the lower left corner of Fig. 6.1, it can be seen that a good resemblance is found for $\vec{T}$ = [0.5, 0.5, 0.333] and for $\vec{T}$ = [0.5, 0.5, 0.667]. This is indicative of a fact that was found from the examination of 218 simulated images covering the entire range of possible rigid body translation vectors. It was found that a given simulated image resembles the standard image for any $\vec{T}$ value which satisfies the following relation:

$$\vec{T} \cdot (01\bar{3}) \cong 0.5 + n \qquad (6.1)$$

where n is any integer. The reason for this can be understood by referring to the two beam equations given in sec. 3.4. Although the diffraction conditions in this case are not suitable for a two beam approximation to be used, the two beam equations can give insight into the reason why eq. 6.1 is obeyed. For a bright field image in which the major diffracted beams are not common, the relevant equation is eq. 3.42, which will be rewritten here for

simplicity:

$$I_{0,0} = \left| \Phi_0 \sum_{i_0} \left(C_{0,0}^{(i_0)}\right)^2 \exp\left(2\pi i \gamma^{(i_0)} t_t\right) + \Phi_g \exp\left[2\pi i \left(\vec{g} - \vec{h}\right) \cdot \vec{r}_{ex}\right] \exp\left(2\pi i \vec{h} \cdot \vec{T}\right) \sum_{i_0} C_{g,0}^{(i_g)} C_{g,-h}^{(i_g)} \exp\left(2\pi i \gamma^{(i_g)} t_t\right) \right|^2 \tag{3.42}$$

In this equation, $\vec{g} = (01\bar{3})$ (in matrix coordinates), and $\vec{h} = (103)$ (in twin coordinates). However, all of the calculations must be done in the same coordinate system. In this case, matrix coordinates are used throughout, and hence, the final rigid body translation vector will be given in matrix coordinates. Therefore, in matrix coordinates, $\vec{h} = (0.017 \;\; 1.017 \;\; \bar{3})$. It can be seen from eq. 3.42, that the factor determining contrast due to the rigid body translation vector is $\exp\left(2\pi i \vec{h} \cdot \vec{T}\right)$. Thus, it can be seen that in the two beam situation, any rigid body translation vector that satisfies $\vec{T} \cdot \vec{h} = (0.5, 0.5, 0) \cdot \vec{h} + n = 0.517 + n$, where n is any integer, will give the same diffraction contrast.

This argument can be extended to include all of the reflections in the systematic row (the row of matrix reflections which contains the major diffracted beam, $(01\bar{3})$, and the transmitted beam) in the following way. In the many-beam equivalent to eq.3.42, (eq. 3.22), each matrix reflection gives rise to another term which is similar to the second term in eq. 3.42 and which can affect the image contrast in a way which depends on $\vec{T}$. On the other hand, strong twin reflections do not give rise to more terms. They do affect the first term in eq. 3.42, however, but this term does not depend on $\vec{T}$. In every new term, the twin reciprocal lattice vector, $\vec{h}$, is almost common with the matrix reflection which gives rise to the term. In the case of terms which result from systematic row reflections, these different twin reciprocal lattice vectors will all be multiples of the one, $\vec{h} = (0.017 \;\; 1.017 \;\; \bar{3})$, for the two beam case described above. This is because the systematic row reflections are all multiples of the major diffracted beam (as long as the major diffracted beam is the lowest order reflection in the row).

Thus, for example, the next most important intense reflection for this orientation, $\vec{g} = (0\bar{1}3)$, will give rise to a term which depends on $\exp\left(2\pi i \vec{h}_1 \cdot \vec{T}\right)$, where

$\vec{h}_1 = (\overline{0.017}\ \ \overline{1.017}\ \ 3)$ is the twin reflection which is almost common with $\vec{g}_1 = (0\bar{1}3)$. This term will be the same for any rigid body translation vector that satisfies the following:

$$\vec{T} \cdot \vec{h}_1 = -\vec{T} \cdot \vec{h} = (0.5, 0.5, 0) \cdot \vec{h}_1 + n = -(0.5, 0.5, 0) \cdot \vec{h} + n$$

where n is any integer. By comparing the second and fourth terms in this equation, it can be seen that the condition is identical to the one for the two beam case. As another example, the matrix reflection, $\vec{g} = (02\bar{6})$ will give rise to a term which is always the same as it is for $\vec{T} = (0.5, 0.5, 0)$ when the following condition is met:

$$\vec{T} \cdot 2\vec{h} = 2(\vec{T} \cdot \vec{h}) = (0.5, 0.5, 0) \cdot 2\vec{h} + m = 2\left[(0.5, 0.5, 0) \cdot \vec{h} + \frac{m}{2}\right]$$

where m is an integer. Again, by comparing the second and fourth terms in this equation, it can be seen that this condition will be met whenever $\vec{T} \cdot \vec{h} = (0.5, 0.5, 0) \cdot \vec{h} + n$, since the two cases are the same when m is an even integer. Thus, the term caused by this matrix reflection will always give the same value when the condition for the two beam case is met. It can also be seen that there will also be other rigid body translations which give the same value for this term, but for these values of $\vec{T}$, the terms in the equation which are due to the two most important matrix reflections, which were discussed above, will be completely different from the case where $\vec{T} = (0.5, 0.5, 0)$.

Therefore, as long as the most important matrix reflections all lie in the same systematic row, one experimental image can give the component of $\vec{T}$ which lies in the direction of the systematic row. One way of estimating the importance of a particular reflection is by the intensity of that reflection in the diffraction pattern. The intensities of the eight most intense matrix reflections for the crystal orientation assumed here are shown in Table 4.2. It can be seen that for this orientation, there are significant non-systematic reflections, but the majority of the most intense reflections are in the systematic row. As a result, this orientation has given the component of $\vec{T}$ which lies in the direction of $(01\bar{3})$.

In the case of $Y_1Ba_2Cu_3O_{7-\delta}$, it has been found that for most zone axes, there is always one row of reflections which has much higher structure factors than most other reflections. Therefore, it is usually possible to find an orientation where the reflections of this row are much more important than any other reflections. Conversely, it is usually difficult to find an orientation for which the reflections of a different row are much more intense

than those which are not in that row without going to a new zone axis. Thus, ideally, images should be taken from three different orientations, with three different zone axes, and three non-coplanar systematic rows of important reflections, in order to completely determine the translation vector.

It should be noted that although the explanation above made use of the two beam equation of intensity, this does not imply that a two beam calculation would be sufficient to accurately simulate the twin boundary image for use in comparison with an experimental image. Figure 6.5 shows two simulated images for the same diffraction conditions as the previous three figures, but taking different numbers of reflections into account. In Figs. 6.2, 6.3, and 6.4, the 17 most intense reflections were taken into account in the calculations. The image on the left of Fig. 6.5 was calculated using only two beams, the transmitted beam, and the most intense diffracted matrix reflection, $\vec{g} = (01\bar{3})$. Along with these went the twin and combination reflections, $\vec{h} = (103)$ and $\vec{g} - \vec{h}$, respectively. The image on the right was calculated taking into account the six most intense systematic row reflections. In both cases the assumed translation vector was $\vec{T} = [0.5, 0.5, 0]$, as in the standard image shown in the bottom left hand corner of Fig. 6.2. It can be seen that the two beam image is quite different from the standard image. On the other hand, the image calculated using the six most intense systematic row reflections is fairly similar to the standard image and demonstrates how dominant the systematic row of reflections is for this orientation.

The effects of using dark field images rather than bright field images will now be examined. Figure 6.6 shows a series of dark field images for the diffraction conditions shown in Fig. 6.1, with the objective aperture centered around the $(01\bar{3})$ matrix reflection. The rigid body translation vector varies from [0.5, 0, 0] to [0.5, 0.75, 0]. It can be seen from these images that there is a slight variation in the images as $\vec{T}$ is changed. However, the variation is not nearly as great, and the uncertainty in $\vec{T}$ would be far greater if dark field images were used instead of bright field. Still, the condition, expressed by eq. 6.1, for a given bright field image to resemble the image for which $\vec{T} = [0.5, 0.5, 0]$, also holds for dark field images. Thus, in principle, this dark field image can also give the component of $\vec{T}$ in the direction of $(01\bar{3})$. The principles behind this are the same as in the bright field case described above.

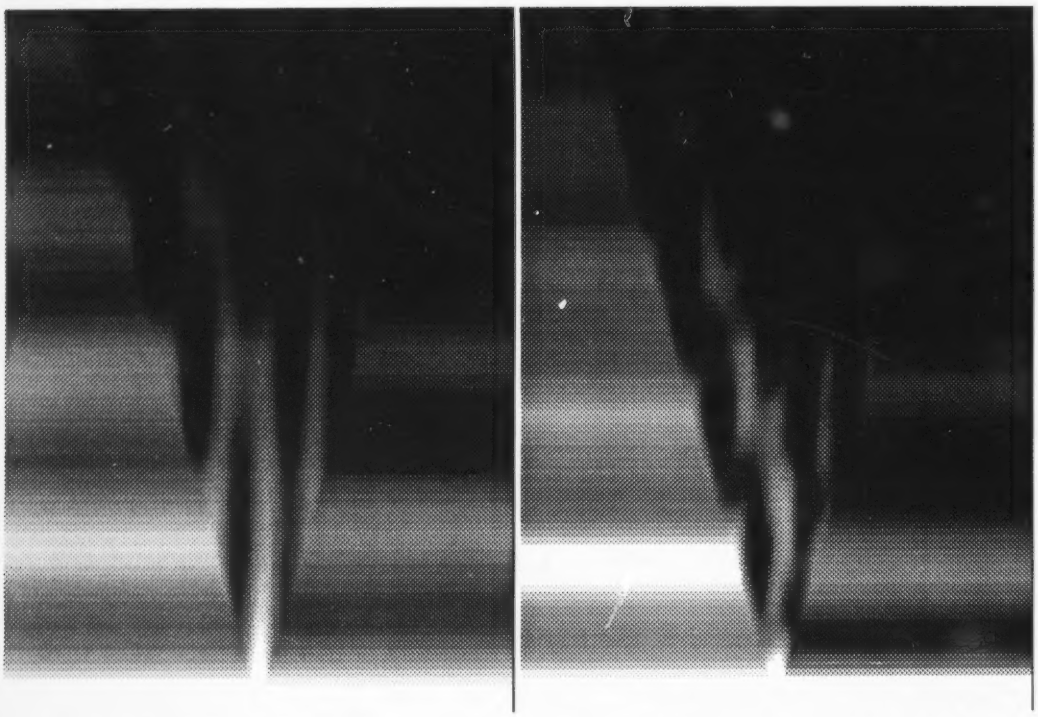

2 Beam Calculation 6 Beam Systematic Row Calculation

Fig. 6.5. Simulated bright field twin boundary images for a rigid body translation vector of $\vec{T}$ = [0.5, 0.5, 0]. The matrix zone axis is [131] and the matrix tie point projection is (-6 1.13 2.62). The image on the left is a result of a two beam calculation, while the image on the right takes into account the six most intense reflections in the systematic row.

[101] Matrix Zone Axis

It is now necessary to investigate another orientation in order to determine the component of the rigid body translation vector in the direction of a different systematic row of reflections. Figure 6.7 shows the diffraction conditions which will be assumed for the following simulations. In this case the matrix zone axis is [101] and the twin zone axis is $[01\bar{1}]$. The matrix tie point projection is (-2.2 0.8 2.2). The most intense matrix reflection in this diffraction pattern is (010), which is in its Bragg condition. The next two most intense reflections (as calculated by eq. 4.32 or eq. 4.33) are (020) and $(0\bar{1}0)$. Thus, again, the most intense reflections belong to the systematic row, and hence, it would be expected

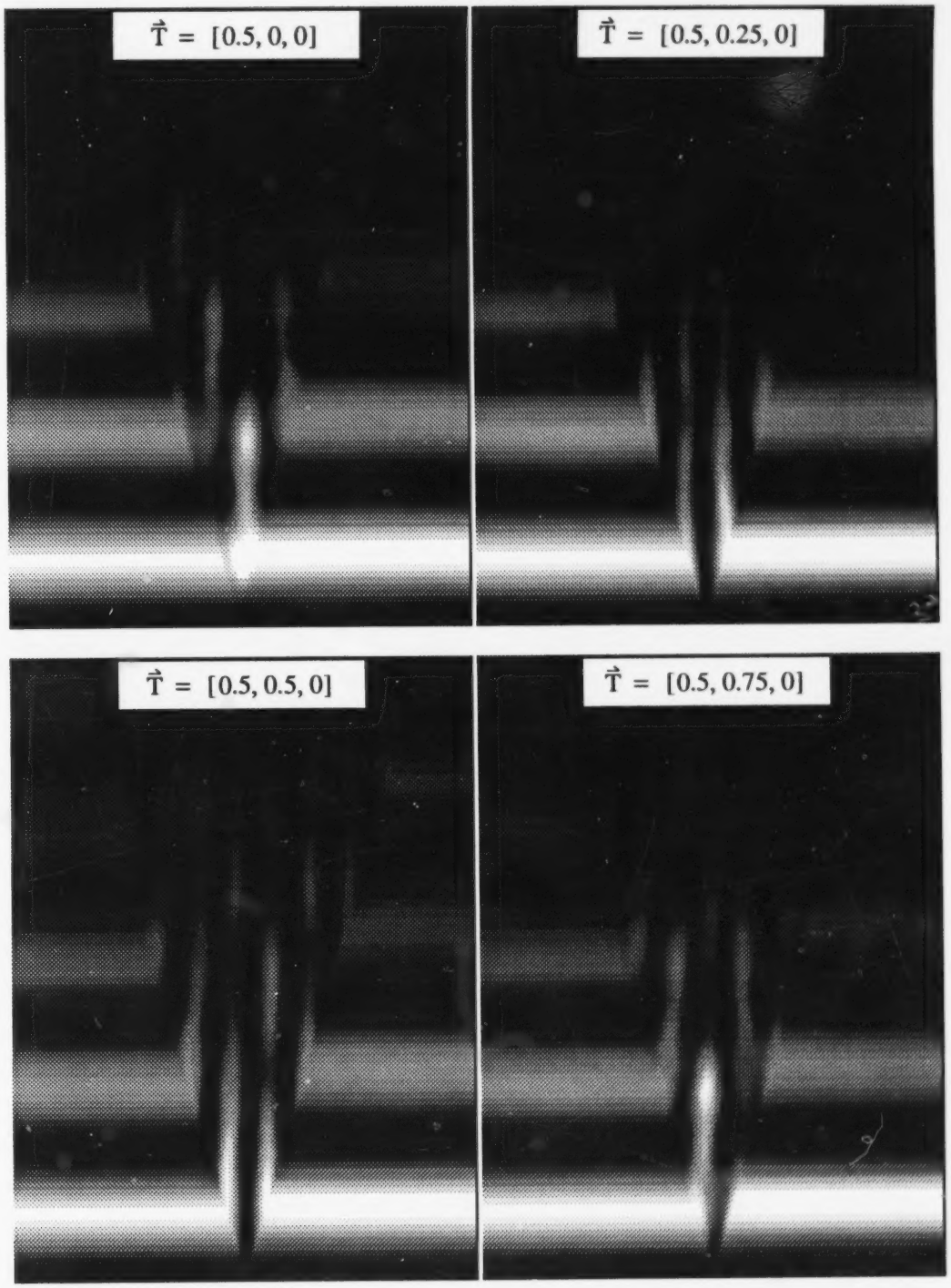

Fig. 6.6. Simulated dark field twin boundary images for a rigid body translation vector ranging from $\vec{T}$ = [0.5, 0, 0] to $\vec{T}$ = [0.5, 0.75, 0]. The matrix zone axis is [131] and the matrix tie point projection is (-6.0 1.13 2.62).

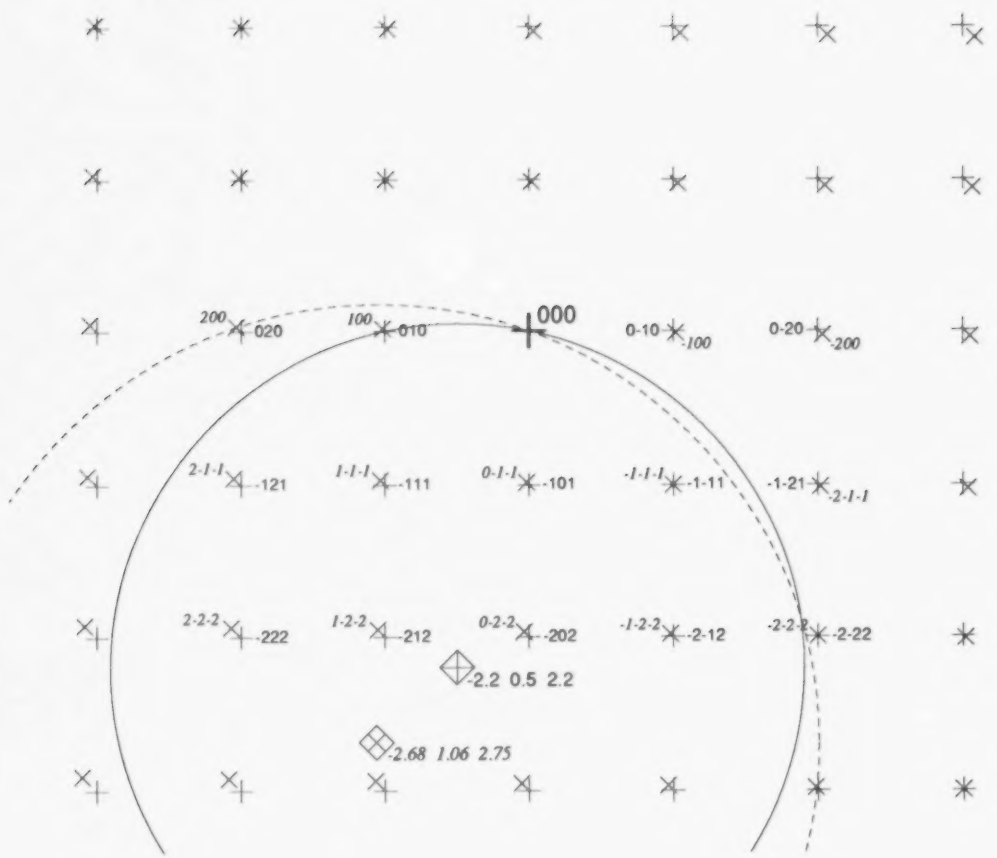

Fig. 6.7. Simulated diffraction pattern from a (110) twin boundary of $Y_1Ba_2Cu_3O_{7-\delta}$. The matrix zone axis is [101] and the twin zone axis is $[01\bar{1}]$. The Miller indices are indicated for some of the reflections in their own coordinate systems. The intersections of the Ewald sphere with the matrix and twin zero order Laue zones are indicated by the solid and dashed lines respectively. The matrix tie point projection is (-2.2 0.5 2.2).

that this orientation would give the component of $\vec{T}$ in the direction of (010).

Figure 6.8 shows a series of simulated images for these diffraction conditions, for a range of rigid body translations from [0.5, 0, 0] to [0.5, 0.75, 0]. It was found that changing the first and third components in $\vec{T}$ had no effect on the image contrast, as expected. It can be seen that there is a definite variation in the twin boundary contrast as the second component of $\vec{T}$ is varied. However, these images do not exhibit the regular set of fringes which usually characterize a twin boundary image, and, as a result, they can be confusing to look at in order to find differences between the images. This leads to an alternate way of comparing images. Instead of comparing two dimensional images which contain information for a large range of different thicknesses, it is possible to compare one dimensional plots of intensity for a given crystal thickness. The experimental plot can be obtained by running a microdensitometer across a twin boundary image for a constant thickness. Thus, for example, a microdensitometer could be run along the a line in the experimental image which corresponds with the white line shown in the simulated standard image in Figure 6.9 (b). This line corresponds to a total crystal thickness of 600 Å. The plot generated in this way could be compared with simulated plots for the same thickness and for a range of rigid body translation vectors.

Figure 6.9 (a) shows three such plots for translation vectors, $\vec{T}$, ranging from [0.5, 0.25, 0] to [0.5, 0.75, 0]. It can be seen from this figure that the variation in intensity profile as a function of $\vec{T}$ can be unmistakeable in such a one dimensional plot. Care must be taken, however, to insure that the microdensitometer trace comes from a line with the correct thickness.

The situation for the dark field images is more straightforward to analyse. Figure 6.10 shows a series of dark field images for $\vec{T}$ ranging from [0.5, 0, 0] to [0.5, 0.75, 0]. The diffraction conditions are the same as are shown in Fig. 6.7, and the objective aperture is centered around the (010) matrix reflection. This set of images shows that the variation in image contrast as a function of $\vec{T}$ is quite large in this case. Therefore, from these images, and others that were also analysed, it can be determined that $\vec{T}$ must satisfy the following

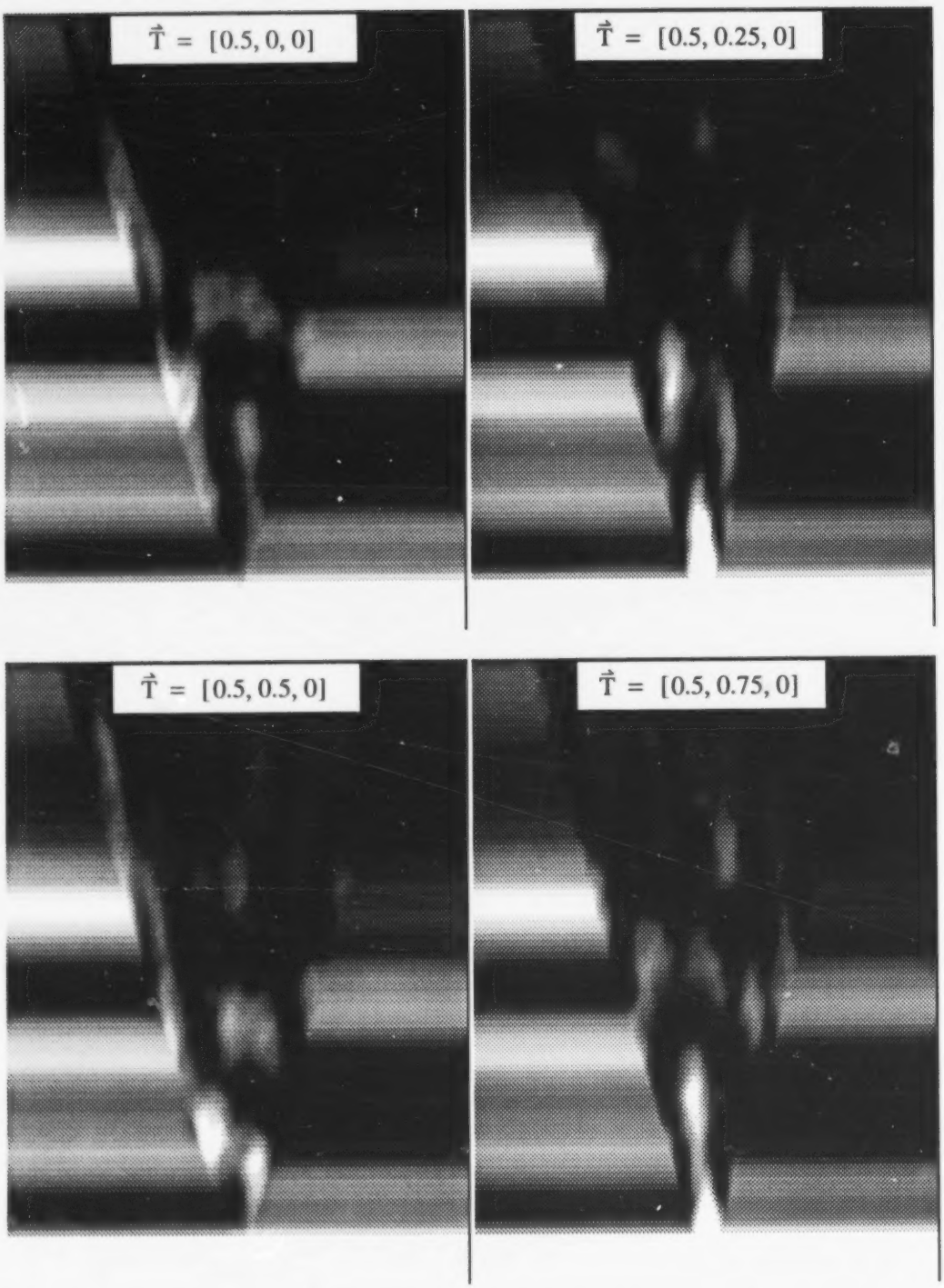

Fig. 6.8. Simulated bright field twin boundary images for a rigid body translation vector ranging from $\vec{T}$ = [0.5, 0, 0] to $\vec{T}$ = [0.5, 0.75, 0]. The matrix zone axis is [131] and the matrix tie point projection is (-2.2 0.5 2.2).

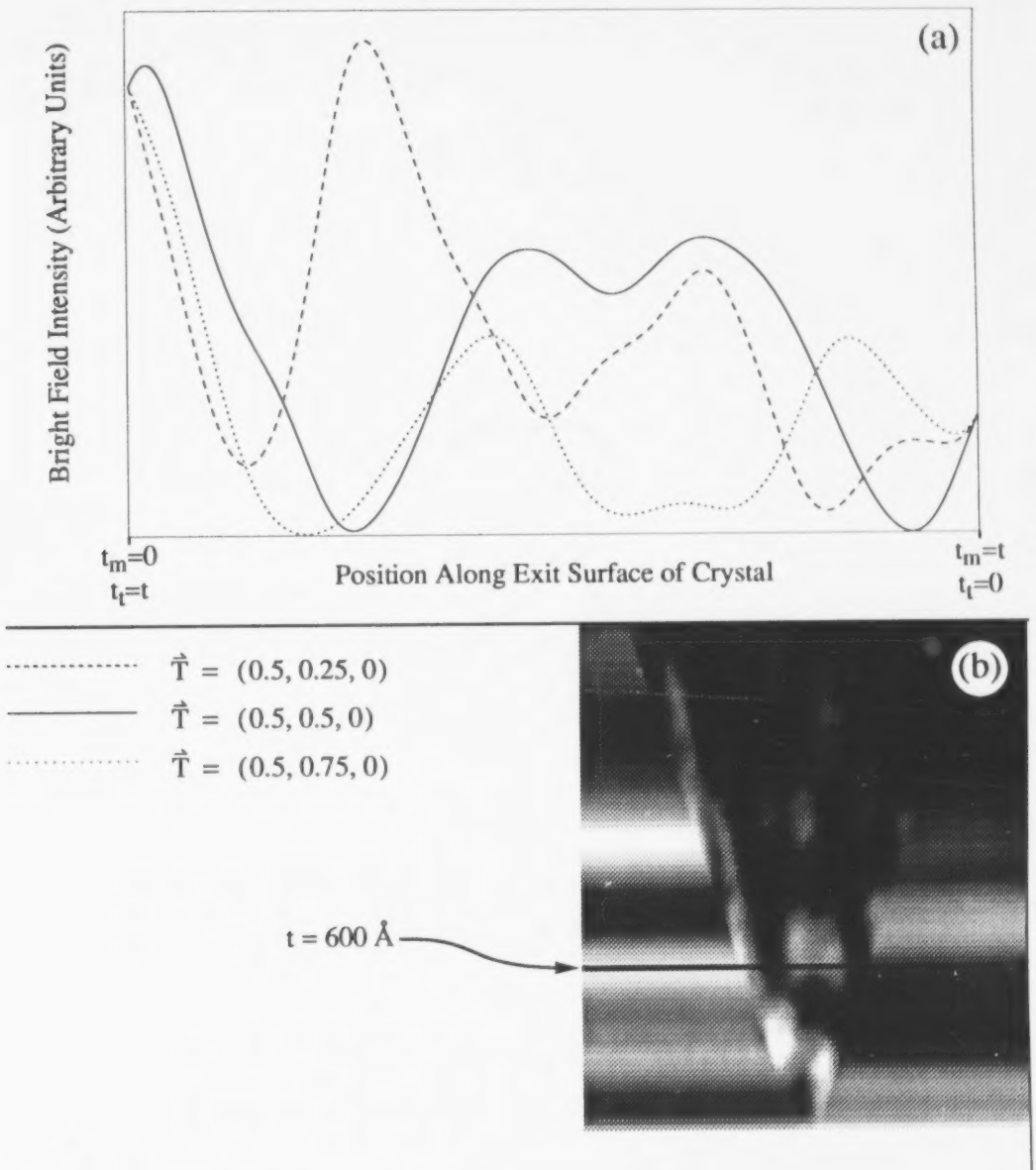

Fig. 6.9. (a) One dimensional plot of bright field intensity as a function of distance along the exit surface of the crystal for a constant total crystal thickness, t, of 600 Å. The rigid body translation vector ranges from $\vec{T}$ = [0.5, 0.25, 0] to $\vec{T}$ = [0.5, 0.75, 0]. The matrix zone axis is [131] and the matrix tie point projection is (-2.2 0.5 2.2).
(b) Two dimensional simulated bright field image for the same orientation as in (a) and a rigid body translation vector of $\vec{T}$ = [0.5, 0.5, 0]. The white line indicates a total crystal thickness of 600 Å.

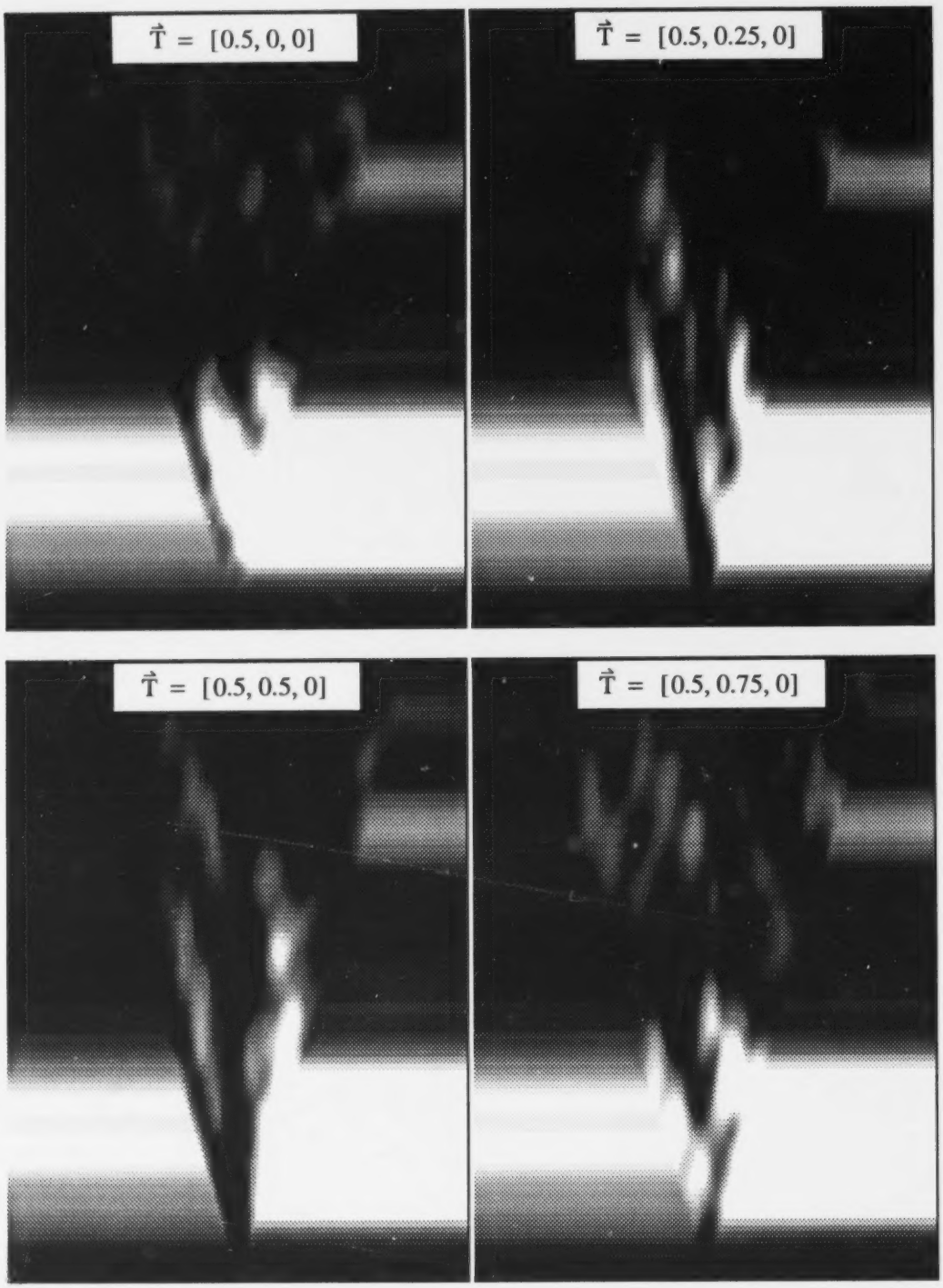

Fig. 6.10. Simulated dark field twin boundary images for a rigid body translation vector ranging from $\vec{T}$ = [0.5, 0, 0] to $\vec{T}$ = [0.5, 0.75, 0]. The matrix zone axis is [101] and the matrix tie point projection is (-2.2 0.5 2.2).

condition:

$$\vec{T} \cdot (010) = T_2 = 0.5 + n$$

However, it is natural impose the further condition that no component of $\vec{T}$ can be larger than one or less than zero, and therefore, $T_2 = 0.5$.

[211] Matrix Zone Axis

The last orientation which will be used demonstrates that it is important to select a systematic row of reflections which has large structure factors. The matrix zone axis for this orientation is [211]. The diffraction pattern for this orientation is shown in Figure 6.11. The matrix tie point projection is (0.9 2.67 -0.87). It can be seen from the figure, that the $(\bar{1}02)$ reflection is in its Bragg condition. Thus, it might be assumed that the important systematic row is the one which contains this reflection. This is not the case, however.

Figures 6.12 and 6.13 show a series of simulated twin boundary images for the orientation given in Fig. 6.11. In Fig. 6.12, the rigid body translation vector is varied from [0.5, 0, 0] to [0.5, 0.75, 0], while in Fig. 6.13, $\vec{T}$ ranges from [0.3, 0.7, 0] to [0.3, 0.7, 0.5]. The standard image is shown in the bottom left hand corner of Fig. 6.12. These figures illustrate a fact which has been confirmed through the examination of many more simulated images for this orientation. That is that the images which closely resemble the standard image all have rigid body translation vectors given by:

$$\vec{T} \cdot (11\bar{3}) = n$$

Thus, it would seem that the dominant systematic row in this case is the $(11\bar{3})$ row. Although it is not necessary to know this before doing the comparison of theoretical and experimental images, it is helpful in indicating what to look for. Also, if the dominant row is known beforehand, an orientation can be chosen for which it is as dominant as possible. This makes the later interpretation of results clearer. Thus, it would be useful to know why the $(11\bar{3})$ row is dominant in this case. The first thing to note is that the $(11\bar{3})$ row of reflections have larger structure factors than the $(\bar{1}02)$ row of reflections. Nevertheless, $(\bar{1}02)$ is still the most intense reflection in the diffraction pattern. There is another element, however, which contributes to the relative importance of a given reflection. Up until now, only the intensity of the matrix reflections, $\vec{g}$, have been considered. However,

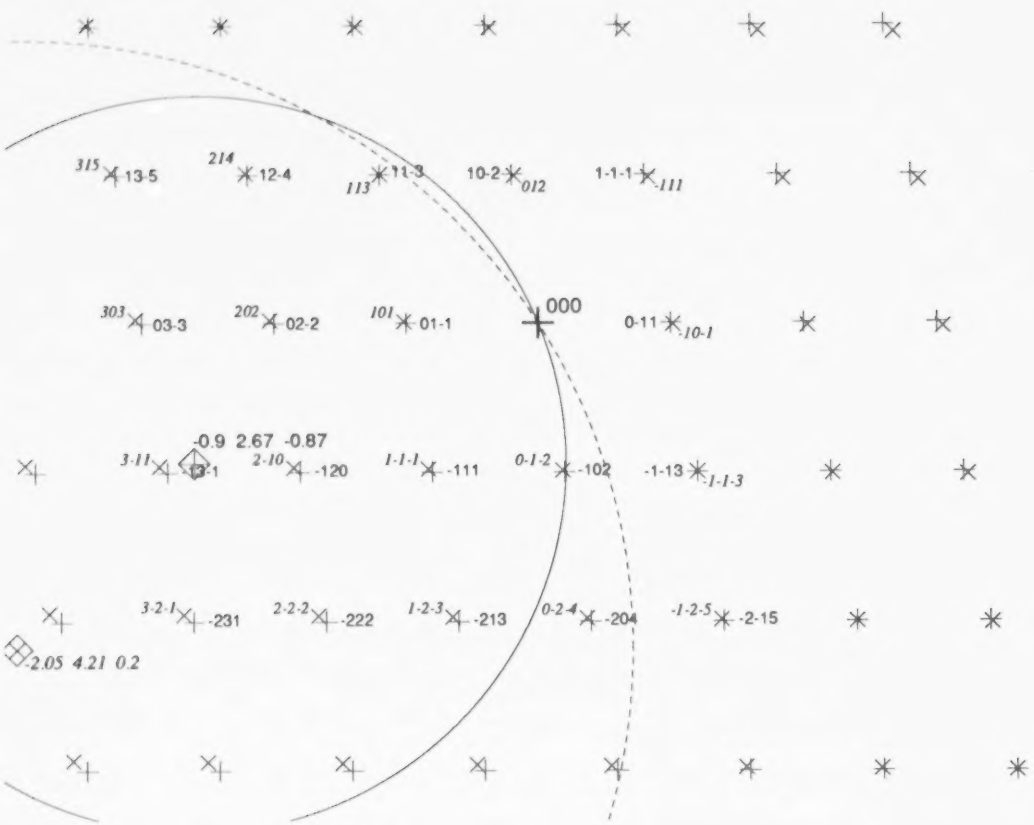

hkl matrix reflection

hkl twin reflection

matrix tie point projection

twin tie point projection

Fig. 6.11. Simulated diffraction pattern from a (110) twin boundary of $Y_1Ba_2Cu_3O_{7-\delta}$. The matrix zone axis is [211] and the twin zone axis is $[12\bar{1}]$. The Miller indices are indicated for some of the reflections in their own coordinate systems. The intersections of the Ewald sphere with the matrix and twin zero order Laue zones are indicated by the solid and dashed lines respectively. The matrix tie point projection is (-0.9 2.67 -0.87).

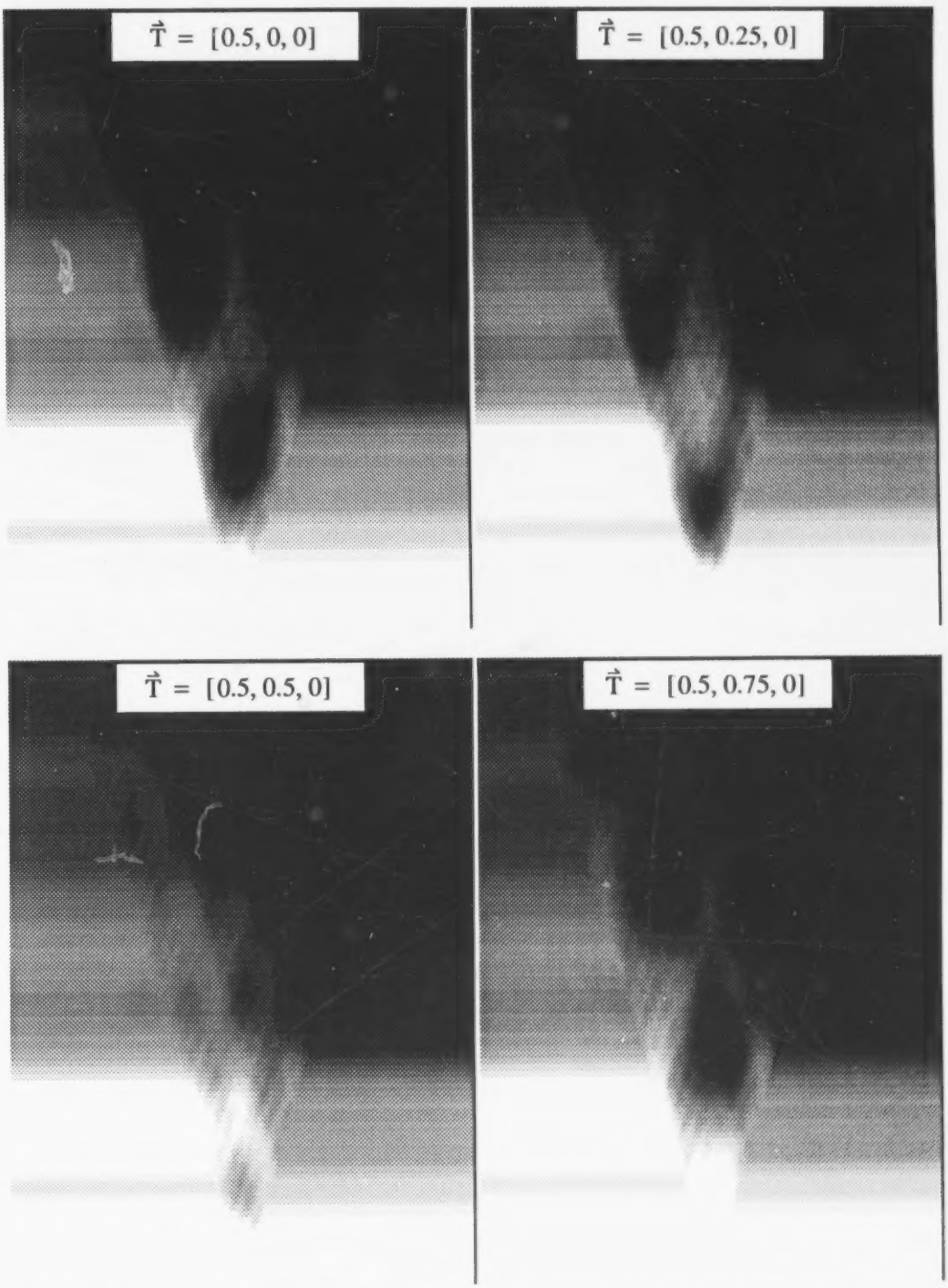

Fig. 6.12. Simulated bright field twin boundary images for a rigid body translation vector ranging from $\vec{T}$ = [0.5, 0, 0] to $\vec{T}$ = [0.5, 0.75 ,0]. The matrix zone axis is [211] and the matrix tie point projection is (-0.9 2.67 -0.87).

Fig. 6.13. Simulated bright field twin boundary images for a rigid body translation vector ranging from $\vec{T}$ = [0.3, 0.7, 0] to $\vec{T}$ = [0.3, 0.7, 0.5]. The matrix zone axis is [211] and the matrix tie point projection is (-0.9 2.67 -0.87).

what is really important is the intensity of the combination reflections, $\vec{g}+\vec{h}$, which are derived from the matrix reflections. One component in this intensity is the intensity of the originating matrix reflection and this is what has been used for previous orientations. However, there are other factors, one of which depends on the deviation parameter of $\vec{g}+\vec{h}$ as compared to the deviation parameters of the other reflections which pass through the aperture. Because the $(11\bar{3})$ row of reflections is common, the combination reflections $\vec{g}+\vec{h}$, which are closest to the origin, and which will pass through the objective aperture to contribute to a bright field image, are, in fact, common with the transmitted beam. Therefore, their deviation parameters are exactly zero, and they will tend to be more intense than the other combination reflections, such as the one originating from the $(\bar{1}02)$ reflection, which pass through the objective aperture. Therefore, there is a tendency of the row of common reflections to be the dominant row of reflections for bright field images, although this is not always the case, as was seen in the previous two orientations. Another component to the intensity of $\vec{g}+\vec{h}$ is the structure factor of $\vec{h}$. For the matrix reflection, $(11\bar{3})$, $\vec{h} = (\bar{1}\bar{1}\bar{3})$, whereas for the matrix reflection, $(\bar{1}02)$, $\vec{h} = (012)$. Of these two reflections, $\vec{h} = (\bar{1}\bar{1}\bar{3})$ has the larger structure factor. As a result of these two factors, the $(11\bar{3})$ systematic row is dominant for this orientation.

Thus, it can be seen from the images that despite the fact that there is a very intense non-systematic row reflection, the images still look very similar for any translation vector which has the same component in the direction of the systematic row.

In the dark field images, the situation is much the same. Figure 6.14 shows a series of dark field images for the diffraction conditions shown in Fig. 6.11, with the objective aperture centered around the $(11\bar{3})$ matrix reflection. The rigid body translation vectors vary between [0.5, 0, 0] and [0.5, 0.75, 0]. Again, it can be seen that there is a definite dependence of the image on the rigid body translation vector, and again, the dependence is the same for the dark field case as it was for the bright field case. It can be seen that for $\vec{T} = [0.5, 0.5, 0]$, the image of the twin boundary almost disappears. This is because the systematic row of reflections is common, and therefore, there is no interference between the waves travelling in the directions of the matrix and twin reflections since these directions are the same. Also, the term involving $\vec{T}$, $\exp(2\pi i\vec{h}\cdot\vec{T})$, is the same for

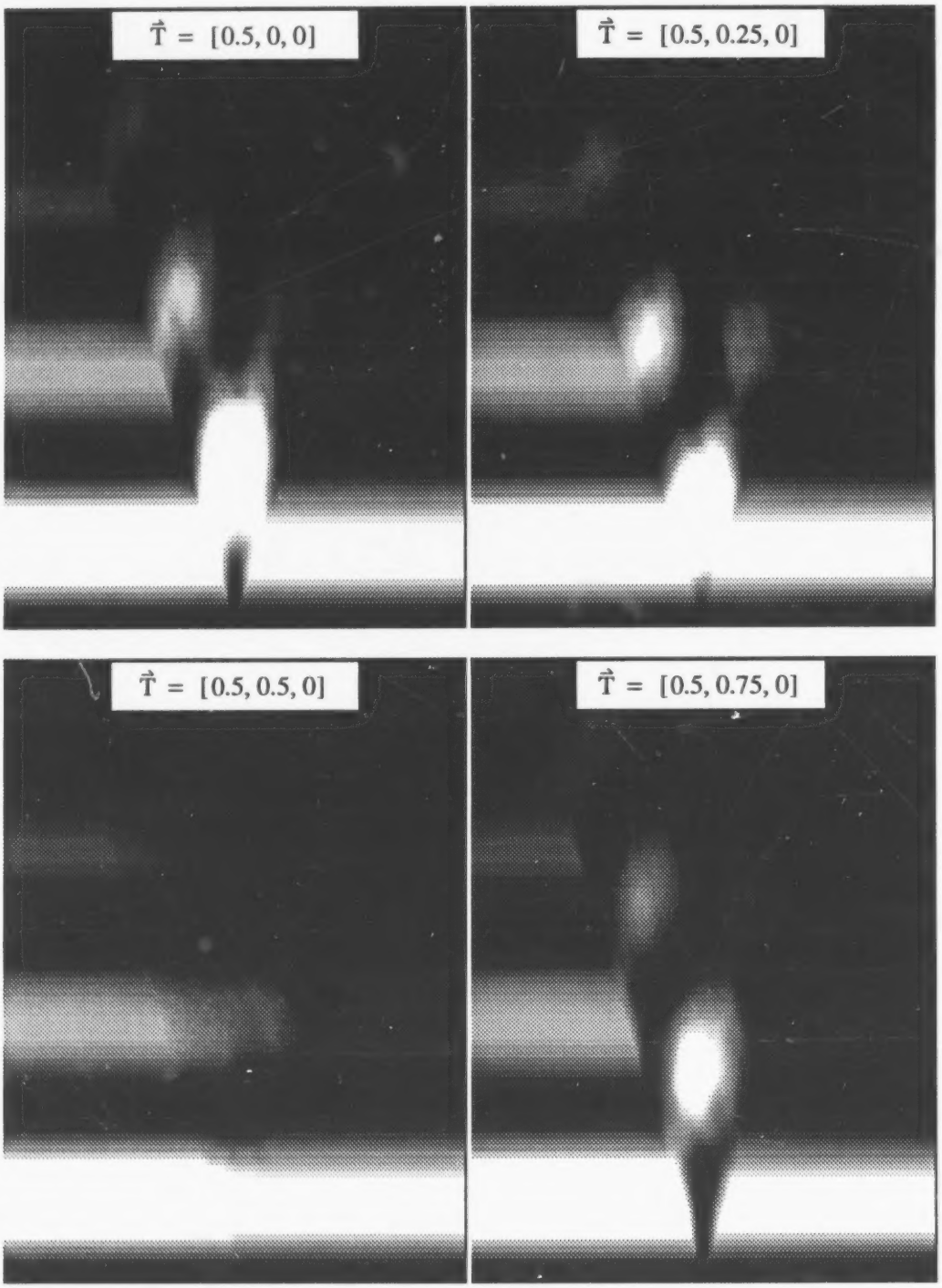

Fig. 6.14. Simulated dark field twin boundary images for a rigid body translation vector ranging from $\vec{T}$ = [0.5, 0, 0] to $\vec{T}$ = [0.5, 0.75, 0]. The matrix zone axis is [211] and the matrix tie point projection is (-0.9 2.67 -0.87).

$\vec{T} = [0.5, 0.5, 0]$ as it is for no translation vector at all since $\vec{h}$ is a multiple of $(\bar{1}\bar{1}\bar{3})$ for all terms which are derived from matrix reflections in the systematic row. Thus, it is as if there were no translation vector at the boundary, and no orientation difference (since the matrix and twin reflections are travelling in the same directions), and hence, no boundary at all. The boundary is still slightly visible, however, because of the presence of non-systematic reflections.

Summary

The components of $\vec{T}$ in the directions of three non-colinear systematic rows of reflections have now been investigated. Thus, it might be thought that the rigid body translations vector has been completely defined. This is not the case because for each orientation, the equation defining which values of $\vec{T}$ give the correct image contrast involves an unknown integer, n. Therefore, from the preceding work, the following set of equations has been obtained:

$$\begin{aligned} T_2 - 3T_3 &= n_1 + 0.5 \\ T_2 &= 0.5 \\ T_1 + T_2 - 3T_3 &= n_3 \end{aligned} \qquad (6.2)$$

where T_1, T_2, and T_3 are the components of $\vec{T}$ in matrix coordinates. By subtracting the first equation from the third, it can be found that T_1=0.5. However, by substituting these values into the first and third equations, it can only be determined that $T_3 = n/3$, where n can be any integer. Thus, T_3 could be 0 or 1/3 or 2/3, and another orientation must be investigated. For this case, an orientation should be chosen such that if the (hk*l*) systematic row is dominant, l =1 or 2. This will not be demonstrated here, but the procedure would be identical to what has been done in the previous three orientations. One more point is worth noting here. That is that the lower the indices, h, k, and *l*, of the lowest order reflection in the systematic row, the less ambiguity there will be in the results. In the case which was studied here, there were three possibilities for T_3 because *l* was three in both the first and the third orientations. The fourth orientation would not have been necessary if either *l* had been different for the first and third orientations, or if *l* had been one in both cases.

6.1.2. Effects of Inaccurate Tie Point Projections

In this section, the effects of slight inaccuracies in the assumed tie point projections will be investigated. This will be done by redoing the work of the previous section, but assuming a different tie point projection. For the first zone axis, [131], an orientation will be chosen such that the deviation parameters of the systematic row of reflections are approximately correct, but that those of the non-systematic reflections are inaccurate. This will give some insight as to the importance of non-systematic reflections. For the next two zone axes, orientations will be chosen for which the deviation parameters of the systematic row reflections are inaccurate as well.

[131] Matrix Zone Axis

Figure 6.15 shows the diffraction pattern for the orientation chosen for the first zone axis, (113). It can be seen by comparing this diffraction pattern with the one shown in Fig. 6.1, that the $(01\bar{3})$ matrix reflection and the (103) twin reflection are again close to their Bragg conditions, and the $(01\bar{3})$ matrix reflection is still the most intense matrix reflection. The tie point projection has changed considerably, however. In this case, it is (-4 0.79 1.63), whereas in Fig. 6.1, it is (-6 1.13 2.62). Figure 6.16 shows the simulated images which result from the assumption of this tie point projection for $\vec{T}$ ranging from [0.5, 0, 0] to [0.5, 0.75, 0]. It can be seen from a comparison of Fig. 6.16, and 6.2, that the changes in the images brought about by the different tie point projections is detectable, but not significant. If the tie point projection was assumed to be (-4 0.79 1.63), while the actual tie point projection was (-6.0 1.13 2.62), this would not result in an inaccurate determination of the component of $\vec{T}$ in the direction of the $(01\bar{3})$ matrix reflection. This shows that as long as all of the relatively intense matrix reflections in the experimental diffraction pattern have approximately correct theoretical intensities for the assumed tie point projection, the simulated image will be quite accurate.

The effects of the inaccurate tie point projection are similar in the case of dark field images as they are for bright field images. Figure 6.17 shows simulated dark field images for the orientation just studied in the bright field case. These images should be compared directly to those in Fig. 6.6, which are the dark field simulated images for the same

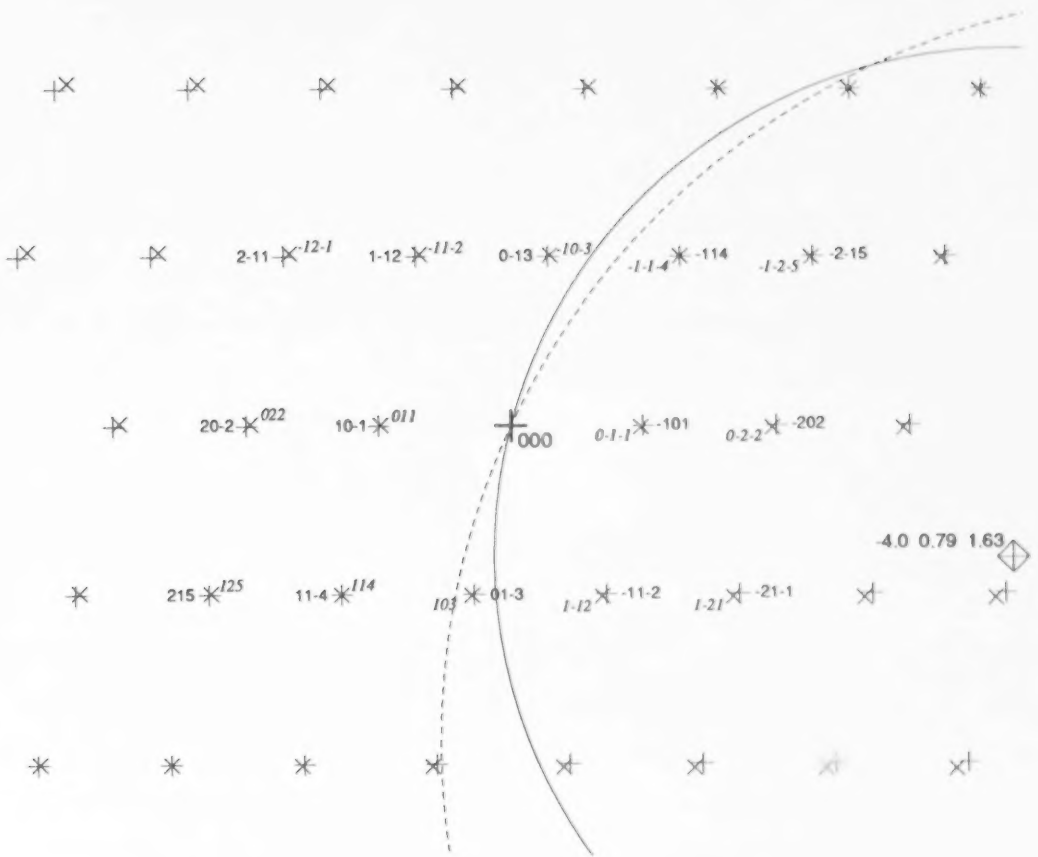

hkl matrix reflection

hkl twin reflection

matrix tie point projection

Fig. 6.15. Simulated diffraction pattern from a (110) twin boundary of $Y_1Ba_2Cu_3O_{7-\delta}$. The matrix zone axis is [131] and the twin zone axis is $[31\bar{1}]$. The Miller indices are indicated for some of the reflections in their own coordinate systems. The intersections of the Ewald sphere with the matrix and twin zero order Laue zones are indicated by the solid and dashed lines respectively. The matrix tie point projection is (-4.0 0.79 1.63).

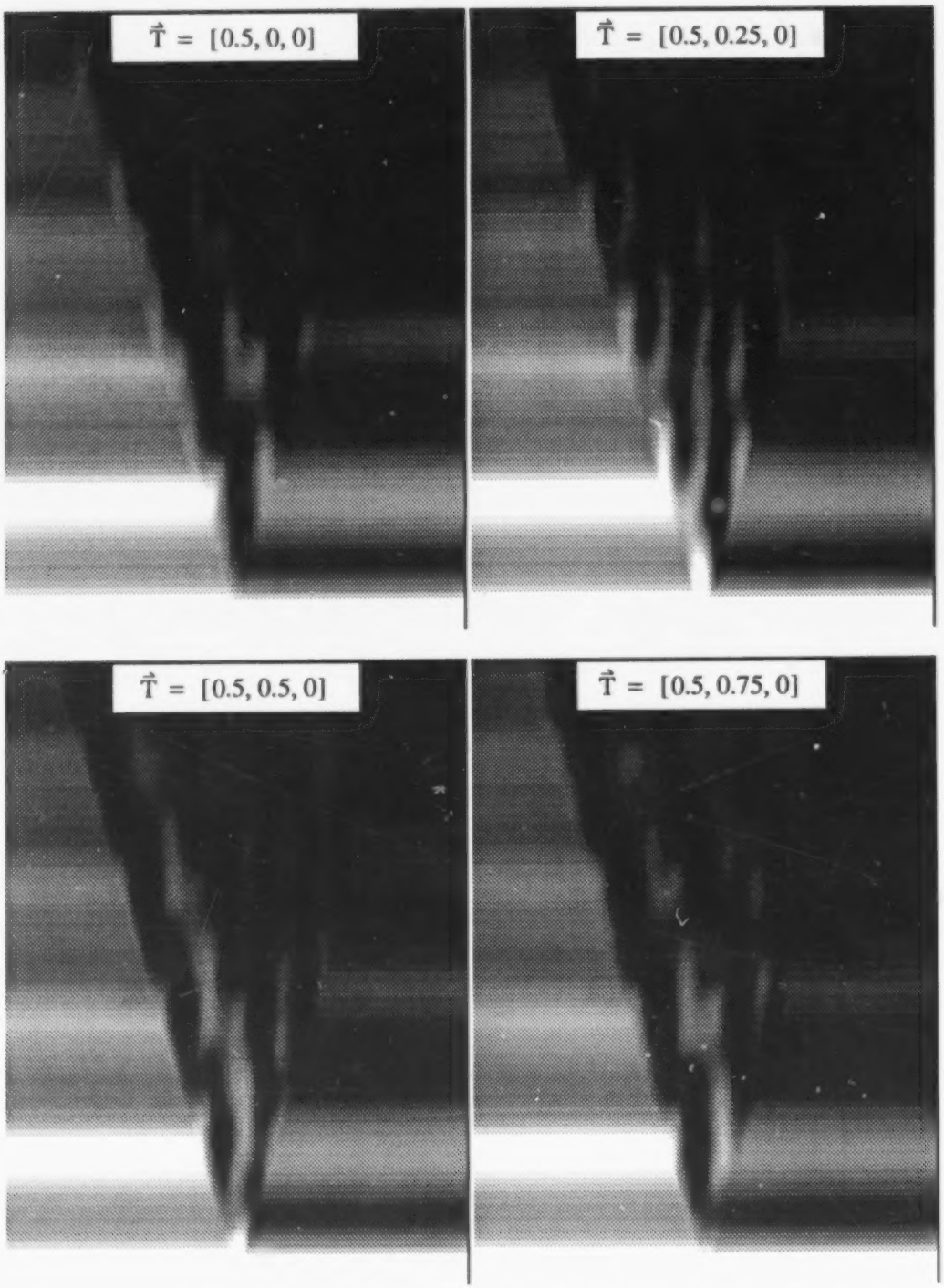

Fig. 6.16. Simulated bright field twin boundary images for a rigid body translation vector ranging from $\vec{T}$ = [0.5, 0, 0] to $\vec{T}$ = [0.5, 0.75, 0]. The matrix zone axis is [131] and the matrix tie point projection is (-4.0 0.79 1.63).

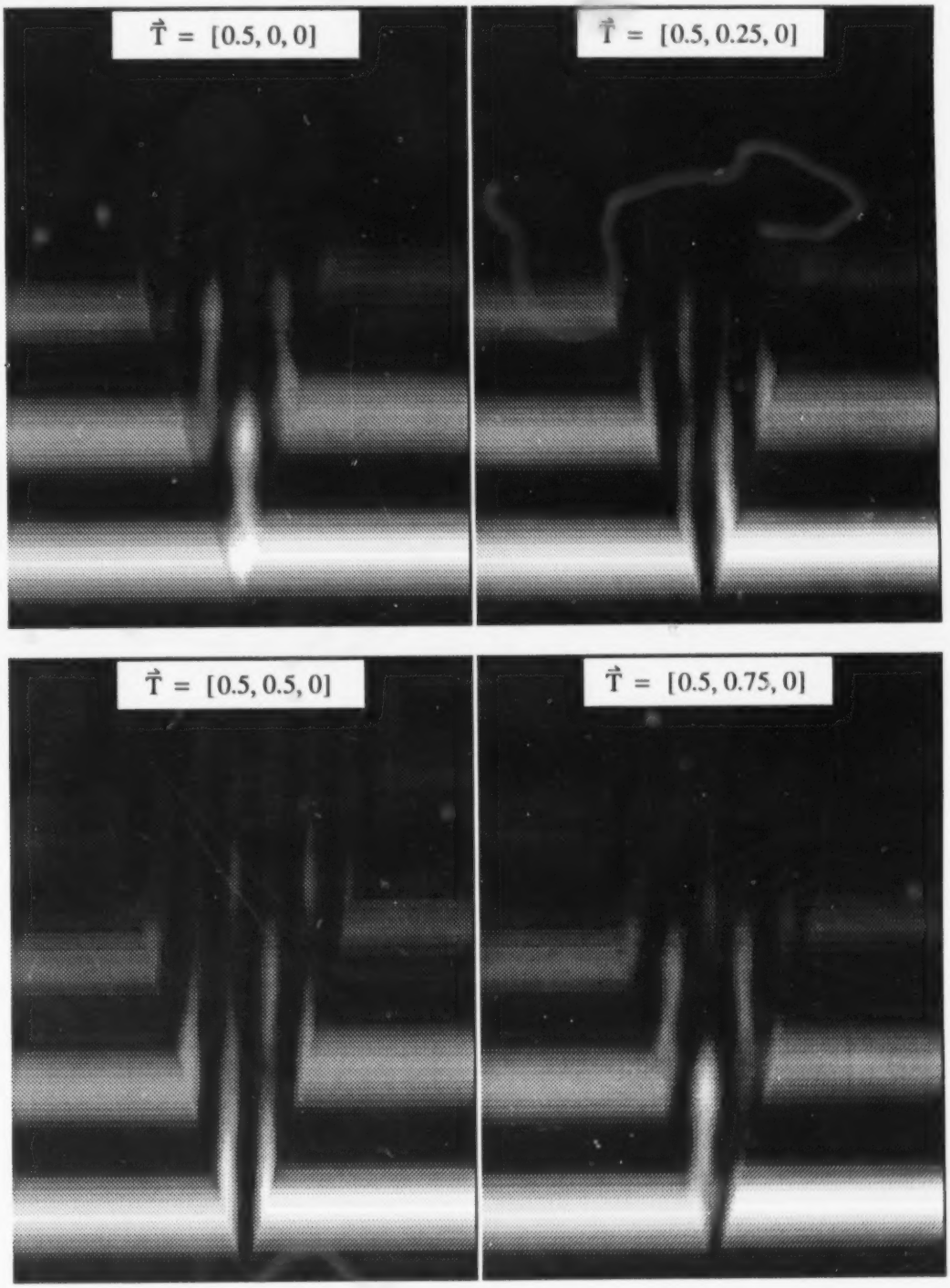

Fig. 6.17. Simulated dark field twin boundary images for a rigid body translation vector ranging from $\vec{T}$ = [0.5, 0, 0] to $\vec{T}$ = [0.5, 0.75, 0]. The matrix zone axis is [131] and the matrix tie point projection is (-4.0 0.79 1.63).

translation vectors, but a tie point projection of (-6.0 1.13 2.62). Once again, it can be seen that the substantial change in tie point projection has relatively little effect on the images because no new reflections are excited.

[101] Matrix Zone Axis

For the second zone axis, an orientation has been chosen which is very close to the original orientation. Figures 6.18 shows the diffraction pattern for the assumed tie point projection of (-2.2 0.75 2.2). The most important difference between this orientation and the one shown in Fig. 6.7 is that the (020) matrix reflection is now more strongly excited, and the (010) reflection is no longer in the Bragg condition. Also, since the (020) reflection has a much larger structure factor than the (010) reflection, the (020) reflection is now the most intense reflection in the diffraction pattern. Figure 6.19 shows a series of simulated images calculated assuming this tie point projection. The rigid body translation vectors range from [0.5, 0, 0] to [0.5, 0.75, 0]. It can be seen by comparing Fig. 6.19 with Fig. 6.8, that the change in orientation has had a noticeable effect on the image contrast. However, the image for which $\vec{T} = [0.5, 0.5, 0]$ still bears the greatest resemblance to the standard image in Fig. 6.8. This is particularly true for relatively thin regions of the crystal.

Nevertheless, it might be thought that by looking at more images, one might be found which resembles the standard image better than the image for which $\vec{T} = [0.5, 0.5, 0]$ does. Since the first and third components of $\vec{T}$ have very little effect on image contrast for this orientation (just as in the original orientation for this zone axis), images for which only the second component of $\vec{T}$ is varied will be examined. Figure. 6.20 shows a series of simulated bright field images which assume rigid body translation vectors ranging from [0.5, 0.4, 0] to [0.5, 0.55, 0]. It can be seen that the image obtained for $\vec{T} = [0.5, 0.5, 0]$ is still the best match to the standard image for small crystal thicknesses, although for larger thicknesses, the best match is probably for $\vec{T} = [0.5, 0.45, 0]$. Thus, although the inaccurate tie point projection makes it more difficult to find a match to the experimental image (which presumably resembles the standard image in Fig. 6.8), it would probably still result in a reasonably accurate determination of the component of $\vec{T}$ in the direction of the systematic row. There is one more thing to be noticed, however. A comparison of the thickness fringes on either side of the twin boundary in Fig. 6.8 with those in Fig. 6.19 or 6.20

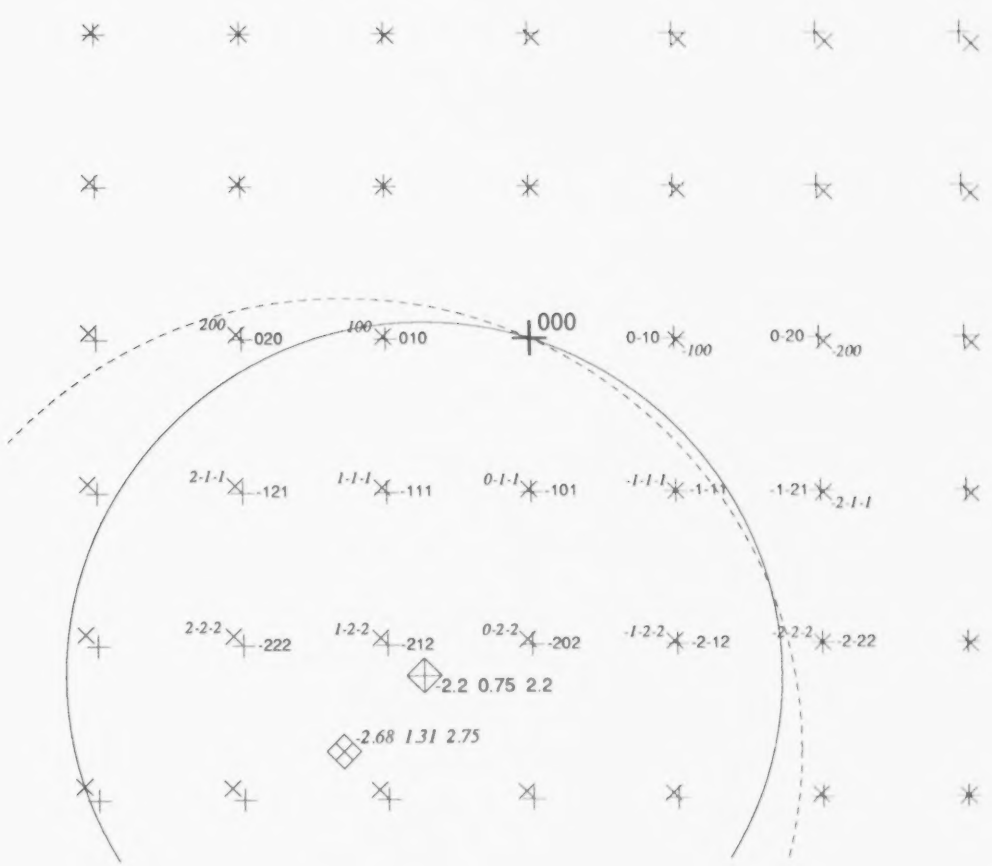

hkl matrix reflection

hkl twin reflection

matrix tie point projection

twin tie point projection

Fig. 6.18. Simulated diffraction pattern from a (110) twin boundary of $Y_1Ba_2Cu_3O_{7-\delta}$. The matrix zone axis is [101] and the twin zone axis is $[01\bar{1}]$. The Miller indices are indicated for some of the reflections in their own coordinate systems. The intersections of the Ewald sphere with the matrix and twin zero order Laue zones are indicated by the solid and dashed lines respectively. The matrix tie point projection is (-2.2 0.75 2.2).

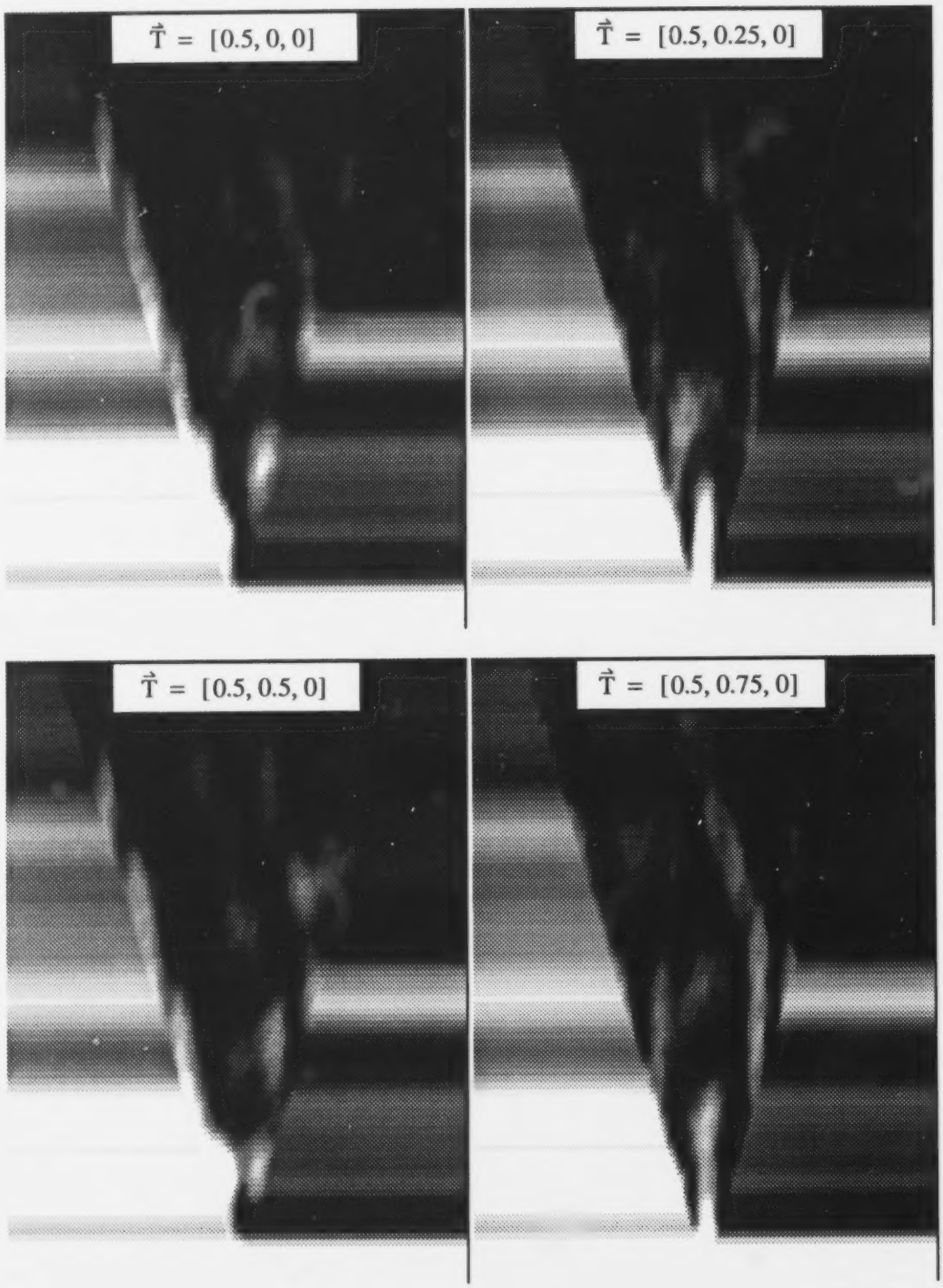

Fig. 6.19. Simulated bright field twin boundary images for a rigid body translation vector ranging from $\vec{T}$ = [0.5, 0, 0] to $\vec{T}$ = [0.5, 0.75, 0]. The matrix zone axis is [101] and the matrix tie point projection is (-2.2 0.75 2.2).

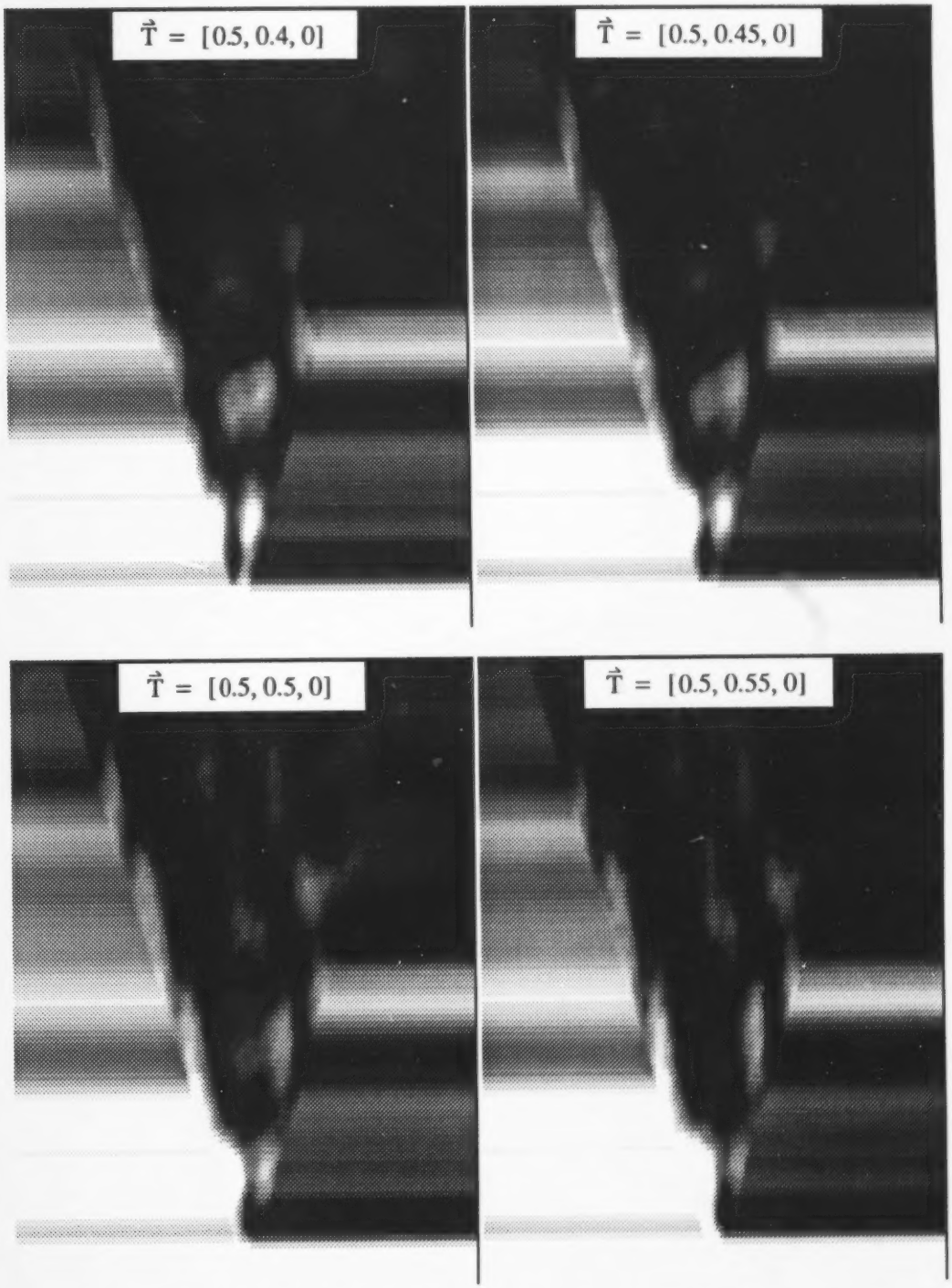

Fig. 6.20. Simulated bright field twin boundary images for a rigid body translation vector ranging from $\vec{T}$ = [0.5, 0.4, 0] to $\vec{T}$ = [0.5, 0.55, 0]. The matrix zone axis is [101] and the matrix tie point projection is (-2.2 0.75 2.2).

reveals that there are large differences between the two sets of fringes. Therefore, this fact would make is clear that the matrix zone axis which was assumed was not correct.

The dark field situation is very similar to the bright field situation for this orientation. Figure. 6.21 shows a series of dark field simulated images for the same orientation and translation vectors used for Fig. 6.19. The objective aperture is assumed to be centered around the (010) reflection. By comparing these images with those found in Fig. 6.10, it can be seen that once again, no translation vector provides a perfect match to the standard image, but the best match is found for $\vec{T} = [0.5, 0.5, 0]$.

[211] Matrix Zone Axis

Finally, a new set of images for the (211) zone axis will be examined. In the new, inaccurate, orientation, the $(11\bar{3})$ reflection is in its Bragg condition, and the $(10\bar{2})$ reflection, which was in its Bragg condition, is not any longer. The diffraction pattern for this orientation is shown in Figure 6.21. A series of simulated images for $\vec{T}$ ranging from [0.5, 0, 0] to [0.5, 0.75, 0] is shown in Figure 6.22. A comparison of Fig. 6.22 with Fig. 6.12 shows that this error leads to simulated twin boundary images which bear no resemblance at all to those which assume the correct orientation. In this case, it would be impossible to match the simulated images to experimental ones, and this fact should alert the microscopist to the fact that the orientation must be wrong.

Figure 6.23 shows the simulated dark field images for the same orientation assuming the objective aperture is centered around the $(11\bar{3})$ reflection. These images should be compared to those found in Fig. 6.14. This comparison reveals the fact that the images bear no resemblance except for the special case where $(11\bar{3}) \cdot \vec{T} = n$. For this translation vector, the twin boundary is effectively invisible for the same reasons as were described in the description of the original (211) zone axis orientation. This illustrates the fact that if an orientation can be found for which the twin boundary is invisible in a dark field image formed with the objective aperture centered around a common reflection, the translation vector must satisfy the following condition:

$$\vec{g} \cdot \vec{T} = n$$

where $\vec{g}$ is the common reflection used to form the image.

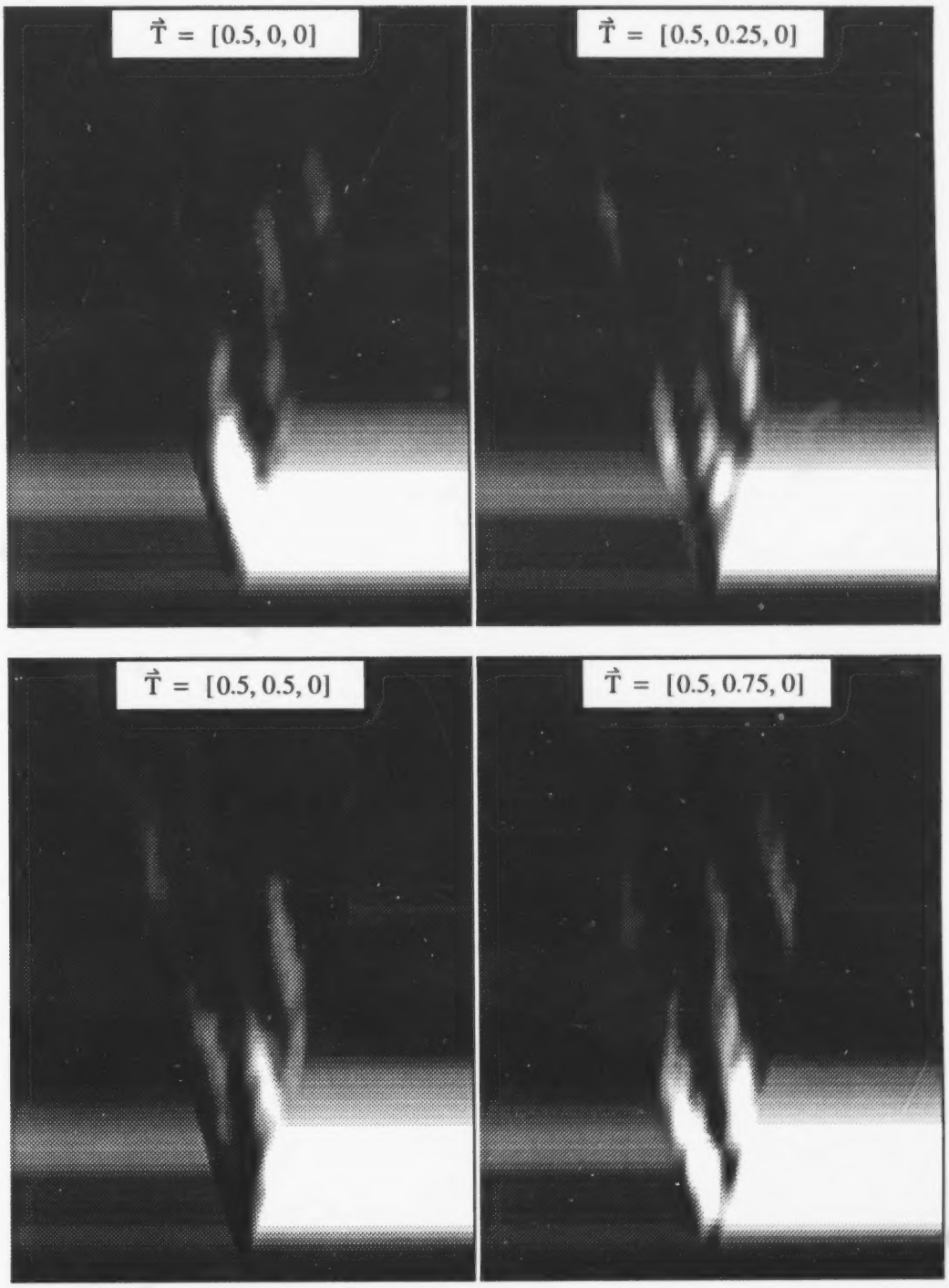

Fig. 6.21. Simulated dark field twin boundary images for a rigid body translation vector ranging from $\vec{T}$ = [0.5, 0, 0] to $\vec{T}$ = [0.5, 0.75, 0]. The matrix zone axis is [101] and the matrix tie point projection is (-2.2 0.75 2.2).

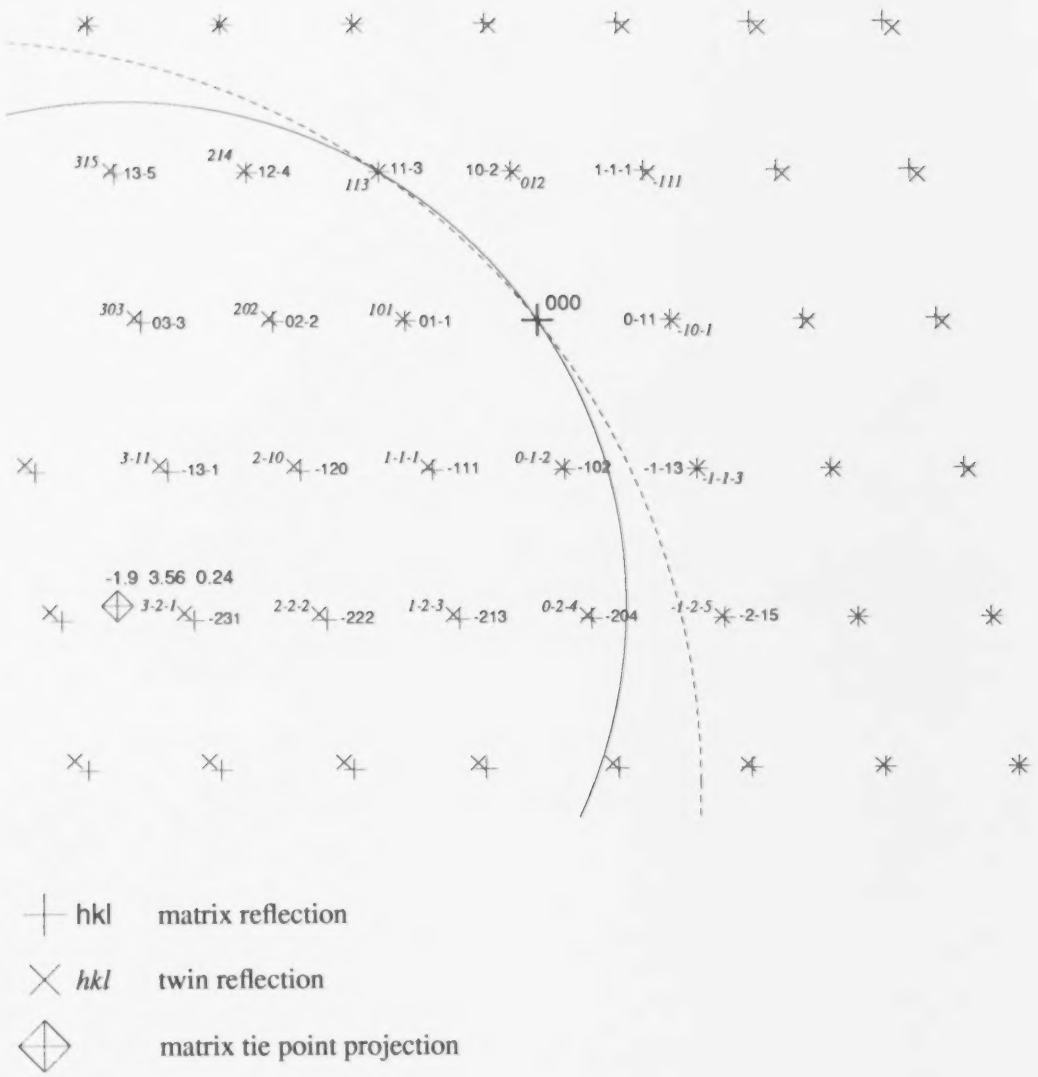

Fig. 6.22. Simulated diffraction pattern from a (110) twin boundary of $Y_1Ba_2Cu_3O_{7-\delta}$. The matrix zone axis is [211] and the twin zone axis is $[12\bar{1}]$. The Miller indices are indicated for some of the reflections in their own coordinate systems. The intersections of the Ewald sphere with the matrix and twin zero order Laue zones are indicated by the solid and dashed lines respectively. The matrix tie point projection is (-1.9 3.56 0.24).

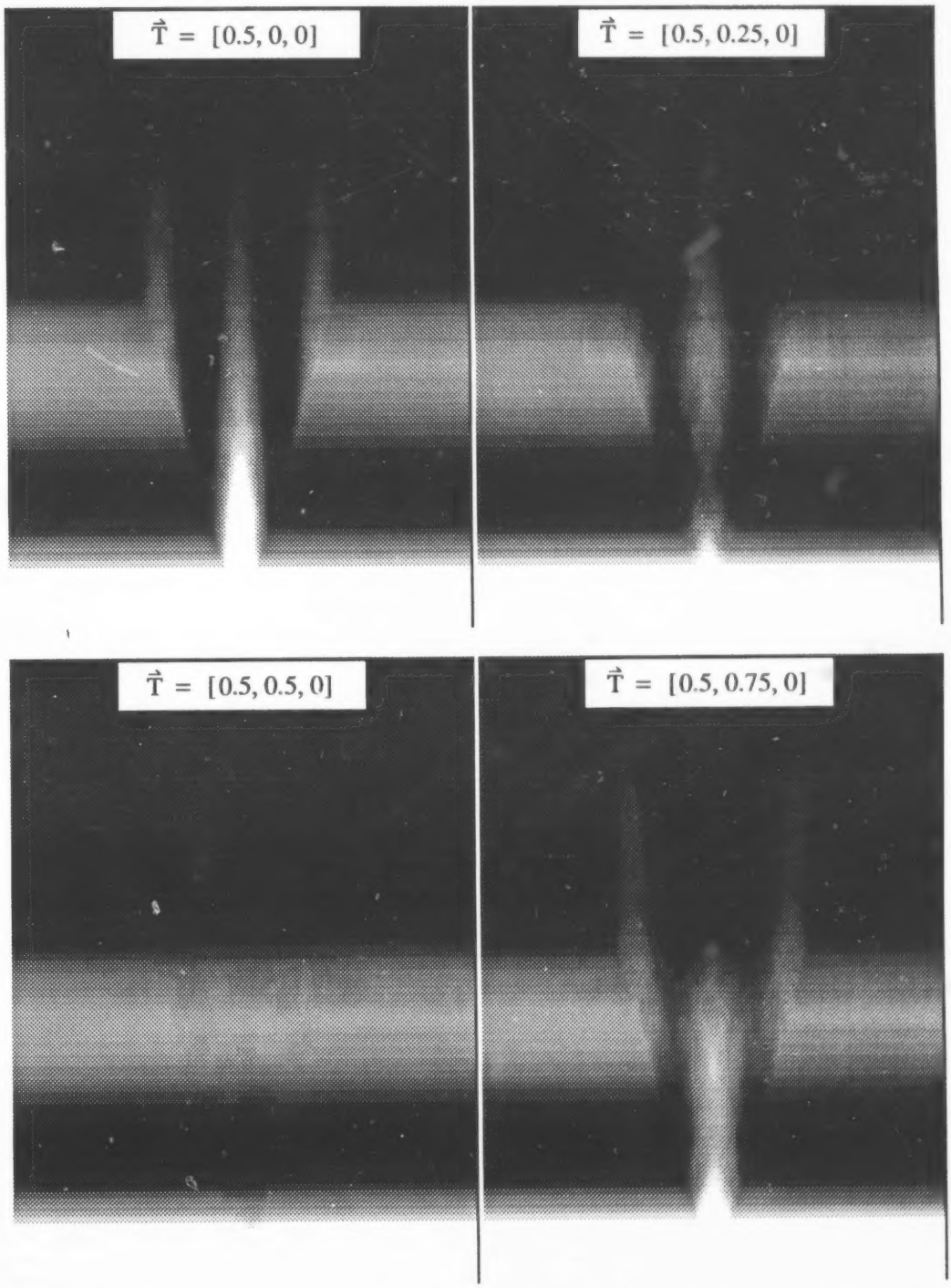

Fig. 6.23. Simulated bright field twin boundary images for a rigid body translation vector ranging from $\vec{T}$ = [0.5, 0 ,0] to $\vec{T}$ = [0.5, 0.75 ,0]. The matrix zone axis is [211] and the matrix tie point projection is (-1.9 3.56 0.24).

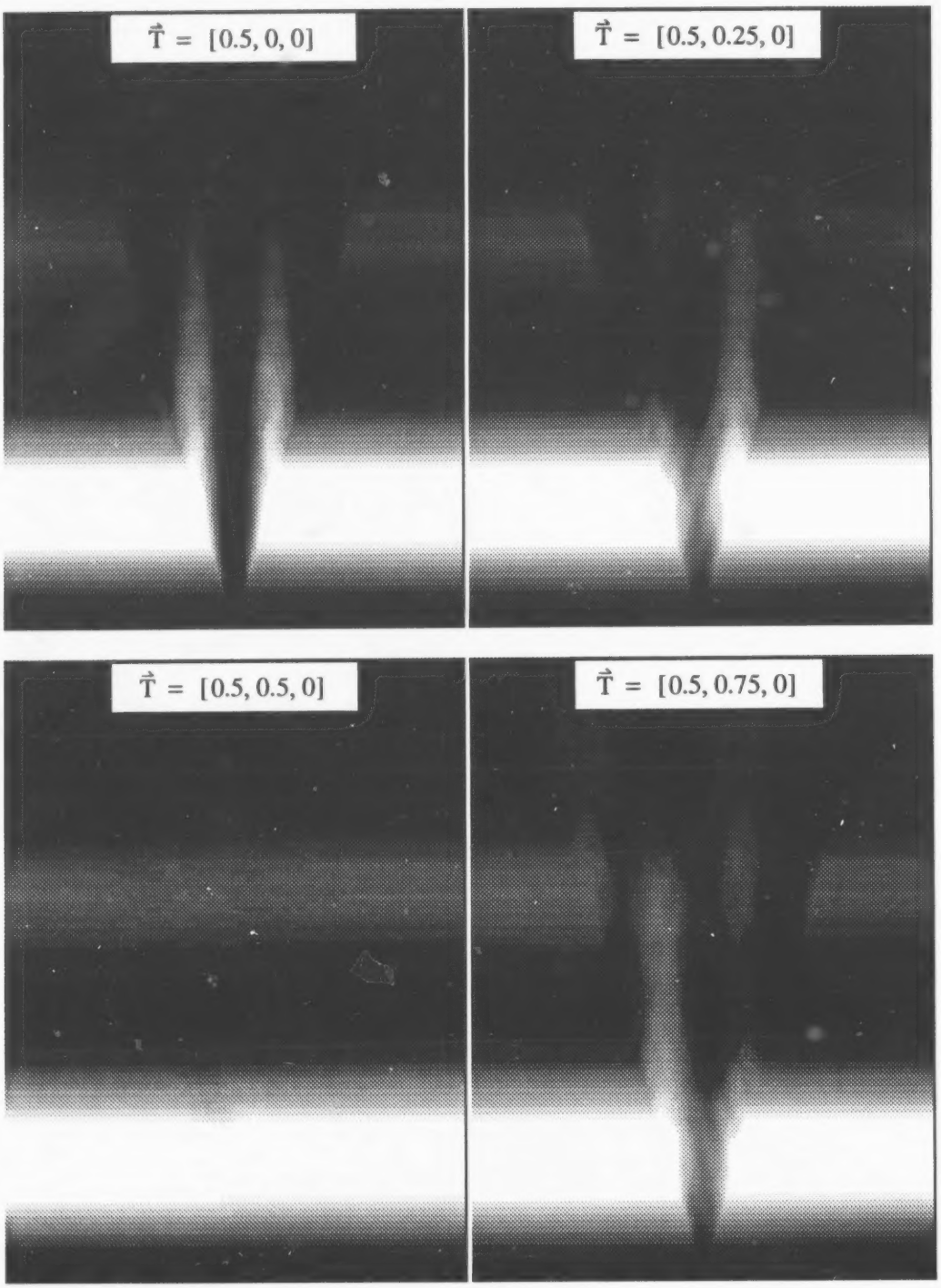

Fig. 6.24. Simulated dark field twin boundary images for a rigid body translation vector ranging from $\vec{T}$ = [0.5, 0 ,0] to $\vec{T}$ = [0.5, 0.75 ,0]. The matrix zone axis is [211] and the matrix tie point projection is (-1.9 3.56 0.24).

Summary

The previous examples serve to illustrate the following principles. If the deviation parameters of all of the intense reflections in the diffraction pattern are reasonably accurate, the resulting images will generally be accurate also. This is true even if the actual tie point projection is very inaccurate. This was shown by the example for the [131] zone axis. This is because large changes in tie point projection will have very small effects on the deviation parameters of the systematic row reflections as long as the deviation parameter of the major diffracted beam remains accurate.

The second example demonstrated that even a small change in the tie point projection can have noticeable effects on the simulated images if it results in significantly different deviation parameters for the systematic row reflections. This example, along with the third example, also demonstrated that an inaccurate tie point projection may make it difficult, or even impossible, to find a simulated twin boundary image which matches the experimental image, but will usually not lead to inaccurate determinations of the rigid body translation vector. This is because, as was seen in the example for the [101] zone axis, if it is possible to find a match at all (even though it may not be perfect), it will probably give the correct result. However, if the determination of the tie point projection is so inaccurate that it is impossible to find a match at all, as in the example for the [211] zone axis, this will simply serve to demonstrate that the tie point projection is incorrect.

6.2. Conclusions and Recommendations

In this thesis the groundwork has been laid for an experimental determination of the rigid body translation vector of a twin boundary. The twins which are the primary concern of this thesis are called pseudo-merohedral and pseudo-reticular merohedral twins. These types of twins are fairly common among complex crystals such as ceramics. From an electron microscopy point of view, the most significant feature of these twins is that the crystals on either side of the twin boundary will have reflections which are nearly, but not exactly common with reflections on the other side. Therefore, an experimental image of such a twin boundary which results from placing the objective aperture around a particular reflection will sometimes also have contributions from other beams which are not travelling in the same direction. Previous theories of diffraction contrast of twin boundaries have either been limited to a maximum of two excited reflections in the crystals or have not been applicable to twin boundaries which can have nearly common reflections. Therefore, the most important part of the work done in this thesis is the development of a theory which can give the diffraction contrast of such a twin boundary. This has been done in section 3.4.

It has also been found that crystals which exhibit pseudo-merohedral or pseudo-reticular-merohedral twins generally have an element of pseudo-symmetry. As a result of this fact, special care must be taken in determining the orientation of the crystal based on an experimental diffraction pattern. In section 4.2.1 a method was presented by which the zone axes of the two crystals can be reliably determined. Aside from that, it is crucial to know the inclination of the twin boundary which determines which crystal the electrons enter first. This is important because reflections which are excited in this top crystal can be further diffracted in the second crystal. Therefore, a method had to be developed to make this determination. This method is presented in section 4.2.2.

The pseudo-symmetry of these crystals also means that in most cases, the zone axes of the two crystals will not be exactly parallel. This has the effect that reflections from different sides of the twin boundary which may lie very close to each other in a diffraction pattern of the twin boundary will not necessarily be excited for the same orientations. Thus, it may be that one member of a pair of nearly common reflections is strongly excited and

the other member is only weakly excited. This can cause problems in the determination of the orientation of the crystals unless the difference in the two zone axes is properly taken into account. A method for showing where the Ewald sphere intersects the two different zero order Laue zones is given in section 4.3.1.

Besides knowing the correct orientation of the two crystals, another requirement for the calculation of theoretical images of twin boundaries is the correct electron scattering factors for the atoms involved in the crystal. Since the crystals which exhibit these forms of twinning are often ceramics, the atoms in the crystal are frequently bonded ionically. Thus, the electron scattering factors for the correct ions must be used in the calculations. Up to the present, there has been no source of inelastic scattering factors for ions, and, as a result, it has been impossible to correctly account for inelastic scattering in the crystal. Therefore, a new procedure has been developed for calculating these inelastic scattering factors. This process also lead to a new method for calculating the scattering factors for neutral atoms, which is simpler, and more accurate, than existing methods. These new methods were presented in Chapter 5. It was found that the method given for calculating inelastic scattering factors gives much more accurate scattering factors for those ions than simply using the factors for the corresponding neutral atoms.

In Chapter 6, a relatively straightforward method for finding the rigid body translation vector of a twin boundary through the use of simulated images was demonstrated. It was found that these simulated images depended quite sensitively on the translation vector for some crystal orientations. The method requires that at least three experimental images be obtained for which the systematic rows of reflections are non-coplanar. Each image then gives the component of the rigid body translation vector in the direction of the systematic row of reflections for that image. This is similar to techniques which are used to find the Burgers vectors of dislocations and the rigid body translation vector of twin boundaries from twins with many common reflections. These methods are based on finding an orientation for which the defect of interest becomes invisible. The difference between these methods and the present technique is that the procedure presented here does not require special orientations for which the twin boundary is invisible. Instead, it can make use of any experimental image from any given orientation. This is not only convenient, but also

necessary for the following reason. The crystals which exhibit pseudo-merohedral and pseudo-reticular merohedral twins do not generally have common reflections in three non-coplanar directions. Since the previous techniques which require the finding of invisibility conditions also require that only common reflections be used, they cannot usually completely define the rigid body translation vector.

The next step which should logically be undertaken is to use the theory and the practical groundwork which has been given in this thesis to make an experimental determination of the rigid body translation vector of a given twin boundary. Another possible line for the continuation of this work is the derivation of a theory for pseudo-merohedral and pseudo-reticular merohedral twin boundary contrast which does not make use of the assumption of symmetrical Laue conditions or the column approximation. Although these approximations are widely used in calculations of diffraction contrast for a variety of situations, it remains to be seen whether they lead to accurate results for the kind of twin boundaries studied in this thesis.

References

1. Gevers, R., Van Landuyt, J., and Amelinckx, S. (1965). Phys. Stat. Solidi 11, 69.
2. Amelinckx, S. and Van Landuyt, J. (1978). In Diffraction and Imaging Techniques in Materialsl Science vol. 1, (Amsterdam, North-Holland Publishing Co.), 107.
3. Sheinin, S. S. and Corbett, J. M. (1976). Phys. Stat. Solidi (a) 38, 675.
4. Sutton, A. P. and Pond, R. C. (1978). Phys. Stat. Solidi (a) 45, 149.
5. Sheinin, S. S. and Perez, R. (1983). Phys. Stat. Solidi (a) 79, 367.
6. Bethe, H. A. (1928). Ann. Physik Lpz. 87, 55.
7. Saldin, D. K., Whelan, M. J., and Rossouw, C. J. (1978). Inst. Phys. Conf. Ser. 41, 50.
8. Sheinin, S. S., and Jap, B. K. (1979). Phys. Stat. Sol. (b) 91, 407.
9. Kim, H. S., Perez, R., and Sheinin, S. S. (1982). Phys. Stat. Solidi (a) 72, 561.
10. Slater, J. C. (1937). Phys. Rev. 51, 840.
11. Moliere, K. (1939). Ann. Physik Lpz. 34, 461.
12. Yoshioka, H. (1957). J. Phys. Soc. Japan 12, 618
13. Humphreys, C. J., and Hirsch. P. B. (1968). Phil. Mag. 18, 115.
14. Radi, G. (1970). Acta. Cryst. A26, 41.
15. Bird, D. M., and King, Q. A. (1990) Acta. Cryst. A46, 202.
16. Weickenmeier, A., and Kohl, H. (1991). Acta. Cryst. A47, 590.
17. Fujiwara, K. (1962). J. Phys. Soc. Japan, 17 (Suppl. B. II), 118.
18. Howie, A. (1962). Discussion of Fujiwara, K. (1962). J. Phys. Soc. Japan, 17 (Suppl. B. II), 118.
19. Hashimota, H., Howie, A., and Whelan, M. J. (1962). Proc. Roy. Soc. A269, 80.
20. Hashimota, H. (1964). J. Appl. Phys. 35, 277.
21. Buerger, M. J. (1945). Amer. Min. 30, 469.
22. Donnay, J. D. H. (1940). Amer. Min. 25, 578.
23. Friedel, G. (1904). Bull. Soc. Minéralogie, Minérale 3, 877.
24. Cahn, R. W. (1954). Adv. Phys. 3, 363.
25. Clark, R., and Craig, G. B. (1953). Prof. Metal Phys. 3, 115.

26. Cava, R. J., Batlogg, B., van Dover, R. B., Murphy, D. W., Sunshine, S., Siegrist, T., Remeiko, J. P., Rietman, E. A., Zahurak, S., and Espinosa, G. P. (1987). Phys. Rev. Lett. 58, 1676

27. Goringe, M. J. and Valdré, U. (1966). Proc. Roy. Soc. A295, 195.

28. Gleiter, H. and Klein, H. P. (1973). Phil. Mag. 27, 1009.

29. Corbett, J. M. and Sheinin, S. S. (1976). Phys. Stat. Sol. (a) 38, 151.

30. Gomez, D., Romeu, D., and Yacaman, M. J. (1980). Proc. EMAG Conf., Inst. Phys. Conf. Ser. 52, 215.

31. Gratias, D. and Portier, R. (1980). J. Microscopy 120, 129.

32. Takagi, S. (1962). Acta. Cryst. 15, 1311.

33. Gevers, R., DeVelignette, P., Blank, H., and Amelinckx, S. (1964). Phys. Stat. Solidi 4, 383.

34. Doyle, P. A. and Turner, P. S. (1968). Acta. Cryst. A24, 390.

35. Doyle, P. A. and Cowley, J. M. (1974). In International Tables of X-Ray Crystallography, Vol. IV, (Birmingham, Kynoch Press), 152.

36. Mott, N. F. (1930). Proc. Roy. Soc. A127, 658.

37. Cromer, D. T. and Waber, J. T. (1974). In International Tables of X-Ray Crystallography, Vol. IV, (Birmingham, Kynoch Press), 71.

38. Sanger, P. L. (1969). Acta. Cryst. A25, 695.

39. Lonsdale, K. (1962), In International Tables of X-Ray Crystallography, Vol. III, (Birmingham, Kynoch Press), 232.

40. Williams, A., Kwei, G. H., Von Dreele, R. B., Larson, A. C., Raistrick, I. D., and Bish, D. L. (1988). Phys. Rev. B 37, 7960.

41. Calestani, G. and Rizzoli, C. (1987). Nature 328, 606.

42. Capponi, J. J., Chaillout, C., Hewat, A. W., Lejay, P., Marezio, M., Nguyen, N., Raveau, B., Soubeyroux, J. L., Tholence, J. L., and Tournier, R. (1987). Europhys. Lett. 3, 1301.

43. Hoydoo You, R. K., McMullan, J. D., Axe, J. D., Cox, D. E., Liu, J. Z., Crabtree, G. W., and Lam, D. J. (1987). Solid State Comm. 64, 739.

44. Antson, O. K., Hiismäki, P. E., Pöyry, H. O., Tiitta, A. T., Ullakko, K. M., Trunov, V. A., and Ul'yanov, V. A. (1987). Solid State Comm. 64, 757.

45. François, M., Walker, E., Jorda, J. -L., Yvon, K., and Fischer, P. (1987). Solid State Comm. 63, 1149.

46. Hewatt, A. W., Capponi, J. J., Chaillout, C., Marezio, M., and Hewat, E. A. (1987). Solid State Comm. 64, 301.

47. Beno, M. A., Soderholm, L., Capone, D. W., Hinks, D. G., Jorgensen, J. D., Grace, J. D., Schuller, I. K., Segre, C. U., and Zhang, K. (1987). Appl. Phys. Lett. 51 57.

48. Ritchie, R. H. and Howie, A. (1977). Phil. Mag. 36, 463.

49. Hall, C. R. and Hirsch, P. B. (1965). Proc. Roy. Soc. A286, 158.

50. Hirsch, P. B., Howie, A., Nicholson, R. B. Pashley, D. W., and Whelan, M. J. (1977). Electron Microscopy of Thin Crystals, (Huntington, N. Y., Krieger).

51. Andrews, K. W., Dyson, D. J., and Keown, S. R. (1967). Interpretation of Diffraction Patterns, (London, Hilger and Watts Ltd.).

52. Head, A. K., Humble, P., Clarebrough, L. M., Morton, A. J., and Forwood, C. T. (1973). Computed Electron Micrographs and Defect Identification, (Amsterdam, North-Holland Publishing Co.).

53. Thomas, G. and Goringe, M. J. (1979). Transmission Electron Microscopy of Materials, (New York, John Wiley and Sons).

Appendix A: Calculation of Excitation Coefficients

The twin wavefunction is given as follows:

$$\Psi = \sum_{p,n} \phi_{p,n} \tag{A.1}$$

where

$$\phi_{p,n} = \sum_{i_p} X^{(i_p)} C_{p,n}^{(i_p)} \exp\left[2\pi i \,(\vec{k}^{(i_p)} + \vec{g}_p + \vec{h}_n) \cdot (\vec{r} - \vec{T})\right] \tag{A.2}$$

This wavefunction must be equal at the twin boundary to the wavefunction in the matrix at the twin boundary. The matrix wavefunction is given by eq. 2.12.

$$\Psi_{ma}(\vec{r}_{tb}) = \sum_{j,g} \psi^{(j)} D_g^{(j)} \exp\left[2\pi i \,(\vec{\kappa}^{(j)} + \vec{g}) \cdot \vec{r}_{tb}\right]$$

$$= \sum_{j,p,m} \psi^{(j)} D_{g_p + q_m}^{(j)} \exp\left[2\pi i \,(\vec{\kappa}^{(j)} + \vec{g}_p + \vec{q}_m) \cdot \vec{r}_{tb}\right]$$

where the symbols for the electron wavevectors, the excitation coefficients, and the Bloch wave amplitudes have been changed to indicate that they are not the same in the matrix as in the twin. Therefore:

$$\Psi_{ma}(\vec{r}_{tb}) = \Psi_{tw}(\vec{r}_{tb})$$

$$\therefore \sum_{j,p,m} \psi^{(j)} D_{g_p + q_m}^{(j)} \exp\left[2\pi i \,(\vec{\kappa}^{(j)} + \vec{g}_p + \vec{q}_m) \cdot \vec{r}_{tb}\right]$$

$$= \sum_{p,n,i_p} X^{(i_p)} C_{p,n}^{(i_p)} \exp\left[-2\pi i \,(\vec{k}^{(i_p)} + \vec{g}_p + \vec{h}_n) \cdot \vec{T}\right] \exp\left[2\pi i \,(\vec{k}^{(i_p)} + \vec{g}_p + \vec{h}_n) \cdot \vec{r}\right] \tag{A.3}$$

The subscripts, $\perp$ and $\parallel$, will now refer to the components of a vector perpendicular and parallel to the twin boundary, respectively. The component of $\vec{r}_{tb}$ which is parallel to the twin boundary, $\vec{r}_{tb\parallel}$, is different at different points on the boundary. With the twin Bloch functions defined as they are here, this equation has no solution in the general case. Only with the use of the column approximation does a solution become possible. Under the

column approximation, the twin boundary is considered to be parallel to the entrance surface of the crystal. The result of this is that the components of the matrix wavevectors, parallel to the twin boundary, $\vec{\kappa}_{\parallel}^{(i)}$ are all equal. Therefore, $\vec{k}_{\parallel}^{(i_p)} \cdot \vec{r}_{tb\parallel} = \vec{\kappa}_{\parallel}^{(j)} \cdot \vec{r}_{tb\parallel}$ as long as $\vec{k}_{\parallel}^{(i_p)} = \vec{\kappa}_{\parallel}^{(j)}$ for all i_p and j. If both sides of eq. A.3 are divided by $\exp(2\pi i \vec{k}_{\parallel}^{(i_p)} \cdot \vec{r}_{tb\parallel})$, the following is obtained:

$$\sum_{p,m} \left(\sum_{j} \psi^{(j)} D^{(j)}_{g_p + q_m} \exp\left[2\pi i \left(\kappa_{\perp}^{(j)} + g_{p\perp} + q_{m\perp}\right) r_{tb\perp}\right] \right) \exp\left[2\pi i \left(\vec{g}_{p\parallel} + \vec{q}_{m\parallel}\right) \cdot \vec{r}_{tb\parallel}\right]$$

$$= \sum_{p,n} \left(\sum_{i_p} X^{(i_p)} C^{(i_p)}_{p,n} \exp\left[2\pi i \left(k_{\perp}^{(i)} + g_{p\perp} + h_{n\perp}\right) r_{tb\perp}\right] \exp\left[-2\pi i \left(\vec{k}^{(i_p)} + \vec{g}_p + \vec{h}_n\right) \cdot \vec{T}\right] \right)$$

$$\times \exp\left[2\pi i \left(\left(\vec{g}_{p\parallel} + \vec{h}_{n\parallel}\right) \cdot \vec{r}_{tb\parallel}\right)\right] \qquad \text{(A.4)}$$

On the left hand side of this equation, the summation over p and m consists of all of the matrix reflections, while the summation over p and n on the right hand side includes all of the reflections of any kind in the twin. Thus, each term, $\exp\left[2\pi i \left(\vec{g}_{p\parallel} + \vec{q}_{m\parallel}\right) \cdot \vec{r}_{tb\parallel}\right]$, on the left has an equal term on the right. That is to say that the set of q_m's is a subset of the set of h_n's. Therefore, the coefficients of these similar exponential terms must be made equal:

$$\sum_{j} \psi^{(j)} D^{(j)}_{g_p + q_m} \exp\left[2\pi i \left(\kappa_{\perp}^{(j)} + g_{p\perp} + q_{m\perp}\right) r_{tb\perp}\right]$$

$$= \sum_{i_p} X^{(i_p)} C^{(i_p)}_{p,n_m} \exp\left[2\pi i \left(k_{\perp}^{(i)} + g_{p\perp} + h_{n_m\perp}\right) r_{tb\perp}\right] \exp\left[-2\pi i \left(\vec{k}^{(i_p)} + \vec{g}_p + \vec{h}_{n_m}\right) \cdot \vec{T}\right]$$

where $h_{n_m} \equiv q_m$. This can be divided by $\exp\left[2\pi i \left(g_{p\perp} + q_{m\perp}\right) r_{tb\perp}\right]$ to get:

$$\sum_{i_p} X^{(i_p)} C^{(i_p)}_{p,n_m} \exp\left(2\pi i k_{\perp}^{(i)} r_{tb\perp}\right) \exp\left[-2\pi i \left(\vec{k}^{(i_p)} + \vec{g}_p + \vec{h}_{n_m}\right) \cdot \vec{T}\right]$$

$$= \sum_{j} \psi^{(j)} D^{(j)}_{g_p + q_m} \exp\left(2\pi i \kappa_{\perp}^{(j)} r_{tb\perp}\right) \qquad \text{(A.5a)}$$

The coefficients of the exponential terms, $\exp\left[2\pi i \left(\vec{g}_{p\parallel} + \vec{h}_{n\parallel}\right) \cdot \vec{r}_{tb\parallel}\right]$, on the right hand side of eq. A.4 must also be set equal to zero for $h_n \neq q_m$ for any m.

$$\sum_{i_p} X^{(i_p)} C^{(i_p)}_{p,n} \exp\left[2\pi i \left(k_{\perp}^{(i)} + g_{p\perp} + h_{n\perp}\right) r_{tb\perp}\right] \exp\left[-2\pi i \left(\vec{k}^{(i_p)} + \vec{g}_p + \vec{h}_n\right) \cdot \vec{T}\right] = 0 \qquad \text{(A.5b)}$$

for $h_n \neq q_m$ for any m.

The set of equations given in eq. A.5 can be written in matrix form:

$$\mathbf{E}_{hTp}\mathbf{C}_p\mathbf{E}_{kTp}\mathbf{E}_p\mathbf{X}_p = \mathbf{E}_{0p} \tag{A.6}$$

where

$$\mathbf{E}_{hTp} = \begin{bmatrix} \exp[-2\pi i(\vec{g}_p + \vec{h}_1)\cdot T] & 0 & \dots & \dots & 0 \\ 0 & \exp[-2\pi i(\vec{g}_p + \vec{h}_2)\cdot T] & & & \\ 0 & & \dots & & \dots \\ \dots & & & \dots & 0 \\ 0 & & \dots & 0 & \exp[-2\pi i(\vec{g}_p + \vec{h}_{N_t})\cdot T] \end{bmatrix}$$

$$\mathbf{C}_p = \begin{bmatrix} C_{p,1}^{(1)} & C_{p,1}^{(2)} & \dots & \dots & C_{p,1}^{(N_t)} \\ C_{p,2}^{(1)} & C_{p,2}^{(2)} & \dots & \dots & C_{p,2}^{(N_t)} \\ \dots & \dots & \dots & & \\ \dots & \dots & \dots & & \\ C_{p,N_t}^{(1)} & C_{p,N_t}^{(2)} & & & C_{p,N_t}^{(N_t)} \end{bmatrix}$$

$$\mathbf{E}_{kTp} = \begin{bmatrix} \exp(-2\pi i\vec{k}^{(1)}\cdot\vec{T}) & 0 & 0 & \dots & \dots & 0 \\ 0 & \exp(-2\pi i\vec{k}^{(2)}\cdot\vec{T}) & & & & \dots \\ 0 & & \dots & & & \dots \\ \dots & & & & \dots & 0 \\ 0 & \dots & \dots & 0 & 0 & \exp(-2\pi i\vec{k}^{(N_t)}\cdot\vec{T}) \end{bmatrix}$$

$$\mathbf{E}_p = \begin{bmatrix} \exp(2\pi i k_\perp^{(1)} r_{tb\perp}) & 0 & 0 & \dots & \dots & 0 \\ 0 & \exp(2\pi i k_\perp^{(2)} r_{tb\perp}) & & & & \dots \\ 0 & & \dots & & & \dots \\ \dots & & & & \dots & 0 \\ 0 & \dots & \dots & 0 & 0 & \exp(2\pi i k_\perp^{(N_t)} r_{tb\perp}) \end{bmatrix}$$

$$\mathbf{X}_p = \begin{bmatrix} X^{(1_p)} \\ X^{(2_p)} \\ \cdots \\ \cdots \\ X^{(N_{tp})} \end{bmatrix} \qquad \mathbf{E}_{0p} = \begin{bmatrix} \varphi_{p,1} \\ \varphi_{p,2} \\ \cdots \\ \cdots \\ \varphi_{p,N_t} \end{bmatrix}$$

where

$$\varphi_{p,n} = \sum_j \psi^{(j)} D_{g^{(j)}+h_n} \exp\left(2\pi i \kappa_\perp^{(j)} r_{tb\perp}\right)$$

when h_n is a common reciprocal lattice vector, and

$$\varphi_{p,n} = 0$$

when h_n is not a common reciprocal lattice vector.

Equation A.6 can be solved for $X^{(i_p)}$ as follows:

$$\mathbf{X}_p = \mathbf{E}_p^{-1}\mathbf{E}_{kTp}^{-1}\mathbf{C}_p^{-1}\mathbf{E}_{hTp}^{-1}\mathbf{E}_{0p} \tag{A.7}$$

The inverses of $\mathbf{E}_p$, $\mathbf{E}_{kTp}$, and $\mathbf{E}_{hTp}$ are all simply obtained by multiplying the argument of the exponentials on the diagonals by -1. If inelastic scattering processes are ignored for the time being, $\mathbf{C}^{-1} = \mathbf{C}^T$. Therefore:

$$\mathbf{E}_{hTp}^{-1}\mathbf{E}_{0p} = \begin{bmatrix} \varphi'_{p,1} \\ \varphi'_{p,2} \\ \cdots \\ \cdots \\ \varphi'_{p,N_t} \end{bmatrix}$$

where

$$\varphi'_{p,n} = \exp\left[2\pi i \left(\vec{g}_p + \vec{h}_n\right) \cdot \vec{T}\right] \varphi_{p,n}$$

Therefore:

$$\mathbf{C}_p^T \mathbf{E}_{hTp}^{-1} \mathbf{E}_{0p} = \begin{bmatrix} \sum_n C_{p,n}^{(1_p)} \varphi'_{p,n} \\ \sum_n C_{p,n}^{(2_p)} \varphi'_{p,n} \\ \cdots \\ \cdots \\ \sum_n C_{p,n}^{(N_{tp})} \varphi'_{p,n} \end{bmatrix}$$

However, since most of the $\varphi'_{p,n}$ are equal to zero, this becomes:

$$\mathbf{C}_p^T \mathbf{E}_{hTp}^{-1} \mathbf{E}_{0p} = \begin{bmatrix} \sum_m C_{f_{p,n_m}}^{(1_p)} \varphi'_{p,n_m} \\ \sum_m C_{f_{p,n_m}}^{(2_p)} \varphi'_{p,n_m} \\ \cdots \\ \cdots \\ \sum_m C_{f_{p,n_m}}^{(N_{tp})} \varphi'_{p,n_m} \end{bmatrix}$$

where

$$\varphi'_{p,n_m} = \exp\left[2\pi i \left(\vec{g}_p + \vec{q}_m\right) \cdot \vec{T}\right] \sum_j \psi^{(j)} D_{g_p+q_m}^{(j)} \exp\left(2\pi i \kappa_\perp^{(j)} r_{tb\perp}\right)$$

The rest of the matrix multiplication is straightforward and the following expression is finally obtained:

$$X^{(i_p)} = \sum_m \varphi_{p,n_m} C_{p,n_m}^{(i_p)} \exp\left[2\pi i \left(\vec{k}^{(i_p)} + \vec{g}_p + \vec{q}_m\right) \cdot \vec{T}\right] \exp\left(-2\pi i k_\perp^{(i_p)} r_{tb\perp}\right)$$

$$= \sum_m \sum_j \psi^{(j)} D_{g_p+q_m}^{(j)} \exp\left[2\pi i \left(\vec{k}^{(i_p)} + \vec{g}_p + \vec{q}_m\right) \cdot \vec{T}\right] \exp\left[2\pi i \left(\vec{\kappa}^{(j)} - \vec{k}^{(i_p)}\right) \cdot \vec{r}_{tb}\right] \quad \text{(A.8)}$$

where use has been made of the fact that $\kappa_\perp^{(j)} r_{tb\perp} - k_\perp^{(i_p)} r_{tb\perp} = \left(\vec{\kappa}^{(j)} - \vec{k}^{(i_p)}\right) \cdot \vec{r}_{tb}$ in the symmetrical Laue approximation.

This expression for $X^{(i_p)}$ can now be substituted into eq. A.2 to get the following:

$$\phi_{p,n} = \sum_{i_p}\sum_{m}\sum_{j} \psi^{(j)} D^{(j)}_{g_p+q_m} C^{(i_p)}_{p,n_m} C^{(i_p)}_{p,n} \exp\left[2\pi i\,(\vec{\kappa}^{(j)} - \vec{k}^{(i_p)}) \cdot \vec{r}_{tb}\right]$$

$$\times \exp\left[2\pi i\,(\vec{k}^{(i_p)} + \vec{g}_p + \vec{h}_n) \cdot \vec{r}\right] \exp\left[2\pi i\,(\vec{q}_m - \vec{h}_n) \cdot \vec{T}\right]$$

If the expression given in eq. 2.29 for ψ (in eq. 2.29 the symbol for ψ is X) is now substituted into this equation, the following equation is found:

$$\phi_{p,n} = \sum_{i_p,m}\sum_{j} (D^{(j)}_0 D^{(j)}_{g_p+q_m} \exp\left[2\pi i\,((\vec{\chi} - \vec{\kappa}^{(j)}) \cdot \vec{r}_{en})\right] \exp\left[2\pi i\,(\vec{\kappa}^{(j)} \cdot \vec{r}_{tb})\right])$$

$$\times C^{(i_p)}_{p,n_m} C^{(i_p)}_{p,n} \exp\left[-2\pi i\,(\vec{k}^{(i_p)} \cdot \vec{r}_{tb})\right] \exp\left[2\pi i\,(\vec{k}^{(i_p)} + \vec{g}_p + \vec{h}_n) \cdot \vec{r}\right] \exp\left[2\pi i\,(\vec{q}_m + \vec{h}_n) \cdot \vec{T}\right]$$

Some terms can be removed from the summations to get the following:

$$\phi_{p,n} = \exp(2\pi i \vec{\chi} \cdot \vec{r}_{en}) \exp\left[2\pi i \vec{K} \cdot (\vec{r} - \vec{r}_{en})\right] (\exp\left[2\pi i\,(\vec{g}_p + \vec{h}_n) \cdot \vec{r}\right])$$

$$\times \sum_{i_p,m} \Phi_{g_p+q_m} C^{(i_p)}_{p,n_m} C^{(i_p)}_{p,n} \exp\left[2\pi i\,(\vec{q}_m - \vec{h}_n) \cdot \vec{T}\right] \exp\left[2\pi i \gamma^{(i_p)} \hat{z} \cdot (\vec{r} - \vec{r}_{tb})\right] \tag{A.9}$$

where

$$\Phi_{g_p+q_m} = \sum_{j} D^{(j)}_0 D^{(j)}_{g_p+q_m} \exp(2\pi i \gamma^{(j)}_{ma} t_m) \tag{A.10}$$

where $\gamma^{(j)}_{ma}$ is the eigenvalue of the j^{th} Bloch wave in the matrix.

Appendix B: Principles of Twin Boundary Diffraction Patterns

A computer program has been developed to generate simulated twin boundary diffraction patterns. It works only for crystals whose primitive lattice vectors are all at right angles to each other, i.e. cubic, tetragonal, and orthorhombic crystals. The program is based on the following principles, given by Hirsch, et. al.[47], for 180 degree rotation twins.

The first thing which must be determined is which twin zone axis is parallel to the electron beam. If it is assumed that the [uvw] matrix zone axis is parallel to the beam, the matrix direction must be found which, through the process of twinning, becomes parallel to the [uvw] direction (i.e. after the process of twinning, this direction becomes the twin direction which is parallel to the beam). As a result of twinning, each crystal direction in the matrix is rotated through 180 degrees about the twin axis, which will be denoted [pqr]. If the [uvw] direction undergoes this operation, it will then have a new direction, with new Miller indices. If this new vector, which has Miller indices of $[u'v'w']$ in the matrix coordinates, is again rotated through 180 degrees about the twin axis, it will again be parallel to the [uvw] direction. Therefore, these are the indices, in twin coordinates, of the direction which is parallel to the [uvw] direction in matrix coordinates.

Referring to Figure B.1, and noting that the vectors [uvw] and $[u'v'w']$ are equal in length, the following can be written:

$$[uvw] + [u'v'w'] = n[pqr] \tag{B.1}$$

where n is some factor which depends in [uvw] and [pqr].

$$\begin{aligned} u + u' &= np \\ v + v' &= nq \\ w + w' &= nr \end{aligned} \tag{B.2}$$

The equality in the lengths of the two vectors results in:

$$\begin{aligned} u^2a^2 + v^2b^2 + w^2c^2 &= u'^2a^2 + v'^2b^2 + w'^2c^2 \\ &= (np-u)^2a^2 + (nq-v)^2(b)^2 + (nr-w)^2c^2 \end{aligned}$$

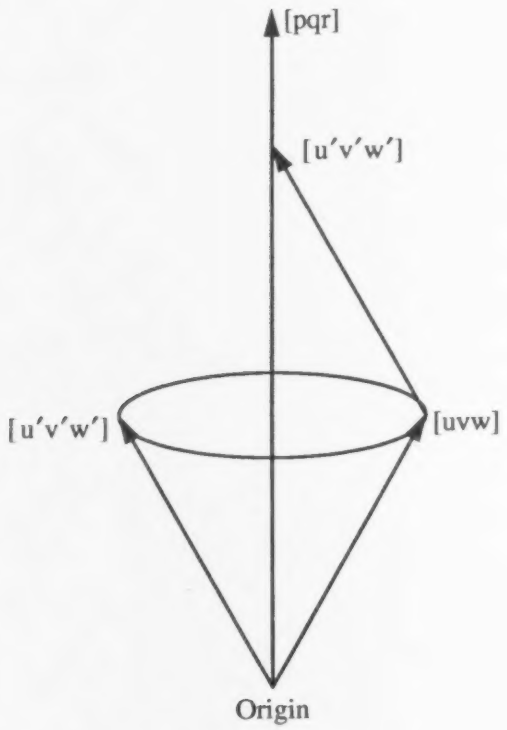

Fig. B.1. The rotation of a matrix direction, [uvw], through 180 degrees about the twin axis, [pqr].

If this equation is solved for n, the following expression is obtained:

$$n = \frac{2\,(pua^2 + qvb^2 + rwc^2)}{p^2a^2 + q^2b^2 + r^2c^2}$$

This can now be substituted into eq. B.2 to give the following expression for $[u'v'w']$:

$$u' = \frac{p\,(pua^2 + 2qvb^2 + 2rwc^2) - u\,(q^2b^2 + r^2c^2)}{p^2a^2 + q^2b^2 + r^2c^2}$$

$$v' = \frac{q\,(2pua^2 + qvb^2 + 2rwc^2) - v\,(p^2a^2 + r^2c^2)}{p^2a^2 + q^2b^2 + r^2c^2}$$

$$w' = \frac{r\,(2pua^2 + 2qvb^2 + rwc^2) - w\,(p^2a^2 + q^2b^2)}{p^2a^2 + q^2b^2 + r^2c^2} \qquad \text{(B.3)}$$

These are the Miller indices, in twin coordinates, of the twin zone axis. It will frequently happen, especially with crystals which have an element of pseudo-symmetry, that these indices are not rational. This means that there is no reciprocal lattice plane in the twin which is normal to the matrix zone axis. However, the twin zone axis Miller indices will very often be nearly rational. In this case, it can generally be assumed that the twin zone axis has the nearest rational indices to the irrational ones given by eq. B.3. If this is done, however, it is important to remember that the matrix reciprocal lattice plane and the twin reciprocal lattice plane are not parallel.

Once the twin zone axis is known, it is an easy matter to determine the twin reflections which should appear on the diffraction pattern. However, the indices of these reflections will be in twin coordinates. Since the entire diffraction pattern, including the matrix reflections, is in matrix coordinates, the indices of these twin reflections in matrix coordinates must be found. The procedure for finding these coordinates is very similar to the method used to find the twin zone axis.

The twin reciprocal lattice point can be considered to be a matrix reciprocal lattice point which has undergone a rotation through 180 degrees about the twin axis. The pre-rotation indices of the point in matrix coordinates, are the same as the post-rotation indices in twin coordinates. Let the original indices in matrix coordinates be (hkl), and its new indices, after the rotation, be $(h'k'l')$, also in matrix coordinates. The direction in reciprocal space which is parallel to the twin axis will be referred to as $(p'q'r')$. For normal twins, these will be the indices of the twin plane. Again, the argument that the two reciprocal lattice vectors, (hkl) and $(h'k'l')$, have the same length can be used and as a result, the following equation can be written:

$$(hkl) + (h'k'l') + n\,(p'q'r') \qquad \text{(B.4)}$$

where n is some factor which depends on (hkl) and $(p'q'r')$. The rest of the derivation is identical to the previous one for the twin zone axis except that the equality in lengths of the

two reciprocal lattice vectors is now expressed as:

$$\frac{h^2}{a^2}+\frac{k^2}{b^2}+\frac{l^2}{c^2} = \frac{h'^2}{a^2}+\frac{k'^2}{b^2}+\frac{l'^2}{c^2}$$

$$= \left(\frac{np'-h}{a}\right)^2 + \left(\frac{nq'-k}{b}\right)^2 + \left(\frac{nr'-l}{c}\right)^2$$

This results in the following expressions for $(h'k'l')$

$$h' = \frac{p'\left(\frac{p'h}{a^2}+\frac{2q'k}{b^2}+\frac{2r'l}{c^2}\right) - h\left(\frac{q'^2}{b^2}+\frac{r'^2}{c^2}\right)}{\left(\frac{p'}{a}\right)^2+\left(\frac{q'}{b}\right)^2+\left(\frac{r'}{l}\right)^2}$$

$$k' = \frac{q'\left(\frac{2p'h}{a^2}+\frac{q'k}{b^2}+\frac{2r'l}{c^2}\right) - k\left(\frac{p'^2}{a^2}+\frac{r'^2}{c^2}\right)}{\left(\frac{p'}{a}\right)^2+\left(\frac{q'}{b}\right)^2+\left(\frac{r'}{l}\right)^2}$$

$$l' = \frac{r'\left(\frac{2p'h}{a^2}+\frac{2q'k}{b^2}+\frac{r'l}{c^2}\right) - l\left(\frac{p'^2}{a^2}+\frac{q'^2}{b^2}\right)}{\left(\frac{p'}{a}\right)^2+\left(\frac{q'}{b}\right)^2+\left(\frac{r'}{l}\right)^2} \qquad \text{(B.5)}$$

These are the indices in matrix coordinates of the twin reflection, (hkl). These equations can also be expressed in terms of [pqr], the indices of the twin axis, rather than $(p'q'r')$, the indices of the direction in reciprocal space which is parallel to the twin axis. These two sets of indices are related to each other in the following way:

$$\frac{p}{p'}a^2 = \frac{q}{q'}b^2 = \frac{r}{r'}c^2$$

Therefore:

$$\begin{aligned} p' &= pa^2 \\ q' &= qb^2 \\ r' &= rc^2 \end{aligned} \qquad \text{(B.6)}$$

When these expressions are substituted into eq. B.5, the following relations are obtained for the indices, in matrix coordinates, of the twin reflection, (hkl), in terms of the twin axis, [pqr]:

$$h' = \frac{pa^2(ph + 2qk + 2rl) - h(q^2b^2 + r^2c^2)}{p^2a^2 + q^2b^2 + r^2c^2}$$

$$k' = \frac{qb^2(2ph + qk + 2rl) - k(p^2a^2 + r^2c^2)}{p^2a^2 + q^2b^2 + r^2c^2} \qquad (B.7)$$

$$l' = \frac{rc^2(2ph + 2qk + rl) - l(p^2a^2 + q^2b^2)}{p^2a^2 + q^2b^2 + r^2c^2}$$

These reflections along with the matrix reflections, are then plotted by finding their components in the x and y-directions. These directions are arbitrary as long as they are perpendicular to the beam direction and to each other. In carrying out these plots, it can be determined whether or not the fact that the twin reciprocal lattice plane may not be parallel to the matrix reciprocal lattice plane has any noticeable effect on the positions of the twin reflections. This is because this procedure prints the projections, along the beam direction, which is usually taken to be the matrix zone axis, of the twin reflections on the zero order Laue zone of the matrix. Figure B.2 shows a twin boundary diffraction pattern of $Y_1Ba_2Cu_3O_{7-\delta}$ for a matrix zone axis of [101]. The coordinates of the matrix and twin reciprocal lattice points, in matrix coordinates, are printed to the right and left of the points, respectively. The twin direction, in twin coordinates, which is parallel to the matrix zone axis is [0.017 0.983 -1], but the twin diffraction pattern for a $[01\bar{1}]$ zone axis is printed. This reciprocal lattice plane is not parallel to the matrix reciprocal lattice plane [101], but there is no noticeable effect on the placement of the points. The line where the two planes intersect is shown by the dashed line. This line runs along the row of unsplit reflections. It can be confirmed that these unsplit reflections are, indeed, common by comparing the coordinates of the twin reciprocal lattice reflection with those of the matrix reflection. Since both sets of coordinates are in the same coordinate system, and the coordinates are identical, it is apparent that the reflections must be coincidental, and this must mean that the two reciprocal lattice planes intersect here. If the angle between the two planes was large enough to produce a noticeable effect on the apparent location of the twin points, the effect would be that the twin reflections would be closer to the dashed line than the nearest matrix

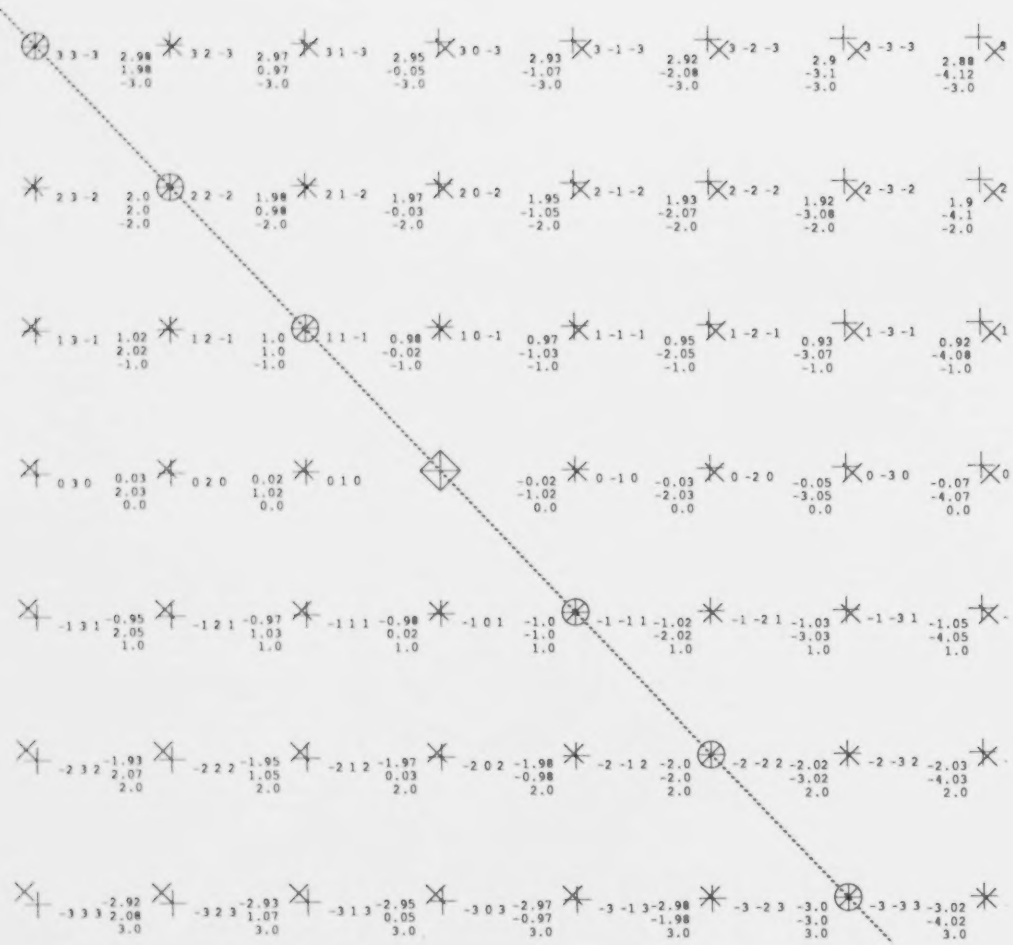

Fig. B.2. Diffraction pattern of $Y_1Ba_2Cu_3O_{7-\delta}$ for a matrix zone axis of [101] and a twin zone axis of [01$\bar{1}$]. The Miller indices, in matrix coordinates, of the twin reciprocal lattice points are to the left of the points, while those of the matrix points are to the right. The line of intersection of the two reciprocal lattice planes is indicated by the dashed line.

reciprocal lattice reflections. This is effect is not noticeable, and so the fact that the two reciprocal lattice planes are not parallel can generally be ignored, as far as the location of the reciprocal lattice points goes.

The previous derivation was for the case of rotation twins. However, as was stated earlier, for all centrosymmetric crystals, reflection twins can be considered to be normal rotation twins since a reflection across a plane has the same effect on such a crystal as a rotation through 180 degrees about an axis which is normal to the plane. However, for non-centrosymmetric crystals, these two operations do not have the same effect and this difference may have an effect on the diffraction pattern. In order to determine what effect, if any, there is on the diffraction pattern, expressions similar to those given above will be derived, but for the case of reflection twins. The new coordinates, $[u'v'w']$ of a matrix lattice vector, [uvw], which has just undergone a reflection across the twin plane, $(p'q'r')$ must be found. Referring to Figure B.3, and noting the equality in length of the vectors, [uvw] and $[u'v'w']$, it can be written:

$$[uvw] - [u'v'w'] = n[pqr] \tag{B.8}$$

where [pqr] is the crystal direction which is normal to the plane $(p'q'r')$. The rest of the derivation would be very similar to the derivation of eq. B.3. The fact that the vector $[u'v'w']$ is now subtracted in eq B.6, rather than added eventually leads to the fact that the equations for $[u'v'w']$ are now the negative of the expressions given in eq. B.3. Since the twin reciprocal lattice planes, $[u'v'w']$ and $[-u'-v'-w']$, each contain the exact same reciprocal lattice points, this change is not significant. However, it is interesting to note that it is this change which causes non-centrosymmetric crystals to have a different orientation after reflection across a twin boundary from rotation through 180 degrees about an axis which is normal to the twin boundary. This is because if [uvw] are the coordinates of a certain atom, rather than a lattice vector, then $[u'v'w']$ and $[-u'-v'-w']$, the coordinates of that atom after the two different operations, are the same only for centro-symmetric crystals.

Using the relations given in eq. B.3 and eq. B.6, the expressions for the Miller indices of the twin zone axis after reflection across the twin boundary, $(p'q'r')$, can be written

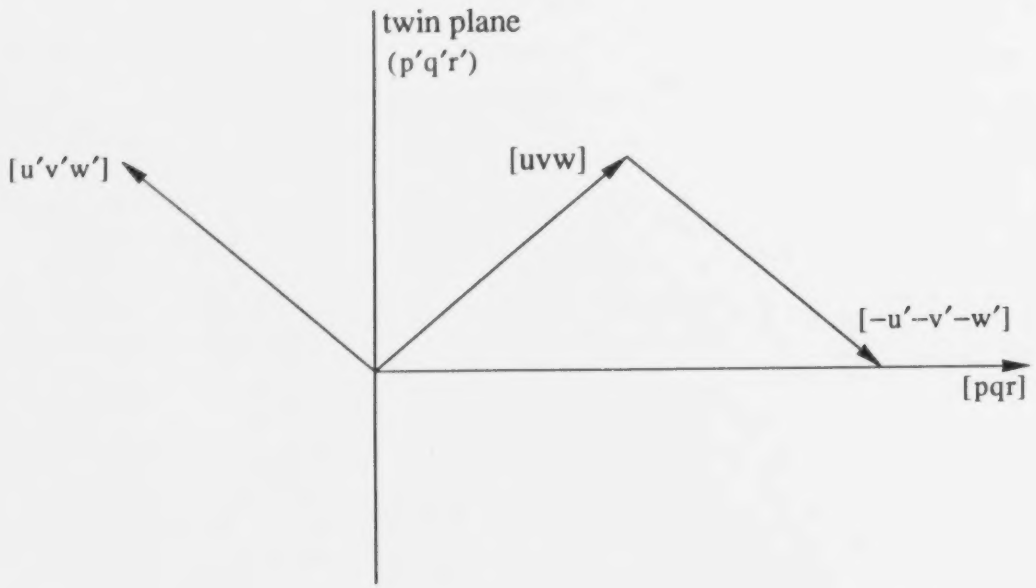

Fig. B.3. The reflection of a matrix vector, [uvw], across a twin plane to give the new vector, [u′v′w′].

as follows:

$$u' = \frac{-\frac{p'}{a^2}(p'u + 2q'v + 2r'w) + u\left[\left(\frac{q'}{b}\right)^2 + \left(\frac{r'}{c}\right)^2\right]}{\left(\frac{p'}{a}\right)^2 + \left(\frac{q'}{b}\right)^2 + \left(\frac{r'}{c}\right)^2}$$

$$v' = \frac{-\frac{q'}{b^2}(2p'u + q'v + 2r'w) + v\left[\left(\frac{p'}{a}\right)^2 + \left(\frac{r'}{c}\right)^2\right]}{\left(\frac{p'}{a}\right)^2 + \left(\frac{q'}{b}\right)^2 + \left(\frac{r'}{c}\right)^2}$$

$$w' = \frac{-\frac{r'}{c^2}(2p'u + 2q'v + r'w) + w\left[\left(\frac{p'}{a}\right)^2 + \left(\frac{q'}{b}\right)^2\right]}{\left(\frac{p'}{a}\right)^2 + \left(\frac{q'}{b}\right)^2 + \left(\frac{r'}{c}\right)^2} \qquad \text{(B.9)}$$

The equations for $(h'k'l')$ in terms of the twin reciprocal lattice coordinates (hkl) are also the negative of eq. B.5, where $(p'q'r')$ are the Miller indices of the twin plane. This change from positive to negative is more important than in the case of the zone axis. This is because, for non-centrosymmetric crystals, $U_g \neq U_{-g}$. Therefore, the intensity of the reflections will be different from what they would be in the case of rotation twins. However, in the case of centrosymmetric crystals, the two situations can still be considered to be the same. In either case, the correct equations for the new indices, $(h'k'l')$, in matrix coordinates, of the reflection, (hkl), as a result of reflection across the twin plane, $(p'q'r')$, are the following:

$$h' = \frac{-p'\left(\frac{p'h}{a^2} + \frac{2q'k}{b^2} + \frac{2r'l}{c^2}\right) + h\left(\frac{q'^2}{b^2} + \frac{r'^2}{c^2}\right)}{\left(\frac{p'}{a}\right)^2 + \left(\frac{q'}{b}\right)^2 + \left(\frac{r'}{l}\right)^2}$$

$$k' = \frac{-q'\left(\frac{2p'h}{a^2} + \frac{q'k}{b^2} + \frac{2r'l}{c^2}\right) + k\left(\frac{p'^2}{a^2} + \frac{r'^2}{c^2}\right)}{\left(\frac{p'}{a}\right)^2 + \left(\frac{q'}{b}\right)^2 + \left(\frac{r'}{l}\right)^2} \qquad \text{(B.10)}$$

$$l' = \frac{-r'\left(\frac{2p'h}{a^2} + \frac{2q'k}{b^2} + \frac{r'l}{c^2}\right) + l\left(\frac{p'^2}{a^2} + \frac{q'^2}{b^2}\right)}{\left(\frac{p'}{a}\right)^2 + \left(\frac{q'}{b}\right)^2 + \left(\frac{r'}{l}\right)^2}$$